- The STUFF Between The STARS -

$\sim$

On
The Evolution
of
The Interstellar Medium
in the
Real and Simulated Universe

by

Jenifer Serena Millard-Parry

A Thesis submitted to Cardiff University
for the degree of Doctor of Philosophy

11th January 2021

Author: Jenifer Serena Millard-Parry

Title: - The STUFF Between The STARS -

~

On

The Evolution

of

The Interstellar Medium

in the

Real and Simulated Universe

Date of submission: 11th January 2021

This one's for me.

DEDICATION

> *'Hi babes. All the best for later. We're all behind you (not literally though, might be a bit crowded in your room!) Love to speak to you, so if your up to it, give us a call. If not I understand babes. If you fancy a walk (clear your head - let me know). Speak to you later. Go get 'em babes [emojis: smiling, dog, cat, rocket, satellite, Saturn, Sun, Moon, stars, Welsh flag, penguin]. Love Mum, Dad & Harry Xxxx'*
>
> JOHN MILLARD; TUES 23 MARCH 2021; 10:43AM

When I was in school, my teachers told me that hardest thing I'd ever do was my A-levels.

They lied.

Maybe that was because they didn't envisage many of us going to University, let alone daring to complete a PhD in Astrophysics. Not bad for a first-gen academic with mild cerebral palsy, right?

This PhD has been so much harder than I ever thought it would be. The past 4.5 years have been filled with the highest highs and lowest lows, both in terms of my professional and personal life. I'm not ashamed to say that I thought about quitting more than once, in those darkest moments. But, I didn't, and here I am at the finish-line. I am so glad I stuck it out. I got to study the Universe and learn

things about it that, for a brief moment (until I told somebody), nobody else knew. I travelled the world for observing trips and conferences, during which I had some of the most extraordinary experiences of my life. I'm sure I will never forget those moments. Of course, I wouldn't have been able to do that without an enormous support network around me. They say it takes a village to raise a child, and a PhD is no different.

Firstly, I wish to thank my supervisors, without whom this thesis (and me joining the ranks of Space Doctor) simply wouldn't have happened. **Haley**, thank you for taking me on as part of team Cosmic Dust, it has been an honour to work with you. You fully dedicate yourself to every facet of your life, always giving 110% - you are an inspiration. Thank you for always supporting my love of outreach - you never stopped me from going on my little adventures which brought me so much joy and made me a more well-rounded person. I hope our paths will cross again. **Steve**[1], we have worked together for some 8 years now and I am truly going to miss working with you. I always enjoyed our meetings - half hard-core sciencing, half putting the world to rights. And although I still like to venture near rabbit-holes, I think I'm much better at spotting them now. Thank you also for introducing me to the magical COSMOS field in my second year, on which much of my thesis is based. You guided and encouraged me out of my second-year rut, and undoubtedly, I would not have finished this thesis without your support and patience[2]. You're a good egg Steve, it's been an honour to work with you.

My PhD was definitely unusual, particularly since I didn't start my thesis work until half-way through my second year. Prior to that, I was lost in the enigmatic world of exoplanets with **Enzo Pascale**. It's thanks to you that I went on a truly once-in-a-lifetime observing trip to South Africa to gather data on transiting exoplanets. Although that work didn't end up in my thesis, I learnt so much from you about good coding practices and the glorious art of converting raw telescope data into scientific splendour. Thanks also to **Sam Gill**, for being a brilliant observing buddy and showing me the ropes - or buttons and keywords, I guess.

[1] Uncle Steve, as we 53-ers often refer to you.

[2] Including a seemingly unlimited willingness to put up with my panicky emails, which I often ended up answering myself. I guess that's just good mentoring.

It wouldn't be right in this section of supervisors to not mention the unofficial third supervisor to us all, **Matt Smith**[3]. The delegated 'grown-up' of 53, you were always willing to help us out with our insignificant PhD-problems, no matter how busy you were. Thank you for answering all the sanity checks, 'quick questions' and solving our never-ending issues with Linux, Python and LaTeX. Thanks also for hosting the Galaxies BBQ year after year, and for the spectacular New Years Eve soirées. You're a diamond geezer and it's been wonderful working with you. Thanks also to my examiners **Tim Davies** and **Jim Geach**. Everyone kept telling me I'd enjoy my viva, and thanks to you, I did. Thank you for some really thoughtful conversation about my work - and for your patience in the beginning, when I was almost too terrified to speak.

It was insightful being part of a diverse team like Cosmic Dust, although there are a few who stand out in particular. **Phil**, you were a joy to have in 53. Thank you for inviting me on the observing trip to La Palma. I had an absolute blast and learnt so much - who knew looking at something *resolved* could be so much fun?! The late-night astrophotography was awesome (even if your photos turned out much better than mine, which I'm not bitter about at all). **Rosie**, thank you for the never-ending support and pep-talks, particularly as I made my way towards the end of the PhD. You were the best cheerleader, and continue to be. **Zoe** and **Hannah**, I'm so glad we went on this crazy journey together, from undergrad to PhD. Particularly Zoe - your strength is truly remarkable. Thank you to all three of you for putting up with my rants and sporadic attempts at comedy to lighten the mood. It was an honour to work with you, and I cannot wait to see what exciting futures lie ahead for us all.

There are too many from 53 to continue to mention in detail, but special mention to Eve (another who has been on this journey with me since undergrad), Tom, Lil' Dan, James, Nikki (for helping make Pint of Science 2019 a literal sell-out event), Andy, Chris (who is dearly missed across the pond, and whom[4] we almost replaced with an Alexa due to his near encyclopedic knowledge of grammar and ... well, everything), and **Gayathri** (next-gen Steve student, dear colleague, true friend). There are also the honorary 53-ers - **Liz** (your eccentric ways brightened all our days), **Alex** (PPMAP genie and connoisseur of the finer things in life), Andrew

[3] Laaandaaan *cockney arms*

[4] I think this is the correct use... I'm sure you'll tell me if not...

(for most excellent board game nights), and Amber (another class of 2016). To the **'Ladies Wot Sciences'** - you are all brilliant researchers, and I am glad to be part of this ever-growing network of amazing women in science. Thank you all for your support in the run-up to thesis submission and viva. The pet pictures helped enormously. To all my fellow **'Plague Doctors'**[5] - we made it. A PhD is a triumph in of itself, but to finish in the middle of a pandemic requires something special[6].

During my 8 years, I worked with, or was taught by, countless members of staff - thank you for showing me the Universe. Special mention to **Jane Greaves** - you are amazing, and your knitted creations deserve an art exhibition. Thank you for always offering a friendly ear and sage advice. Thanks also to the IT team and admin team. We literally would not be able to science without you.

As if doing a PhD wasn't enough, I somehow got myself roped into almost endless amounts of outreach - for that, I have **Chris North** to thank, who got me hooked in undergrad and ceaselessly presents me with amazing opportunities to teach others about space. I hope we'll continue to work together in the future. Special thanks also to **Sarah**, particularly for our adventure to North Wales (I told you I'd fit the car through that gap), and **Mat** - Cardiff Science Festival is a stroke of genius. Frankly, doing outreach kept me sane during this PhD, and reminded me that the world is so much bigger than my tiny research project.

Although, saying that, there are several people who frequently reminded me that the world is so much bigger than my tiny research project - **Ralph, Paul, John, Damien** and our newest member **Dustin**; otherwise known as team **'Awesome Astronomy'**. Co-hosting the podcast with you for the past 4 years has been an utter delight, and I honestly find it hard to put into words how much your support has meant. You've been through it all with me - fortifying me through the lows and celebrating the highs. You've all taught me so much (Elephant's Trunk Nebula, anyone?) and I look forward to every recording session[7]. Thank you all, for everything.

I am lucky to have incredibly supportive family and friends. Thank you for all your patience and love over the past few years - particularly **Ben**, **Jo**, **Tegan**,

[5] If, by some miracle, you are reading this Dedication in the 2030s or later, ask your current house-robot about the Covid-19 Pandemic.

[6] Madness. Complete and utter insanity. Or true grit. Let me know what your pink elephant thinks...

[7] Read: invasion attempt

and **Lauren**. You have always been there for me when I needed you, no questions asked. **Gran** and **Chris** - losing you both in my final year within the space of a week was devastating. Gran, you were always so proud of me for pursuing my dreams - I know because you told everyone you met about your granddaughter who's doing a PhD. You had a hard life, but you did everything to make Mum's life better - which ultimately made mine better. Thank you for all the thought-provoking conversations, and for always asking about my work. I miss you, but I know how proud you'd be of me. Chris - thank you for making undergrad so fantastically random and fun. I could have done with your silly commentary in my final year. Thank you for always being there, and always making me smile. You are dearly missed.

There are just three people left to mention. **Mum** and **Dad** - you are truly the best parents a girl could ever dream of having. You supported my love[8] of space right from the very beginning. In fact, Dad - I blame this whole adventure entirely on you. It was you who first showed me the Moon through your old telescope - and that was it; space, or nothing. Mum - you were breaking down barriers and showing me what it was to be a strong woman in this world before I even knew it was something we had to fight for. You are an amazing role model. I would not have been able to do this without your support, both of you. You wiped away my tears of anger and frustration, and were the first to pop the champagne when it was time to celebrate. I love you both so much.

Finally, **Nick**, who during the course of this PhD went from boyfriend, to fiancé, to husband - but always my rock. This PhD would have been impossible without your unwavering love and support. You gave me the strength to continue when things were at their worst. You always know what to say - and your terrible jokes (and perfect comedic timing) saved the day more than once. Thank you for all your sacrifices[9] so that I could follow my dreams. You are truly amazing, I don't know what I did to deserve you. You make me a better person, every day. I love you, and I can't wait to see what the future holds for us.

And finally finally, Oreo. You didn't make this thesis happen any quicker, but your furry interruptions kept me smiling.

[8] Read: obsession

[9] Although, I will say, you did manage to sneak a couple of good trips abroad out of this PhD, so it wasn't always tough times...

ACKNOWLEDGEMENTS

Beyond my wonderful supervisory team and fellow researchers at Cardiff University, there are several brilliant astronomers without whom this Thesis would not have been possible. I thank Luke Davies and Simon Driver for providing the MAGPHYS dataset, on which much of the work in this Thesis is based. I also thank the *Herschel* Extragalactic Legacy Project (HELP) team, but most notably Kasia Małek, for providing the CIGALE dataset. My thanks go also to Pieter De Vis, for providing average gas fraction measurements for local galaxies. I thank James Simpson for providing the S2COSMOS data and error maps, which are imperative to the work done in this Thesis. I also thank Benedikt Diemer for providing the data from IllustrisTNG, which led to some really quite interesting results.

Additionally, I wish to express my gratitude to the co-authors of my two first-author papers, the content of which constitutes the bulk of this Thesis. Thank you all for your helpful suggestions and insights at several stages of paper development. I also thank Ian Smail, Claudia Lagos, Dylan Nelson and Annalisa Pillepich for their comments on paper drafts. Finally, I thank the Anonymous Referee for Paper I and Matthieu Béthermin for reviewing Paper II. Thank you for not only taking the time to read my papers, but for providing comments and suggestions which ultimately improved the manuscripts.

I acknowledge support from the European Research Council in the form of Consolidator Grant CosmicDust (ERC-2014-CoG-647939, PI H L Gomez).

The James Clerk Maxwell Telescope is operated by the East Asian Observatory on behalf of The National Astronomical Observatory of Japan; Academia Sinica Institute of Astronomy and Astrophysics; the Korea Astronomy and Space Science Institute; the Operation, Maintenance and Upgrading Fund for Astronomical Telescopes and Facility Instruments, budgeted from the Ministry of Finance (MOF) of China and administrated by the Chinese Academy of Sciences (CAS), as

well as the National Key R&D Program of China (No. 2017YFA0402700). Additional funding support is provided by the Science and Technology Facilities Council of the United Kingdom and participating universities in the United Kingdom and Canada (ST/M007634/1, ST/M003019/1, ST/N005856/1). The James Clerk Maxwell Telescope has historically been operated by the Joint Astronomy Centre on behalf of the Science and Technology Facilities Council of the United Kingdom, the National Research Council of Canada and the Netherlands Organization for Scientific Research and data from observations undertaken during this period of operation is used in this manuscript. This research used the facilities of the Canadian Astronomy Data Centre operated by the National Research Council of Canada with the support of the Canadian Space Agency. The data used in this work were taken as part of Program ID M16AL002.

Physical parameters in IllustrisTNG were calculated using COLOSSUS, a public, open-source python package for calculations related to cosmology, the large-scale structure of matter in the universe, and the properties of dark matter halos (Diemer, 2018).

This research as made use of `Astropy`, a community-developed core Python package for Astronomy (Astropy Collaboration et al. 2013; Price-Whelan et al. 2018). This research also used the Python libraries `APLpy` (Robitaille & Bressert 2012; Robitaille 2019), `Matplotlib` (Hunter 2007), `NumPy` (van der Walt et al. 2011), `pandas` (McKinney 2010), and `SciPy` (Virtanen et al. 2020), which were critical to the data analysis performed in this Thesis. I thank Dr Gao, Siyu for the development of `curlyBrace`, a useful addition to Python plots. At several stages of data-wrangling, this work made use of TOPCAT (Taylor, 2005a), initially developed under the UK Starlink project, and has since been supported by PPARC, the VOTech project, the Astro- Grid project, the AIDA project, the STFC, the GAVO project, the European Space Agency, and the GENIUS project. Data maps were also viewed using SAOImageDS9, developed by the Smithsonian Astrophysical Observatory with support from the Chandra X-ray Science Center (CXC), the High Energy Astrophysics Science Archive Center (HEASARC), and the JWST Mission office at the Space Telescope Science Institute (STSI).

PUBLICATIONS

1. **Millard, Jenifer S.;** Eales, Stephen A.; Smith, M. W. L.; Gomez, H. L.; Małek, K.; Simpson, J. M.; Peng, Y.; Sawicki, M.; Beeston, R. A.; Bunker, Andrew; Ao, Y.; Babul, A.; Ho, L. C.; Hwang, Ho Seong; Michałowski, M. J.; Scoville, N.; Shim, H.; Toba, Y., *S2COSMOS: Evolution of gas mass with redshift using dust emission*, 2020, MNRAS, Volume 494, Issue 1, pp.293-315

2. **Millard, Jenifer S.;** Diemer, Benedikt; Eales, Stephen A.; Gomez, Haley L.; Beeston, Rosemary A.; Smith, Matthew W. L., *IllustrisTNG and S2COSMOS: possible conflicts in the evolution of neutral gas and dust*, 2020, MNRAS, Volume 500, Issue 1, pp.871-888

3. Maddox, S. J.; Valiante, E.; Cigan, P.; Dunne, L.; Eales, S.; Smith, M. W. L.; Dye, S.; Furlanetto, C.; Ibar, E.; de Zotti, G.; **Millard, J. S.;** Bourne, N.; Gomez, H.L.; Ivison, R. J.; Scott, D.; Valtchanov, I., *The Herschel-ATLAS Data Release 2. Paper II. Catalogs of Far-infrared and Submillimeter Sources in the Fields at the South and North Galactic Poles*, 2018, ApJ, Volume 236, Issue 2, article id. 30

4. Dunne, L.; Zhang, Z.; De Vis, P.; Clark, C. J. R.; Oteo, I.; Maddox, S. J.; Cigan, P.; de Zotti, G.; Gomez, H. L.; Ivison, R. J.; Rowlands, K.; Smith, M. W. L.; van der Werf, P.; Vlahakis, C., **Millard, J. S.**, *The unusual ISM in blue and dusty gas-rich galaxies (BADGRS)* , 2018, MNRAS, Volume 479, Issue 1, p.1221-1239

CONTENTS

Dedication **vii**

Acknowledgements **xiii**

Publications **xv**

Prologue **xxix**

Summary **xxxi**

1 Introduction **1**

1.1 The Dawn of Extra-galactic Astronomy 1

1.1.1 A Brief History of the Time Before 1

1.1.2 The Great Debate 2

1.2 Galaxy types 5

1.2.1 Morphology 5

1.2.2 Colour 8

1.3 Galaxy formation and evolution 10

1.3.1 The Main Sequence 10

1.3.2 The Peak of Cosmic Star Formation 13

1.3.3 Evolutionary Mechanisms 14

1.3.4 ΛCDM and the CMB 15

1.4 The Interstellar Medium 17

1.4.1 The Multi-phase ISM 18

1.4.2 Traditional Tracers of Molecular and Atomic Hydrogen 20

1.5 Cosmic Dust 22

1.5.1 A Brief History 22

1.5.2 What is Cosmic Dust? . . . 24
1.5.3 Production and Destruction . . . 24
1.5.4 Dust Emission and Dust Mass . . . 26
1.5.5 Dust Masses Beyond the Local Universe . . . 29
1.5.6 Dust Mass Functions . . . 30
1.5.7 Using Dust to Trace the ISM . . . 31
1.6 Sub-mm astronomy . . . 33
1.6.1 Observing Dust From Space . . . 33
1.6.2 From the Ground: JCMT and SCUBA-2 . . . 35
1.7 Cosmological hydrodynamical simulations . . . 37
1.7.1 Overview . . . 37
1.7.2 IllustrisTNG . . . 37
1.8 Thesis Outline . . . 39

2 The COSMOS Field: Submillimetre and Ancillary Observations 43
2.1 Introduction and Motivation . . . 43
2.2 The Sub-millimetre image of the COSMOS field . . . 44
2.3 COSMOS galaxies: constructing a source catalogue . . . 46
2.3.1 Driver/magphys catalogue of galaxies . . . 47
2.3.2 HELP/CIGALE catalogue of galaxies . . . 48
2.3.3 Cross check and validation of the catalogues available in the literature . . . 50
2.3.4 The COSMOS2015 Catalogue . . . 54
2.4 Final COSMOS catalogue of galaxies . . . 56
2.4.1 Removing Active Galactic Nuclei . . . 57
2.4.2 Precision of photometric redshifts in the final sample . . . 60
2.5 Conclusions . . . 61

3 Evolution of Gas Fraction in the COSMOS Field 63
3.1 Introduction and Motivation . . . 63
3.2 Deriving Sub-millimetre fluxes: A stacking analysis . . . 65
3.2.1 Error Estimation using Monte Carlo Simulations . . . 66
3.2.2 Biases in the stacking? SIMSTACK . . . 70
3.2.3 Results . . . 74

3.3 Deriving Gas Masses and Gas Fractions using Sub-millimetre Fluxes 77
3.4 The Evolution of gas fraction with redshift 80
3.4.1 Comparison to literature scaling relations 82
3.4.2 Star-forming and Passive Galaxies 88
3.5 Discussion and Caveats 94
3.6 Conclusions 99

4 The Evolution of Dust Mass: A View from Simulations and Observations 101
4.1 Introduction and Motivation 101
4.2 Datasets 104
4.2.1 Observed data 104
4.2.2 Simulated data: IllustrisTNG 105
4.3 Dust Masses 108
4.3.1 Empirical dust masses from stacking on S2COSMOS map . . 108
4.3.2 Dust Masses from IllustrisTNG 109
4.3.3 A constant dust to metals ratio? 110
4.4 A Local Dust Mass Function 114
4.5 Evolution of the Dust Mass Fraction at High Redshifts 119
4.6 Conclusions 123

5 Investigating the Discrepancy between Simulations and Observations 125
5.1 Introduction and Motivation 125
5.2 Caveats and Assumptions 126
5.2.1 Observed Dust Properties 126
5.2.2 The Dust-to-metals ratio 129
5.3 IllustrisTNG caveats 133
5.3.1 Bound versus 2rad 133
5.3.2 Satellites versus Central sources 136
5.3.3 Metal enrichment prescriptions 141
5.3.4 Investigating Dust Estimates using Total Gas Mass 142
5.3.5 Gas mass evolution 145
5.3.6 Feedback mechanisms 147
5.3.7 Comparison with EAGLE simulations 148
5.4 Conclusions 149

6 Dust Density: A First Look **153**
6.1 Introduction and Motivation . . . 153
6.2 Datasets . . . 155
6.2.1 Dust-to-stellar-mass ratios from MAGPHYS-COSMOS2015 . . 155
6.2.2 Stellar mass functions from Davidzon et al. 2017 . . . 156
6.3 Catalogue Comparison . . . 157
6.3.1 Cross-matching by position . . . 158
6.3.2 Comparing redshifts . . . 159
6.3.3 Comparing stellar masses . . . 160
6.3.4 Distribution in Stellar Mass - Redshift space . . . 163
6.4 Recalculated dust-to-stellar-mass ratios . . . 165
6.4.1 Deriving Sub-millimetre Fluxes - Restacking . . . 165
6.4.2 Dust-to-stellar mass ratios . . . 166
6.5 Dust mass density . . . 169
6.5.1 Dust mass functions . . . 169
6.5.2 Dust mass density . . . 172
6.5.3 Discussion and Caveats . . . 172
6.6 Conclusions . . . 176

7 Conclusions **179**
7.1 Key Results I - The Evolution of Gas Mass Using Dust Emission . . . 180
7.2 Key Results II - Conflicting Dust Mass Evolution in Observations and Simulations . . . 183
7.3 Key Results III: A First-Look at the Evolution of Dust Mass Density . 186
7.4 Future Work . . . 188
7.5 Seeing the Wood for the Trees . . . 190
7.5.1 Final Remarks . . . 191

Appendices **195**

A Estimating Interstellar Gas Mass using Dust Emission **197**
A.1 Defining the constant of proportionality . . . 197
A.2 Deriving the ISM mass equation . . . 199

B Evolution of Simulated and Observed Dust Mass Functions including all Bound Particles in IllustrisTNG **203**

Bibliography **208**

LIST OF FIGURES

1 The dust lanes of the Milky Way, as observed from the southern hemisphere. xxx

1.1 Thomas Wright's 1750 depiction of the Milky Way as a flat layer of stars. 3

1.2 William Herschel's 1785 sketch showing the disk-shape of the Milky Way. 3

1.3 First sketch of M51 by William Parsons in 1845, compared with a modern composite optical and near-infrared image. 4

1.4 Historical and modern period-luminosity relations of Cepheid variable stars in the SMC and LMC. 5

1.5 Edwin Hubble's original 'Tuning Fork' diagram, the first effort made to categorise galaxies by their morphology. 6

1.6 Colour-magnitude diagrams of galaxies in the local ($z < 0.1$) Universe, for both optical and sub-mm selected populations. 9

1.7 Distribution of local ($z < 0.085$) galaxies in the SFR-M_* plane, showing the galaxy Main Sequence and passive clouds. 11

1.8 The evolution of the galaxy Main Sequence up to $z < 1.35$. 12

1.9 The evolution of star formation rate density with redshift. 13

1.10 The 'stuff' between the stars in the constellation of Orion. 18

1.11 Schematic Spectra Energy Distributions of the most important backgrounds in the Universe. 23

1.12 Ejected dusty material surrounding the red supergiant star Betelguese. 25

1.13 Determining the constant of proportionality between sub-mm emission from dust and molecular gas mass. 32

1.14 The atmospheric transmission of sub-mm and mm wavelengths as seen from Mauna Kea, Hawai'i. 34
1.15 The superior resolution of JCMT/SCUBA-2 as compared to *Herschel* at sub-mm wavelengths. 36
1.16 A projection of the distribution of stars across a 50Mpc region of space from the TNG100 simulation at $z = 0$. 38

2.1 The location of the COSMOS field in the constellation of Sextans. . . 45
2.2 The χ^2 distribution of a filtered sub-sample of galaxies in the COSMOS field that have both MAGPHYS and CIGALE fits. 53
2.3 The redshift distribution of a filtered sub-sample of 23,164 galaxies in the COSMOS field that have both MAGPHYS and CIGALE fits and matching redshifts. 54
2.4 A comparison of the stellar masses for a filtered sub-sample of galaxies in the COSMOS field that have both MAGPHYS and CIGALE fits. 55
2.5 The extent of MAGPHYS sources in the COSMOS field (lime square), covering approximately 1 deg^2, across the 850μm match-filtered SCUBA-2 map. 57
2.6 The distribution of sources in the MAGPHYS catalogue but not in the COSMOS2015 catalogue. 58
2.7 The stellar mass and redshift distribution of sources in the MAGPHYS catalogue but not in the COSMOS2015 catalogue. Orange marks all the sources; purple marks sources with $\log(M_*/M_\odot) > 9.5$. 59

3.1 Redshifts for sources in the COSMOS field with $\log(M_*/M_\odot) > 9.5$ and the distribution of MAGPHYS sources in the COSMOS. 67
3.2 Examples of the 850μm IVW stacked stamps. 68
3.3 Normalised histograms of the central pixel values determined using 1000 random source catalogues and MC methodologies for a random selection of $(M_* - z)$ bins. 69
3.4 The resulting stacked 850 μm fluxes from the Inverse-Variance Weighting (IVW) method and SIMSTACK. 76

3.6 The resulting stacked ISM mass fractions with redshift, based on 850μm fluxes in the COSMOS field. 81
3.7 A comparison of a range of scaling relations for gas fraction with redshift presented in Tacconi et al. (2018). 84
3.8 The star formation rate versus stellar mass for the galaxy catalogue used in this work, split into redshift bins. 89
3.9 The star formation rate versus stellar mass for the galaxy catalogue used in this work, split into redshift bins with the χ^2 value of the fits. 90
3.10 The stacked ISM mass fractions with redshift, based on 850μm fluxes in the COSMOS field for star-forming galaxies. 92
3.11 The stacked ISM mass fractions with redshift, based on 850μm fluxes in the COSMOS field for passive galaxies. 93
3.12 The relation between assumed mass-weighted dust temperature, T_d, and calculated ISM mass, M_{ISM}, using emission observed at 850μm, for different discrete redshifts. 95

4.1 Distributions of the stellar masses of galaxies in different redshift bins for TNG100 and MAGPHYS-COSMOS sources. 107
4.2 The dust-to-metal ratio for the local Universe and our samples. . . . 112
4.3 Low redshift DMFs for IllustrisTNG galaxies compared with the literature. 116
4.4 Dust mass versus stellar mass for the TNG100 galaxies at $z = 0$ and for various low-redshift galaxy samples. 118
4.5 Dust-to-stellar mass ratios obtained from TNG100 simulations in redshift and stellar mass bins. 121
4.6 Dust-to-stellar mass ratios obtained from the stacked S2COSMOS fluxes (Millard et al., 2020) and TNG100 galaxies. 122

5.1 The variation of dust mass with assumed mass-weighted dust temperature for discrete redshifts. 128
5.2 The variation of dust mass with redshift for two assumed values of the dust emissivity spectral index, β. 129
5.3 Dust-to-stellar mass ratios obtained from the stacked S2COSMOS fluxes and TNG100 galaxies. 132

5.4 Low redshift DMFs for bound IllustrisTNG galaxies. 134
5.5 Dust-to-stellar-mass ratios of MAGPHYS-COSMOS and TNG100 galaxies for bound sources. 138
5.6 Low redshift DMFs for IllustrisTNG galaxies and local DMFs from the literature. 139
5.7 Dust-to-stellar-mass ratios for TNG100 galaxies plotted against redshift. 140
5.8 Neutral-to-total gas mass ratios for TNG100 galaxies. 143

6.1 Distribution of matched and un-matched sources across the COSMOS field. 159
6.2 Comparing the catalogues' redshift distribution. 161
6.3 Comparing the catalogues' stellar mass distribution. 162
6.4 Percentage difference in ($M_* - z$) bin number counts. 164
6.5 The resulting stacked 850μm fluxes using the same redshift bins as used to calculate COSMOS SMFs. 167
6.6 Dust-to-stellar-mass ratios obtained from the restacked S2COSMOS fluxes. 168
6.7 SMFs from D17 and DMFs from stacked dust masses. 171
6.8 Dust mass density estimates and comparison to literature values. . . 173

B.1 Distributions of the stellar masses of galaxies in different redshift bins for TNG100 and MAGPHYS-COSMOS sources for bound galaxies. 204
B.2 Dust mass versus stellar mass for the bound TNG100 galaxies at $z = 0$ and for various low-redshift galaxy samples. 205
B.3 Dust -to-stellar-mass ratios of TNG100 galaxies for bound data 206
B.4 Low redshift DMFs for IllustrisTNG galaxies for bound sources. . . . 207

LIST OF TABLES

2.1 Line offsets for the best fit lines fit to the MAGPHYS and CIGALE ratio of stellar masses. 56

3.1 Stacked fluxes, gas mass fractions and relevant ancillary data. Red values indicate calculations using 3σ upper limits. Gas mass fractions are not calculated for SIMSTACK results where 3σ upper limits are used for IVW fluxes. 71
3.1 *Continued* 72
3.1 *Continued* 73
3.2 Details of the $(M_* - z)$ bins displayed in Figure 3.3. Additional information can be found in Table 3.1. 74

4.1 Number of TNG100 galaxies considered at each redshift, after removal of un-physical galaxies and resolution mass cuts to $200m_b$ (N_{filt}). 107

PROLOGUE

'The Cosmos is all that is or ever was or ever will be. Our feeblest contemplations of the Cosmos stir us - there is a tingling in the spine, a catch in the voice, a faint sensation, as if a distant memory, or falling from a height. We know we are approaching the greatest of mysteries.'

CARL SAGAN

Human civilisation has always had an affinity for the wonders of the night sky, and evidence of our obsession with the heavens is scattered throughout history. The myths and legends of ancient civilisations rise every night, in the form of constellations and the sprawling dust lanes of our own Milky Way galaxy (dubbed 'The Great Emu in the Sky' by Ancient Aboriginals, see Figure 1). Features of the celestial sphere influenced the construction of some of humanities most prominent architectural endeavours. For example, the Ancient Egyptians aligned the Great Pyramids of Giza with Alnitak, Alnilam and Mintaka (the stars marking Orion's Belt in traditional Western astronomy mythology), many Ancient Mayan buildings were orientated with respect to the rising and setting of Venus, and it is speculated that Stonehenge was built to mark events of astronomical importance.

Despite our curiosity, an understanding of our place in the Universe is something that has long escaped humanity. Arguably, even though we stand on the shoulders of giants and see further than any before, our understanding of the Cosmos is still woefully lacking. Indeed, many of the questions that plagued our forebears are ones we still grapple with today. This Thesis represents a small contribution to our attempt to understand the complex Universe we inhabit.

Figure 1: An unprocessed image of the dust lanes of the Milky Way taken from the South African Astronomical Observatory, Sutherland, during an observing trip. Here, the 'Great Emu in the Sky' is visible, with its head marked by the Coalsack Nebula.

SUMMARY

'Studying whether there's life on Mars or studying how the Universe began, there's something magical about pushing back the frontiers of knowledge.'

SALLY RIDE

In this Thesis, we perform a statistical study of the evolution of the interstellar content of galaxies over cosmic time, using both observational data and results from state-of-the-art cosmological hydrodynamical simulations.

We first investigate the evolution of the gas mass fraction for galaxies in the COSMOS field using sub-millimetre emission from dust at 850μm. We use stacking methodologies on the 850 μm S2COSMOS map, the deepest 850 μm map of the region to-date, to derive the gas mass fraction of galaxies out to high redshifts, $0 \leq z \leq 5$, for galaxies with stellar masses of $10^{9.5} < M_{*}\ (\mathrm{M}_{\odot}) < 10^{11.75}$. In comparison to previous literature studies we extend to higher redshifts, include more normal star-forming galaxies (on the Main Sequence), and also investigate the evolution of the gas mass fraction split by star-forming and passive galaxy populations. We find our stacking results broadly agree with scaling relations in the literature. We find tentative evidence for a peak in the gas mass fraction of galaxies at around $z \sim 2.5 - 3$, just before the peak of the star formation history of the Universe. We find that passive galaxies are particularly devoid of gas, compared to the star-forming population. We find that even at high redshifts, high stellar mass galaxies still contain significant amounts of gas.

We next investigate the evolution in galactic dust mass over cosmic time through i) empirically derived dust masses using stacked sub-millimetre fluxes

at 850μm in the COSMOS field, and ii) dust masses derived using a robust post-processing method, developed as part of this Thesis, on the results from the cosmological hydrodynamical simulation IllustrisTNG. We effectively perform a 'self-calibration' of the dust mass absorption coefficient by forcing the model and observations to agree at low redshift and then compare the evolution shown by the observations with that predicted by the model. We create dust mass functions (DMFs) based on the IllustrisTNG simulations from $0 < z < 0.5$ and compare these with previously observed DMFs. We find a lack of evolution in the DMFs derived from the simulations, in conflict with the rapid evolution seen in empirically derived estimates of the low redshift DMF. Furthermore, we observe a strong evolution in the observed mean ratio of dust mass to stellar mass of galaxies over the redshift range $0 < z < 5$, whereas the corresponding dust masses from IllustrisTNG show relatively little evolution, even after splitting the sample into satellites and centrals. The large discrepancy between the strong observed evolution and the weak evolution predicted by IllustrisTNG plus post-processing may be explained by either strong cosmic evolution in the properties of the dust grains or limitations in the model. In the latter case, the limitation may be connected to previous claims that the neutral gas content of galaxies does not evolve fast enough in IllustrisTNG.

We finish with a first-look estimate of the evolution of the comoving dust mass density, ρ_d, with cosmic time, by combining stacked dust masses with previously published stellar mass functions for the COSMOS field. We estimate DMFs for galaxies in the COSMOS field up to $z \sim 2.5$, and find they show a strong evolution in the high dust mass regime ($\log_{10}(M_d) > 8.0$), showing that galaxies were dustier in the past. By approximately integrating under our calculated DMFs, we estimate the evolution of the dust mass density of COSMOS galaxies with redshift. We find a peak in the dust mass density from $z \sim 1 - 1.8$, and a smooth but substantial decline in the dust mass density of the Universe from $z \sim 1$ to $z \sim 0.35$, with ρ_d decreasing by a factor of 2. We find a decrease in the dust mass density to earlier times. Despite agreeing with literature values on the location of the peak of the evolution of dust mass density with redshift, we find our first-look dust mass density estimates to be a factor $\sim 1.5 - 3$ lower, probably due to calculation approximations and integrating to a higher low dust mass limit. However, our dust

mass estimates can be brought more inline with literature values if we assume a lower mass-weighted dust temperature. The peak of our first-look dust mass density is consistent with the peak of cosmic SFR density, at $z \sim 2$, implying that dust production from stellar deaths is an important pathway for dust to form in the Universe.

In summary, this Thesis expands our knowledge of the evolution of the average gas content of galaxies by extending to higher redshifts, considering more galaxies on the Main Sequence, and by splitting the population into star-forming and passive galaxy populations. We examine the **interstellar medium** of IllustrisTNG galaxies through studies of their post-processed estimated dust masses, allowing us to compare this data to robust dust mass observations. In doing so, we provide independent evidence that feedback mechanisms imposed in IllustrisTNG to allow the simulations to better reproduce physical trends in the local Universe may be too aggressive at intermediate-to-early times, forcing a weak evolution in the neutral gas content of IllustrisTNG galaxies. Alternatively, the lack of agreement between the evolution in the dust content of galaxies between COSMOS and IllustrisTNG galaxies may be evidence for a strong evolution in the physical properties of dust with cosmic time. Finally, we test an alternative method for estimating the evolution of dust mass density with cosmic time. Although we make many approximations in this first-look study, the remarkably good general agreement in the shape of the evolution with other more robust literature studies gives hope for a proper treatment of this method in the future.

Chapter 1
Introduction

'For my part I know nothing with any certainty, but the sight of the stars makes me dream.'

Vincent Van Gogh

1.1 The Dawn of Extra-galactic Astronomy

1.1.1 A Brief History of the Time Before

The first written observation of an extra-galactic object is credited to the 10th century Persian astronomer al-Sufi, who described the Andromeda Galaxy as a small cloud in his 'Book of Fixed Stars' (al-Sufi A. a. R., 964). Musings on the nature of this permanent 'fuzzy blob' and the Milky Way, the river of diffuse light marring the night sky, continued in this abstract fashion for centuries until technology was developed to allow astronomers to escape the constraints of our natural eyesight. In the early 17th century, Galileo Galilei's adaptation of the magnifying tool developed by Dutch eyeglass-makers into an instrument to survey the night sky was revolutionary. Using his telescope, Galileo became the first to resolve the Milky Way into countless stars (Galilei, 1610). Building on Galileo's insight, French astronomer Charles Messier set out to chart comets, and in his quest to avoid 'fuzzy blobs' that weren't comets, inadvertently became the first to catalogue galaxies (Messier, 1774). He called them simply 'spiral nebulae'.

The middle of the 18th century brings us to English astronomer Thomas Wright, who made the first attempt to describe the shape of our galaxy as a flat layer of stars (Figure 1.1), and is credited as the first to speculate that faint nebulae might be distant galaxies (Wright, 1750). German philosopher Immanuel Kant built on Wright's work, elaborating on the idea that 'spiral nebulae' may be other galaxies in their own right, and coined the term 'Island Universes' (Kant, 1755). Towards the end of the 18th century, German-British astronomers William and Caroline Herschel utilised instrument advancements to make the first estimates of the shape of the Milky Way. By assuming that: i) the telescope could resolve all the stars in the Milky Way; ii) there were no stars beyond our galaxy boundary, and iii) stars were reasonably evenly distributed, William Herschel derived an estimate for the shape of the galaxy based on the number of stars he could see in over 680 regions of the sky. He correctly concluded that our galaxy was disk-shaped (Figure 1.2; Herschel 1785; Timberlake 2011).

By the mid-19th century, telescope technology had advanced enough to allow William Parsons, the then Earl of Rosse, to become one of the first to really resolve the detailed spiral structure of some of these 'spiral nebulae' (Figure 1.3; Parsons 1850). As larger and more sophisticated instruments were built, the nature of these contentious 'spiral nebulae', and indeed the extent of our own Milky Way, became the focus of astronomers.

1.1.2 THE GREAT DEBATE

In 1912, Henrietta Swan Leavitt published a new method for determining the distance to objects (Leavitt & Pickering, 1912). She discovered that Cepheid variable stars have a relationship between their luminosity and pulsation period (Figure 1.4). Combined with observations of apparent brightness, a distance to these stars (and therefore the objects they reside in) can be determined. This discovery enabled Harlow Shapley, in 1919, to make the first measurements of the size of the Milky Way. He was also the first to realise that the Sun is not located at the centre of the galaxy (Shapley, 1919).

[10] Full source - https://longstreet.typepad.com/.a/6a00d83542d51e69e20192abb7ce29970d-pi
[11] Full source - http://www.astronomy.ohio-state.edu/~thompson/1101/Herschel_MW_1785.jpg

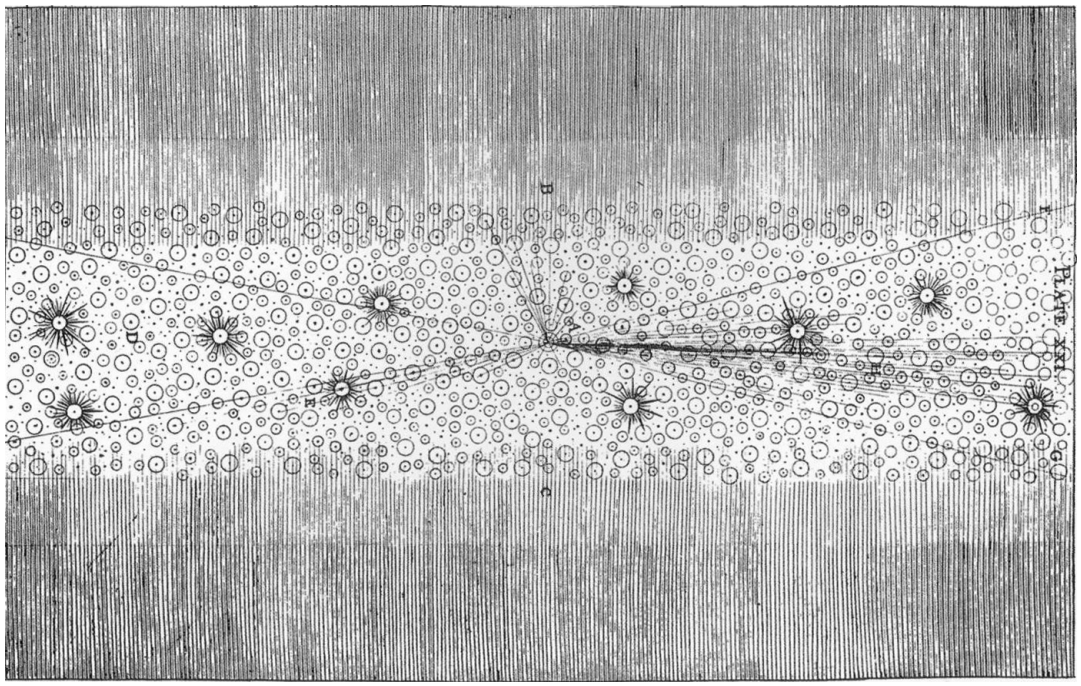

Figure 1.1: An engraved illustration from Wright's 1750 publication *An Original Theory of the Universe*, depicting the Milky Way as a flat layer of stars. Illustration provided by longstreet.typepad.com[10]

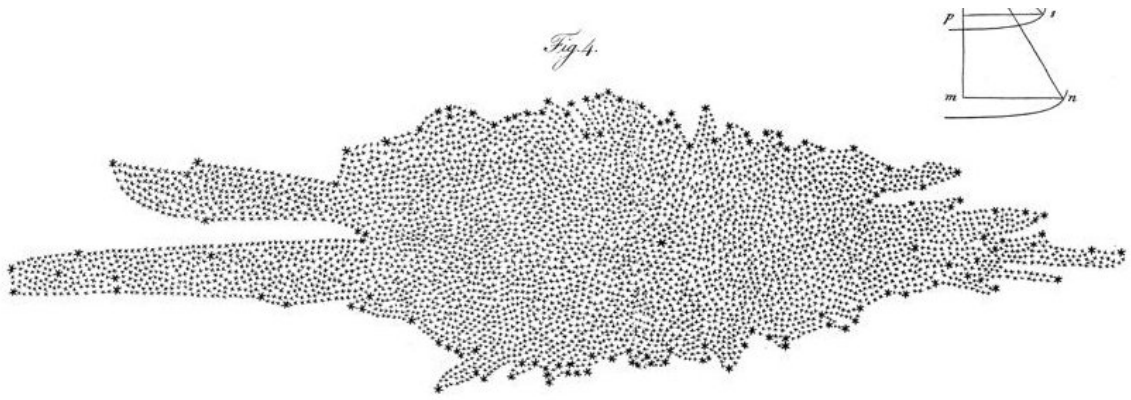

Figure 1.2: Herschel's depiction of the shape of the Milky Way, from his 1785 publication *On the Construction of the Heavens*, illustrating that the Milky Way is disk-shaped. The bold star near the centre of the diagram is the location of the Sun. Illustration provided by astronomy.ohio-state.edu[11]

Figure 1.3: *Left:* first sketch of the Whirlpool Galaxy, M51, by William Parsons (3rd Earl of Rosse) in 1845 (sourced from Steinicke 2012). *Right:* composite optical and near-infrared image of M51. The similarity in the depictions of the structure of the galaxy is remarkable. M51 image credit: NASA, ESA, S. Beckwith (STScI) and the Hubble Heritage Team.

With conflicting evidence mounting as to the nature of the Universe, Harlow Shapley and Heber Curtis organised The Great Debate of 1920. The subject of discussion was 'spiral nebulae' and the size of the Universe (Shapley & Curtis, 1921). Shapley argued that 'spiral nebulae' were small, and part of the Milky Way. Simply put, Shapley argued that the Milky Way *was* the Universe. He supported his argument by pointing out that if the 'Andromeda Nebula' was a galaxy like the Milky Way, it would have to be some 10^7 to 10^8 light years (ly) away - a distance that seemed impossible. A colleague, Adriaan van Maanen, had also claimed to have observed the 'Pinwheel Nebula' (M101) rotating (van Maanen, 1916). Therefore, the nebula must reside within the Milky Way to avoid it breaking the speed of light. Curtis, on the other hand, was in favour of the 'Island Universe' theory. He noted that the number of novae in the 'Andromeda Nebula' was at least comparable to the number noted in the Milky Way. Why should a small patch of our galaxy have just as many novae? He also noted that many of the 'spiral nebulae' hosted dark lanes, much like our own Milky Way.

The debate was resolved a few years later by Edwin Hubble who used Cepheid variable stars to estimate the distance to the 'Andromeda Nebula' (Hubble, 1925). His distance estimates placed the 'Andromeda Nebula' far beyond the best estimates of the size of the Milky Way, at some 285,000 parsecs[12] ($\sim 10^6$ ly). His observational work confirmed the 'Island Universes' hypothesis of Wright and

[12] A revised distance of 275,000 parsecs was published in Hubble (1929).

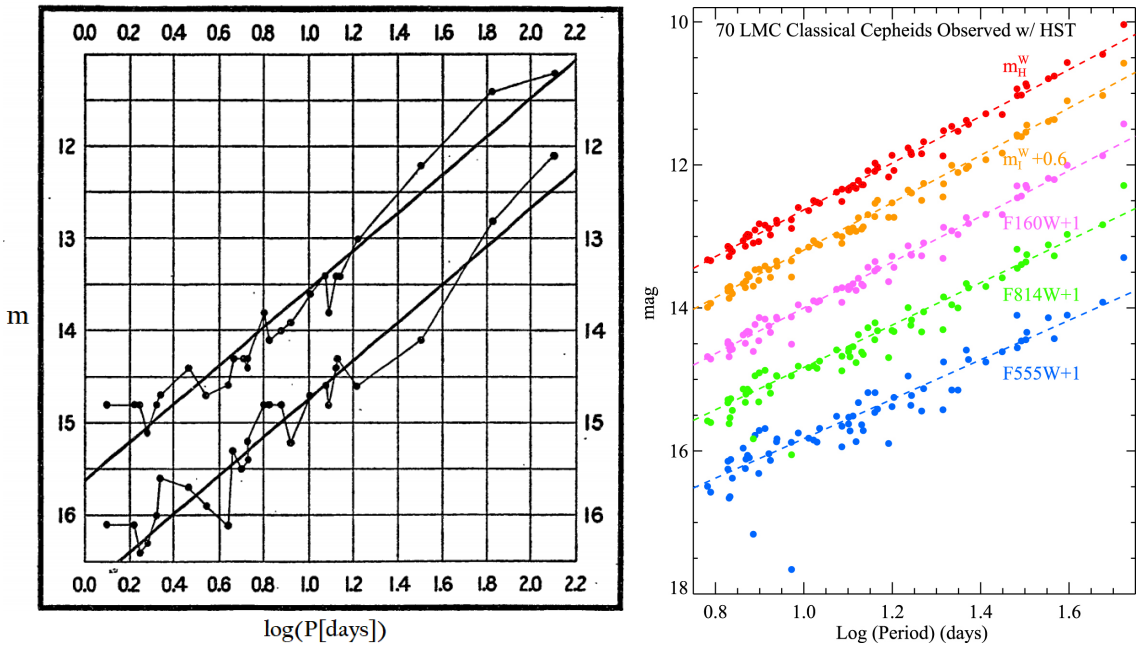

Figure 1.4: *Left:* first observations showing the luminosity-period relation of Cepheid variables in the Small Magellanic Cloud (SMC) from Leavitt & Pickering (1912). The two lines are for maximum and minimum estimated magnitudes. Since it can be reasonably assumed that all Cepheids in the SMC are at the same distance from the observer, the plot illustrates that the period of pulsation for Cepheids is intrinsically linked to their luminosity. *Right:* a modern version of the same plot, courtesy of Riess et al. (2019). The figure shows the luminosity-period relation for 70 long-period Cepheid variables in the Large Magellanic Cloud (LMC) observed with the Hubble Space Telescope through various bands.

Kant, and inspired a whole new branch of astronomy research to begin.

1.2 GALAXY TYPES

1.2.1 MORPHOLOGY

With the establishment of 'spiral nebulae' as 'Island Universes' in their own right, astronomers quickly sought to understand these new astrophysical bodies. The obvious way to begin to understand galaxies was to categorize them based on their visual appearance, or morphology. Although a somewhat subjective undertaking, even today's astronomers agree that galaxies fall largely into three main classifications; ellipticals, spirals and lenticulars. A minority are described as irregular or dwarf galaxies.

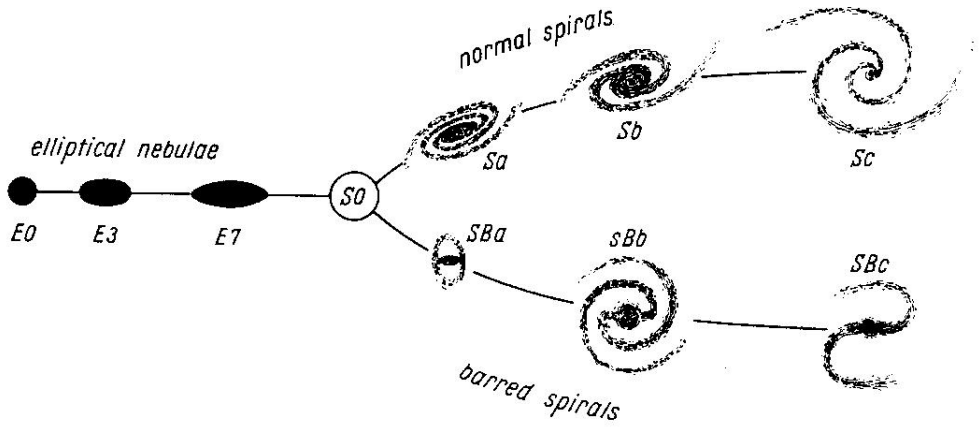

Figure 1.5: Hubble's original Tuning Fork Diagram (Hubble, 1936). Spiral galaxies sit along the prongs of the tuning fork under two designations, 'barred' and 'normal', depending on the shape of their central bulges. Lenticular galaxies sit at the intersection of the fork. Irregular and dwarf galaxies are notably missing from the original diagram. Image provided by people.virginia.edu[14]

The first classification scheme for galaxies was published in 1926 by Edwin Hubble (Hubble, 1926). Known as the 'Tuning Fork diagram' (Figure 1.5), it was never intended to represent an evolutionary path, although it was often assumed that this was the case. As a consequence of the incorrect interpretation of the diagram's meaning, elliptical galaxies, which lie along the handle of the tuning fork, were labelled as 'early-type galaxies' (ETGs), and spirals, which lie along the prongs of the tuning fork, as 'late-type galaxies' (LTGs) - and as is the wont of astronomers, the naming convention remains. In a delightful moment of serendipity,[13] Hubble included a third category of galaxy at the intersection of the handle and prongs - a hybrid galaxy, today known as a lenticular - despite there being no evidence at the time for such galaxies.

At optical wavelengths, elliptical galaxies appear as smooth balls of diffuse light, which are more concentrated at the centre and fade away at the edges. They can be spherical or more oblate, and are distinctly more yellowish-red in colour. On the Tuning Fork diagram, they are denoted 'E', with a classification number ranging from 0-7 denoting their oblateness (Figure 1.5). The lower the number, the more spherical the elliptical galaxy appears on the sky. Their spherical nature is supported by the random motion of stars - from the chaos, something remarkably refined emerges. The stellar population of elliptical galaxies is dominated by

[13] Or profound foresight, as some may argue...

older, cooler, less massive and therefore longer-lived stars (which are themselves yellowish-red in colour). Typically, elliptical galaxies are largely devoid of star-forming gas and dust, and thus contain little to no active star-formation.

Spiral galaxies, on the other hand, are positively vibrant and dynamic in comparison. Structurally, the disks of spiral galaxies are dominated by spiral arms, regions of active and intense star formation. The newly formed (but short-lived) massive, young and hot stars of the spiral arms give the disk of spiral galaxies their distinct blue colour. Marring the blue disks of spiral galaxies are dark dust lanes. Dust was long considered a nuisance due to its ultraviolet (UV) and optical light obscuring nature. However, as we shall explore in this Thesis, dust is a key tool for understanding galaxy evolution. The core of a spiral galaxy is small and more yellowish-red in colour as it is dominated by older stars and is not typically highly star-forming. However, this does not mean that there is no star-formation at all in the cores of spiral galaxies. Up to 30 per cent of the stellar mass of bulges may have formed within the past 2Gyr (e.g. Thomas & Davies 2006). However, we typically find that the dominate stellar population in the bulges of spiral galaxies is old ($\sim$ 10Gyr), and likely formed at the same time in an intense burst of star-formation. At later times, minor bursts of star-formation can occur with the rare availability of suitable star-forming gas in the complex, dynamical, turbulent environment that is the core of a spiral galaxy.

As indicated by the Hubble Tuning Fork diagram (Figure 1.5), there are two main types of spiral galaxy. Along one prong of the fork sit 'normal' spirals (denoted 'S') and along the other sit 'barred' spirals (denoted 'SB'), both with sub-classifications 'a-c' indicating bulge size and nature of the spiral arms. Sa/SBa galaxies have tightly wound spiral arms with large central bulges; Sc/SBc galaxies have very small bulges and loosely wound, flocculent spiral arms; Sb/SBb galaxies are in between the two. For barred spiral galaxies, the spiral arms extend from the ends of these structures, and so typically have only two spiral arms. Normal spiral galaxies can have up to four well-defined spiral arms, or a more 'fluffy', undefined nature in the form of flocculent arms. In the local Universe, at least half of all spiral galaxies contain a bar. Galaxy bars are considered to be transient features tied to galaxy evolution. It is thought that they funnel gas towards galaxy centres, fuelling sporadic bursts of late star-formation (Sheth et al., 2008).

Lenticular galaxies (denoted 'S0' on the Hubble Tuning Fork diagram; Figure 1.5) are intermediate between spiral and elliptical galaxies. Like spiral galaxies, they have a distinctive disk. However, they lack spiral arms, facilitating the need for a separate category for such galaxies. Similarly to elliptical galaxies, they contain little gas and dust and so have little to no active star-formation. Their stellar populations are typically older, and as such, are often classified as ETGs along with elliptical galaxies, since they share many of the same physical properties.

In the local Universe, by mass, ∼70 per cent of galaxies are ETGs, with the rest LTGs[15] (Kelvin et al., 2014). For ETGs, the relative proportion of lenticular to elliptical varies by mass, with lenticular galaxies dominating at lower stellar masses ($\sim 10^{10.5} M_{\odot}$) and elliptical galaxies dominating at higher masses ($\sim 10^{12} M_{\odot}$; see Wilman & Erwin 2012). However, it is worth noting that the fraction (by mass) of LTGs and ETGs varies with galaxy environment, with ETGs dominating the centres of galaxy clusters (Wilman & Erwin, 2012).

1.2.2 COLOUR

The subjective nature of classifying galaxies by their morphology leads to the desire for a classification scheme that is more physically meaningful. The clear difference between the optical colours, even by eye, of ETGs and LTGs suggests that exploring optical colour-space is a reasonable place to begin.

The dichotomy of the galactic population is readily identified in a (*g*-*r*) colour-magnitude diagram (Figure 1.6). Two distinct clouds of galaxies emerge, commonly described as the 'red sequence' and 'blue cloud'. In between is the 'green valley', a region of optical colour-magnitude space largely devoid of galaxies.

At first glance, the sharp division between the optically-selected galaxy population in the bottom left panel of Figure 1.6 suggests that galaxies quickly transition between the two regions. The traditional interpretation is that LTGs occupy the blue cloud and then eventually evolve towards the red sequence populated by ETGs (e.g. Baum 1959; Visvanathan 1981; Strateva et al. 2001; Bell et al.

[15] This is, of course, negating a minor contribution from irregular and dwarf galaxies.
[15] Full source - http://people.virginia.edu/~dmw8f/astr5630/Topic02/t2_hubble_tfork.html

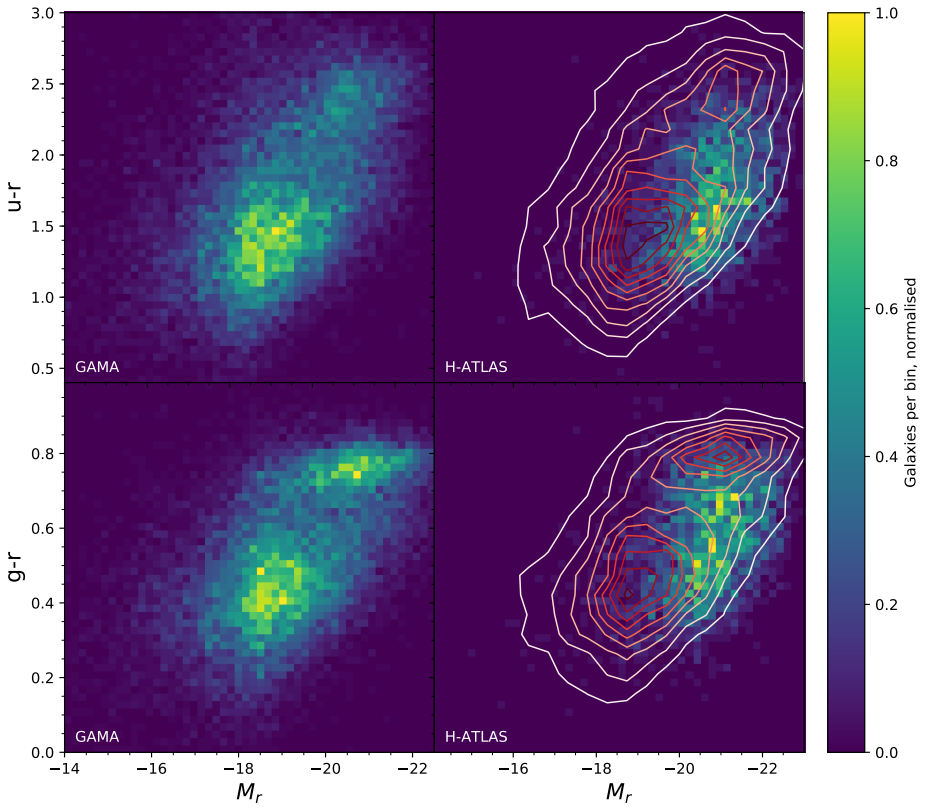

Figure 1.6: The distribution of nearby galaxies ($z < 0.1$) in the colour verses absolute r-band magnitude plane, courtesy of Eales et al. (2018b). The colour-scale illustrates the density of galaxies. The *bottom panels* clearly show the dichotomy of the galactic population. *Left panels*: optically selected galaxies from the GAMA survey (Driver et al. 2009; Liske et al. 2015). *Right panels*: sub-mm selected galaxies of the H-ATLAS (Eales et al., 2010). The overlaid contours are the distribution of GAMA galaxies from the *left panels*.

2003; Cortese 2012 and references therein). This is logical, since the stellar population of LTGs is dominated by hot, young, massive, short-lived stars, as indicated by its bluer colour, and this is therefore evidence of ongoing star formation. Conversely, the stellar population of ETGs is dominated by older stars and this implies a lack of recent star formation. Since the green valley is largely devoid of galaxies, the implication is that the transition is quick. This in turn implies that the transition cannot simply be due to a slow decline in star formation as the fuel for stars is gradually used up. It implies that there may be other mechanisms influencing the transition from LTG to ETG.

However, evidence is emerging that the apparent dichotomy in the galaxy population might be a selection effect (e.g. Eales et al. 2018a; Eales et al. 2018b;

Corcho-Caballero et al. 2020). Malmquist bias means that optical surveys miss galaxies with high-gas content (i.e. a significant amount of the fuel for star formation, as opposed to the stars themselves) and high dust content (since dust acts to block optical light). When incorporating such galaxies traditionally missed by optical surveys, a more general galaxy sequence emerges, with a smoother transition between morphological types, color and physical properties. As can be seen in the lower right panel of Figure 1.6, in the same colour-magnitude diagram, the sub-millimetre (sub-mm) selected H-ATLAS galaxies occupy a region typically devoid of optically-selected galaxies (Eales et al., 2018b). This new and emerging picture highlights the importance of studying the dust content of galaxies.

1.3 GALAXY FORMATION AND EVOLUTION

1.3.1 THE MAIN SEQUENCE

The clear dichotomy in the morphology and optical colour of galaxies calls for an examination of physical properties, to allow us to begin to understand the origins of the clear diversity in the galactic population. Based on the previously identified visual differences between galaxies, it seems that a diagram exploring the star formation rate (SFR) and stellar mass (M_*) of galaxies might be appropriate. In particular, the former parameter quantifies many of the visual differences of galaxies - for example, the optical colour of a galaxy is rooted in how well it is forming stars, or not, as the case may be.

The distribution of galaxies on the SFR-M_* (or specific star formation rate, sSFR, the SFR per unit M_*) plane shows that, for a vast majority of the galactic population, there is a tight correlation between these two parameters (Figure 1.7). Typically, this region is well described by a power law with a logarithmic slope. Many studies have proposed that this region is populated by actively star-forming blue cloud galaxies, and it has earned the name 'Main Sequence' (MS), indicating that this region of parameter space is where galaxies spend the majority of their lives (e.g. Noeske et al. 2007; Peng et al. 2010; Rodighiero et al. 2011; Renzini & Peng 2015; Oemler et al. 2017; Corcho-Caballero et al. 2020 and references therein). The small amount of scatter around the MS is thought to indicate homogeneity between star-forming galaxies.

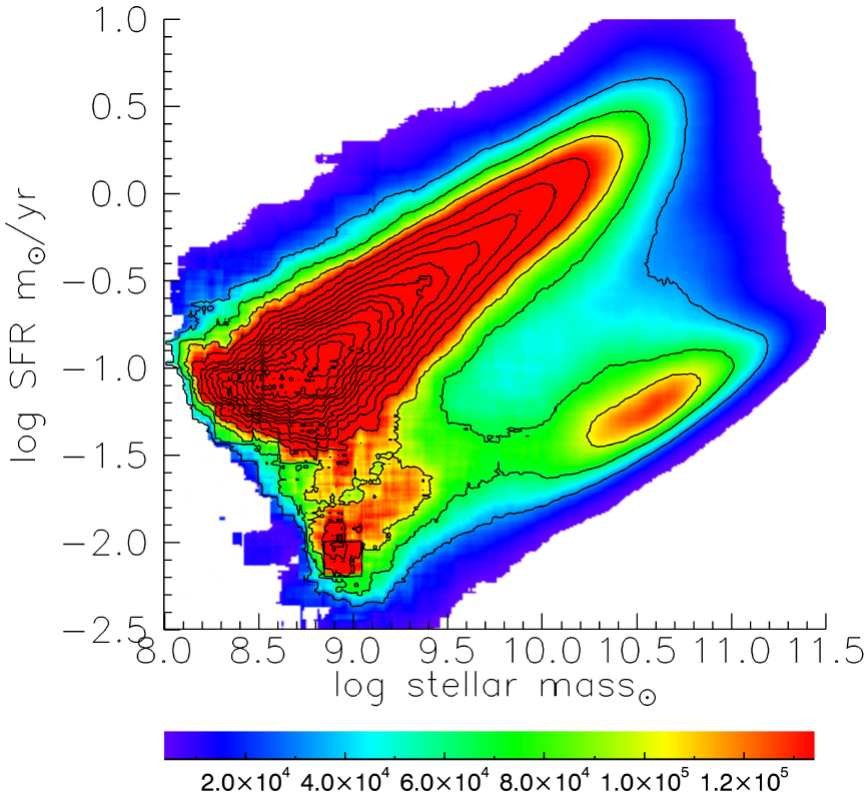

Figure 1.7: Distribution of ∼240,000 local galaxies ($0.02 < z < 0.085$) extracted from the Sloan Digital Sky Survey (SDSS) DR7 release (Abazajian et al., 2009) in the SFR-M_* plane, courtesy of Renzini & Peng (2015). Contours illustrate the number density of galaxies, as does the colour scale. There are two passive clouds - the high-mass one is attributed to mass quenching and the low-mass one to environment quenching.

A minority of galaxies occupy a 'passive cloud' which sits below the MS, typically at higher stellar masses (Figure 1.7). These galaxies have exceptionally low star formation rates and are mostly red-and-dead elliptical galaxies or ETGs, having formed most of their stars in the past at high-redshifts (Renzini & Peng, 2015). Sitting at least 10× above the MS are 'starburst' galaxies - galaxies undergoing extraordinarily high amounts of star formation for a short period (e.g. Hung et al. 2013; Luo et al. 2014; Cibinel et al. 2019). It is worth noting that some studies show a turnover in the MS at high-masses (Figure 1.8; e.g. Whitaker et al. 2014; Lee et al. 2015; Schreiber et al. 2015; Tomczak et al. 2016; Bisigello et al. 2018; Lee et al. 2018; Leslie et al. 2020). The characteristic turnover mass is $\sim 10^{10} M_\odot$. Much like the existence of the passive cloud, the shift of high-mass galaxies to correspondingly lower star formation rates indicates some fundamental change, an

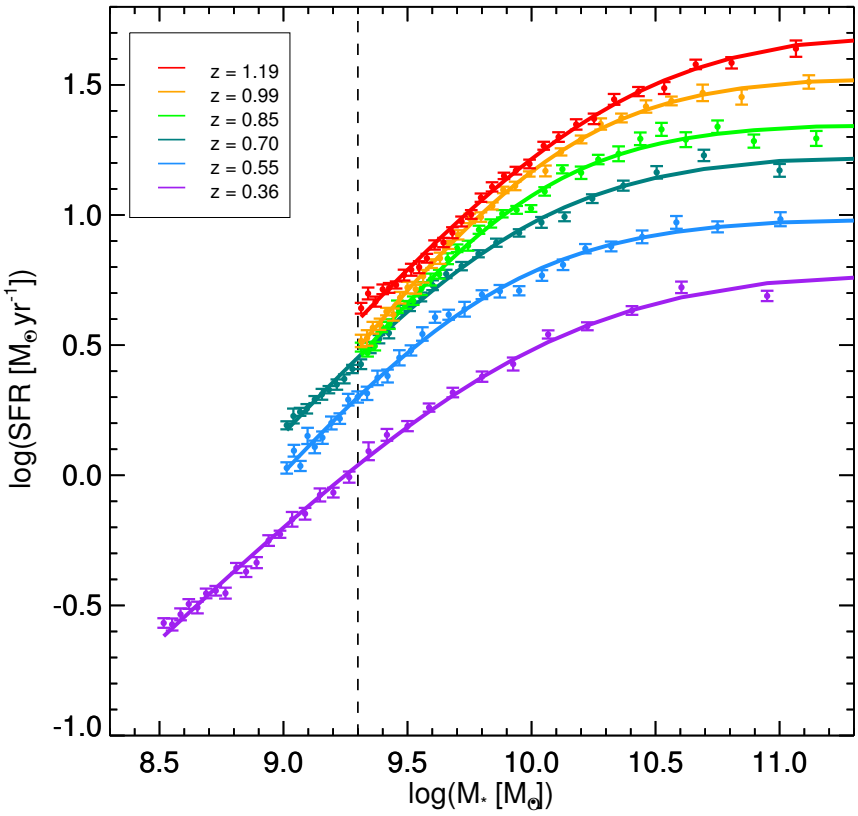

Figure 1.8: The evolution of the galaxy MS with redshift, for ∼62,000 star-forming galaxies at $z < 1.3$, courtesy of Lee et al. (2015). Note the turnover in the MS at high stellar masses. The galaxies have been split into approximately equally populated stellar mass bins.

evolutionary mechanism that halts or inhibits star formation in massive galaxies (Renzini & Peng, 2015).

The Main Sequence can be examined for galaxies at a myriad of redshifts, giving us snapshots of the galactic population at different epochs (e.g. Daddi et al. 2007; Elbaz et al. 2007; Sargent et al. 2014). Although the slope of the MS remains largely the same for epochs sampling most of the history of the Universe, its normalization changes (Figure 1.8), indicating that galaxies formed stars more proficiently in the past (at least out to $z \sim 1.2$ in Figure 1.8). Even out to high-redshifts, the MS correlation between SRF and M_* is tight, suggesting that across most of the history of the Universe, galaxies follow the same evolutionary path. Note that this does not mean that individual galaxies move along the MS. The persistence of the MS implies that galaxy evolution is driven by the same underlying physics and mechanisms throughout cosmic time, the result of which is a tight correlation

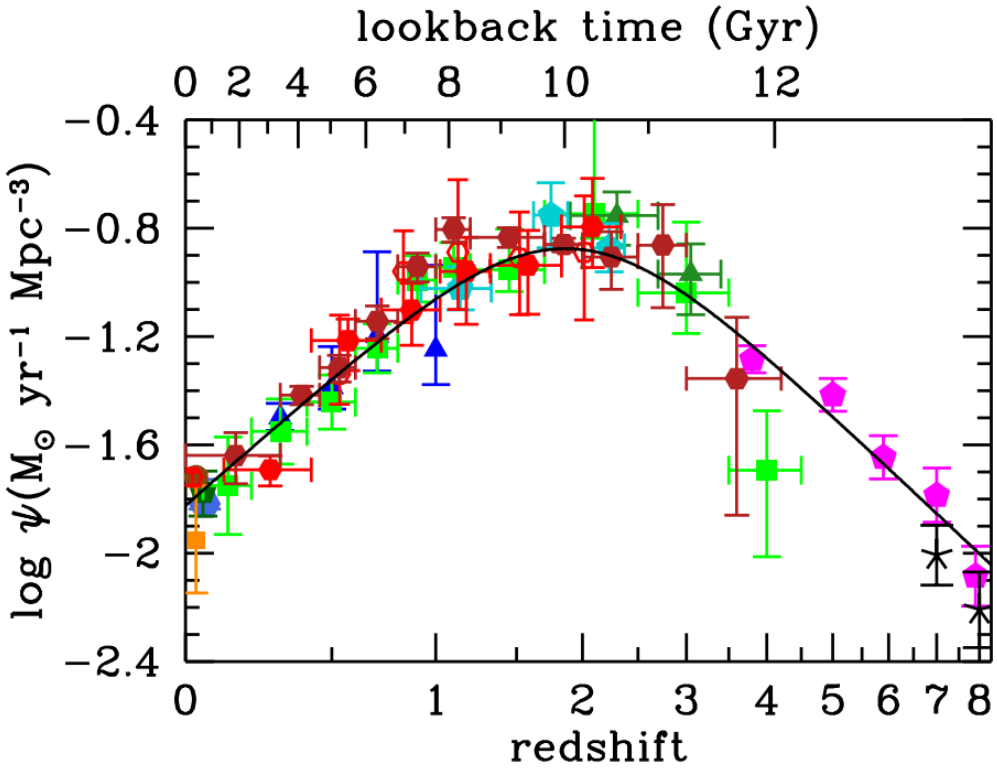

Figure 1.9: The evolution of star formation rate density with redshift (the history of cosmic star formation), courtesy of Madau & Dickinson (2014). *Red/orange*: IR rest-frame measurements. *Blue/green/magenta*: FUV rest-frame measurements.

between SFR and M_* seen at all epochs.

1.3.2 THE PEAK OF COSMIC STAR FORMATION

Understanding the rate at which galaxies convert gas into stars over cosmic history is important. It allows us to probe the evolution of galaxies and understand how the diverse galactic population that we observe today came to be. The Main Sequence has shown us that there is a strong evolution in the SFR of galaxies with cosmic time. We can probe this further by considering the evolution of the SFR density of galaxies with redshift (Figure 1.9), where the SFR density probes the SFR of all galaxies contained within a cosmological volume (or redshift slice). We can see that the SFR density of galaxies in the local Universe is at least an order of magnitude below that of galaxies at $z \sim 2$, the peak of star formation in the Universe (Madau & Dickinson, 2014).

Understanding why the peak of star formation occurs at $z \sim 2$ is an important question, and motivates investigations into the fuel for star formation, molecular gas. It also drives investigations into the dust content of galaxies, since dust is a by-product of star formation. Of particular interest is the evolution of these quantities with cosmic time, themes that we investigate in this Thesis.

1.3.3 EVOLUTIONARY MECHANISMS

The downturn of star formation in recent times and the evolution of galaxies from active, star-forming LTGs to passive ETGs motivates considerations as to the mechanisms behind the quenching of star formation. Much like the galactic population is diverse, there is a huge variety of mechanisms that might cause star formation in a galaxy to cease. These mechanisms vary strongly with environmental density i.e. with location in a cluster environment, and also between different types of galaxies.

In particularly dense regions, galaxy interactions can play a dominant role in dictating a galaxy's evolution. Mergers can trigger intense bouts of star formation for short periods in the resulting large galaxy. Such intense activity can cause the galaxy to use up most of its star-forming gas, causing a galaxy to become passive (e.g. Davies et al. 2015b; Weigel et al. 2017). Other gravitational interactions between galaxies, like close-passes, can disturb the content of galaxies, interfering with current and future star formation (e.g Boselli & Gavazzi 2006; Klimentowski et al. 2010).

Galaxy clusters have unique environmental features that can inhibit star formation. The space between galaxies contains hot gas known as the intra-cluster medium. Galaxies falling into the large potential well of the cluster pass through this gas. If the gas pressure of the intra-cluster medium is enough to overcome the gravitational potential of the infalling galaxy, cold star-forming gas and dust can be stripped out of a galaxy, impeding star formation and eventually quenching a galaxy (e.g. Boselli & Gavazzi 2006; Cortese et al. 2010; Gomez et al. 2010; Boselli et al. 2014). This is often known as 'ram pressure stripping'.

There are also quenching mechanisms that can happen on a local galaxy scale. In low-mass galaxies (which have a lower gravitational potential well), stellar feedback is an important star formation regulator by generating turbulence and

galactic outflows, the latter of which can physically remove star-forming gas from galaxies. Supernovae winds can also act to expel star-forming gas from low-mass galaxies (e.g. Hayward & Hopkins 2017 and references therein).

When the super-massive black holes (SMBHs) at the centres of massive galaxies are accreting mass, they are known as active galactic nuclei (AGN). Generally, in terms of observations and models, there are two modes of AGN feedback, both of which can quench star formation. There is 'thermal/radiative' feedback, and 'kinetic/mechanical' feedback (Barai et al. 2014; Combes 2015; Harrison 2017; Morganti 2017; Bieri 2018; Harrison et al. 2018). Distinguishing between the two is non-trivial since their impact on the star-forming gas can be similar. Thermal/radiative feedback from AGN is usually associated with high accretion rates onto the SMBH. Feedback happens via the injection of thermal energy into the gas - essentially, the star-forming gas in the galaxy is prevented from cooling, which inhibits star formation. However, high-speed ($v \sim$ 0.1-0.2c) winds (Harrison, 2017; Harrison et al., 2018) can also drive star-forming material out of a galaxy. Thermal/radiative feedback is observationally rarer and is associated with lower-mass galaxies with ongoing star formation. Kinetic/mechanical feedback, also known as 'radio' or 'jet' mode feedback, is associated with lower accretion rates and, observationally, is typically associated with higher-mass galaxies ($M_* > 10^{11} M_\odot$) with older stellar populations (see Harrison (2017) and references therein). Instead of thermal energy being imparted to the surrounding gas, kinetic energy and momentum is imparted, boosting the velocity of the gas. Kinetic/mechanical feedback from AGN suppresses star formation by physically ejecting cool gas from the galaxy altogether, or by inhibiting gas cooling processes.

1.3.4 ΛCDM AND THE CMB

A seemingly obvious question that we have thus far circumvented is: how did structures as complex as galaxies first arise? What seeded these behemoths of the Universe? The current concordance model of the Universe is ΛCDM (Peebles, 1980). The name of this model derives from: i) the dominant form of matter in the Universe, Cold Dark Matter (CDM), a form of matter that only gravitationally interacts with other matter particles and does not emit, or interact with, electromagnetic radiation, and ii) the cosmological constant, Λ, which refers to Dark

Energy, a theoretical form of energy believed to be the driving force behind the accelerating expansion of the Universe. In this model, the Universe that emerged from the Big Bang was remarkably homogeneous. However, small quantum fluctuations present during inflation (Guth, 1981), a brief period of faster-than-light exponential expansion[16] of the Universe, led to small matter over-densities in the 'Cosmic Soup', the baryon-photon plasma constituting the Universe at early times. These quantum fluctuations are imprinted in the minute temperature fluctuations of the Cosmic Microwave Background (CMB), which acts as a record of the inhomogeneities present in the Universe when matter and light decoupled in the Era of Recombination, around 380,000 years after the Big Bang. These inhomogeneities, on the order of $\sim 10^{-5}$ in the CMB, are the seeds of the structure of the Universe, which grow under the influence of gravity, with both normal and dark matter gathering at these perturbations. From these density perturbations, the first galaxies formed and then over time, merged to form larger galaxies in a process known as 'hierarchical assembly'.

The very existence of galaxies and the 'lumpy' Universe we see today is strong evidence for Cold Dark Matter. Before recombination, pressure from photons coupled to baryonic matter prevents the inhomogeneities in the baryons from growing. Although the density perturbations can grow *after* recombination, there is simply not enough time for these small perturbations to grow and create the structure we see in the Universe today. However, since CDM does not interact with light, the inhomogeneities in CDM can grow *before* recombination. After recombination, baryons can then fall towards the density enhancements already present in the dark matter, accelerating the formation of the dense structures that we see today in the Universe. Hierarchical assembly continues, with small dark matter haloes merging to form larger ones, with baryonic matter in the form of galaxies following this behaviour.

However, there are some issues with this model, the most notable of which is 'downsizing'. This refers to the observation that more massive elliptical galaxies have older stellar populations compared to disk galaxies, which are less massive, have younger stellar populations and are actively star-forming (Neistein et al., 2006). This implies that the stars of the most massive galaxies formed at earlier

[16] The Universe increased in size by around 60 e-folds over $\sim 10^{-34}$s.

epochs, seemingly in contrast to hierarchical assembly. Although, this does not necessarily mean that ΛCDM is wrong - there are environmental factors to consider. For example, Cattaneo et al. (2008) showed that 'downsizing' could be a natural result of star formation ceasing in galaxies that reside in the most massive dark matter haloes ($M_{\rm halo} > 10^{12} M_{\odot}$) early on due to AGN feedback or shocks, then only growing through 'dry mergers' that do not bring additional star-forming gas into the galaxy. These galaxies form the most massive elliptical galaxies that we see today. Smaller star-forming galaxies are then shut-down at later times. Arguably, such evolution *is* consistent with hierarchical assembly.

Understanding the underlying physical model of the Universe is a strong motivator for continuing to study galaxy evolution. This itself motivates investigations into the content of galaxies, particularly the 'stuff' between the stars, the Interstellar Medium, which we discuss in the next Section.

1.4 THE INTERSTELLAR MEDIUM

The Interstellar Medium (ISM) refers to the material found between the stars (Figure 1.10). For typical star-forming galaxies in the local Universe, the mass of the ISM is around 10-20% the mass of the stars (Jones et al. 2004; Yin et al. 2009). But as we shall see in this Thesis, this fraction varies with galaxy type and mass and evolves significantly over cosmic history. The vast majority of the ISM is gas, with around 1% (by mass) in the form of cosmic dust (Ferrière, 2001), tiny solid grains that pervade the ISM like smoke particles. A significant proportion of the gas of the ISM is made of Hydrogen, followed by Helium, reflecting the primordial ratios determined by nucleosynthesis in the early Universe. A few percent of the mass of the ISM is in the form of heavier elements collective termed as 'metals' (Jones et al., 2004). These metals have largely been produced in the cores of dying stars or in supernovae. From these metals, cosmic dust forms (see Section 1.5), and although dust is an insignificant part of the ISM in terms of mass, its influence is disproportionately large.

The ISM is often described as low density, with $\sim 10^6$ atoms per cubic metre (~ 1 atom per cubic centimetre). However, this generalisation is woefully misleading. The nature of the ISM is complex, spanning a wide range of temperatures of

Figure 1.10: *Left:* Optical image of the Orion constellation, clearly showing stars and some gas emission from the Great Nebula of Orion. Generally, the space between the stars appears empty (courtesy of NASA APOD, credit to Matthew Spinelli). *Right:* Emission from Hydrogen, Oxygen and Sulphur in the vicinity of the constellation. The gas glows as brightly as the stars (courtesy of NASA APOD[17], credit to Andrew Klinger).

densities. In the next Section, we explore the multi-phase ISM, with a focus on the cooler phases.

1.4.1 THE MULTI-PHASE ISM

Broadly, there are five phases of the ISM representing gas at distinct temperatures and densities, although it is worth noting that the boundaries between the different phases often overlap. Much of the volume of the ISM is occupied by ionised gas, but most of the mass is occupied by neutral atomic or molecular gas. See Klessen & Glover (2016) for a detailed review of the phases of the ISM, from which much of the following is sourced. See also the reviews of Ferrière (2001) and Cox (2005).

The first attempt to identify phases of the ISM is often attributed to Field et al. (1969), who presented a two-phase model for the ISM. They showed that if one assumes that the atomic gas of the ISM is in thermal equilibrium, then for

a variety of pressures, there emerges two stable solutions. Today, we recognise these as the Cold Neutral Medium (CNM), with temperatures of around 100 K and densities of around 10 atoms/cm^3, and the Warm Neutral Medium (WNM), with temperatures of thousands of K and densities of 0.1-1 atoms/cm^3 (Cox, 2005).

A third phase was suggested by McKee & Ostriker (1977), with hot ionized gas produced by supernovae explosions. We now recognise this as the Hot Ionized Medium (HIM) with temperatures around 10^6 K and densities on the order of 0.01 atoms/cm^3 (Cox, 2005). There is also some evidence of a Warm Ionized Medium (WIM) with a similar temperature and density of the WNM.

The final phase of the ISM can be considered part of the CNM, although its specific features and importance to star formation warrant its own distinction. Containing up to half of the mass but occupying just 1-2% of the volume of the ISM (Ferrière, 2001) are cool, dense molecular hydrogen (H_2) clouds. These clouds are very cold, with typical temperatures of 10-20 K, and very dense in comparison to the rest of the ISM, with $> 10^2$ atoms/cm^3. It is within these clouds that star formation happens. As such, these clouds are sometimes associated with ionized hydrogen (HII regions) caused by UV radiation emitted by newly formed hot and young OB stars photodissociating molecular hydrogen molecules (Jones et al., 2004).

The very existence of molecular hydrogen in great abundances in the ISM is only possible due to the presence of dust grains - a somewhat surprising notion, considering the density of hydrogen atoms in these regions. When two atoms of hydrogen collide, in order to create a stable molecule, some 4.5eV of energy must be released (Pirronello et al., 1998). Normally such energy is released via the emission of a photon, but in the case of molecular hydrogen, such transitions are forbidden. The typical result is that the atoms separate and continue their random paths through the gas cloud. However, the inclusion of a third body to absorb the excess energy circumnavigates this issue. As early as 1949, a small dust grain was identified as the perfect third body (e.g. van de Hulst 1949; Gould & Salpeter 1963; Hollenbach & Salpeter 1970, 1971; Hollenbach et al. 1971). Typically an incoming hydrogen atom adsorps to the dust grain, diffuses along its surface, eventually combining with a second to form a hydrogen molecule. The excess 4.5eV of energy

[17] Full sources: https://apod.nasa.gov/apod/ap030207.html and https://apod.nasa.gov/apod/ap190605.html

may be transferred to the dust grain in the form of random motion, or manifest in the form of kinetic energy for the newly formed molecule (e.g. Cazaux & Tielens 2002; Perets et al. 2005; Vidali et al. 2005; Roberts et al. 2007; Takeuchi et al. 2016; Wakelam et al. 2017). This process alone highlights the importance of dust when studying the ISM and the evolution of galaxies.

1.4.2 TRADITIONAL TRACERS OF MOLECULAR AND ATOMIC HYDROGEN

Despite the abundance of neutral gas in the ISM, tracing the gas is non-trivial. Here, we briefly explore the traditional methods of mapping the molecular and atomic gas phases. We will return to tracers of gas in galaxies in Chapter 3, where we discuss a relatively new method that is gaining popularity, and one that is used in this Thesis - using dust emission to trace the gas.

1.4.2.1 ATOMIC HYDROGEN

Neutral atomic hydrogen is most readily traced using 21cm radio emission. The existence of this emission line was predicted by van de Hulst (1945) and first observed by Ewen & Purcell (1951). The line originates from the hyperfine structure of the hydrogen atom, where the electronic ground level is split into two - one corresponding to the spins of the proton and electron being aligned (excited state), and the other corresponding to them being anti-aligned (relaxed state). The 'spin-flip' transition from the excited state to the relaxed state is the origin of the 21cm radio emission. Although the likelihood of this transition is rare, the abundance of hydrogen atoms makes using the 21cm-line a viable tracer for HI in the local Universe. In addition, the long-wavelength nature of the light means it can traverse the ISM largely unimpeded (Ferrière, 2001).

However, the usefulness of 21cm radio emission to trace atomic hydrogen beyond the local Universe (z>0.4) is limited. Simply, the emission is too weak to be detected with current radio telescopes without many hours of telescope time, a prohibitive cost for such observations (Lah et al. 2007; Fernández et al. 2016). Some progress is being made for intermediate redshifts by employing stacking methodologies (e.g. Chowdhury et al. 2020). Alternatively, at high redshifts ($z > 2$), atomic

hydrogen transitions from the ground state to an excited state can be observed in the form of damped Lyman-α absorbers, where UV light from a background quasar is absorbed by the atomic hydrogen gas in an intervening galaxy. However, the sample size of such systems is low, and it is not always easy to determine the nature of the foreground system, whose light is often drowned out by the bright background quasar (Lah et al. 2007; Fernández et al. 2016).

1.4.2.2 MOLECULAR HYDROGEN

Much like atomic hydrogen, molecular hydrogen is difficult to directly detect. It has no permanent electric dipole moment and because it is a low mass molecule, ro-vibrational transitions can only happen due to excitation by high temperatures ($\sim$1000 K). Such H_2 emission in the infrared only traces gas that has been heated extensively or shocked, therefore missing most of the H_2 i.e. that of the cool, dense molecular clouds (Ferrière 2001; Klessen & Glover 2016). Molecular hydrogen can also be detected through optical and UV absorption lines along lines of sight to young, bright stars or AGN. Similar to atomic hydrogen, such methods are limited in terms of sample size. In addition, cosmic dust coincident with the gas clouds can absorb this UV light, limiting the usefulness of such detection methods in examining the bulk of dense molecular hydrogen gas.

Traditionally, the best way to trace molecular hydrogen is by using radio emission from a molecule known to exist in the same location. The most common molecule used as a tracer is $^{12}C^{16}O$ (otherwise known as ^{12}CO or CO in the literature) because it is the next most abundant gas in the ISM with easily detectable emission. CO has a rotational transition line at a rest frame wavelength of 2.6mm for $J = 1 \rightarrow 0$. CO is readily detected in galaxies in the local Universe and even out to high redshifts (e.g. Scoville et al. (2016) and references therein).

However, there are several issues with using CO emission to trace H_2, the most contentious being the 'CO conversion factor' X_{CO}, an empirically determined constant of proportionality which is used to transform carbon monoxide emission line brightness to molecular hydrogen mass. The value of X_{CO} has been found to vary by orders of magnitude in different regions of a galaxy, between galaxies and also vary with metallcity (e.g. Narayanan et al. 2012; Bolatto et al. 2013; Sandstrom et al. 2013; Genzel et al. 2015). A second significant issue is 'CO dark' gas,

molecular hydrogen without significant amounts of CO mixed in. For example, this could be due to the dissociation of CO by UV photons from newly formed massive stars (Inoguchi et al., 2020). Various studies using dust continuum and other carbon tracers suggest that $\sim 30-50\%$ of molecular gas could be CO dark (e.g. Planck Collaboration et al. 2011; though see also Smith et al. 2012 and Pineda et al. 2013). Finally, emission from CO is typically optically thick, meaning that it can only probe the surface regions of dense molecular clouds.

All these caveats point towards a requirement for a different tracer of molecular hydrogen. In recent years, using long-wavelength dust continuum emission is one such method which has been gaining popularity. We explore the usefulness of dust as a tool for studying the ISM in the next Sections.

1.5 COSMIC DUST

As already alluded to, cosmic dust has a profound effect on our ability to study and understand the evolution of galaxies, despite constituting around only 0.1% of the baryonic content of a galaxy by mass (e.g. Vlahakis et al. 2005; Dunne et al. 2011; Clemens et al. 2013; Beeston et al. 2018; Driver et al. 2018). Dust obscures and absorbs the optical and UV light from stars and AGN, and re-emits this energy at far-infrared (FIR) and sub-mm wavelengths. Dust is thought to have absorbed around half of the starlight ever emitted in the Universe (e.g. Puget et al. 1996; Fixsen et al. 1998; Dole et al. 2006; see Figure 1.11).

Dust is a by product of star formation, but also key for star formation to occur, by allowing the formation of H_2. Dust is pervasive throughout the ISM, existing in all phases except the hottest, where it is liable to sublimation (Jones et al., 2004). As we discuss in Section 1.5.7, its pervasiveness makes it a useful tracer of the ISM.

1.5.1 A BRIEF HISTORY

Much as the study of galaxies is a young branch of astronomy, so is the field of cosmic dust (Whittet, 2002). In 1811, a little over a decade after he had discovered infrared light (Herschel, 1800), William Herschel suggest that the space between the stars may not be empty (Herschel, 1811). Wilhelm Struve presented the

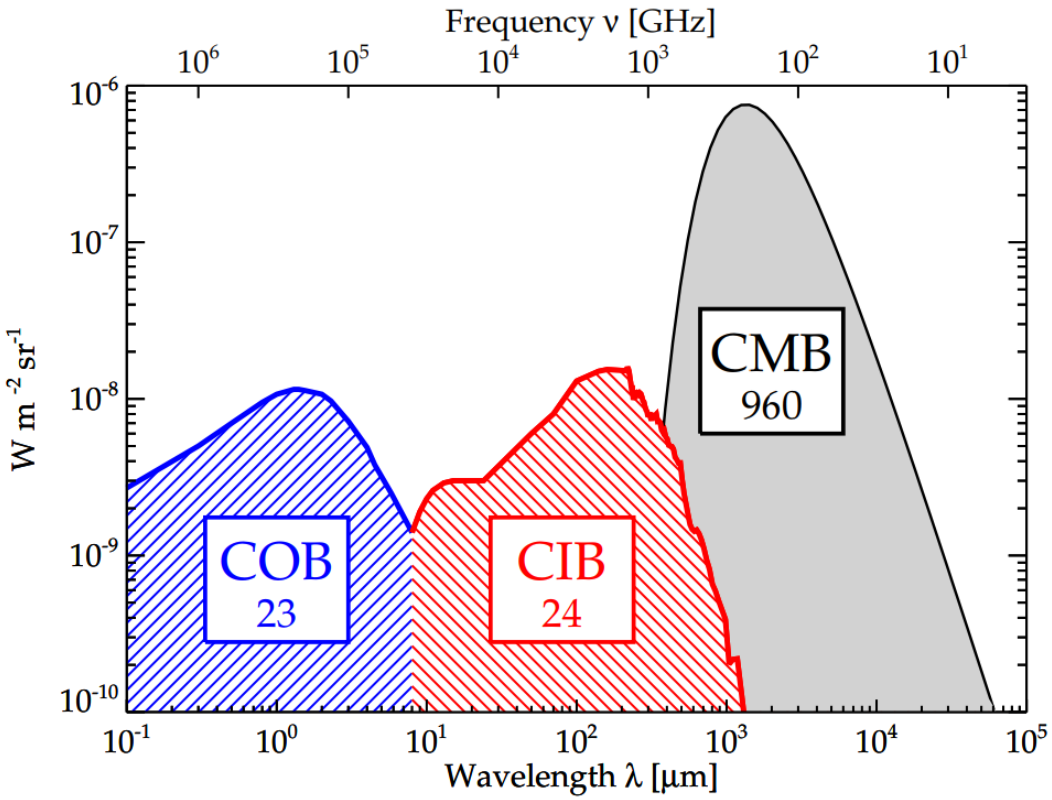

Figure 1.11: Schematic Spectral Energy Distributions of the most important backgrounds in the Universe, courtesy of Dole et al. (2006). *CMB:* Cosmic Microwave Background. *CIB:* Cosmic Infrared Background. *COB:* Cosmic Optical Background. The number in the box is the approximate brightness in [nW m^{-2} sr^{-1}].

first evidence of such material between the stars, when he showed that star counts decrease with increasing distance (Struve, 1847). However, it wasn't until the early 20th Century that the idea that some intervening medium may be dimming the stars began to gain some momentum. Kapteyn (1909) recognised the difficulty in understanding the distribution of stars in our galaxy if such a medium existed, due to the dimming of light it causes. Barnard (1907, 1910) provided evidence of dark 'nebulae', and noted their spatial variation across the sky. Finally, it was Robert Trumpler who provided mathematical evidence of light absorbing material between the stars, when he proved that the inverse square law is not enough to explain the dimming of distant stars (Trumpler, 1930), concluding that 'fine cosmic dust particles' could be the root cause.

1.5.2 WHAT IS COSMIC DUST?

Cosmic dust refers to the small, solid grains that pervade the ISM like smoke. The size of dust grains can vary substantially, from ∼0.01 to ∼10 μm in size (e.g. Kim et al. 1994). Through observations of the gas of the ISM, depletion measurements show that dust is largely composed of C, N, O, Mg, Si, and Fe (e.g. Jenkins 2009). Based on measurements from the local Universe, around half of the metals in the ISM are locked up in dust grains (James et al., 2002). Typically, larger dust grains (>0.1μm) are considered to be made of silicate or amorphous carbon. These are the cold (T_d ∼25 K) dust grains that absorb UV and optical light from stars and radiate this energy at longer FIR/sub-mm wavelengths. Dust can also be made of individual molecules known as polycyclic aromatic hydrocarbons, which exhibit strong spectral features in the mid-infrared (Draine & Li, 2007).

1.5.3 PRODUCTION AND DESTRUCTION

One origin of cosmic dust is from the post-main-sequence evolution of stars. The stellar winds of low-to-intermediate mass stars (1-8 $M_\odot$; LIMS) that have evolved to the asymptotic giant branch (AGB) phase and massive stars (>10$M_\odot$) that have evolved to Red Supergiants (RSGs) are proficient dust factories (Figure 1.12). More recently, observations have shown that supernovae, the violent end of the most massive stars, produce large quantities of dust. Dust can also form directly in the ISM, via grain growth.

Upon finishing hydrogen fusion in their cores, low mass stars progress to fusing helium into heavier elements, such as carbon and oxygen. These metals are dredged up from deep within the star via the convective envelope and enrich the cool (∼ 1000 K) outer layers of the star, where the density and pressure is conducive to the condensation of metals into solid particles. These particles can then coagulate together into grains, which are then swept out into the ISM via stellar winds (Whittet, 2002).

Some studies argue that the majority of dust observed in the ISM is produced in the winds of evolved stars (e.g. Ferrarotti & Gail 2006; Sargent et al. 2010), even out to higher redshifts (e.g. Valiante et al. 2009; Dwek & Cherchneff 2011). However, other studies have pointed out a 'Dust Budget Crisis' at high

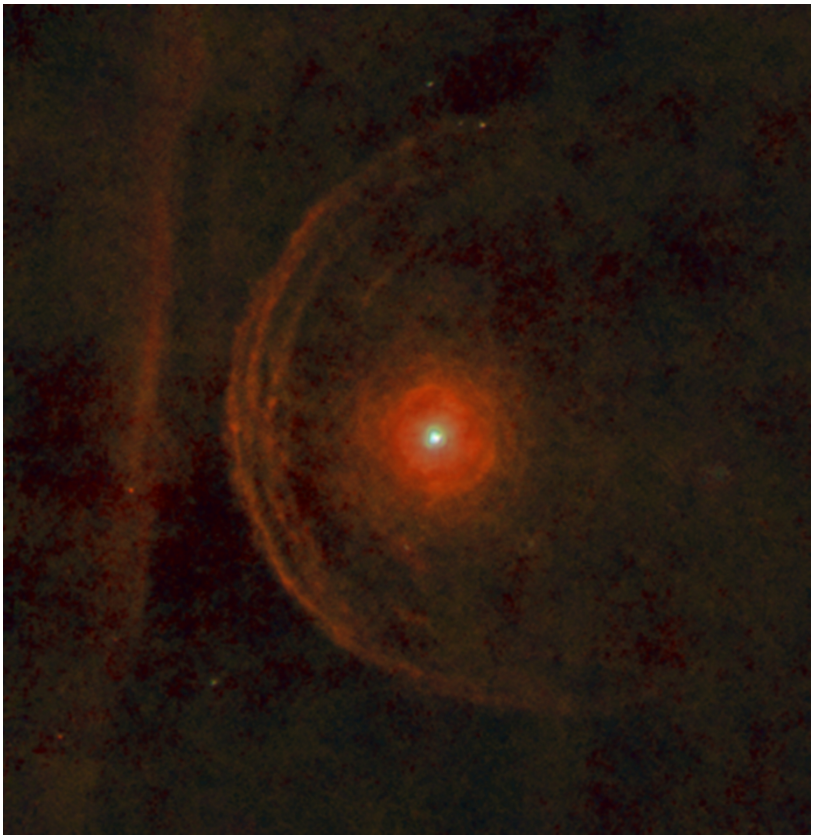

Figure 1.12: The Herschel Space Observatory's FIR view of the red supergiant star Betelguese, marking the left shoulder of Orion (left as viewed on the sky). To the left of the star are clearly visible arc-like bow-shocks, caused by the interaction of dusty material ejected from the evolved star with the surrounding ISM. Credit: ESA/*Herschel*/PACS/MESS[18].

redshifts. Based on the typical stellar lifespans of smaller stars, it is difficult to explain the high quantities of dust observed at high-redshifts, when the Universe was young (e.g. Morgan & Edmunds 2003; Dwek et al. 2007; Michałowski et al. 2010b,a; Santini et al. 2010; Valiante et al. 2011). However, since supernovae occur on a much quicker timescale, it has been argued that they could be an important source for dust in the early Universe (and naturally at later times too). Observations have shown that a singular event can produce up to a solar mass of dust (e.g. Dunne et al. 2003b; Sugerman et al. 2006; Matsuura et al. 2011; Gomez et al. 2012; Matsuura et al. 2015; Chawner et al. 2019). Dust from supernovae is not produced directly in the explosion, but condenses out of the leftover expanding material, which leads to an interesting conundrum. The shocks produced in supernovae are known to be extremely dust-destructive (e.g. Jones et al. 1996; Jones & Nuth 2011).

As such, it is not entirely clear how long the dust produced by supernovae can survive.

Dust can also be produced in the ISM directly, via grain growth. Small dust grains can coagulate during low-velocity collisions, producing larger dust grains. Alternatively, small dust grains can grow through mantle growth, depleting metal atoms from the ISM which are then adsorbed onto the dust grain (Whittet, 2002).

Another way in which dust can be destroyed in the ISM, aside from the aforementioned supernova shocks, is 'sputtering'. Sputtering involves gas-grain collisions and results in dust destruction by causing the sublimation of matter from the dust grains back into gaseous form. Effective sputtering of dust grains requires a dense environment with high-velocity gas particles, making the WIM the perfect environment for effective dust destruction (Tielens et al. 1994; Whittet 2002; Jones 2004).

1.5.4 DUST EMISSION AND DUST MASS

The thermal emission from cool dust (which constitutes the bulk of the dust in the ISM) is in the FIR/sub-mm region of the electromagnetic spectrum. This light is UV/optical starlight that has been absorbed and re-radiated by the dust grains as imperfect blackbodies.

According to Kirchhoff's law of radiation (Kirchhoff, 1860), at any given temperature, the coefficient of emission (emissivity) of a body is equal to the coefficient of absorption. Therefore, the rate at which energy is emitted by blackbody is equivalent to the rate at which energy is absorbed from the local radiation field. The spectrum of a perfect blackbody emitter at a given temperature T, as a function of frequency ν, is described by the Planck function:

$$B_\nu(T) = \frac{2h\nu^3}{c^2} \frac{1}{e^{\frac{h\nu}{k_B T}} - 1} \tag{1.1}$$

where B_ν is the Planck function spectral radiance, h is the Planck constant, c is the speed of light and k_B is the Boltzmann constant.

For a blackbody emitter in radiative equilibrium with the local radiation

[18] Full source: https://herscheltelescope.org.uk/results/betelgeuse/

field, the temperature T is described by the Stefan-Boltzmann law:

$$T^4 = \frac{Uc}{4\sigma} \tag{1.2}$$

where U is the energy density of the local radiation field, and σ is the Stefan-Boltzmann constant.

Since dust is not a perfect blackbody emitter, we modify the the Planck function with a parameter, Q_ν, that describes the efficiency with which it emits. Q_ν is the ratio of the emitting power of an imperfect blackbody (sometimes known as a 'greybody') to that of a perfect blackbody emitter, at a given equilibrium temperature and a given frequency. For FIR/sub-mm emission from dust grains, the wavelength (λ) of the light being emitted is larger than the size of the grain, so we can use the small grain approximation for Q_ν:

$$Q_\nu \propto \nu^\beta \propto \lambda^{-\beta} \tag{1.3}$$

where β is the dust emissivity spectral index, with typical values between 1 and 2, depending on the composition of dust. Theoretically, $\beta = 1$ would be expected for amorphous grains, and $\beta = 2$ for metallic and crystalline materials (Tielens & Allamandola, 1987), and Planck observations of dust in our galaxy suggest a value of $\beta = 1.8$ (Planck Collaboration et al., 2011). β is the spectral index of the power-law slope of the Rayleigh-Jeans tail of the dust emission spectral energy distribution. For a modified blackbody, the observed flux density, S_ν (in units of Jy) is therefore:

$$S_\nu \propto \nu^\beta B_\nu(T) \tag{1.4}$$

To estimate the mass of dust causing the observed emission, we make the assumption that dust grains are spherical and of constant size. Then, the mass, M_d, of a cloud of n dust grains is:

$$M_d = \frac{4}{3}\pi a^3 \rho n \tag{1.5}$$

where a is the radius of the dust grain, and ρ is the mass volume density of the grain material. Assuming that Kirchoff's law holds, and the dust grains are in

radiative equilibrium, radiative transfer by dust is described by:

$$I_{UA,\nu} = (1 - e^{-\tau_\nu})B_\nu(T) \tag{1.6}$$

where $I_{UA,\nu}$ is the spectral radiance per unit cross-sectional area of the cloud at a given frequency, and τ_ν is the optical depth at a given frequency. As previously mentioned, dust grains are generally considered to be much smaller than the wavelengths of the FIR/sub-mm light they emit. This means we can assume that the cloud of dust grains is optically thin ($\tau_\nu \ll 1$), and so we can make the approximation:

$$I_{UA,\nu} \simeq \tau_\nu B_\nu(T) \tag{1.7}$$

Optical depth is described as:

$$\tau_\nu = \pi a^2 N Q_\nu = \pi a^2 Q_\nu \frac{n}{A} \tag{1.8}$$

where πa^2 is the cross-sectional area of the grains, $N(= n/A)$ is the column density of the grains, where A is the cross-sectional area of the dust cloud. Combining Equations 1.7 and 1.8:

$$I_{UA,\nu} = \pi a^2 N Q_\nu B_\nu(T) \tag{1.9}$$

and we can multiply through by A to give the spectral radiance over the whole cross-sectional area, I_ν:

$$I_\nu = \pi a^2 n Q_\nu B_\nu(T) \tag{1.10}$$

Of course, this is not what we observe - the spectral radiance follows the inverse square law, and decreases with increasing distance from the source to the observer, D. The flux density at a given frequency, S_ν, actually observed from the cloud is:

$$S_\nu = \frac{\pi a^2 n Q_\nu B_\nu(T)}{D^2} \tag{1.11}$$

Rearranging this in terms of n, we can substitute into Equation 1.5 to find an expression for dust mass:

$$M_d = \frac{4a\rho S_\nu D^2}{3Q_\nu B_\nu(T)} \tag{1.12}$$

There are several terms in this equation which are poorly constrained, or for

which the basic assumptions made in the derivation are likely to not fully represent the true physical situation. Q_ν is dependent on the physical properties of dust grains (e.g. composition, size, mass) which are not easily determined. Further, we have assumed that all dust grains are spherical, which is unlikely to be true - not only because dust grains are not likely to be spherical, but they are also not likely to all be the same size, an implicit assumption in this derivation. Since dust grains form through a variety of mechanisms in a variety of environments, they are also unlikely to all have the same composition. It is also extremely difficult to measure the density of dust grains in a cloud in distant galaxies. We therefore group all of the uncertain parameters into a singular uncertain parameter, κ_ν, encompassing all of these unknowns:

$$\kappa_\nu = \frac{3Q_\nu}{4a\rho} \tag{1.13}$$

where κ_ν is the dust mass absorption coefficient. We can therefore express M_d as:

$$M_d = \frac{S_\nu D^2}{\kappa_\nu B_\nu(T)} \tag{1.14}$$

and the frequency dependence of κ_ν is described by:

$$\kappa_\nu = \kappa_0 \left(\frac{\nu}{\nu_0}\right)^\beta \tag{1.15}$$

where κ_0 is the value of the dust mass absorption coefficient at a given reference frequency, ν_0[19].

Note that κ_ν is woefully unconstrained. A typical value of κ_ν is $0.051 \mathrm{m}^2\mathrm{kg}^{-1}$ at $500\mu m$ (Clark et al., 2016). Considering efforts from the community over the past four decades, estimates of κ_ν vary over nearly four orders of magnitude, with an overall uncertainty of around one order of magnitude (Clark et al., 2019).

1.5.5 DUST MASSES BEYOND THE LOCAL UNIVERSE

Equation 1.14 holds for the local Universe. However, beyond around $z \sim 0.05$ we must factor in the implications of the cosmological model that describes

[19] In the literature, κ_ν is often quoted for a reference *wavelength*, κ_λ, rather than reference *frequency*. This is simply another wilful astronomical convention, and one that we follow in this Thesis.

our expanding Universe. Equation 1.14 becomes:

$$M_d = \frac{S_{\nu_o} D_L^2}{\kappa_{\nu_e} B_{\nu_e}(T_d)(1+z)} \tag{1.16}$$

where we explicitly denote parameters with ν_o to refer to the observers rest frame, and ν_e for the object's rest frame (i.e. the original emission frequency). D_L is the luminosity distance, which factors in frequency changes to light, and also time dilation, caused by an expanding Universe. The factor $(1+z)$ accounts for the change in frequency in the observer's frame for sources at high redshift.

1.5.6 DUST MASS FUNCTIONS

We have now reached an era of such technological advancement in telescope optics and detectors that we can measure the dust content of thousands or tens of thousands of galaxies (e.g. Dunne et al. 2011; Beeston et al. 2018; Driver et al. 2018). Such datasets warrant a statistical approach to describing the dust content of galaxies by measuring the dust mass function (DMF), the space density of dust in galaxies. As with mass and luminosity functions, the DMF is typically described by a Schechter function (Schechter, 1976):

$$\phi = \phi^* \left(\frac{M}{M^*}\right)^{\alpha} e^{-\frac{M}{M^*}} \tag{1.17}$$

where ϕ is the number volume density at a given mass M, M^* is the characteristic mass (i.e. the mass of the turnover point in the Schechter function, or the 'knee' of the Schechter function), ϕ^* is the number volume density at the characteristic mass, and α is the power law index of the low mass slope.

Of particular interest is the evolution of the dust mass function with cosmic time, a feat we can now only begin to attempt with the advent of large scale sub-mm surveys. Sub-mm surveys are key to this statistical measurement, since it is at these long wavelengths that the coldest dust, accounting for the bulk of the dust in the ISM, emits light.

1.5.7 USING DUST TO TRACE THE ISM

As discussed in Section 1.4, the traditional methods of tracing the gas content of the ISM are limited. In response to this, an alternative approach to measure the molecular gas content of galaxies has been gaining momentum: using the optically thin dust continuum emission detected at a single sub-mm wavelength as a tracer of the gas (Eales et al. 2012; Scoville et al. 2014; Scoville et al. 2016; Scoville et al. 2017).

The FIR or sub-mm emission from galaxies generally originates from two major sources. Firstly, is the previously discussed re-emission of UV and optical starlight that has been absorbed by dust grains. Secondly, AGN are prominent emitters of FIR/sub-mm radiation, due to dust near to the AGN (e.g. in the torus) being heated (Scoville et al. 2016; Symeonidis et al. 2016). However, dust is the primary source of FIR/sub-mm emission in most galaxies.

The idea of using dust to trace the mass of the ISM in a galaxy is not new, having been suggested some forty years ago by (Hildebrand, 1983). As previously discussed, dust grains are pervasive throughout many phases of the ISM, they are robust, and the continuum emission of dust is optically thin (Eales et al., 2012). This allows us to trace the bulk of the ISM, as opposed to extrapolating based on emission from only surface regions, in the case of optically thick tracers.

With knowledge of the emissivity of dust per unit mass and the gas-to-dust ratio, we can use the emission from dust to trace the mass of gas in galaxies. Scoville et al. (2016) and Scoville et al. (2017) used samples of galaxies that have both 850μm measurements from the Atacama Large Millimeter/sub-millimeter Array (ALMA) and molecular gas masses estimated using CO observations, to derive an empirical relation to estimate gas masses using optically thin emission from dust (Figure 1.13). The advantage of this method lies in the opportunity it provides to quickly derive molecular gas masses for large numbers of galaxies at high redshifts, opening up the possibility of probing the gas mass fraction in galaxies at particularly interesting epochs, and over a large fraction of the history of the Universe. This method is particularly timely; the *Herschel Space Observatory* (hereafter *Herschel*, Pilbratt et al. 2010) has provided FIR-sub-mm (70-500μm) measurements for hundreds of thousands of galaxies. ALMA can also be used to provide sub-mm (0.3 – 1mm) continuum measurements to estimate the mass of the ISM in high-z

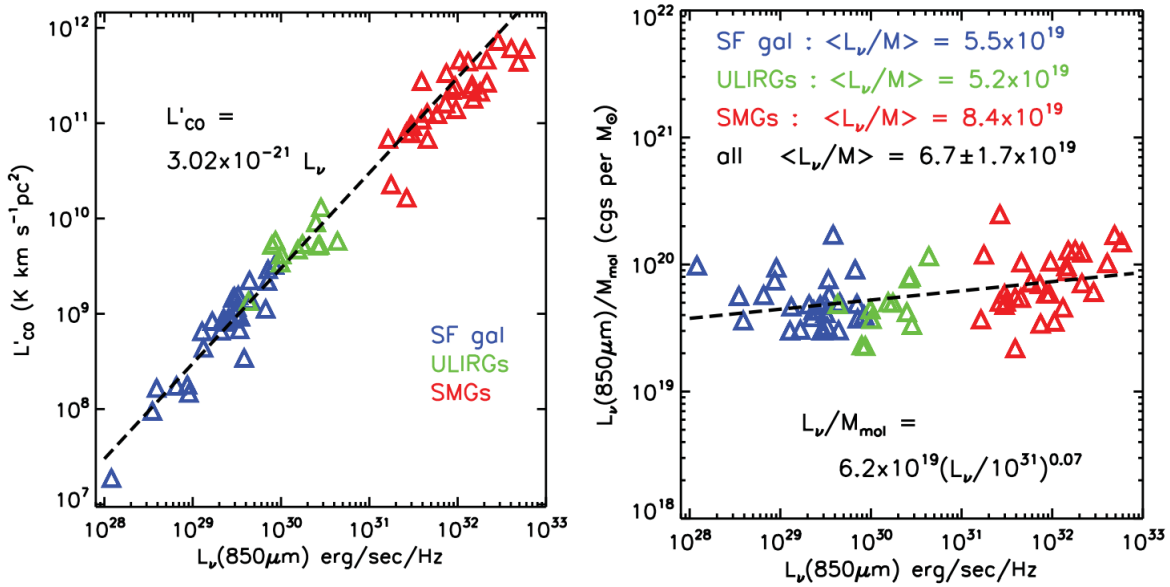

Figure 1.13: *Left:* CO(1-0) luminosity and $L_{850\mu m}$ for three samples of galaxies: normal low-z star-forming galaxies, low-z ULIRGs, $z \sim 2$ SMGs. *Right:* Ratio of $L_{850\mu m}$ to M_{mol} for the same galaxies, showing a similar proportionality constant between dust continuum flux and molecular gas masses derived using traditional CO(1-0) methods. Courtesy of Scoville et al. (2016).

galaxies (e.g. Scoville et al. 2016). Finally, the Sub-mm Common User Bolometer Array 2 (SCUBA-2; Holland et al. 2013) on the James Clerk Maxwell Telescope (JCMT) has been used to conduct large scale surveys of the sky at 450 and 850μm, ideal for statistical extra-galactic studies.

Recent studies comparing gas masses estimated using sub-mm dust continuum emission to gas masses estimated using more traditional methods, such as CO line emission, have added support to the validity of this method. Genzel et al. (2015) simulated the sub-mm emission produced by a population of galaxies, based on stacked *Herschel* FIR data from Magnelli et al. (2014), and scaling relations[20] developed using this dataset. They compared the known molecular gas masses to those determined using the simulated sub-mm emission and found that gas masses were successfully estimated within 0.35 dex of the true value, with most of the scatter caused by uncertainties in the dust temperature. Tacconi et al. (2018) built upon the work of Genzel et al. (2015), incorporating new CO data into their studies (e.g. Decarli et al. 2016; Saintonge et al. 2017), additional stacked data

[20] A scaling relation describes the strong trend observed between important physical properties of galaxies. In this instance, the mentioned scaling relations typically relate stellar mass, star formation rate (and sometimes metallicity) to gas mass.

from *Herschel* (e.g. Santini et al. 2014; Béthermin et al. 2015), and further sub-mm emission observations (e.g. Scoville et al. 2016). They found that no matter the method used to determine the gas masses, the results all converged to the same scaling relations.

Although using dust as a tracer of the gas masses may be efficient in terms of integration time required to detect dust emission (e.g. Genzel et al. 2015; Scoville et al. 2016; Scoville et al. 2017; Tacconi et al. 2018), unfortunately sub-mm telescopes suffer from poor resolution. Indeed, the resolution of 850μm images produced by the SCUBA-2 on JCMT (Holland et al. 2013) is typically around 13″ (Dempsey et al. 2013). This makes it difficult to measure accurate sub-mm measurements for individual galaxies; multiple optical sources will often lie within one beamsize. A possible solution is to stack individual galaxies in bins, this can help mitigate the limitations of poor resolution data. Although stacking cannot improve the resolution, it can enable us to use poor resolution data to study galaxies in a statistical way. We lose information on individual galaxies, but gain information on the galactic population as a whole.

1.6 SUB-MM ASTRONOMY

FIR/sub-mm observations are key to understanding galaxy evolution via dust emission. However, electromagnetic radiation at these wavelengths is notoriously difficult to observe from the ground due to a plethora of water vapour absorption bands in this regime limiting our observations to a serious of narrow atmospheric windows (Figure 1.14). This means sub-mm astronomy can only be performed at high-altitude, arid locations on Earth, such as at the summit of Mauna Kea, Hawai'i, or from space.

1.6.1 OBSERVING DUST FROM SPACE

Launched in May 2009, the *Herschel* Space Observatory (Pilbratt et al., 2010) revolutionised studies of dust in galaxies. To-date, *Herschel* had the largest singular primary mirror ever launched into space, with a diameter of 3.5m, corresponding to twice the collecting area of Hubble. *Herschel* observed the sky in bands covering the wavelength range 60-671μm. A larger mirror was imperative

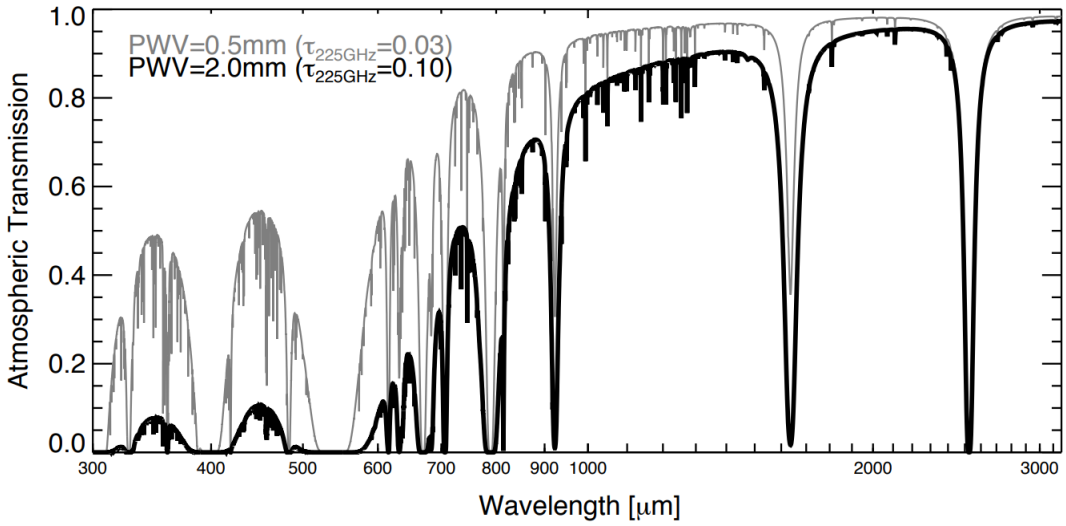

Figure 1.14: The atmospheric transmission of sub-mm and mm wavelengths as seen from Mauna Kea, Hawai'i. Two weather conditions are shown with with precipitable water vapor (PWV) levels of 0.5mm and 2.0mm (the amount of water vapour in the atmosphere as integrated from the top of the atmosphere down to the telescope. At sub-mm wavelengths, observations can only happen in limited atmospheric windows. Of particular interest to this work is the window at $\sim 850\mu$m, one of the operational wavelengths of SCUBA-2 on JCMT. Courtesy of Casey et al. (2014).

to the mission's success, since in the FIR/sub-mm range, resolution is of the order of 1000 times worse than in the optical. *Herschel* had an angular resolution of $\sim 7'' \times (\lambda_{\rm obs}/100\mu m)$, where $\lambda_{\rm obs}$ is the observation wavelength. This was an enormous improvement over previous space telescopes at the same wavelength e.g. $2'$ at 100μm for *IRAS* (Cernicharo, 2011), and $40''$ at 160μm for *Spitzer* (Rieke et al., 2004). Poor angular resolution impedes observations due to 'confusion', whereby the flux from unresolved sources (e.g. distant galaxies) overlap. Individual sources cannot be detected below this limit, and it is difficult to assign flux to individual objects. However, higher angular resolution helps combat this issue. FIR/sub-mm observations are especially susceptible to source confusion due to 'negative k-correction', which causes distant objects to appear in images with comparable brightness to nearby sources. Particularly for 850μm observations on the Rayleigh-Jeans tail of dust emission, high-z galaxies have approximately constant brightness from $z = 1 - 8$ (Casey et al., 2014). The flux density of galaxies is roughly constant at sub-mm wavelengths since diminishing brightness with increasing distance (redshift) is negated by the observation wavelength climbing

the steep Rayleigh-Jeans tail in the rest frame, thereby capturing a more luminous part of the galaxies' SED. That is, at fixed observation wavelength, further back in cosmic history, the rest-frame wavelength is closer to the peak of dust emission. Observations are therefore more luminous at these shorter wavelengths since dust emits as a modified blackbody. Although negative k-correction contributes to source confusion (since many more sources are visible over cosmic time, and are not lost simply because they exist in a more distant part of the Universe), it does help us explore galaxies at early epochs.

1.6.2 FROM THE GROUND: JCMT AND SCUBA-2

Despite the difficulties in observing sub-mm emission from the ground (Figure 1.14), there are a number of notable FIR observatories scattered across the globe. One of these is the JCMT, the largest sub-mm telescope currently in operation, with a segmented mirror 15m in diameter. It was built in 1987 and is located close to the summit of Mauna Kea, Hawai'i, at an altitude of $\sim$ 4100m, thereby escaping a significant proportion of the Earth's atmosphere, enabling it to perform sub-mm observations in some of the atmospheric windows. JCMT has a multitude of instruments, but of interest to this work is SCUBA-2 (Holland et al., 2013), installed in 2011. This instrument is the successor to SCUBA (Holland et al., 1999), installed in 1997 as one of the first sub-mm cameras on JCMT. SCUBA-2 was designed to operate at the same wavelengths as SCUBA, but with a 270 fold increase in the number of available pixels at its longest operational wavelength, enabling a much greater mapping speed. SCUBA-2 also has a field of view over 10 times that of SCUBA.

SCUBA-2 is a 10,000 pixel bolometer operating simultaneously at 450μm and 850μm, corresponding to main beam resolutions of 7.9$''$ and 13$''$ respectively (Dempsey et al., 2013), with an approximately 45 arcmin^2 field of view (Holland et al., 2013). These resolutions are almost unparalleled for a single dish telescope at these wavelength ranges (Figure 1.15). In comparison, *Herschel*'s resolution at 350 and 500μm is $\sim$ 25$''$ and $\sim$ 35$''$, respectively. The bolometers of SCUBA-2 are Transition Edge Sensors, which are balanced on the normal to superconducting transition edge, to make them as sensitive as possible to any temperature change caused by heat input (i.e. from an incoming photon). At this transition, a small

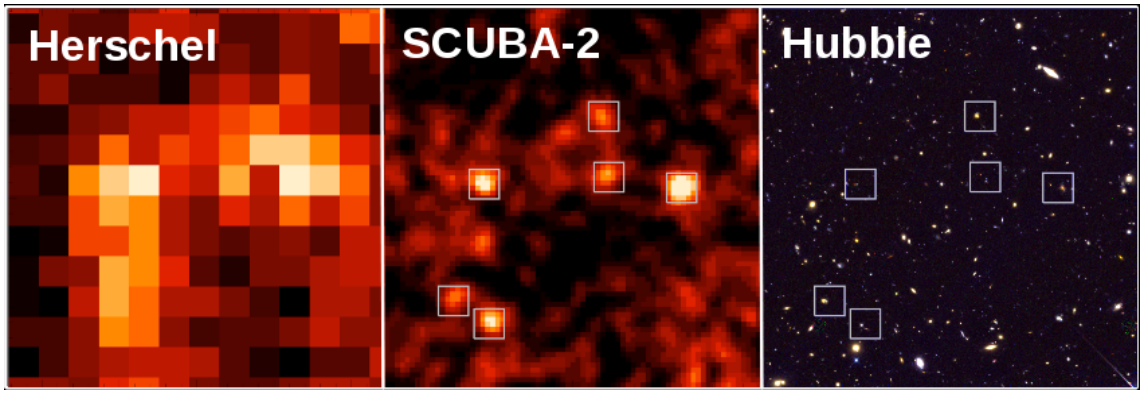

Figure 1.15: The same region of sky observed with *Herschel* at 500μm, JCMT/SCUBA-2 at 450μm and Hubble (optical). The distinct sub-mm sources visible in JCMT/SCUBA-2 are blended in the *Herschel* image due to poorer resolution. The sub-mm sources are resolved in the Hubble images, revealed to be massive star-forming disc galaxies at $z \sim 2$. Credit: ROE / JCMT / SCUBA-2 / James Dunlop[21].

temperature change corresponds to a large change in resistance, which changes the current flowing through the system and so a detection can be made.

The better sensitivity and faster mapping speeds of SCUBA-2 have, for the first time, enabled large scale surveys at 850μm. Soon after installation of the new bolometer on JCMT, the SCUBA-2 Cosmology Legacy Survey (S2CLS; Geach et al. 2017) was undertaken, totalling some 5 deg^2. The S2CLS covers key extra-galactic survey fields that have been studied by several other telescopes, with observations spanning much of the electromagnetic spectrum. The S2CLS survey was completed in February 2015, and since then, additional deeper surveys at 850μm have been conducted including the SCUBA-2 COSMOS survey (S2COSMOS; Simpson et al. 2019) - the largest and deepest 850μm map of the 2deg^2 Cosmic Evolution Survey (COSMOS; Scoville et al. 2007) field to-date (see Chapter 2). In this Thesis, we exploit these unparalleled sub-mm observations to probe the nature of the galactic population and its evolution with cosmic time.

1.7 COSMOLOGICAL HYDRODYNAMICAL SIMULATIONS

1.7.1 OVERVIEW

Our ever more resolved and sensitive observations of the Universe have allowed us to test theories of galaxy evolution to unprecedented levels of understanding. Although state-of-the-art telescopes and instruments allow us to probe earlier and earlier epochs with ever increasingly clarity, observations can only tell us so much. To really understand galaxy evolution, we must turn to modelling - specifically, cosmological computer simulations. These simulations allow us to probe the underlying physics governing the observations we make.

Over the past few decades, a huge variety of cosmological simulations have been developed, which probe galaxy evolution at different scales using different methods (Vogelsberger et al., 2020a). Broadly, these simulations fall into two categories: large-volume simulations that enable statistical studies of the galactic population, and zoom simulations with better resolution that allow studies of intricate galaxy formation and evolution details. There are also simulations that model the dark matter content of galaxies only (N-body simulations), and those that incorporate baryonic physics alongside modelling the dark matter (hydrodynamical simulations). In this Thesis, we use results from the large-volume cosmological hydrodynamical simulation IllustrisTNG.

1.7.2 ILLUSTRISTNG

IllustrisTNG (Marinacci et al. 2018; Naiman et al. 2018; Nelson et al. 2018a; Pillepich et al. 2018a; Springel et al. 2018) models the Universe based ΛCDM cosmology and is consistent with results from Planck Collaboration et al. (2016). IllustrisTNG models the Universe at three resolutions and each iteration traces the coupled evolution of dark matter, gas, stars and supermassive black holes. We use data from the TNG100 simulations (Figure 1.16), where the box-side-length is 106.5Mpc and there are 1820^3 gas cells.

[21] Full source - https://scuba2.files.wordpress.com/2012/03/cls-panel.png; see also https://phys.org/news/2012-03-scuba-camera-reveals-wild-youth.html

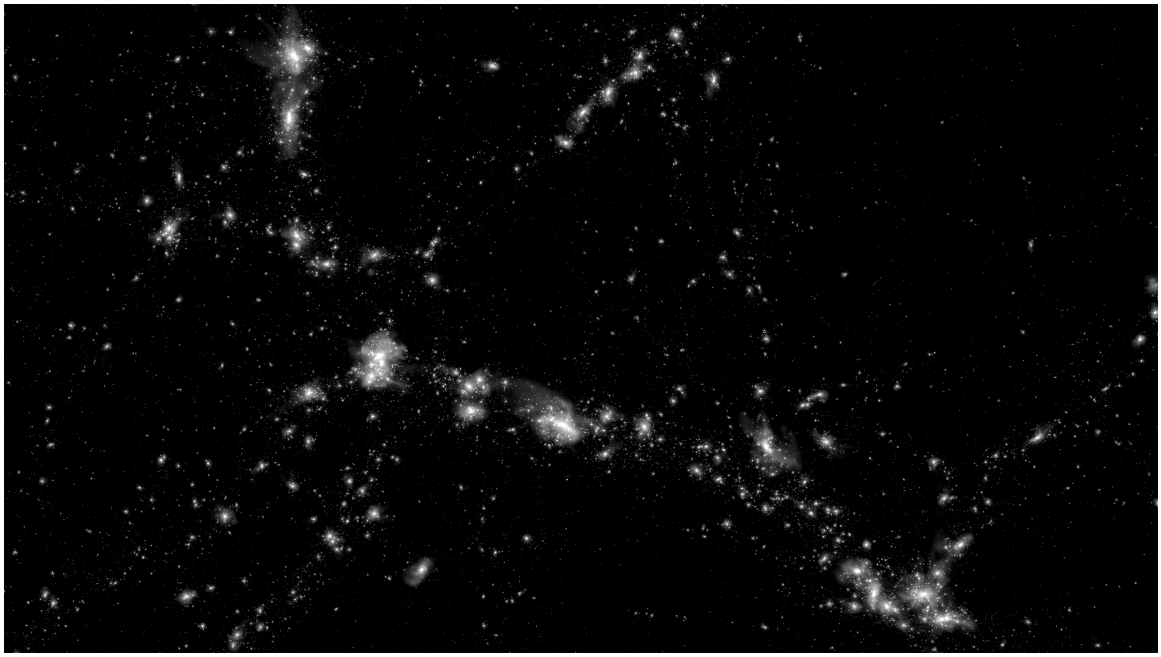

Figure 1.16: A projection of the distribution of stars across a 50Mpc region of space from the TNG100 simulation at $z = 0$, courtesy of the TNG Collaboration[22].

The moving mesh code AREPO (Springel, 2010) is used to solve equations of magnetohydrodynamics and self-gravity. Several key astrophysical processes are modelled in IllustrisTNG, including: star formation, stellar evolution, chemical enrichment (the production of heavy elements), primordial and metal-line gas cooling, stellar feedback-driven galactic outflows, and supermassive black hole formation, growth and feedback. However, it is important to note that the scales resolved by IllustrisTNG are much bigger than the scales these processes happen on (Nelson et al., 2019). For TNG100, the smallest resolvable gas scale length is 190pc at the centres of galaxies (Davé et al., 2020) and the minimum resolved mass of particles for gas and stars is $M_{\mathrm{gas,min}} = M_{*,\mathrm{min}} = 1.4 \times 10^6 M_\odot$. As such, these astrophysical processes are traced in a 'sub-grid' manner.

Of particular interest to this project is the treatment of chemical enrichment, star formation and feedback (Nelson et al., 2019). Gas above a star formation density threshold ($n_H \sim 0.1$ cm^{-3}) forms stars stochastically following the Kennicutt-Schmidt relation, assuming a Chabrier (Chabrier, 2003) initial mass function. Metals are returned to the ISM via supernovae and AGB stars, following tabulated metal and mass yields where nine chemical elements are tracked. Metal-enriched

[22] Full source: https://www.tng-project.org/media/

gas can cool in the presence of a UV background, and self-shielding in the dense ISM is accounted for. At low accretion rates, supermassive black hole (SMBH) feedback is kinetic, which produces black hole driven winds. Momentum is imparted to the gas, which causes shocks and acts to heat surrounding gas (Weinberger et al., 2017). At high accretion rates, 'quasar-mode' SMBH feedback, analogous to thermal/radiative feedback, injects thermal energy into the surrounding gas. This two-phase feedback model is key to producing red, passive galaxies at late times and for quenching massive galaxies, particularly via kinetic feedback (Weinberger et al., 2018). Finally, star formation also drives galaxy outflows.

Galaxies in TNG100 are identified using SUBFIND (Springel et al., 2001), and quantities associated with galaxies can be calculated based on a variety of different physical radii. In this Thesis, we use physical properties calculated for IllustrisTNG galaxies from $z = 0 - 5$, using their gas mass, stellar mass and metallicity values.

IllustrisTNG has been calibrated to reproduce several basic observed galaxy properties, such as the galaxy stellar mass function and black-hole galaxy-mass relation. Additionally, studies have shown that the code successfully produces; i) separate star-forming and quiescent galaxy populations (Genel et al., 2018); ii) quenched galaxies at low redshift (Weinberger et al., 2018); iii) the $z = 0$ evolution of the gas-phase mass-metallicity relation (Torrey et al., 2019); iv) estimates of molecular hydrogen in the local universe (Diemer et al. 2018; Stevens et al. 2019). These are therefore good indications that the simulations successfully reproduce many physical properties of galaxies in the local Universe, and successfully model many of the physical laws that we understand are important to galaxy formation. These successes allow us to probe beyond what the simulation has been designed to reproduce, and test how useful IllustrisTNG is as a tool for understanding galaxy evolution.

1.8 THESIS OUTLINE

In this Thesis, we aim to explore the evolution of the ISM content of a large sample of galaxies over cosmic time. Firstly, we examine the evolution of the average gas mass of galaxies in the COSMOS field using long-wavelength dust

emission on the Rayleigh-Jeans tail. We then determine the average dust masses of these COSMOS galaxies over cosmic time, and compare the evolution to post-processed estimates of the average dust content of galaxies in the IllustrisTNG simulation. This allows us to provide an independent investigation of the evolution of the neutral gas content of IllustrisTNG galaxies as compared to robust observations. Finally, we finish with a first-look estimate of the evolution of the comoving dust mass density with redshift, estimated using average dust masses combined with stellar mass functions from the literature. The outline of the Thesis is below.

- In Chapter 2, we introduce the S2COSMOS 850μm map used in this Thesis. We construct a source catalogue by performing a detailed comparison of two possible source catalogues based on two different SED fitting routines, MAGPHYS and CIGALE. We identify and remove AGN from our chosen galaxy catalogue.

- In Chapter 3, we classify galaxies in our source catalogue into stellar mass and redshift bins. We introduce our stacking methodology, and determine average 850μm fluxes and ISM masses using these stacked fluxes and empirical relations developed by Scoville et al. (2016, 2017). For our binned galaxies, we calculate gas fractions, examine the evolution with redshift, and compare our results to scaling relations from the literature. We split our sample into star-forming and passive galaxies and examine the evolution of the gas content of these two different galactic populations. We discuss our results and explore assumptions and caveats associated with the study.

- In Chapter 4, we introduce IllustrisTNG and the specific iteration of the simulation we use in this Thesis. We derive average dust masses using the stacked 850μm fluxes calculated in Chapter 3, and develop our post-processing method for estimating the average dust properties of IllustrisTNG galaxies. We construct local DMFs for IllustrisTNG galaxies, and compare to ones from the literature. We explore the $z = 0$ dust-and-stellar-mass distribution of IllustrisTNG galaxies, and compare to average relations from the literature and from our stacking results. We calculate dust-to-stellar mass ratios for COSMOS and IllustrisTNG galaxies, and compare the evolution of

the two catalogues out to high redshifts.

- In Chapter 5, we explore the assumptions made in producing the results of Chapter 4, including assumptions on the properties of dust and our chosen dust-to-metal ratio. We also explore the assumptions made in developing our post-processing method for estimating the dust content of IllustrisTNG galaxies, including our choice of dataset. We split the IllustrisTNG galaxies into central and satellite galaxies, and examine the evolution of the dust content of these two populations. We explore reasons to explain the dichotomy in the evolution of dust mass content as illustrated by the observed and simulated galaxy catalogues.

- In Chapter 6 we calculate a first-look estimate of the evolution of the comoving dust mass density with cosmic time, using dust masses derived using our stacking methodology presented in Chapter 3 and stellar mass functions from the literature. We compare our first-look estimate to results from the literature, and explore reasons to explain the similarities and differences between our results and ones from previous works.

- In Chapter 7, we summarize our conclusions and describe the next stages of this research.

We use the cosmological parameters from *Planck* (Planck Collaboration et al. 2016) and make use of `astropy.cosmology` (Astropy Collaboration et al. 2013, Price-Whelan et al. 2018) assuming `FlatLambdaCDM` and $H_0 = 67.7 \text{km Mpc}^{-1}\text{s}^{-1}$, $\Omega_{M_0} = 0.307$ and $\Omega_{B_0} = 0.0486$.

Chapter 2
The COSMOS Field: Submillimetre and Ancillary Observations

'So far as hypotheses are concerned, let no one expect anything certain from astronomy, which cannot furnish it.'

Nicolaus Copernicus

2.1 Introduction and Motivation

The literature consists of many studies of scaling relations (including for example Béthermin et al. 2015; Genzel et al. 2015; Scoville et al. 2017; Tacconi et al. 2018) that attempt to examine the evolution of the gas mass fraction of galaxies over cosmic time, at redshifts beyond the peak of star formation activity.

A recent study examining the evolution of dust emission in galaxies in the COSMOS field using stacking methodologies was performed by Béthermin et al. (2015). Like other *Herschel*-based SED stacking analyses (e.g. Genzel et al. 2015; Tacconi et al. 2018), average dust masses of binned sources were inferred by fitting SEDs to average stacked long-wavelength fluxes - specifically in that study, fluxes ranging from the mid-infrared to millimetre wavelengths. The fitted SEDs were constructed using dust emissivity models (the models from Draine & Li 2007),

wherein dust temperatures, and therefore dust masses, are luminosity-weighted. Molecular gas masses were then estimated using the derived dust masses, and an assumed gas-to-dust mass ratio (specifically, a metallicity dependent gas-to-dust ratio from Leroy et al. 2011).

Béthermin et al. (2015) examined galaxies with stellar masses (>3 $\times 10^{10} M_{\odot}$) and redshifts $z \leq 4$. In this Chapter, we will create a catalogue of galaxies using the COSMOS field, observed at 850 μm, to probe galaxies at lower stellar masses and higher redshifts (> 4). We note that the redshift data used in this study (Davies et al. 2015a; Andrews et al. 2017; Driver et al. 2018; see also Sections 2.3.1 and 2.4.2) is a combination of spectroscopic and photometric redshifts, with more sources having photometric redshifts as we progress further back through cosmic time. A discussion on the uncertainties of assigned redshifts for sources used in this study can be found in Section 2.4.2. We caution the reader that although we do probe to higher redshifts, these redshifts are photometric, and therefore are associated with a higher uncertainty compared to redshifts derived from spectroscopic observations. We describe the datasets, the source catalogues, ancillary measurements for each source, and a final selection of sources for the field. The work in this Chapter has been published in Millard et al. (2020).

2.2 THE SUB-MILLIMETRE IMAGE OF THE COSMOS FIELD

SCUBA-2 is a 10,000 pixel bolometer camera installed at the JCMT, which operates in the sub-mm wavelength regime (Holland et al., 2013). Specifically, it surveys the sky at 450μm and 850μm. SCUBA-2 has been used to target the COSMOS field (Scoville et al., 2007), a 2 deg^2 area of sky centred at RA = 10:00:28.60 and Dec = +02:12:21.00 (J2000; see Figure 2.1). We make use of the 850μm map from the S2COSMOS survey (Simpson et al., 2019), the deepest and most sensitive sub-mm image of the COSMOS field of this size to-date. This map incorporates archival data from S2CLS (Geach et al. 2017; Michałowski et al. 2017) and new data from S2COSMOS, providing a complete and homogeneous map of the COSMOS field at 850μm.

The median instrumental noise level over the central 1.6deg^2 region of

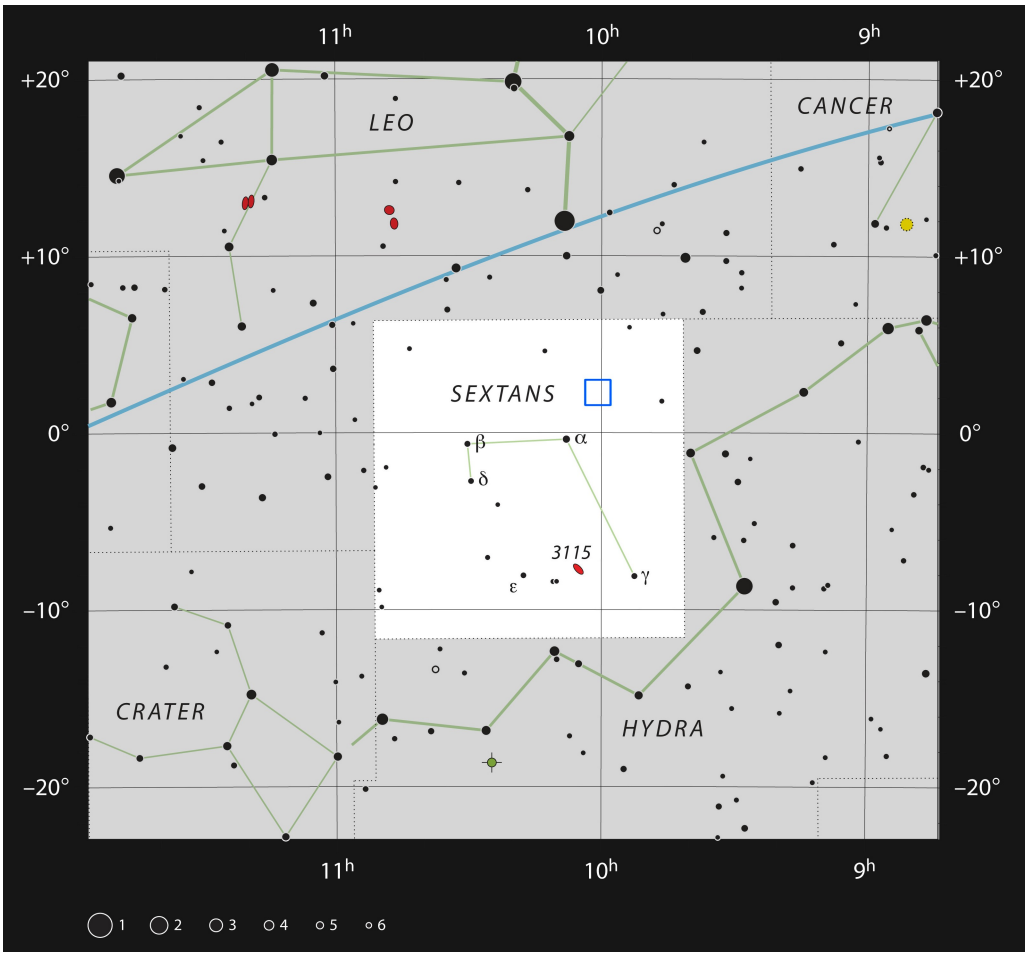

Figure 2.1: The location of the COSMOS field in the constellation of Sextans (blue square). Credit: ESO, IAU and *Sky & Telescope*[23].

the S2COSMOS survey is $\sigma_{850\mu m}$ = 1.2mJy beam^{-1}. There is also further coverage of 1deg^2, which has median instrumental noise levels of $\sigma_{850\mu m}$ = 1.7mJy beam^{-1}. Confusion noise is less than the instrumental noise, and is estimated to be $\sigma_c \sim$ 0.4mJy beam^{-1} (Simpson et al., 2019). Confusion noise represents the ideal noise level, the ultimate noise limit, for FIR/sub-mm observations. Confusion noise in the S2COSMOS map is created by unresolved background sources, faint galaxies blended within the JCMT beam (Simpson et al., 2019). Since this sensitivity limit is largely dictated by telescope aperture and observation wavelength (i.e. telescope resolution), if this level is reached and confusion noise is the dominant source of image noise, additional or longer exposures cannot improve image noise. However, in reality, instrumental noise dominates the S2COSMOS maps. We note that, unless otherwise stated, we make use of the matched-filtered map,

which is more sensitive to point source emission. For further details, we refer the reader to Simpson et al. (2019).

We will later stack on positions of galaxies in the 850μm S2COSMOS map to determine the average sub-mm properties of the population. We therefore require a source catalogue to provide the locations of COSMOS galaxies; our choice of catalogue is discussed in Section 2.3.

2.3 COSMOS GALAXIES: CONSTRUCTING A SOURCE CATALOGUE

In this study, we wish to make use of stacking techniques to determine statistical information about the gas properties of galaxies as they evolve through cosmic time. Stacking will allow us to push to lower stellar masses where one cannot detect an individual object, and potentially provide a more unbiased estimate of the population. For example, it gives us the opportunity to probe gas masses across galaxies with a wider range of star-forming properties than could necessarily be achieved by studying individual objects.

To study the evolution of gas mass, we divide our sources into bins of stellar mass (M_*) and redshift (z). A common way of estimating the stellar mass of galaxies is to use SED fitting routines. Since the COSMOS field is one of the most well studied areas of sky, with data covering almost the entire electromagnetic spectrum, photometric catalogues have been created for COSMOS sources, and subsequently exploited using many SED fitting routines.

In the following sections we compare the source catalogue from Driver et al. (2018) made using the SED fitting code MAGPHYS (da Cunha et al., 2008) to one created using the SED fitting routine CIGALE (Noll et al., 2009; Boquien et al., 2019) as part of the *Herschel* Extragalactic Legacy Project (HELP) database (Vaccari, 2016; Małek et al., 2018; Malek et al., 2019; Shirley et al., 2019) to justify the source list used in this work. The subsequent analysis shows that our choice of source catalogue is not likely to significantly impact the results of this study, and choosing, say, the CIGALE catalogue over the Driver/MAGPHYS catalogue would not change our conclusions.

[23] Full source https://www.eso.org/public/images/eso1124b/

2.3.1 DRIVER/MAGPHYS CATALOGUE OF GALAXIES

MAGPHYS (da Cunha et al., 2008) is an SED fitting code that fits pre-determined libraries of physically motivated model SEDs to panchromatic photometry data, returning probabilistic estimations of various physical parameters of the sources in question. This includes, for example, stellar masses and star formation histories. The stellar emission is based on synthetic spectra from Bruzual & Charlot (2003), wherein a Chabrier (2003) stellar initial mass function (IMF) is assumed. Dust attenuation follows the model present by Charlot & Fall (2000), where starlight can be attenuated by dust in both spherically symmetric birth clouds and in the ambient ISM. MAGPHYS employs an energy balance between the Ultraviolet-to-Near-Infrared (UV-NIR) and the Mid-Infrared-to-Far-Infrared (MIR-FIR) components; the UV-optical light attenuated by dust is re-emitted in the FIR. The dust emission responsible for the MIR to FIR originates from three sources: polycyclic aromatic hydrocarbons, small dust grains and large grains. Grains have temperatures of 30-60 K in birth clouds, and another cooler component with temperatures of 15-25 K is also modelled in the diffuse clouds with dust emissivity index β of 1.5 and 2.0 in the warm and cold components. The best fit model is determined using a χ^2 minimization technique, and, subsequently, best-fit values for each parameter are returned. In addition to this, probability distribution functions (PDFs) are generated for each parameter, from the summation of $e^{-\chi^2/2}$ over all models. The PDFs detail the most likely value for a given parameter. Here, we make use of the 50th-percentile values for any given parameter, since these are more representative of the range of models that fit the photometry than the single best-fit model.

We consider the MAGPHYS source catalogue, presented in Driver et al. (2018), which makes use of photometry provided by Andrews et al. (2017) using 22 filters (FUV, NUV, *ugriz*YJHK, IRAC1234, MIPS24/70, PACS100/160, SPIRE250/350/500); note that not all sources have fluxes for all of the filters, see Driver et al. (2018) for more details. This photometric catalogue is based on G10-COSMOS, a small region (1 deg^2) within the COSMOS field. Driver et al. (2018) use a i-band < 25 mag limited catalogue, based on results from a Source Extractor (Bertin & Arnouts, 1996) analysis of i-band[24] Subaru observations. The final photometric catalogue was created using the LAMBDAR routine (Wright et al. 2016;

[24] Note that the i-band Subaru central wavelength is 7709Å (Miyazaki et al., 2002).

Andrews et al. 2017). LAMBDAR produces aperture-matched photometry, and, for coarser resolution long-wavelength maps (such as the *Herschel* maps), deblends the flux from multiple sources by sharing the flux between overlapping apertures. The final MAGPHYS source catalogue used by Driver et al. (2018) is that presented in Andrews et al. (2017), with some additional minor adjustments to the selection process for assigning FIR fluxes to sources using LAMBDAR. This process resulted in an extension to the number of sources with associated FIR data (see Appendix A of Driver et al. 2018) compared to those presented in Andrews et al. (2017). We make use of the photometric catalogue `G10CosmosLAMBDARCatv06`, containing 185,907 sources.

In their MAGPHYS fitting work, Driver et al. (2018) make use of the BC03 stellar libraries and a modified version of MAGPHYS that includes the derivation of model FIR fluxes based on photon energy, as opposed to photon number, and the use of the latest PACS and SPIRE filter curves. We make use of their MAGPHYS catalogue `MagPhysG10v05`, which contains 173,399 sources. When cross-matched to `G10CosmosLAMBDARCatv06`, we find a match for every MAGPHYS source.

Redshifts in the MAGPHYS catalogue are sourced from an updated catalogue from Davies et al. (2015a). Where possible, spectroscopic redshifts are used; these are obtained via an independent extraction of spectroscopic redshifts from the zCOSMOS-Bright sample (see Davies et al. (2015a) and Andrews et al. (2017) for full details of their bespoke pipeline) combined with additional redshifts from PRIMUS, VVDS and SDSS (Lilly et al. 2007; Cool et al. 2013; Le Fèvre et al. 2013; Ahn et al. 2014). Where there are multiple spectroscopic redshifts for a given source, the most robust one is chosen. If spectroscopic redshifts are unavailable, photometric redshifts are sourced from COSMOS2015 (Laigle et al., 2016). The MAGPHYS sample contains 21,494 sources with reliable spectroscopic redshifts; the remaining 151,905 have photometric redshifts. The source catalogue for MAGPHYS is considered redshift complete down to the magnitude limit ($i < 25$ mag).

2.3.2 HELP/CIGALE CATALOGUE OF GALAXIES

CIGALE (Noll et al. 2009, Boquien et al. 2019) is an SED fitting routine wherein SED models are built using several modular components in a similar way to MAGPHYS, but also includes different dust attenuation curves, AGN emission,

and radio emission (Ciesla et al. 2016, Hunt et al. 2019).

Several modules for a given component can be considered in the fitting process to try and help disentangle different physical implications of similarly looking SEDs. Much like MAGPHYS, CIGALE also makes use of the concept of energy-balance; the energy absorbed by dust in the UV-NIR is re-emitted in the MIR-FIR. The parameters returned for the physical systems fitted by CIGALE are chosen by the user. Values of physical parameters returned by CIGALE are either the best-fit values (from the best-fitting SED), or likelihood-weighted means and likelihood-weighted standard deviations. The likelihood is taken to be $e^{-\chi^2/2}$. We use the likelihood-weighted values in this analysis, and refer the interested reader to Boquien et al. (2019) for further details.

In this work, we make use of photometry and CIGALE data from the HELP database (Vaccari 2016; Małek et al. 2018; Malek et al. 2019; Shirley et al. 2019; Oliver et al. *in prep.*). HELP provides a homogenized, multi-wavelength database of all the fields observed by *Herschel*, covering 1270 square degrees over 23 different fields (Shirley et al., 2019), including the COSMOS field. As the *Herschel* maps suffer from source confusion (Nguyen et al., 2010), XID+, a probabilistic deblending tool that uses Bayesian techniques to assign FIR fluxes to sources based on NIR and MIR positional prior catalogues (Hurley et al., 2017), was used by those authors to assign FIR fluxes to sources.

The HELP-COSMOS database includes 33 photometric bands, per source, that are suitable for SED fitting. To avoid over-dense photometry data causing forced SED fits, and to ensure that the deepest data are used, where there is photometry in similar bands for a given object, priority is given to the deepest observations. We refer the reader to Małek et al. (2018) for details, but briefly, the 19 bands used in the CIGALE COSMOS fits are: *ugriz*, N921 (a narrow band filter on Suburu/HSC), *y*JK, IRAC1234, MIPS24, PACS100/160, SPIRE250/350/500. Again, note that not every source may have fluxes for all filters.

Unlike MAGPHYS, CIGALE offers the user a choice for the input parameters. We refer the reader to Małek et al. (2018) for details, but briefly, the HELP consortium uses the Single Stellar Population (SSP) model of Bruzual & Charlot (2003), assuming a Chabrier (2003) IMF. They follow the dust attenuation curve of Charlot & Fall (2000) and dust emission is based on Draine & Li (2007), with AGN based

on Fritz et al. (2006). Star Formation Histories (SFHs) with delays and additional, optional, bursts are also implemented.

The HELP photometry catalogue for the COSMOS field is based on the COSMOS2015 catalogue from Laigle et al. (2016) (see Section 2.3.4 for a description of the COSMOS2015 catalogue). The CIGALE catalogue we use was compiled by fitting every source within the HELP photometric catalogue for the COSMOS field that has at least four 'optical' and 'NIR' fluxes, where 'optical' bands are defined as *ugrizy* and N921, and 'NIR' bands are *J* and *K* (Małek et al. 2018; Shirley et al. 2019)

Photometric redshifts are calculated as part of the HELP pipeline, using a Bayesian combination approach, which combines popular photometric redshift estimator templates to achieve the best estimate of the redshift, see Duncan et al. (2018a) and Duncan et al. (2018b). Spectroscopic redshifts are used, where possible, and are sourced from various different surveys compiled by the HELP consortium including: SDSS (Albareti et al., 2017), PRIMUS (Cool et al., 2013), zBRIGHT (Lilly et al., 2007) and GAMA (Davies et al., 2015a). In total, CIGALE fits are available for 639,873 sources with photometric redshifts and 39,890 sources with spectroscopic redshifts.

2.3.3 CROSS CHECK AND VALIDATION OF THE CATALOGUES AVAILABLE IN THE LITERATURE

As a consistency check, we cross-match the results from MAGPHYS and CIGALE for the COSMOS field, and compare the calculated stellar masses for the resulting population. We make use of TOPCAT (Tools for OPerations on Catalogues And Tables, Taylor 2005b), selecting sources that are matched within 0.1″ on the sky.

There are several RA and Dec options within the MAGPHYS catalogue - we choose to cross-match to the CIGALE catalogue using the RA and Dec values from the COSMOS2015 catalogue (Laigle et al., 2016) (see also Section 2.3.4). For sources with photometric redshifts in the CIGALE catalogue, the separation between matching sources is well below typical astrometric uncertainties. We find 114,546 matches in this way. Similarly for the sources with spectroscopic redshifts in the CIGALE catalogue, we find most sources are separated by a radius between

0.07960″ and 0.07965″. We find 26,749 matches for sources with spectroscopic redshifts in the CIGALE catalogue. This brings our total number of matches between MAGPHYS and CIGALE to 141,295.

Although we are confident in the accuracy of the cross-matching, there are still likely to be some spurious matches in our resultant catalogue. We estimate the number of false matches as:

$$\text{spurious matches} = \frac{N_M \pi r^2 N_C}{A} \tag{2.1}$$

where N_M is the number of sources in the MAGPHYS catalogue, r is the matching radius (in arcsec), N_C is the number of sources in the CIGALE catalogue within the area covered by the MAGPHYS catalogue, and A is the area covered by the MAGPHYS catalogue (in arcsec^2). For sources in the CIGALE catalogue with photometric redshifts, we estimate that there may be 136 spurious matches with the MAGPHYS catalogue, using a matching radius of 0.1″. For sources in the CIGALE catalogue with spectroscopic redshifts, we estimate that there may be 13 spurious matches. This is a false-positive rate of 0.1% and <0.05%, respectively, and thus are are unlikely to have a significant effect on our analysis.

Since both SED fitting routines use the galaxy redshift as an input, we also filter this 'matched' selection of galaxies to exclude sources with redshift differences between the two catalogues of $\Delta z > 0.02(1+z)$. This is based on the maximum quoted photometric redshift error in the COSMOS2015 catalogue (Laigle et al., 2016), as such is likely a conservative estimate in the uncertainty in z. We choose to use the MAGPHYS redshifts in this selection criteria. We further filter for sources that have poor fits. To do this, we first determine a χ^2 cut to apply to the MAGPHYS and CIGALE catalogues by fitting continuous probability distributions to the χ^2 values, where the mean of the distribution provides our χ^2 cut value. We filter for catastrophic fitting failures, to allow the fitting functions to converge to a result - in practice this means that for MAGPHYS, we do not consider sources with $\chi^2 > 40$, and for CIGALE, we do not consider sources with $\chi^2 > 80$. This leaves us with 141,088 MAGPHYS sources and 138,215 CIGALE sources to determine the χ^2 thresholds. The distribution of the remaining χ^2 results are shown in Figures 2.2 and 2.2 for MAGPHYS and CIGALE respectively.

When logged, the MAGPHYS χ^2 values clearly display a Gaussian distribution (Figure 2.2). A lognormal distribution was fitted to the MAGPHYS χ^2 values, giving a threshold $\chi^2_{\rm thr,MAG} = 1.93$. The CIGALE χ^2 values do not display a Gaussian distribution in log space. The distribution displayed by the data is similar to than of an exponentially modified Gaussian (Figure 2.2). Subsequently, this function was fit to the logged CIGALE χ^2 values, giving a threshold $\chi^2_{\rm thr,CIG} = 5.60$. The difference in the χ^2 threshold values determined for the two different SED fitting codes is related to the different number of free parameters and the way of calculating the final χ^2, which is non-trivial.

Finally, we filter for sources that have $\log(M_*/M_\odot) < 9.5$ in both catalogues, as we do not consider galaxies below this stellar mass in this study (see Chapter 3 for more details). This leaves us with 23,164 sources out to a maximum photometric redshift of $z = 5.4$, and a maximum spectroscopic redshift of $z = 3.1$, for which to compare stellar masses. The distribution of redshifts is shown in Figure 2.3. Figure 2.4 compares the ratio of stellar masses resulting from MAGPHYS and CIGALE. The ratio of stellar masses indicate a systematic offset between CIGALE and MAGPHYS, with a maximum dispersion value of 0.139 dex (the best fit line offsets are displayed in Table 2.1). The offsets are similar in magnitude to the dispersions of the different populations of sources, implying that the offset in results for the different SED fitting programmes is small (at most 25 per cent). We note that this offset is lower than the systematic underestimation of stellar masses from SED fitting due to outshining, where bright young stars can mask underlying older stellar populations (Sorba & Sawicki, 2015, 2018; Abdurro'uf, 2018). We also repeated this exercise for sources where $\Delta z > 0.02(1+z)$ to determine if there were any systematic offsets for those sources with larger uncertainties on their redshifts. In this case, the best fit line offset for all sources is 0.113, around 20 per cent lower than the sources with $\Delta z < 0.02(1+z)$ (which are listed in Table 2.1), but with a stronger evolution with stellar mass. The offset in this case becomes even more pronounced at low stellar masses ($< 10^{10} M_\odot$). Sources with larger Δz showed a larger dispersion; 0.167 for all sources, compared to 0.132 for the sources with smaller Δz (an increase of around 25 per cent).

Therefore the choice of source catalogue is not likely to be our largest source of error, and Figure 2.4 demonstrates that choosing stellar masses from the

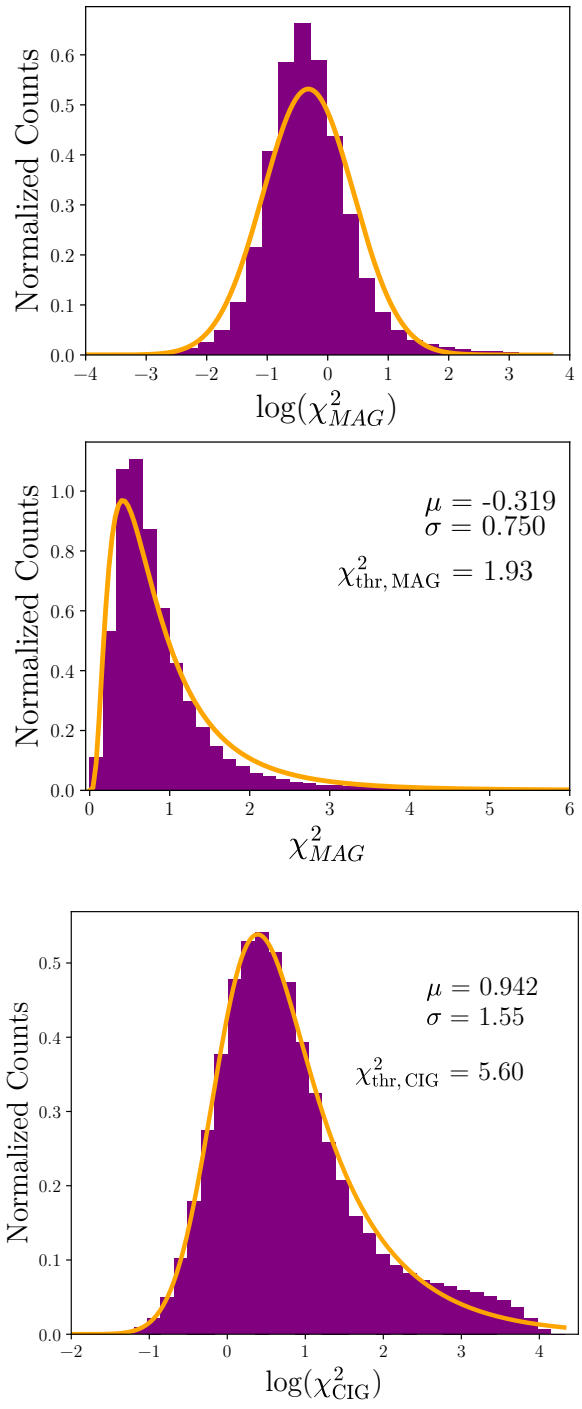

Figure 2.2: The χ^2 distribution of a filtered sub-sample of galaxies in the COSMOS field that have both MAGPHYS and CIGALE fits. The sources displayed here have $\Delta z < 0.02(1+z)$ between the MAGPHYS and CIGALE catalogues. *Top:* logged MAGPHYS χ^2 values (purple) are well fitted with a Gaussian (orange). *Middle*: a lognormal fit to the MAGPHYS χ^2 distribution, with mean μ, standard deviation, σ, and χ^2 threshold, $\chi^2_{\mathrm{thr,MAG}}$. *Bottom:* Logged CIGALE χ^2 values clearly do not display a Gaussian distribution. Instead, an exponentially modified Gaussian is fitted to the logged χ^2 values (orange) with μ, σ and $\chi^2_{\mathrm{thr,CIG}}$ displayed.

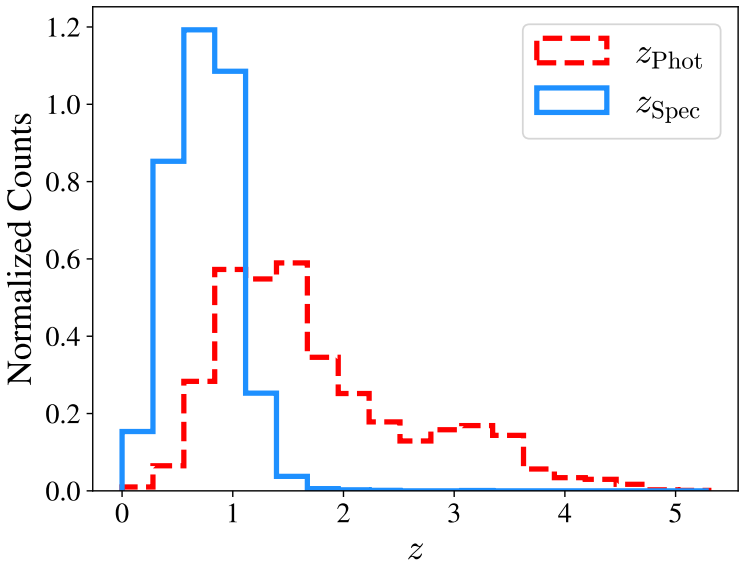

Figure 2.3: The redshift distribution of a filtered sub-sample of 23,164 galaxies in the COSMOS field that have both MAGPHYS and CIGALE fits, $\Delta z < 0.02(1+z)$ and $\log(M_*/M_\odot) \geq 9.5$. The blue solid line indicates the distribution of sources with CIGALE spectroscopic redshifts. The red dashed line indicates the distribution of sources with CIGALE photometric redshifts.

CIGALE catalogue would not change our conclusions. We ultimately choose to use the MAGPHYS dataset for the rest of this study, since it is limited to the central regions of the map (Figure 2.5) where the noise levels are lowest (Simpson et al., 2019). We next cross-match the `MagPhysG10v05` catalogue to the publicly available COSMOS2015 catalogue (Laigle et al., 2016) using RA and Dec. We do this to ensure catalogue completeness, and to exploit the additional photometry provided in the COSMOS2015 survey (see Section 2.4.1).

2.3.4 THE COSMOS2015 CATALOGUE

The COSMOS2015 catalogue (Laigle et al. 2016) contains half a million NIR selected objects over the COSMOS field, with photometry covering wavelengths from the X-ray range through to the radio. The source detection image is a combination of YJHK$_s$ from UltraVISTA DR2 (McCracken et al., 2012) and WIRCAM (McCracken et al., 2010), and z^{++} images from Subaru Suprime-Cam (Taniguchi et al. 2007; Taniguchi et al. 2015). COSMOS2015 is 90% complete to a stellar mass of $10^{10} M_\odot$ out to $z = 4$. Photometric redshifts errors are small; $\sigma_{\Delta z/(1+z)} = 0.007$ for

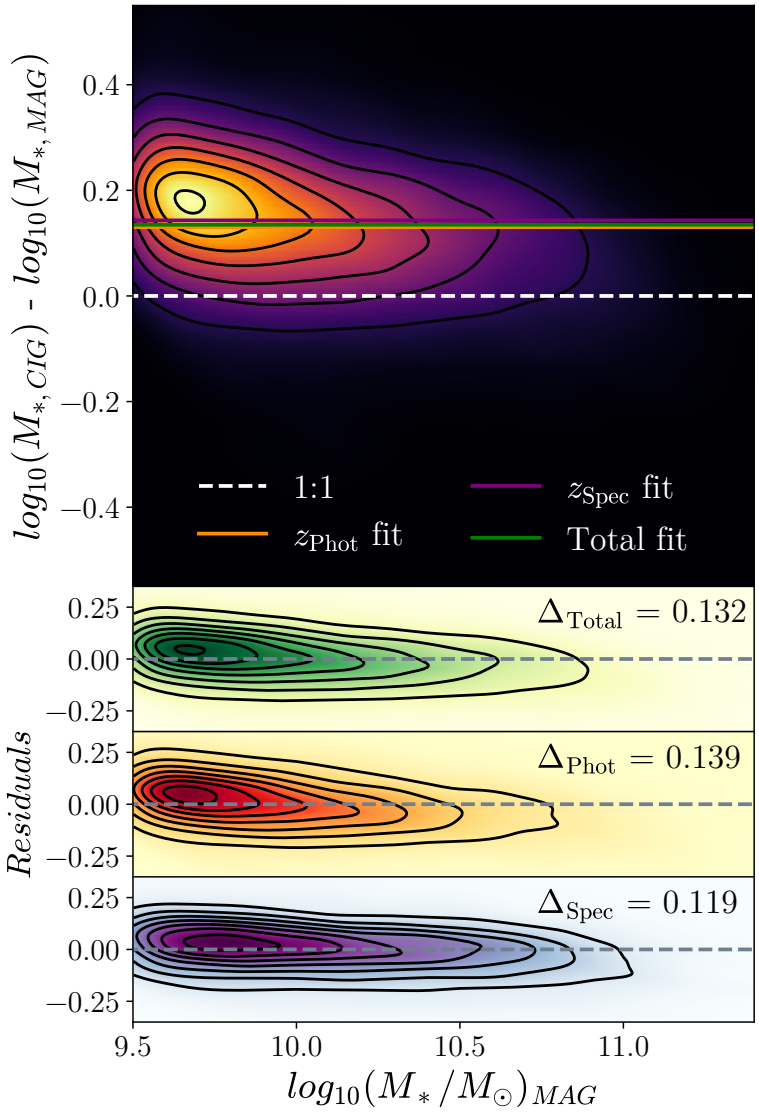

Figure 2.4: A comparison of the stellar masses for a filtered sub-sample of galaxies in the COSMOS field that have both MAGPHYS and CIGALE fits. The sources displayed here have $\log(M_*/M_\odot) > 9.5$ and a redshift difference between the two catalogues of $\Delta z < 0.02(1+z)$. *Upper:* Distribution of the matched sources. White dashed line is the 1:1 line. Green, orange and purple lines are best fits to different populations, with a fixed gradient of zero. *Orange line*: sources with photometric redshifts in the CIGALE dataset. *Purple line*: sources with spectroscopic redshifts in the CIGALE dataset. *Green line*: all matched sources. *Lower three plots:* residuals of best fit line for different populations and corresponding dispersion values, Δ. *Lower-top:* all matched sources. *Lower-middle:* sources with photometric redshifts in the CIGALE catalogue. *Lower-bottom:* sources with spectroscopic redshifts in the CIGALE catalogue.

Name	Offset (dex)
Total fit	0.135
$z_{\rm Phot}$ fit	0.130
$z_{\rm Spec}$ fit	0.143

Table 2.1: Line offsets for the best fit lines fit to the MAGPHYS and CIGALE ratio of stellar masses displayed in Figure 2.4. The lines are fixed to have a gradient of 0. *Total fit*: all of the sources with $\Delta z < 0.02(1+z)$, $\log(M_*/M_\odot) > 9.5$, and with $\chi^2_{\rm thr,MAG} < 1.93$ and $\chi^2_{\rm thr,CIG} < 5.60$. $z_{\rm Phot}$ *fit*: similar to 'total fit', but only for sources that have photometric redshifts in the CIGALE catalogue. $z_{\rm Spec}$ *fit*: similar to 'total fit', but only for sources that have spectroscopic redshifts in the CIGALE catalogue.

$z < 3$, and $\sigma_{\Delta z/(1+z)} = 0.021$ for $3 < z < 6$. The photometric redshift errors were estimated using the normalized median absolute deviation (Hoaglin et al. 1983; Laigle et al. 2016), which calculates the dispersion of the photometric redshifts, as compared to the spectroscopic redshifts. Spectroscopic redshifts were compiled from multiple surveys (see Laigle et al. 2016 for details), and only the highly reliable 97% confidence level spectroscopic redshifts were used (Lilly et al., 2007).

2.4 FINAL COSMOS CATALOGUE OF GALAXIES

Cross matching our Driver/MAGPHYS catalogue to the COSMOS2015 source catalogue reduces our MAGPHYS sample to 155,858 sources. The extent of the MAGPHYS sources across the SCUBA-2 850μm map is shown in Figure 2.5. The sources discarded in the matching process are evenly distributed across the COSMOS field, with the exception of the locations of bright stars in the field, more sources are removed around these than the field average (Figure 2.6). We attribute this effect to more aggressive bright star masking in the COSMOS2015 catalogue compared to the MAGPHYS catalogue. In order to check whether there are any biases introduced by doing this cross match, we compare the stellar mass and redshift distribution of removed sources in Figure 2.7. Many of the sources are relatively nearby, with $z < 1$, where our number counts are highest (see Figure 3.1).

Thus the MAGPHYS-COSMOS2015 sample contains 21,212 sources with reliable spectroscopic redshifts; the remaining 134,646 have photometric redshifts. We next filter out the MAGPHYS-COSMOS2015 matched galaxies with $\log(M_*/M_\odot) <$

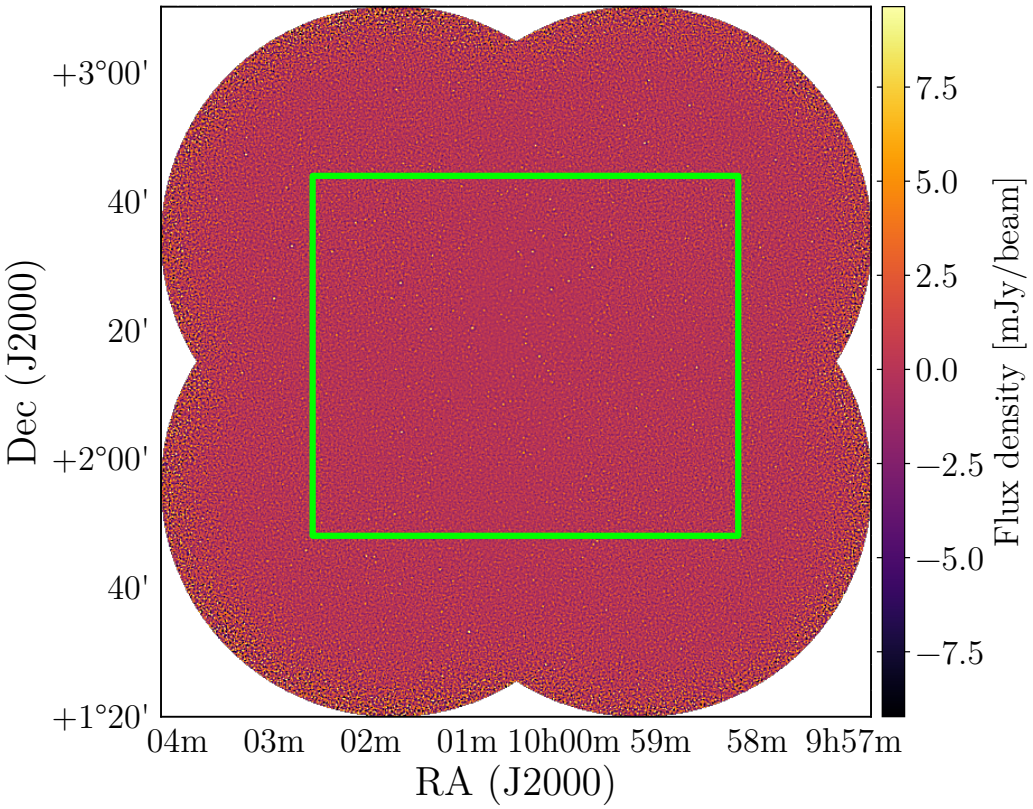

Figure 2.5: The extent of MAGPHYS sources in the COSMOS field (lime square), covering approximately 1 deg^2, across the 850μm match-filtered SCUBA-2 map.

9.5 (see Section 3.3), leaving 64,684 sources, of which 13,955 have reliable spectroscopic redshifts. Figure 2.6 shows the distribution of sources in the MAGPHYS catalogue without matches in COSMOS2015. Figure 2.7 illustrates the stellar mass and redshift distribution of sources removed from the original MAGPHYS catalogue. Note here that only sources with $\log(M_*/M_\odot) > 5$ are considered, as suggested by Driver et al. (2018).

2.4.1 REMOVING ACTIVE GALACTIC NUCLEI

AGN emit radiation across the electromagnetic spectrum. By definition, this means that the emission from AGN contaminates the galactic emission used to estimate physical properties, such as stellar mass and star formation rates, particularly in the infrared (Ciesla et al., 2015). Disentangling the galactic infrared emission

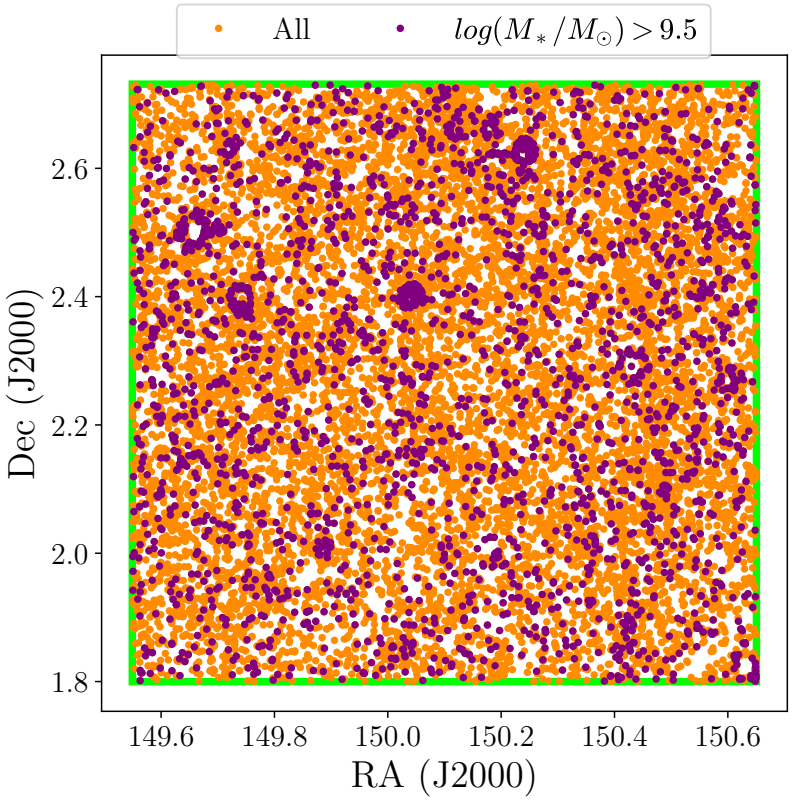

Figure 2.6: The distribution of sources in the MAGPHYS catalogue but not in the COSMOS2015 catalogue. Orange markers are all the sources; purple markers are sources with $\log(M_*/M_\odot) > 9.5$. The green box is the same as that shown in Figure 2.5 i.e. the overall extent of the MAGPHYS sources.

from the AGN infrared emission is difficult. But, if the emission from AGN is not properly accounted for, galactic stellar mass estimates and star formation rates can suffer systematic uncertainties of up to 50% (Ciesla et al., 2015). Accurately estimating physical properties of galaxies hosting AGN using SED-fitting methods is non-trivial. As such, it is important that we remove AGN from our sample.

We first remove potential AGN from our MAGPHYS sample by following the prescription described in Driver et al. (2018) with an additional step. AGN are identified using a combination of IR, radio and X-ray data. Unless otherwise stated, we use photometry from `G10CosmosLAMBDARCatv06`. As in Driver et al. (2018), we remove sources with stellar masses greater than $10^{12} M_\odot$. We remove AGN based on their NIR (3.6-8 μm) colours using the criteria from Donley et al. (2012) (Equations 1 and 2 therein). We remove sources that are radio-loud using the criteria from Seymour et al. (2008), where $\log_{10}(S_{1.4GHz}/S_{Ks}) > 1.5$ and

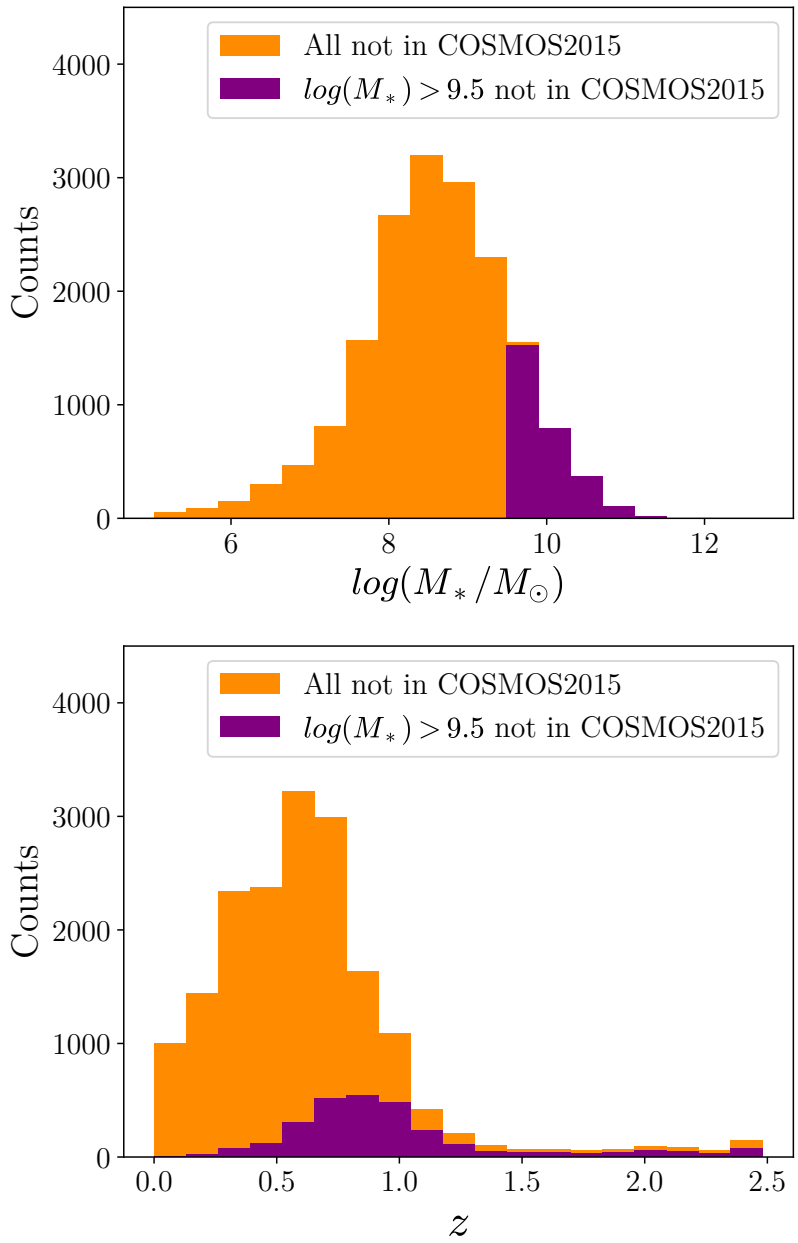

Figure 2.7: The stellar mass and redshift distribution of sources in the MAGPHYS catalogue but not in the COSMOS2015 catalogue. Orange marks all the sources; purple marks sources with $\log(M_*/M_\odot) > 9.5$.

$\log_{10}(S_{24\mu m}/S_{1.4GHz}) < 0.0$. The 1.4GHz radio fluxes are obtained from COSMOS2015 (using the FLUXPEAK photometry). We also reject any source that has a non-zero flux in any of the *XMM-Newton* bands in COSMOS2015 (Laigle et al., 2016).

We additionally make use of the *Chandra*-COSMOS Legacy Survey (CCLS)[25] (Civano et al., 2016; Marchesi et al., 2016), a catalogue of 4016 X-ray point sources across $\sim$2.2 deg^2 of the COSMOS field. We identify AGN in this catalogue by selecting sources that have a reliable optical counterpart, a spectroscopic or photometric redshift, and are not flagged as stars (Suh et al., 2019). Using these criteria, we classify 3713 sources in the CCLS as AGN. Subsequently, we cross-match this reduced CCLS catalogue to the MAGPHYS-COSMOS2015 catalogue, identifying 715 sources that have a *Chandra* counterpart. We additionally reject any sources that have a flux recorded for any of the three *Chandra* bands.

In combining the prescription from Driver et al. (2018) and the AGN flagged in the CCLS, we remove 1026 sources that are potential AGNs, this provides a final sample of 63,658 galaxies. For stacking purposes, we do not filter the catalogue based on the goodness-of-fit threshold $\chi^2_{\rm thr,MAG}$ level (see Section 2.3.3 for details), this ensures that we sample the complete catalogue of sources for our stellar mass cut-off.

2.4.2 PRECISION OF PHOTOMETRIC REDSHIFTS IN THE FINAL SAMPLE

Although in this work we hope to probe the sub-millimetre properties of galaxies out to higher redshifts, some of the redshifts in our sample are photometric, and therefore are associated with a higher uncertainty compared to redshifts derived from spectroscopic observations. The redshift data used in this study is taken from Davies et al. 2015a; Andrews et al. 2017; Driver et al. 2018 is a combination of spectroscopic and photometric redshifts, with more sources having photometric redshifts as we progress further back through cosmic time. We now consider the precision of photometric redshifts for sources in our final sample. We identify sources with reliable spectroscopic redshifts and use their corresponding

[25] https://irsa.ipac.caltech.edu/data/COSMOS/tables/chandra/

COSMOS2015 photometric redshifts (removing sources that have catastrophic failures for photometric redshift), giving us a sub-sample of 12,332 sources to consider, out to a maximum spectroscopic redshift of 3.47, with a median spectroscopic redshift of 0.68. We estimate the precision of the photometric redshifts by following the prescription in Laigle et al. (2016). We calculate the normalized median absolute deviation (Hoaglin et al., 1983), σ:

$$\sigma = 1.48 \times \text{median}\left(\frac{|z_p - z_s|}{(1+z_s)}\right) \tag{2.2}$$

where z_s are the spectroscopic redshifts, and z_p are the photometric redshifts. We find σ = 0.0104, a value roughly 50 per cent higher than the corresponding value calculated in Laigle et al. (2016), for a similar redshift range. Overall, the dispersion of the photometric redshifts is low, giving us confidence that the photometric redshifts are accurate. Therefore, although many of our sources do not have reliable spectroscopic redshifts, we do not anticipate that this will impact significantly on our results.

2.5 CONCLUSIONS

In this Chapter, we have introduced the sub-millimetre data of the COSMOS field obtained using SCUBA2 on the JCMT (the S2COSMOS map). We discussed our selection of source catalogue and the available ancillary datasets. This dataset will ultimately be used to derive gas mass fractions for galaxies in this redshift range and to investigate the evolution of the gas mass fraction in this redshift regime (Chapter 3). Later we will use this to investigate the dust content and evolution in the dust mass content of galaxies (Chapter 4.)

Chapter 3
Evolution of Gas Fraction in the COSMOS Field

'With increasing distance our knowledge fades, and fades rapidly. Eventually, we reach the dim boundary - the utmost limits of our telescopes. There, we measure shadows, and we search among ghostly errors of measurement for landmarks that are scarcely more substantial.'

Edwin Hubble

3.1 Introduction and Motivation

Even though knowing the gas content of galaxies is key to understanding their evolution, estimating the gas content of high-z galaxies is non-trivial. The atomic phase of the ISM can be reliably estimated using the 21 cm line, but telescopes currently in operation are not sensitive enough to detect this at high-z (Catinella et al., 2010). Gas in the molecular phase can be estimated using CO line transitions as a tracer (e.g. Solomon & Vanden Bout 2005; Coppin et al. 2009; Tacconi et al. 2010; Casey et al. 2011; Bothwell et al. 2013; Carilli & Walter 2013; Tacconi et al. 2013; Combes 2018) but this method is costly in terms of telescope time. An

added complication is that the conversion factor used to transform CO detections into mass estimates of molecular hydrogen is notoriously uncertain, particularly at low metallicities, and there are also indications that it can vary across the galactic disc (e.g. Bolatto et al. 2013; Béthermin et al. 2015; Genzel et al. 2015; Scoville et al. 2016). Further, the high-z galaxies observed using CO transitions are often non-typical galaxies including massive star-forming sub-millimeter galaxies, galaxies that host AGN, and lensed sources (e.g. Greve et al. 2005; Bothwell et al. 2013; Carilli & Walter 2013; Riechers et al. 2013; Cañameras et al. 2018; Harrington et al. 2018; Calistro Rivera et al. 2018).

Over the past few years, an alternative approach to measure the molecular gas content of galaxies has been gaining momentum: using the optically thin dust continuum emission detected at a single sub-mm wavelength as a tracer of the gas (Eales et al. 2012; Scoville et al. 2014; Scoville et al. 2016; Scoville et al. 2017). As described in Chapter 1, Scoville et al. (2016) and Scoville et al. (2017) used samples of galaxies that have both 850μm measurements from ALMA and molecular gas masses estimated using CO observations to derive an empirical relation to estimate gas masses using optically thin emission from dust. In this Chapter, we build on the pilot studies of Scoville et al. (2016) and Scoville et al. (2017) and use dust emission to trace the gas content of galaxies over much of the history of the Universe.

Béthermin et al. (2015) recently examined dust properties of galaxies in the COSMOS field. In this Chapter, we use stacking methodologies on the 850μm S2COSMOS catalogue from Chapter 2 to derive stacked sub-millimetre fluxes for galaxies out to high redshifts, $0 \leq z \leq 5$, with stellar masses of $10^{9.5} \leq M_*(M_\odot) \leq 10^{11.75}$.

There is a major difference in method between the analysis in this work and that of Béthermin et al. (2015) because we use mass-weighted rather than luminosity-weighted temperatures. We divide galaxies in the COSMOS field into bins of stellar mass and redshift, and describe a stacking methodology used to increase the signal to noise and measure the 850 μm flux for galaxies in different stellar mass and redshift bins. We make use of relations developed by Scoville et al. (2016) and Scoville et al. (2017) to estimate average gas masses and gas fractions for the binned galactic population. We examine the evolution of the gas mass fraction

of galaxies over cosmic time in different stellar mass bins, beyond the peak of star formation activity and compare these results to scaling relations in the literature. We also split our sample into passive and star-forming galaxies, as a diagnostic tool for understanding the results of our stacking analysis on the collective population. The work in this Chapter has been published in Millard et al. (2020).

3.2 DERIVING SUB-MILLIMETRE FLUXES: A STACKING ANALYSIS

Individually, most of the galaxies in our sample have 850μm fluxes below the noise level of the S2COSMOS map (Simpson et al., 2019). To circumvent this issue, we make use of well-established stacking methodologies, wherein we co-add the emission from many similar sources to determine an average flux, which is representative of the sub-population in question. We lose information about individual sources, but gain information on the sample of galaxies as a whole.

We stack using the COSMOS2015 (Laigle et al. 2016, Section 2.3.4) positions for the sources in our catalogue of 63,658 galaxies. We split the sources into regularly spaced $\log(M_*)$ and z bins. The distribution of sources in this parameter space is displayed in Figure 3.1 (our lower limit on stellar mass is $\log(M_*/M_\odot) \geq 9.5$). For each $(M_* - z)$ bin, small cutouts of the 850μm S2COSMOS data and error maps (Simpson et al., 2019) are made, centred on each individual source. The average 'stamp', $\langle S_{s,850\mu\mathrm{m}} \rangle$, for sources in a bin is calculated using the inverse variance-weighted (IVW) mean of each of the individual cutouts:

$$\langle S_{s,850\mu\mathrm{m}} \rangle = \frac{\Sigma_i S_i/\sigma_i^2}{\Sigma_i 1/\sigma_i^2} \tag{3.1}$$

where S_i is the data map cutout for the ith source, and σ_i is the error map cutout for the ith source. The average flux, $\langle S_{850\mu\mathrm{m}} \rangle$, for a given bin is then taken to be the central pixel value of the final coadded stamp (where the pixel scale of S2COSMOS is 2″), since the maps are in units of mJy/beam. Details of the $(M_* - z)$ bins are listed in Table 3.1 with pictorial examples of the stacks shown in Figure 3.2. The top panel shows an example of a stacked cutout for a $(M_* - z)$ bin with a clear, strong detection of 850μm flux. In this stack, the emission is uniformly and centrally

concentrated, as expected, since the galaxies are all assumed to be point sources in the SCUBA-2 COSMOS map. Conversely, Figure 3.2 (bottom panel) is an example where we do not observe a strong detection of 850μm flux. In this stack, there is no central peak of 850μm flux. This implies that the galaxies used in the stack do not have significant 850μm emission.

3.2.1 ERROR ESTIMATION USING MONTE CARLO SIMULATIONS

To estimate the errors on the average fluxes for each bin, we make use of Monte Carlo (MC) simulations to generate random source positions within the 850μm S2COSMOS map. This gives us an estimation of the significance of the stacked signal determined from our source catalogue. Since the average value of the S2COSMOS map is zero, randomly selected positions should exhibit a Gaussian flux distribution, centred on zero. In other words, on average, flux values from random positions within the data map should not be significant. The width of the average distribution of randomly selected flux values is an estimate of the error on our average fluxes.

We generate 1000 artificial catalogues of random sources, with the maximum extent of the RA and Dec distribution of the sources limited to that of the input source catalogue. For each ($M_* - z$) bin, we consider the number of sources in this bin for the original MAGPHYS-COSMOS2015 catalogue, and randomly extract, without replacement, this many sources from the first artificial catalogue. We then stack these sources, using the 850μm S2COSMOS data map and noise map, as we did for the MAGPHYS-COSMOS2015 catalogue of galaxies. Examples of random stacks are shown in the middle panels of Figure 3.2. In the IVW stacks of randomly selected positions, we see no significant emission detected in the centre of the stacks.

For each ($M_* - z$) bin, 1000 mock stacked stamps are generated, and the central pixel values for each are stored. Subsequently, for each ($M_* - z$) bin, a histogram is made of the central pixel values. Figure 3.3 shows illustrative examples of histograms of the central pixel values determined for a selection of ($M_* - z$) bins, using the 1000 random source catalogues generated for the MC simulation on the location of sources within the S2COSMOS map. The central pixel values of the stacked stamps generated using the random sources broadly display

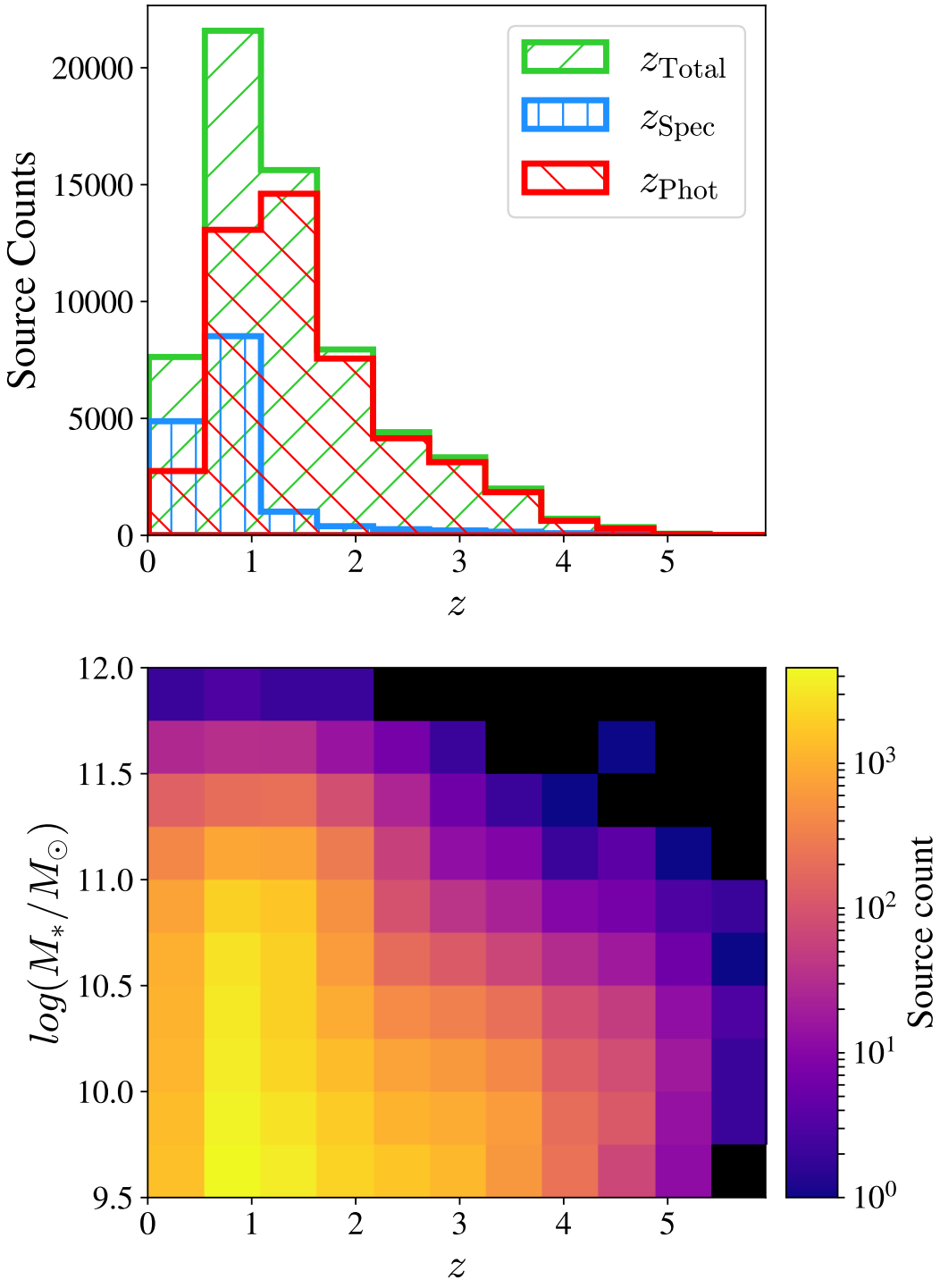

Figure 3.1: *Upper:* A histogram of the redshifts for sources in the COSMOS field with $\log(M_*/M_\odot) > 9.5$. These sources are used in the stacking analysis to determine ISM masses. The z bin resolution is the same as that displayed in the lower figure. Green: all the sources. Blue: sources with spectroscopic redshifts in the MAGPHYS catalogue. Red: sources with photometric redshifts in the MAGPHYS catalogue. *Lower:* A 2D histogram illustrating the distribution of MAGPHYS sources in the COSMOS field with $\log(M_*/M_\odot) > 9.5$, in $(M_* - z)$ space. Black denotes that there are no sources in the bin.

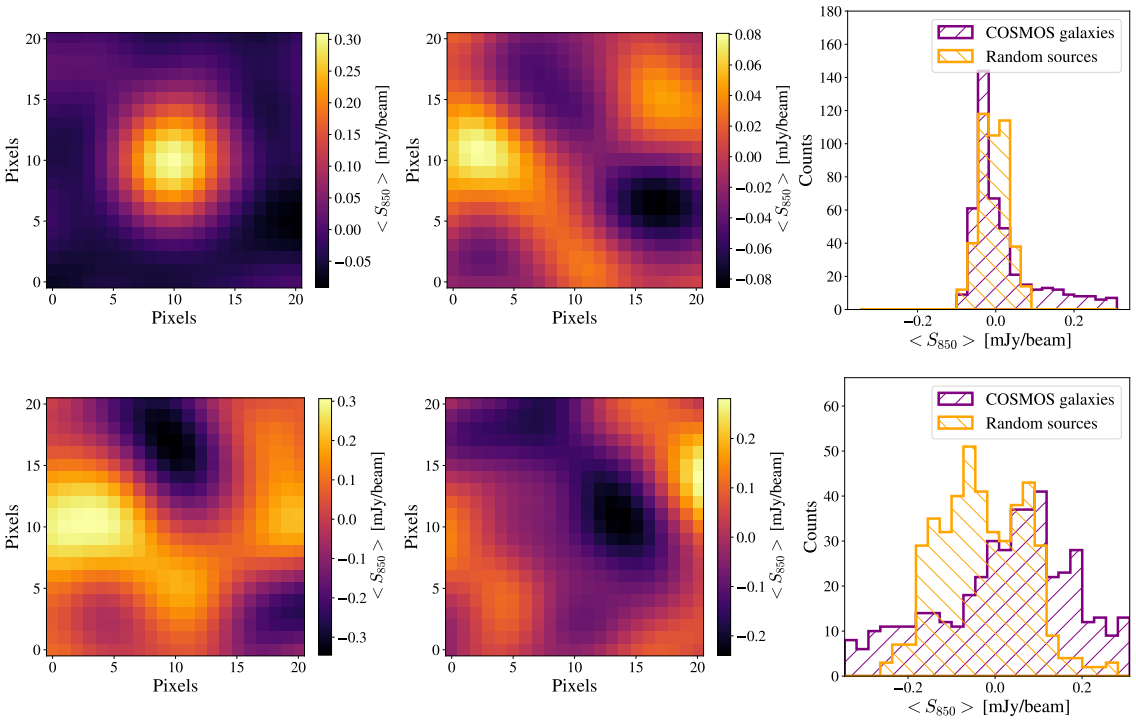

Figure 3.2: Examples of the 850μm IVW stacked stamps for $\langle z_{\rm bin} \rangle$ = 0.82 and $\log(M_*/{\rm M}_\odot)$ bin = 10.75-11.00 (*top*) and $\langle z_{\rm bin} \rangle$ = 0.28 and $\log(M_*/{\rm M}_\odot)$ bin = 11.25-11.50 (*bottom*). In the *left* to *right* panels, we show: *left:* the 850μm IVW stacked stamp resulting from stacking at the location of COSMOS sources (N = 2033 sources in top panel, N = 145 sources in the bottom panel). In the top left panel, we see a clear detection of 850μm flux present in the centre of the stack. In the bottom left panel, we do not detect the source in the 850μm stack. *Middle:* An example of the resulting IVW stack from random positions within the extent of the original MAGPHYS catalogue using the same number of sources as in the left panel. There is no clear detection of emission from these mock sources, as expected. *Right:* Histograms of the pixel values for the IVW stack of our galaxy sample (purple) and mock galaxies (orange). In the top panel, the stacked galaxies show a deviation from a Gaussian distribution, with additional pixels with high positive values, correlating with the strong detection of 850μm flux displayed in the stacked stamp in the left panel. The pixels in the stack of mock sources are approximately Gaussian and centred on zero.

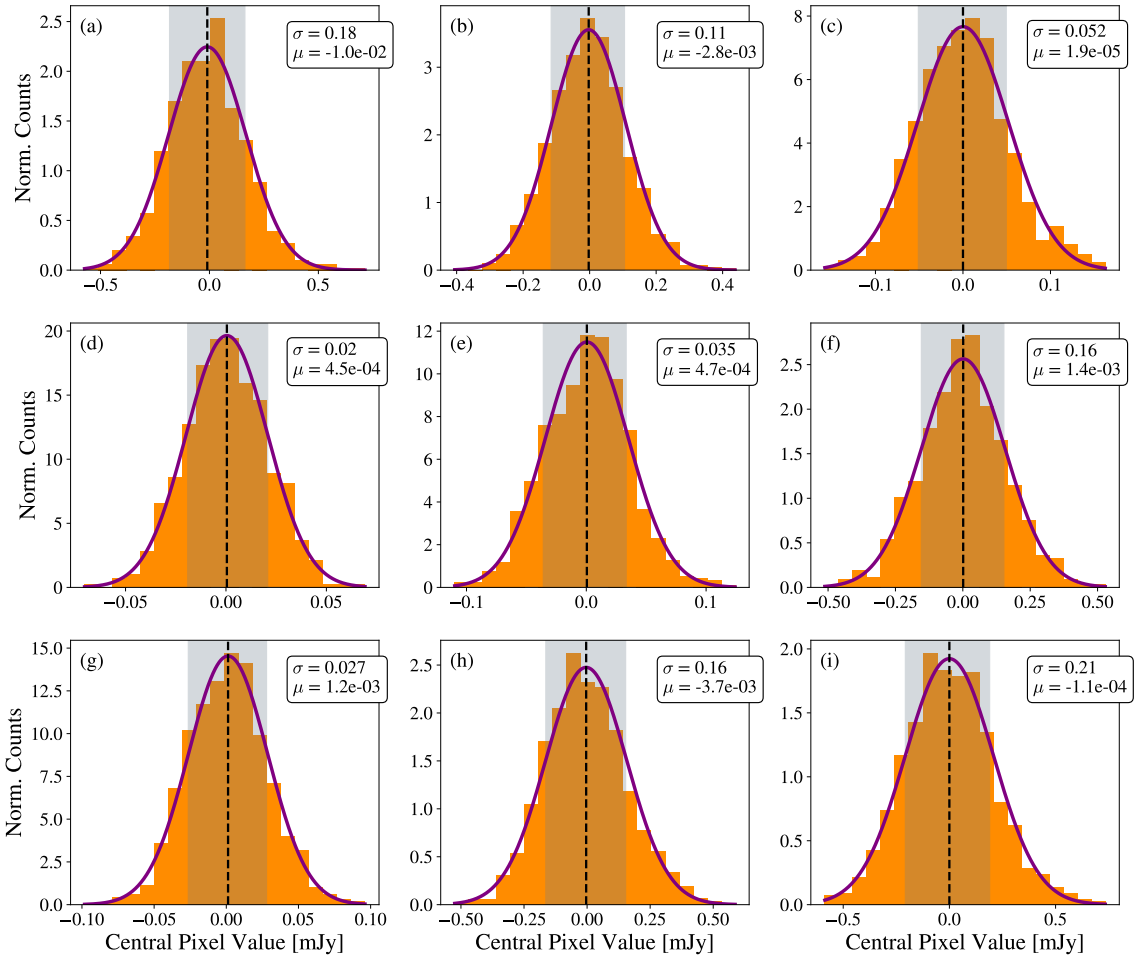

Figure 3.3: Normalised histograms of the central pixel values determined using 1000 random source catalogues and MC methodologies for a random selection of $(M_* - z)$ bins. The black dashed vertical line marks the mean of the distribution. The grey shaded region marks the extent of the 16th- and 84th-percentiles. The standard deviation, σ, and mean, μ, are denoted in the upper right corner. The purple line is a Gaussian fit to the data, calculated using the stated mean and standard deviation. Details of the bins displayed in the figure can be seen in Table 3.2; the letter in the upper left corner of each subplot is the cross-reference for this table. For further details on the displayed bins, see Table 3.1.

a Gaussian distribution centred around zero. This is to be expected; the average of the S2COSMOS map is zero, and these sources are not expected to have any true 850μm flux associated with them. Therefore, on average, stacking on these random sources should return a null result. Since the central pixel values are approximately Gaussian distributed, for a given bin, the width of the distribution is an estimate of the error on our fluxes determined using our sample of MAGPHYS galaxies. We make use of the 16th- and 84th- percentiles of these distributions of central pixel values as our flux errors.

3.2.2 BIASES IN THE STACKING? SIMSTACK

Even with coarse resolution, the standard IVW method of stacking sources does not produce biased fluxes due to multiple sources being within one beamsize as long as the mean of the map is zero and the galaxies are not clustered. We have confirmed this using our MC simulations, which produce a mean signal consistent with zero. However, if the galaxies in the *initial* sample are clustered, the coarse angular resolution will cause a positive bias to the stacked signal, and result in an artificial boost to the stacked fluxes. To check the impact of galaxy clustering on our stacking results, we make use of the Python implementation of SIMSTACK (Viero et al., 2013), a stacking and deblending method that attempts to account for any flux boosting introduced by galaxy clustering. We apply SIMSTACK to the non match-filtered S2COSMOS 850μm map (Simpson et al., 2019) and our MAGPHYS-COSMOS2015 galaxy catalogue, and the sources are split into the same M_* and z bins as for the IVW stacking. We use the non-matched filtered map because SIMSTACK carries out a convolution with a Gaussian beam within its code. We use the standard Python implementation of SIMSTACK (Viero et al., 2013), with one small change: we alter the FWHM of the SCUBA-2 PSF to be 13″, reflecting the latest results from SCUBA-2 calibration tests in Dempsey et al. (2013).

$\log(M_*/M_\odot)$ bin	Bootstrapped $\log(M_*/M_\odot)_{\rm Med}$	$\langle z_{\rm bin}\rangle$	# sources	IVW Stacked Flux (mJy)	IVW ISM Mass ($10^{10}M_\odot$)	IVW $f_{\rm ISM}$	SIMSTACK Stacked Flux (mJy)	SIMSTACK ISM Mass ($10^{10}M_\odot$)	SIMSTACK $f_{\rm ISM}$
9.50 - 9.75	9.62	0.28	1489	$0.087^{+0.034}_{-0.034}$	$0.116^{+0.034}_{-0.034}$	$0.217^{+0.086}_{-0.088}$	0.088	0.117	0.219
	9.62	0.82	4579	$0.051^{+0.018}_{-0.021}$	$0.199^{+0.018}_{-0.021}$	$0.323^{+0.122}_{-0.138}$	0.024	0.096	0.187
	9.62	1.36	3574	$0.094^{+0.022}_{-0.021}$	$0.460^{+0.022}_{-0.021}$	$0.524^{+0.138}_{-0.133}$	0.033	0.164	0.281
	9.62	1.90	2165	$0.130^{+0.027}_{-0.029}$	$0.683^{+0.027}_{-0.029}$	$0.620^{+0.151}_{-0.163}$	0.170	0.895	0.681
	9.62	2.44	1654	$0.060^{+0.032}_{-0.031}$	$0.328^{+0.032}_{-0.031}$	$0.438^{+0.250}_{-0.247}$	0.053	0.286	0.405
	9.63	2.98	1246	$0.106^{+0.035}_{-0.035}$	$0.595^{+0.035}_{-0.035}$	$0.585^{+0.224}_{-0.223}$	0.053	0.298	0.414
	9.63	3.52	603	$0.122^{+0.054}_{-0.050}$	$0.723^{+0.054}_{-0.050}$	$0.629^{+0.325}_{-0.301}$	0.056	0.329	0.435
	9.64	4.05	236	$-0.000^{+0.090}_{-0.079}$	1.696	0.796	0.069	-	-
	9.65	4.59	69	$0.054^{+0.167}_{-0.150}$	$0.367^{+0.167}_{-0.150}$	$0.449^{+1.533}_{-1.373}$	0.218	1.495	0.769
	9.68	5.13	12	$0.442^{+0.371}_{-0.367}$	$3.337^{+0.371}_{-0.367}$	$0.875^{+0.976}_{-0.967}$	0.349	2.634	0.847
9.75 - 10.00	9.87	0.82	4052	$0.131^{+0.020}_{-0.019}$	$0.513^{+0.020}_{-0.019}$	$0.409^{+0.069}_{-0.066}$	0.139	0.544	0.424
	9.87	1.36	2957	$0.155^{+0.021}_{-0.024}$	$0.761^{+0.021}_{-0.024}$	$0.507^{+0.079}_{-0.090}$	0.142	0.698	0.486
	9.87	1.90	1857	$0.178^{+0.030}_{-0.029}$	$0.932^{+0.030}_{-0.029}$	$0.556^{+0.106}_{-0.105}$	0.127	0.666	0.472
	9.87	2.44	1148	$0.201^{+0.039}_{-0.037}$	$1.092^{+0.039}_{-0.037}$	$0.597^{+0.133}_{-0.129}$	0.232	1.259	0.631
	9.87	2.98	958	$0.212^{+0.039}_{-0.041}$	$1.194^{+0.039}_{-0.041}$	$0.616^{+0.133}_{-0.140}$	0.282	1.588	0.681
	9.87	3.52	664	$0.101^{+0.049}_{-0.045}$	$0.596^{+0.049}_{-0.045}$	$0.444^{+0.234}_{-0.215}$	0.206	1.217	0.620
	9.87	4.05	205	$0.167^{+0.087}_{-0.080}$	$1.052^{+0.087}_{-0.080}$	$0.584^{+0.353}_{-0.323}$	0.035	0.220	0.227
	9.88	4.59	118	$0.300^{+0.120}_{-0.107}$	$2.054^{+0.120}_{-0.107}$	$0.730^{+0.360}_{-0.322}$	0.199	1.359	0.642
	9.86	5.13	14	$-0.386^{+0.309}_{-0.313}$	7.017	0.907	-0.276	-	-
10.00 - 10.25	10.12	0.82	3531	$0.132^{+0.020}_{-0.022}$	$0.518^{+0.020}_{-0.022}$	$0.282^{+0.044}_{-0.048}$	0.093	0.366	0.217
	10.12	1.36	2292	$0.192^{+0.027}_{-0.028}$	$0.943^{+0.027}_{-0.028}$	$0.418^{+0.063}_{-0.065}$	0.111	0.545	0.293
	10.12	1.90	1375	$0.326^{+0.031}_{-0.039}$	$1.710^{+0.031}_{-0.039}$	$0.567^{+0.061}_{-0.077}$	0.309	1.625	0.554
	10.11	2.44	773	$0.366^{+0.047}_{-0.046}$	$1.989^{+0.047}_{-0.046}$	$0.605^{+0.091}_{-0.089}$	0.356	1.934	0.598
	10.12	2.98	615	$0.389^{+0.050}_{-0.050}$	$2.187^{+0.050}_{-0.050}$	$0.627^{+0.095}_{-0.096}$	0.369	2.073	0.614
	10.11	3.52	415	$0.209^{+0.062}_{-0.067}$	$1.235^{+0.062}_{-0.067}$	$0.490^{+0.161}_{-0.175}$	0.062	0.365	0.221
	10.12	4.05	138	$0.251^{+0.118}_{-0.105}$	$1.583^{+0.118}_{-0.105}$	$0.547^{+0.293}_{-0.260}$	0.083	0.521	0.285
	10.13	4.59	80	$0.216^{+0.135}_{-0.134}$	$1.477^{+0.135}_{-0.134}$	$0.525^{+0.370}_{-0.368}$	0.223	1.523	0.533
	10.12	5.13	18	$0.387^{+0.299}_{-0.260}$	$2.928^{+0.299}_{-0.260}$	$0.687^{+0.644}_{-0.561}$	0.215	1.624	0.550

Table 3.1: Stacked fluxes, gas mass fractions and relevant ancillary data. Red values indicate calculations using 3σ upper limits. Gas mass fractions are not calculated for SIMSTACK results where 3σ upper limits are used for IVW fluxes.

$\log(M_*/M_\odot)$ bin	Bootstrapped $\log(M_*/M_\odot)_{\rm Med}$	$\langle z_{\rm bin}\rangle$	# sources	IVW Stacked Flux (mJy)	IVW ISM Mass ($10^{10}M_\odot$)	IVW $f_{\rm ISM}$	SIMSTACK Stacked Flux (mJy)	SIMSTACK ISM Mass ($10^{10}M_\odot$)	SIMSTACK $f_{\rm ISM}$
	10.37	0.28	1130	$0.141^{+0.039}_{-0.041}$	$0.186^{+0.039}_{-0.041}$	$0.074^{+0.021}_{-0.021}$	0.053	0.070	0.029
	10.37	0.82	3387	$0.144^{+0.023}_{-0.023}$	$0.563^{+0.023}_{-0.023}$	$0.195^{+0.032}_{-0.031}$	0.074	0.289	0.110
	10.37	1.36	2053	$0.211^{+0.029}_{-0.026}$	$1.038^{+0.029}_{-0.026}$	$0.306^{+0.045}_{-0.040}$	0.124	0.611	0.206
	10.36	1.90	964	$0.377^{+0.041}_{-0.041}$	$1.979^{+0.041}_{-0.041}$	$0.463^{+0.055}_{-0.056}$	0.403	2.114	0.480
10.25 - 10.50	10.35	2.44	452	$0.504^{+0.062}_{-0.061}$	$2.739^{+0.062}_{-0.061}$	$0.550^{+0.077}_{-0.076}$	0.547	2.971	0.570
	10.36	2.98	334	$0.489^{+0.072}_{-0.071}$	$2.753^{+0.072}_{-0.071}$	$0.548^{+0.092}_{-0.091}$	0.446	2.508	0.525
	10.35	3.52	216	$0.565^{+0.091}_{-0.085}$	$3.337^{+0.091}_{-0.085}$	$0.600^{+0.112}_{-0.105}$	0.589	3.480	0.610
	10.36	4.05	85	$0.524^{+0.151}_{-0.128}$	$3.299^{+0.151}_{-0.128}$	$0.592^{+0.198}_{-0.168}$	0.526	3.314	0.593
	10.34	4.59	51	$0.201^{+0.177}_{-0.169}$	$1.375^{+0.177}_{-0.169}$	$0.386^{+0.365}_{-0.348}$	-0.010	-0.071	-0.034
	10.36	5.13	13	$0.514^{+0.336}_{-0.293}$	$3.887^{+0.336}_{-0.293}$	$0.631^{+0.488}_{-0.426}$	0.477	3.604	0.613
	10.62	0.28	1069	$0.199^{+0.035}_{-0.040}$	$0.264^{+0.035}_{-0.040}$	$0.060^{+0.011}_{-0.012}$	0.230	0.305	0.068
	10.61	0.82	2895	$0.225^{+0.023}_{-0.024}$	$0.884^{+0.023}_{-0.024}$	$0.177^{+0.019}_{-0.019}$	0.200	0.786	0.161
	10.62	1.36	2057	$0.386^{+0.027}_{-0.027}$	$1.893^{+0.027}_{-0.027}$	$0.313^{+0.023}_{-0.023}$	0.349	1.712	0.292
	10.61	1.90	678	$0.593^{+0.046}_{-0.049}$	$3.114^{+0.046}_{-0.049}$	$0.431^{+0.037}_{-0.039}$	0.549	2.885	0.413
	10.60	2.44	196	$0.670^{+0.093}_{-0.093}$	$3.641^{+0.093}_{-0.093}$	$0.476^{+0.073}_{-0.073}$	0.640	3.478	0.464
10.50 - 10.75	10.59	2.98	122	$0.843^{+0.108}_{-0.113}$	$4.740^{+0.108}_{-0.113}$	$0.550^{+0.080}_{-0.084}$	0.948	5.334	0.579
	10.60	3.52	66	$0.897^{+0.151}_{-0.156}$	$5.296^{+0.151}_{-0.156}$	$0.571^{+0.110}_{-0.114}$	0.563	3.325	0.455
	10.63	4.05	31	$1.123^{+0.224}_{-0.206}$	$7.076^{+0.224}_{-0.206}$	$0.625^{+0.147}_{-0.135}$	1.384	8.722	0.673
	10.59	4.59	18	$0.428^{+0.316}_{-0.285}$	$2.927^{+0.316}_{-0.285}$	$0.430^{+0.347}_{-0.313}$	0.756	5.176	0.572
	10.86	0.28	783	$0.321^{+0.045}_{-0.043}$	$0.425^{+0.045}_{-0.043}$	$0.056^{+0.008}_{-0.008}$	0.302	0.400	0.053
	10.85	0.82	2033	$0.310^{+0.028}_{-0.029}$	$1.214^{+0.028}_{-0.029}$	$0.145^{+0.013}_{-0.014}$	0.289	1.131	0.137
	10.86	1.36	1653	$0.436^{+0.032}_{-0.029}$	$2.142^{+0.032}_{-0.029}$	$0.228^{+0.017}_{-0.016}$	0.370	1.816	0.200
10.75 - 11.00	10.87	1.90	512	$0.888^{+0.054}_{-0.059}$	$4.663^{+0.054}_{-0.059}$	$0.388^{+0.025}_{-0.028}$	0.876	4.601	0.384
	10.86	2.44	97	$1.490^{+0.134}_{-0.121}$	$8.093^{+0.134}_{-0.121}$	$0.530^{+0.054}_{-0.049}$	1.630	8.850	0.553
	10.88	2.98	39	$2.276^{+0.203}_{-0.193}$	$12.800^{+0.203}_{-0.193}$	$0.630^{+0.066}_{-0.063}$	2.425	13.640	0.645
	10.83	3.52	23	$0.872^{+0.274}_{-0.276}$	$5.146^{+0.274}_{-0.276}$	$0.431^{+0.147}_{-0.148}$	0.841	4.965	0.422
	10.82	4.05	10	$-0.095^{+0.401}_{-0.386}$	7.589	0.532	0.155	-	-

Table 3.1: *Continued*

$\log(M_*/M_\odot)$ bin	Bootstrapped $\log(M_*/M_\odot)_{\rm Med}$	$\langle z_{\rm bin} \rangle$	# sources	IVW Stacked Flux (mJy)	IVW ISM Mass ($10^{10} M_\odot$)	IVW $f_{\rm ISM}$	SIMSTACK Stacked Flux (mJy)	SIMSTACK ISM Mass ($10^{10} M_\odot$)	SIMSTACK $f_{\rm ISM}$
11.00 - 11.25	11.10	0.28	413	$0.194^{+0.063}_{-0.060}$	$0.258^{+0.063}_{-0.060}$	$0.020^{+0.007}_{-0.006}$	0.234	0.310	0.024
	11.09	0.82	864	$0.375^{+0.039}_{-0.043}$	$1.470^{+0.039}_{-0.043}$	$0.106^{+0.011}_{-0.012}$	0.324	1.271	0.093
	11.09	1.36	784	$0.706^{+0.045}_{-0.042}$	$3.466^{+0.045}_{-0.042}$	$0.219^{+0.014}_{-0.013}$	0.692	3.399	0.216
	11.11	1.90	293	$1.339^{+0.080}_{-0.067}$	$7.035^{+0.080}_{-0.067}$	$0.352^{+0.022}_{-0.019}$	1.306	6.856	0.346
	11.12	2.44	58	$1.867^{+0.168}_{-0.154}$	$10.138^{+0.168}_{-0.154}$	$0.437^{+0.043}_{-0.039}$	1.777	9.653	0.425
	11.07	2.98	13	$2.514^{+0.318}_{-0.331}$	$14.140^{+0.318}_{-0.331}$	$0.544^{+0.078}_{-0.081}$	2.401	13.503	0.532
11.25 - 11.50	11.33	0.28	145	$0.019^{+0.108}_{-0.103}$	$0.025^{+0.108}_{-0.103}$	$0.001^{+0.007}_{-0.006}$	0.199	0.264	0.012
	11.32	0.82	204	$0.501^{+0.088}_{-0.085}$	$1.966^{+0.088}_{-0.085}$	$0.085^{+0.015}_{-0.014}$	0.361	1.414	0.063
	11.32	1.36	217	$1.242^{+0.083}_{-0.080}$	$6.095^{+0.083}_{-0.080}$	$0.226^{+0.016}_{-0.015}$	1.316	6.459	0.237
	11.33	1.90	87	$1.594^{+0.142}_{-0.137}$	$8.373^{+0.142}_{-0.137}$	$0.281^{+0.026}_{-0.025}$	1.279	6.716	0.239
	11.32	2.44	26	$3.157^{+0.234}_{-0.216}$	$17.143^{+0.234}_{-0.216}$	$0.449^{+0.037}_{-0.034}$	3.657	19.863	0.486
11.50 - 11.75	11.57	0.28	28	$-0.317^{+0.233}_{-0.232}$	0.928	0.024	-0.270	-	-
	11.62	0.82	35	$0.012^{+0.194}_{-0.203}$	$0.045^{+0.194}_{-0.203}$	$0.001^{+0.018}_{-0.019}$	-0.297	-1.162	-0.029
	11.55	1.36	33	$1.243^{+0.217}_{-0.220}$	$6.100^{+0.217}_{-0.220}$	$0.148^{+0.026}_{-0.026}$	1.589	7.802	0.182
	11.56	1.90	15	$1.875^{+0.321}_{-0.293}$	$9.850^{+0.321}_{-0.293}$	$0.213^{+0.037}_{-0.034}$	1.849	9.712	0.211

Table 3.1: *Continued*

Letter	$\langle z_{\rm bin} \rangle$	$\log M_*$ bin
(a)	4.59	10.25 - 10.50
(b)	2.98	10.50 - 10.75
(c)	2.98	10.00 - 10.25
(d)	0.82	9.75 - 10.00
(e)	1.90	10.00 - 10.25
(f)	3.51	10.50 - 10.75
(g)	1.36	10.00 - 10.25
(h)	4.59	9.50 - 9.75
(i)	0.82	11.50 - 11.75

Table 3.2: Details of the $(M_* - z)$ bins displayed in Figure 3.3. Additional information can be found in Table 3.1.

3.2.3 RESULTS

The results from stacking the binned MAGPHYS-COSMOS2015 sources on the 850μm SCUBA-2 map are presented in Figure 3.4. The number of sources used in each bin is displayed in Table 3.1. For all M_* bins, we see that the fluxes calculated from both stacking methods (Figure 3.4) follow the same general trend; there is little evidence for flux boosting caused by biases in our original catalogue. Curiously, and more notably at higher redshifts and in low SNR $(M_* - z)$ bins, some of the fluxes from SIMSTACK are higher than those calculated using the IVW stacking method. For stellar mass bins $10.0 \leq \log(M_{*\rm bin}/M_\odot) \leq 11.0$, we see a peak in the mean 850μm flux from dust emission at around $z \sim 2.5 - 3.5$, just beyond the peak of star formation (SF) in the history of the Universe, which is at $z \sim 2$ (e.g. Madau & Dickinson 2014). Lower stellar mass bins are too noisy to draw similar conclusions for. Higher stellar mass bins may follow a similar trend, but the lack of high mass galaxies at high redshifts makes it impossible to draw meaningful conclusions about the location of the peak flux in the highest stellar mass bins.

The fluxes for most stacks have good SNRs (71 per cent of the measured fluxes have SNR$\geq$3; see Figure 3.4), but there are a handful of negative stacked fluxes, indicating non-detections. In these instances, upper limits of ISM masses are calculated based on the 3σ flux errors, determined from Monte Carlo simulations.

The similarity of the results from SIMSTACK, which makes a correction

for clustering, and our stacking results suggests that galaxy clustering has little effect on the stacked fluxes. (We note that the PSF FWHM of the SCUBA-2 beam $13''$ at $z = 0.1, 0.5, 1, 2, 3, 4$ translates to a physical scale on the sky, η, of $\approx 25, 82, 108, 112, 103, 93$ kpc, respectively (Wright, 2006).) In contrast, James Simpson (*priv. comm.)* found evidence of flux boosting of up to 20% at 850μm when using a modified version of SIMSTACK (Simpson et al., 2019) that accounts for holes in galactic catalogues caused by bright star masking, and includes background modelling. The flux boosting they observed did not evolve over redshift, so although our stacked flux values may be higher by 20%, there is no evidence to suggest any trends in gas masses estimated based on the 850 μm stacked fluxes would change. We also note that there are other caveats that are likely to have more of an impact on our results - these are discussed later in Section 3.5. Moving forward, we focus mostly on the results from IVW stacking.

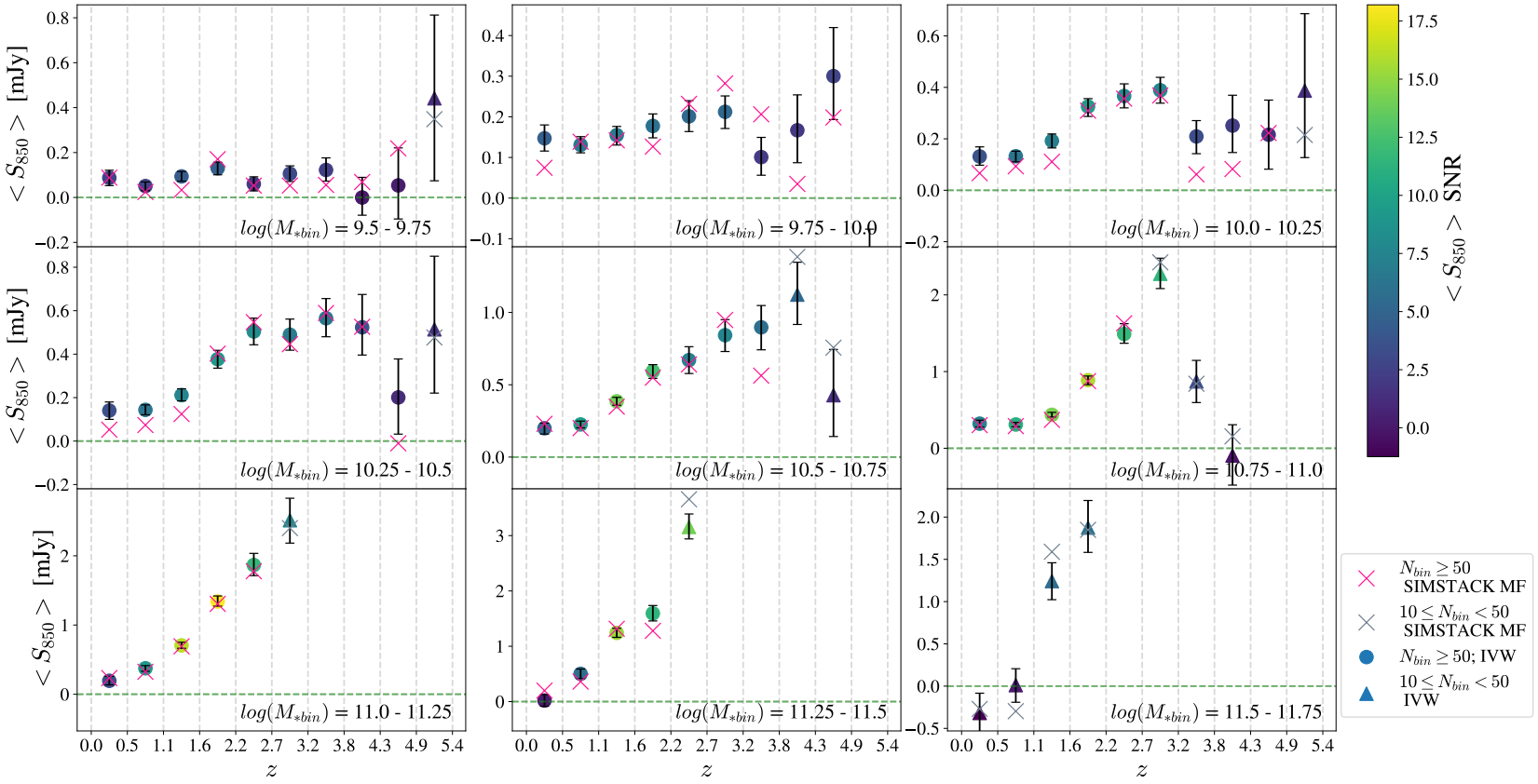

Figure 3.4: The resulting stacked 850 μm fluxes from the IVW method and SIMSTACK. *Filled circles* are the IVW fluxes for stacks containing at least 50 sources. *Filled triangles* are the IVW fluxes for stacks containing at least 10 sources, but less than 50 sources. The colour of the points represents the SNR of the stacked flux for that given point. *Crosses* are the stacked fluxes determined by using SIMSTACK: *pink* means there are at least 50 sources in the stack, *grey* means there are at least 10 sources, but less than 50 sources in the stack. The stellar mass bin that each subplot represents is labelled in the bottom right of the respective subplot. A horizontal green dashed line denotes $\langle S_{850} \rangle = 0$. Vertical grey dashed lines mark borders of redshift bins.

3.3 DERIVING GAS MASSES AND GAS FRACTIONS USING SUB-MILLIMETRE FLUXES

Currently, our knowledge of gas-to-dust ratios and dust emissivities is limited to too few galaxies to be of practical use for statistical evolution studies of the Universe. As such, we follow the methods presented in Eales et al. (2012), Scoville et al. (2016) and Scoville et al. (2017), which allow us to extrapolate the existing data, and calculate gas masses for thousands of galaxies using a calibrated conversion factor, α_{850}, and the specific luminosity of sources at 850μm, L_{850}.

As detailed in Scoville et al. (2016) and Scoville et al. (2017), there is a direct relation between CO(1-0) luminosity and L_{850}. By making use of a standard Galactic CO(1-0) conversion factor, Scoville et al. (2016) and Scoville et al. (2017) show that the RJ emission from dust can be used to calculate ISM masses:

$$M_{\rm ISM} = 1.78\, S_{\nu_{\rm obs}}[mJy]\, (1+z)^{-4.8} \left(\frac{\nu_{850}}{\nu_{\rm obs}}\right)^{3.8} (d_L)^2 \times \left\{\frac{6.7\times10^{19}}{\alpha_{850}}\right\} \frac{\Gamma_0}{\Gamma_{\rm RJ}} \quad 10^{10} M_\odot \tag{3.2}$$

where $S_{\nu_{\rm obs}}$ is the flux density of the source at the observation wavelength, z is the redshift of the source, $\nu_{\rm obs}$ is the observation frequency, d_L is the luminosity distance of the source, in Gpc, $\alpha_{850} = 6.7 \pm 1.7 \times 10^{19} {\rm ergs}^{-1}{\rm Hz}^{-1} M_\odot^{-1}$, and $\Gamma_0/\Gamma_{\rm RJ}$ accounts for the deviation of the Planck function in the rest frame from the RJ form:

$$\Gamma_{\rm RJ}(T_d, \nu_{\rm obs}, z) = \frac{h\nu_{\rm obs}(1+z)/kT_d}{e^{h\nu_{\rm obs}(1+z)/kT_d} - 1} \tag{3.3}$$

where h is the Planck constant, k is the Boltzmann constant and T_d is the temperature of the dust, in Kelvin. In Equation 3.2, Γ_0 is calculated for $z = 0$ and $T_d = 25\,{\rm K}$, as used to calibrate α_{850}. In these calculations, we assume $T_d = 25\,{\rm K}$, as in Scoville et al. (2016), and we refer the interested reader to this paper for full calibration details. In Appendix A, we show the derivation of this relation, largely taken from Scoville et al. (2016).

Note that there is an important difference in our analysis here from the stacking analysis of Béthermin et al. (2015). Bethermin et al. estimated ISM masses

using dust temperatures estimated from the SEDs formed from the stacked flux densities at a large number of FIR and sub-mm wavebands. It is well-known (Eales et al. 1989; Dunne & Eales 2001a) that this procedure produces luminosity-weighted dust temperatures which are higher than the temperature of most of the dust because warm dust is more luminous than cold dust. Ideally, we would use mass-weighted dust temperatures. Since we do not have any direct information about the mass-weighted dust temperatures of the galaxies in our sample, we follow Scoville et al. in assuming that the mass-weighted dust temperature is 25 K. We note that this is consistent with the mass-weighted dust temperatures estimated for both a low-redshift sample (Dunne & Eales, 2001a) and a sample of bright high-redshift sub-mm sources (Pearson et al., 2013). We also note that theoretical simulations (Liang et al., 2019) suggest that the mass-weighted dust temperature does not evolve much with redshift.

Since in Scoville et al. (2016) and Scoville et al. (2017) the equations for calculating ISM masses are calibrated against molecular hydrogen mass measurements conducted using CO line emission, we consider the gas traced by dust to be molecular hydrogen, rather than a combination of molecular and atomic gas phases.

Subsequently, we define the gas fraction, $f_{\rm ISM}$, as:

$$f_{\rm ISM} \equiv \frac{M_{\rm ISM}}{M_* + M_{\rm ISM}} \tag{3.4}$$

where, for each M_* bin, the value of M_* in Equation 3.4 is determined from the bootstrap analysis of the MAGPHYS stellar masses from individual sources in the bin described. In brief, for a given $(M_* - z)$ bin we randomly select, with replacement, X sources, where X is the number of sources in the bin. For the selected sources, we perturb each galaxy's stellar mass within their error (using a Gaussian centred on the 50th-percentile stellar mass, with width as the average of the 16th- and 84th-percentiles from MAGPHYS). 5.6 per cent of our sample have identical values returned by MAGPHYS for the 16th-, 50th- and 84th-percentiles ie there is no error provided from the PDF of the stellar mass for these sources, or the PDF is extremely narrow. The fraction of sources in a given $(M_* - z)$ bin with no stellar mass error varies as a function of stellar mass. In the highest stellar mass bins the fraction increases to around 20-50% (see Figure 3.5). Similarly, the highest redshift bins have slightly higher fractions of galaxies without stellar masses errors,

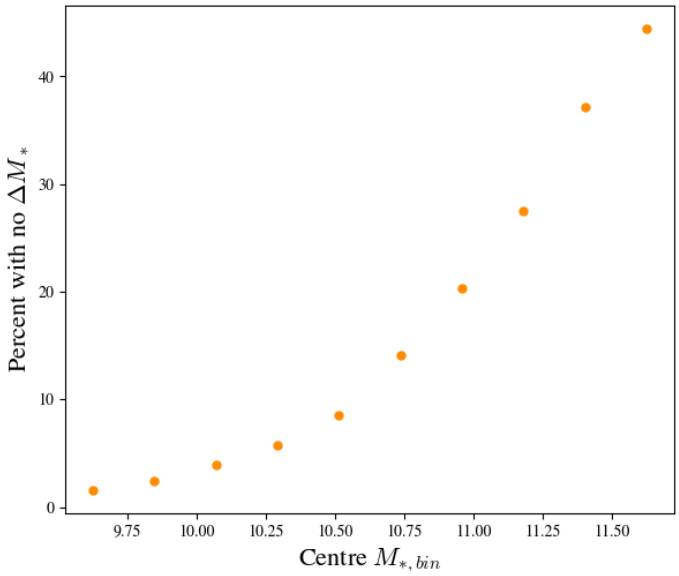

Figure 3.5: the percentage of sources with zero errors in their stellar mass output from MAGPHYS seems to increase exponentially as we get to higher mass systems, potentially reflecting the distribution of MAGPHYS models in this parameter space. Higher mass systems to have $\sim$ 40% of sources with no stellar mass errors, however these are the bins with the least number of sources.

typically up to 30%. We attribute the narrow PDFs/lack of error on stellar mass returned by MAGPHYS for these sources due to the error being smaller than the MAGPHYS parameter grid-spacing used to build up the PDF. This may be caused by over-constrained fitting. For these sources, we allocate them a fractional error based on the average fractional error of sources in their associated bin in the bootstrap estimation.

For each iteration of the bootstrap analysis, we store the median of the perturbed stellar masses, and repeat 10,000 times. We use the 16th-, 50th-, and 84th-percentiles of the median bootstrapped stellar masses as the stellar mass and error in each bin. The errors obtained from the bootstrap analysis are negligible in comparison to the errors on our stacked fluxes. On a bin-by-bin basis, the fractional stellar mass error is at least 30 times lower than the fractional flux error. Thus, we do not consider errors in the stellar mass in determining $f_{\rm ISM}$. The assumed stellar masses for a given bin are displayed in Table 3.1.

$M_{\rm ISM}$ is calculated using Equations 3.2 and 3.3. For each $(M_* - z)$ bin, we derive the gas fraction using the average stacked fluxes at 850μm as the values for $S_{\nu_{\rm obs}}$ in Equation 3.2. d_L is determined using the centre of the z bin in question.

We note that Equation 3.2 was developed with calibration samples limited to $M_* > 5 \times 10^{10} M_\odot$, to avoid contamination by sources which are likely to have below solar metallicity, or where there may be an abundance of gas without CO (Scoville et al., 2016). In this study, we choose to probe masses below this limit, but caution the reader to keep these limitations in mind when considering the results of this work.

3.4 THE EVOLUTION OF GAS FRACTION WITH REDSHIFT

Even with small differences between some of the stacked fluxes calculating using the IVW method and SIMSTACK, Figure 3.6 illustrates that we still see the same evolution in the ISM mass fraction over cosmic time. The largest difference between the two stacking methods is for the lowest stellar mass bin, where the gas mass fractions for several redshift bins determined using the fluxes from SIMSTACK are lower than using fluxes from IVW stacking. However, the fluxes mostly agree within statistical errors. This is also the stellar mass bin with the largest errors on the fluxes, and lies outside of the stellar mass range for which the relation developed in Scoville et al. (2016) and Scoville et al. (2017) has been calibrated. As such, the small discrepancies displayed here are not too concerning. Generally, in low stellar mass bins ($\log(M_*/M_\odot) < 10.5$), we see the ISM mass fraction in galaxies increasing up to a maximum at around $z \sim 2.5 - 3$, and then plateauing out, with some small peaks and dips as we move to higher z. This trend is hard to see for the lowest stellar mass bin, but, within errors, we believe that this bin displays a similar trend to the other low stellar mass bins. For higher stellar mass bins ($\log(M_*/M_\odot) \geq 10.5$), the ISM mass fraction in galaxies increases with redshift, without clearly reaching a maximum, even out to $z \sim 3$. We see that as one progresses to higher stellar mass bins, the overall gas mass fraction decreases. The most massive galaxies in the nearby Universe are particularly gas-poor, as also seen in local galaxy surveys e.g. Saintonge et al. (2011); De Vis et al. (2017a), and previous studies of gas evolution with redshift (Tacconi et al., 2013; Scoville et al., 2017; Tacconi et al., 2018).

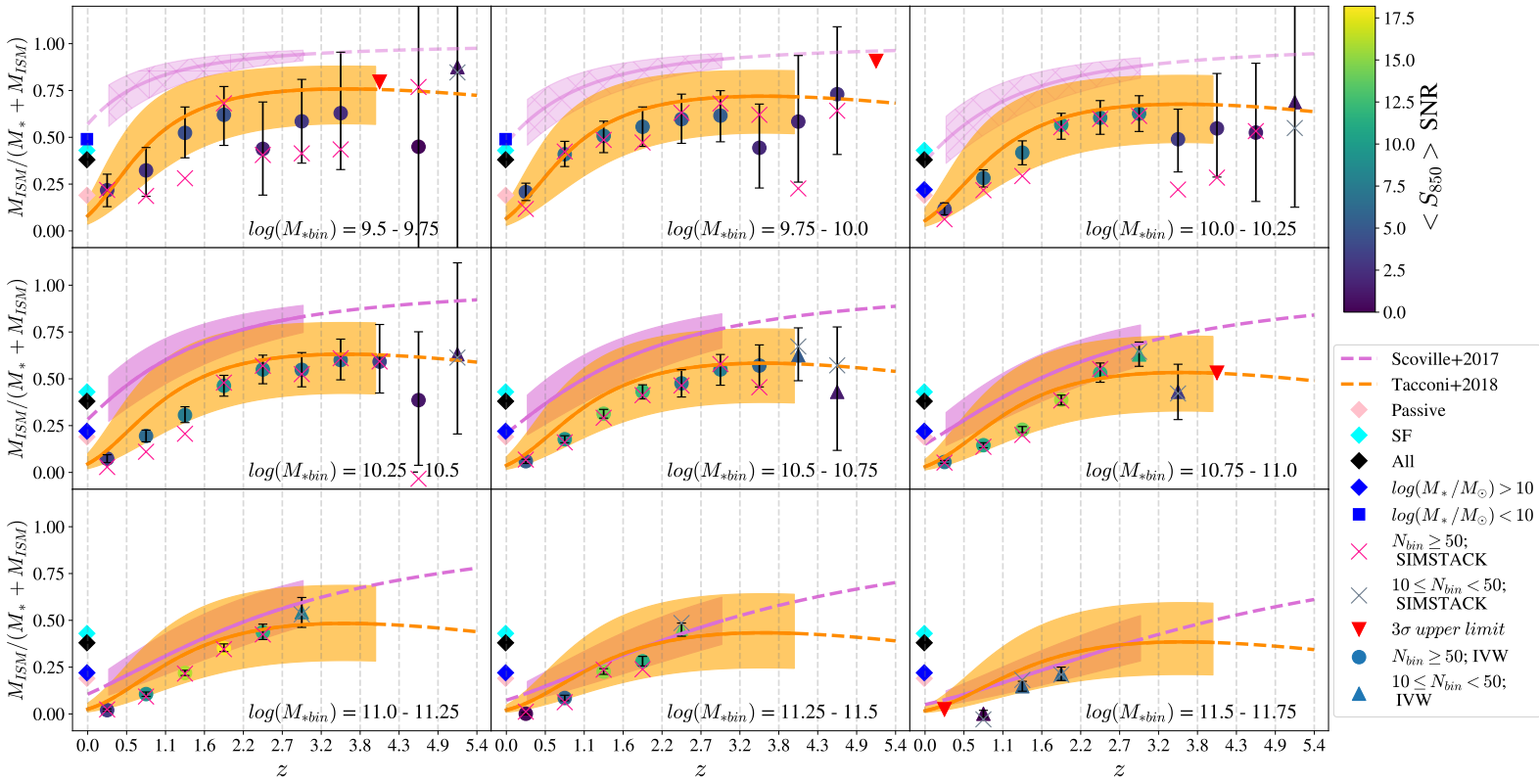

Figure 3.6: The resulting stacked ISM mass fractions with redshift, based on 850μm fluxes in the COSMOS field. We compare both the IVW method (*filled circles*, $N \geq 50$; *filled triangles*, $10 \leq N < 50$; *colour* represents SNR of stacked flux; *red triangles*, negative stacked fluxes) and SIMSTACK (*crosses*). The redshifts used in calculating $M_{\rm ISM}$ are assumed to be the centre of the redshift bins. The *purple and orange lines* are the scaling relations from Scoville et al. 2017 and Tacconi et al. 2018 (shown as the dashed lines where the relationship extends beyond the redshift limit of their samples), for galaxies on the MS. The *shaded regions* show the extent of the scaling relations (over the redshift ranges used in Scoville et al. 2017 and Tacconi et al. 2018) for galaxies 5 times above and below the MS i.e. $0.2 \leq ({\rm sSFR}/{\rm sSFR_{MS}}) \leq 5$ (the shaded region is fainter where the mass limit extends beyond their sample masses). The average gas fraction based on local galaxies *(black diamond)* is shown ($z = 0$, Pieter De Vis, *priv. comm.*), defined as $M_{\rm gas}/(M_{\rm gas} + M_*)$ (see main text). The local fraction split into late and early type galaxies *(cyan and pink diamonds* respectively) and stellar mass (log $M_* < 10$ and > 10, *blue square and diamond* respectively).

3.4.1 COMPARISON TO LITERATURE SCALING RELATIONS

We compare our stacking results to scaling relations from Scoville et al. (2017) and Tacconi et al. (2018) (Figure 3.6, and Equations 3.5 and 3.6) and with observations of the gas fraction derived for local galaxies at $z = 0$. The latter are taken from Pieter De Vis (*priv. comm.*) where the observed gas fraction for 640 galaxies are averaged. (If H_2 measurements are not available, they are estimated using a H_2/HI scaling relation derived for DustPedia galaxies (Casasola et al., 2020).) The gas mass estimates are taken from the DustPedia survey (Davies et al., 2017), HAPLESS, the dust-selected sample from a blind *Herschel* survey (Clark et al. 2015), and the HI selected sample HIGH (De Vis et al., 2017a,b). The gas mass fraction for these observations is defined as $M_{\rm gas}/(M_{\rm gas} + M_*)$ where $M_{\rm gas} = (1 + M_{\rm H_2}/M_{\rm HI})x_i$ and x_i is a metallicity-dependent factor to account for He (Clark et al., 2016; De Vis et al., 2019). We further split the observed gas fractions of local galaxies into late type ($N = 490$ sources) and early type ($N = 150$) galaxies, and by stellar mass (373 galaxies with $\log M_* < 10$ and 267 galaxies with $\log M_* > 10$). The observed gas fractions can act as a benchmark to the scaling relations and the stacked values derived here, and are shown in Figure 3.6.

The scaling relation from Scoville et al. (2017) is based on a reduced sample of 575 galaxies detected with ALMA Bands 6 and 7, with SFRs from the MS up to 50 times the MS, a redshift distribution of $z = 0.3 - 3$, and stellar masses above $3 \times 10^{10} M_\odot$. ISM masses are calculated using 850μm fluxes from the RJ tail of dust emission (Section 3.3). In that scaling relation, it is assumed that $\beta = 2$:

$$f_{\rm ISM} \equiv \frac{M_{\rm ISM}}{M_* + M_{\rm ISM}}$$

$$= \Big\{1 + 1.41(1+z)^{-1.84} \times ({\rm sSFR}/{\rm sSFR_{MS}})^{-0.32} \times \left(M_*/10^{10} M_\odot\right)^{0.70}\Big\}^{-1} \quad (3.5)$$

where $({\rm sSFR}/{\rm sSFR_{MS}})$ is the ratio of the specific star formation rate (sSFR) compared to the specific star formation rate on the MS ($\rm sSFR_{MS}$).

Tacconi et al. (2018) present a few different scaling relations for the ratio of molecular gas to stellar mass ($\mu_{\rm mol}$) with redshift, based on 1444 star-forming galaxies between $z = 0 - 4$. The SFRs of their sample range from ∼20 times lower than the MS, to up to ∼150 times above, probing the stellar mass range $\log(M_*/M_\odot) = 9.0 - 11.8$. Molecular gas masses in Tacconi et al. (2018) are estimated from CO line fluxes, FIR SEDs, and mm photometry. In Figure 3.7, we compare the myriad of scaling relations detailed in Tacconi et al. (2018) for the different studies and where they have assumed a $\beta = 0$ or $\beta = 2$, where β is a parameter introduced in their work that accounts for the redshift evolution in specific star formation rates of galaxies. In their work, these scaling relations have all been corrected for metallicity based on the stellar masses of galaxies in the different samples, by assuming that the dust-to-gas ratio is nearly linearly correlated with metallicity. We also show the Scoville et al. (2017) relationship for comparison. This figure suggests that scaling results based on gas masses derived from dust emission at 1 mm (blue curve) always produces a high gas fraction (this effect is particularly pronounced for low M_*, low z galaxies) and agrees well with the relationship from Scoville et al. (2017). The Figure also shows that the previous literature studies using gas masses derived from dust emission in the FIR instead produces lower gas fractions (red curve). Since all of the Tacconi et al. (2018) have been metallicity corrected, this offset in scaling relation cannot be simply explained due to metallicity of the individual galaxies. Potentially, this suggests that selection effects in the different samples collated by Tacconi et al. (2018) and Scoville et al. (2016, 2017) (and indeed in this work) could be more important. We will explore this in the next few Sections.

Tacconi et al. (2018) define a 'best' scaling relation based on their samples. Here we have taken their best fit relation for the $\beta = 2$ case, for $\mu_{\rm mol}$ (their Table 3 and Equation 6) of:

$$\begin{aligned}\log\frac{M_{\rm mol}}{M_*} = 0.12 - 3.62(\log(1+z) - 0.66)^2 \\ + 0.53\log({\rm sSFR}/{\rm sSFR}_{\rm MS}) \\ - 0.35(\log M_* - 10.7) + 0.11\log(R_e/R_{e,0}) \quad (3.6)\end{aligned}$$

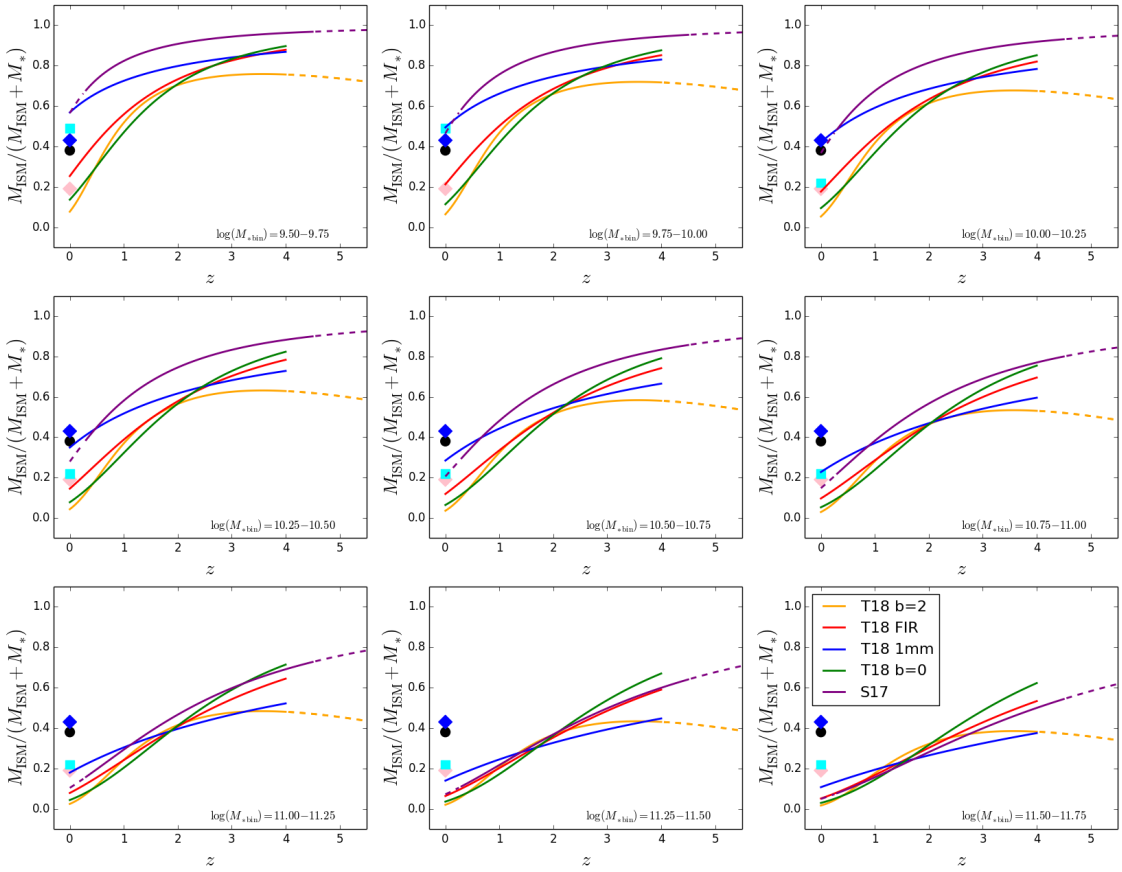

Figure 3.7: A comparison of a range of scaling relations for gas fraction with redshift presented in Tacconi et al. (2018). The gas fraction is estimated using the ratio of molecular gas to stellar mass ($\mu_{\rm mol}$), based on 1444 star-forming galaxies between $z = 0 - 4$. The SFRs of their sample range from ∼20 times lower than the MS, to up to ∼150 times above, probing the stellar mass range $\log(M_*/M_\odot) = 9.0 - 11.8$. Different scaling relations are based on samples where the ISM gas masses are estimated from CO line fluxes, FIR SEDs, and 1 mm photometry. Also shown are the best fit relations in Tacconi et al. (2018) for $\beta = 0$ and $\beta = 2$ where β is a parameter introduced in their work that accounts for the redshift evolution in specific star formation rates of galaxies. Note that all of these scaling relations include corrections for metallicity of the individual sources based on linear dust-to-gas ratios. We also show the Scoville et al. (2017) relationship for comparison (purple) and the local galaxies from Pieter De Vis, *priv. comm.* (black circle). We further split this into late, early types and low mass, high mass (blue diamond, pink diamond, indicated by the cyan squares in the appropriate stellar mass panels respectively.

where $M_{\rm mol}$ is the total mass of molecular gas (including a 36 per cent mass fraction of helium and a correction for CO-dark molecular clouds). $R_{e,0}$ is defined as the mean effective radius of the star-forming population as a function of z and M_* (van der Wel et al., 2014). Since in this study we derived our stacked fluxes from the central pixel values of stacked stamps, measured in Jy/beam, we simply set $(R_e/R_{e,0}) = 1$. Tacconi et al. (2018) show that the evolution of molecular gas fraction only very weakly depends on size. We caution also that they use rest-frame optical sizes rather than sizes of the distribution of gas - measurements of which are extremely uncertain, and will remain so until there are significant sub-mm samples, hopefully obtained with ALMA. Tacconi et al. (2018) suggest that one can approximate the gas mass by $\mu_{\rm mol} \sim \mu_{\rm gas}$ and $f_{\rm mol} \sim f_{\rm gas}$ for $z > 0.4$, where $f_{\rm mol} = (1 + M_*/M_{\rm mol})^{-1}$. (Scoville et al. (2017) and Tacconi et al. (2018) quote errors on the parameters in their scaling relations, though when comparing these relations to our results, we do not consider their errors here.) When comparing to the scaling relations, we consider the relations for galaxies on the MS, such that the ratio $({\rm sSFR})/({\rm sSFR_{MS}}) = 1$ (i.e. we normalize by the sSFR value on the MS).

We note here that although the Scoville et al. (2017) relation for $f_{\rm ISM}$ (Equation 3.5) is said to apply to both the HI and H_2 components, the mm-method described there (and in Section 3.3) is only calibrated against CO and L_{850}. It is possible then that this method may only be strictly valid when using dust emission to trace the molecular component of the gas mass and not the total cool ISM mass. In this scenario, the Scoville et al. (2017) and Tacconi et al. (2018) relations are therefore both tracing the molecular gas component and should be comparable, except that Tacconi et al. (2018) has made a further correction for the metallicity dependence of CO factors and gas-to-dust ratios.

These scaling relations are shown in Figure 3.6. We take the centre of the stellar mass bins quoted in the lower right of each subplot as the assumed stellar mass value. We find our stacking results are more in agreement with the scaling relation from Tacconi et al. (2018) in the lowest stellar mass bins, but as we move to the highest stellar mass bins, we see that our stacking data agrees with both relations, which are comparable with each other. The scaling relations follow a similar trend to our data: the higher the stellar mass of a galaxy, the lower the ISM mass fraction (Saintonge et al., 2011, 2017). The Tacconi et al. (2018) relation

also shows the plateauing in gas mass fraction over cosmic time, as shown in our stacked data points.

Figure 3.6 shows that our stacked data and the Tacconi et al. (2018) relations lie well below the average gas (HI + H_2) fractions derived using local galaxy samples at $z = 0$, though the stacked data most closely agrees with the average gas fractions derived locally for high-mass ($f_{\rm gas}|_{z=0} \sim 0.22$), and passive galaxies samples (based on early type galaxies $f_{\rm gas}|_{z=0} \sim 0.19$).

The Scoville et al. (2017) trends agree well with the observed $z = 0$ gas fractions in the low z bins, particularly when comparing with the average local gas fraction split by stellar mass (blue symbols in Figure 3.6 where $f_{\rm gas}|_{z=0} \sim 0.49$ and $f_{\rm gas}|_{z=0} \sim 0.22$ for low and high stellar mass samples respectively). At first glance this may imply that the Scoville et al. (2017) gas relations are indeed valid for dust emission tracing both the atomic and molecular gas component of galaxies since it matches well the observed properties that include both HI and H_2. However, we note that the average gas fractions for $z = 0$ star-forming galaxies (based on the average properties of late type galaxies, $f_{\rm gas}|_{z=0} \sim 0.43$) are also comparable with Scoville et al. (2017) at low redshifts, so the agreement with local galaxy values could simply be due to their sample containing a higher fraction of star-forming systems compared to this work and the Tacconi et al. (2018) sample. We noted earlier that the measurements of gas mass from Tacconi et al. (2018) and potentially the Scoville et al. (2017) method used here may only be valid in tracing the molecular mass component i.e. our $f_{\rm ISM}$ may in fact only trace $f_{\rm mol}$ with redshift. It is not entirely surprising then that the local observed gas fractions are higher, because these also include the contribution of atomic gas, which is known to be significant at $z = 0$ (Lagos et al., 2011; Saintonge et al., 2011), whereas the calibration relationships that we are using only include molecular gas. The scaling relations based on molecular gas will always be biased low compared to the total gas fractions measured in the lowest redshift bins.

The difference in the gas fractions for $\log M_* < 10.75$ between our work/the scaling relations of Tacconi et al. (2018) and Scoville et al. (2017) may be due to two effects: (i) metallicity and/or (ii) the sample selections. The Scoville et al. (2017) gas fractions were defined using ALMA mm fluxes without any metallicity corrections (indeed, they caution against using their relationship at $\log M_* < 10.3$ for

this reason). We note that our earlier comparison of the scaling relations derived from metallicity-corrected samples in Tacconi et al. (2018) suggests that even after having corrected for the metallicity dependence of the gas-to-dust ratio, the gas fractions derived from mm photometry are always higher at stellar masses $\log M_* < 11$ and redshifts $z < 3$, compared to gas fractions derived using CO or FIR SED fitting methods (Figure 3.7).

Beyond this redshift, and at higher stellar masses, they tend to have slightly lower gas fractions than seen in the best fit scaling relations from Tacconi et al. (2018) and our work, though the differences are small in this stellar mass regime. The fact that the trends are very similar no matter how the gas fraction is determined at higher stellar masses (ie mm photometry or from CO observations), may, at first glance, suggest that the metallicity correction applied by Tacconi et al. (2018) is not valid in the lowest redshift and stellar mass bins, and causes the gas fractions to be overestimated in this regime. However, Tacconi et al. (2018) applies the same metallicity dependence to gas masses derived from dust masses based on FIR SED fitting, which produces scaling relations similar to CO and our stacked data. Thus the differences can not entirely be due to metallicity corrections. Although, like Scoville et al. (2017), we have not corrected for metallicity dependence in gas-to-dust ratios, our data is in close agreement with the Tacconi et al. (2018) best fit relationship. This suggests that the largest driver in the differences here is not the metallicity correction, or method used to derive the gas masses, but rather the sample selection. By stacking on a sub-millimetre map based on optical/NIR source catalogues, we are less likely to sample dust rich galaxies compared to Scoville et al. (2017) and the combined samples from Tacconi et al. (2018). It also means that our gas fractions in Figure 3.6 may be lower if we are including passive galaxies or less star-forming systems, compared to the more biased sample of Scoville et al. (2017), or the galaxies in the local samples, since it is well known that galaxies below the main sequence have lower gas fractions (e.g. Saintonge et al. 2012). This could partly explain the offset at $z = 0$ seen between our stacked $f_{\rm ISM}$ and the higher range of gas fractions observed in local galaxies ($f_{\rm gas} \sim 0.4 - 0.5$) since these are dominated by star-forming and low mass galaxies. We will return to this in the next Section.

3.4.2 STAR-FORMING AND PASSIVE GALAXIES

Here we test whether the stacked gas fractions in Figure 3.6 are lower at low redshifts due to passive galaxies, compared to the observed local gas fractions and the mm dust photometry from Scoville et al. (2017). Figure 3.8 compares the SFRs (derived using MAGPHYS) with the stellar masses in redshift bins. We can see that at $z < 1.6$, there is clear evidence of two populations of galaxies. A tight correlation between SFR and stellar mass exists for the more star-forming galaxies: this is the so-called MS relation. Figure 3.8 shows the MS relation from Sargent et al. (2014) which evolves with redshift (see also Noeske et al. 2007; Daddi et al. 2007), with scatter around the line of approximately 0.3 dex (Peng et al., 2010; Sargent et al., 2014). (The $z = 0$ MS from Saintonge et al. (2016) is also shown). Most of our sample lies along the MS indicative of normal star-forming systems, but a significant fraction of sources have lower star formation rates for a given stellar mass, by approximately two orders of magnitude. These are quiescent/passive sources i.e. red and dead galaxies, with potentially some galaxies with intermediate star-forming properties, so-called green valley sources. This passive population quickly disappears from our sample at redshifts greater than 1.6, where our sample becomes dominated by main sequence galaxies at higher redshifts. Figure 3.8 also demonstrates the lack of high mass systems in our higher redshift bins. We note that there is significant striping in the distribution of sources at low SFRs in the lowest redshift bins. Figure 3.9 demonstrates that this is mainly due to sources with high values of χ^2 output by MAGPHYS i.e. due to poorer fits.

As we are interested in whether a galaxy in our sample is more-or-less star-forming, rather than the absolute value of SFR, we simply split our sample into two sets: a star-forming and a passive set based on a split in SFR-M_* space, as indicated by the black line in Figure 3.8. This split region is offset by -1.25 dex compared to the MS relation of Sargent et al. (2014). Although this offset is somewhat arbitrary, it is sufficient for this test.

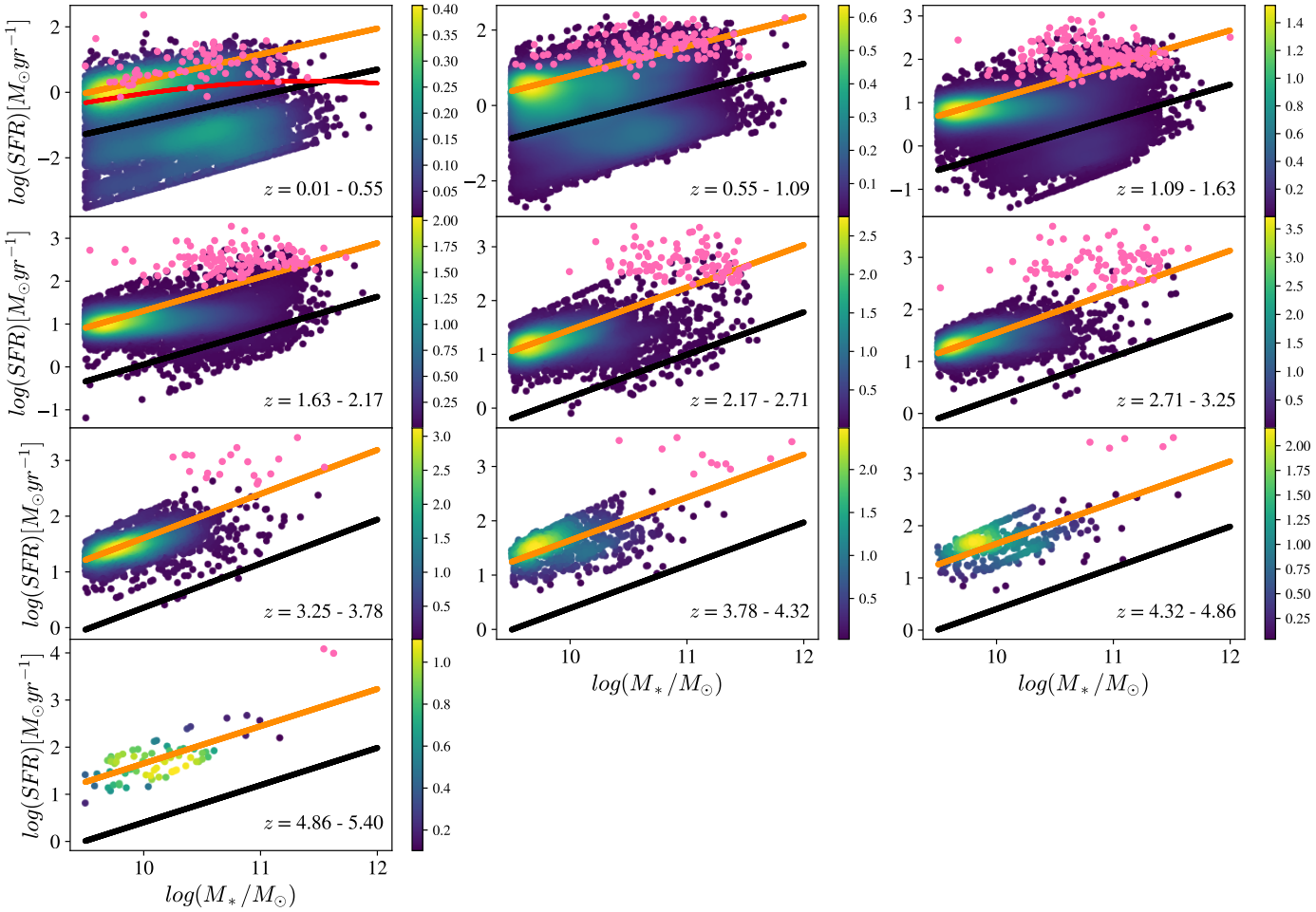

Figure 3.8: The star formation rate versus stellar mass for the galaxy catalogue used in this work, split into redshift bins. SFRs and stellar masses are taken from the MAGPHYS fits to the SEDs. The colour bar shows the number density of galaxies in the sample, the orange line is the so-called Main Sequence line of Sargent et al. (2014) which evolves with redshift. The red line in the lowest redshift bin is the MS trend from Saintonge et al. (2016). The black line denotes where we split our sample into 'star-forming' and 'passive' sources, this evolves with redshift in a similar manner to the orange line; there is a fixed offset between the two. The galaxies from Scoville et al. (2017) are shown in pink.

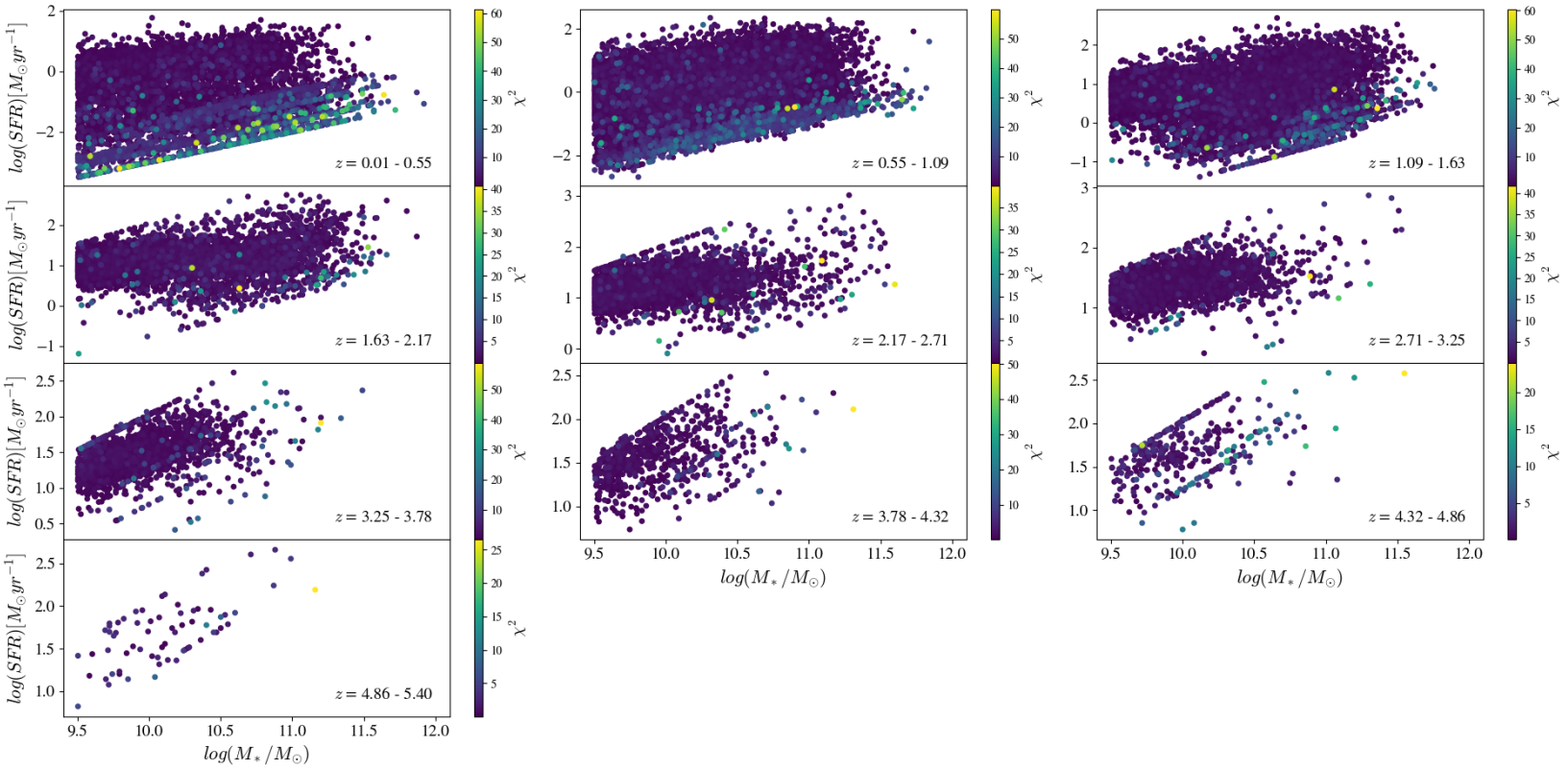

Figure 3.9: The star formation rate versus stellar mass for the galaxy catalogue used in this work, split into redshift bins with colours denoting the χ^2 value of the MAGPHYS SED fits used to derive the stellar mass and SFRs.

Figure 3.8 compares the SFR-M_* plane with the Scoville et al. (2017) mm sample. We can see that their sample contains more massive systems in each redshift bin and, except for the lowest redshift bin, these tend to sit above the MS trend from Sargent et al. (2014). Furthermore, in every redshift bin we see that the Scoville et al. (2017) galaxies are on average more star-forming than our sample. Thus the sample selection can explain the differences in our observed scaling relations. The lack of passive galaxies in the sample of Scoville et al. (2017) biases their scaling relation high compared to our results, which are based on a more representative galaxy sample. By stacking on a catalogue of optical/NIR sources in a deep sub-millimetre field, we have improved on number counts in each redshift range, probed down to lower stellar masses out to $z = 5$, and include galaxies with lower star formation rates. We will return to the issue of selection effects in Section 3.5.

Figures 3.10 & 3.11 shows the stacked gas mass fractions for the star-forming and passive galaxies respectively. The SNR is very low for the passive galaxies and the number counts too are low at higher redshifts and low stellar masses. As such, we do not draw any conclusions from this except that passive galaxies do not have much 850μm emission and therefore not much gas (as expected), and that the inclusion of these galaxies in our low z sample does indeed bias our gas fraction scaling relation low in Figure 3.6. We see still that the gas mass fractions derived from stacking on the COSMOS map for our star-forming and passive samples are lower than those derived for local samples of galaxies (even when split into LTGs and ETGs). This likely originates from the fact that the tracer we use here to measure gas mass does not include the atomic phase, whereas the local measurements do.

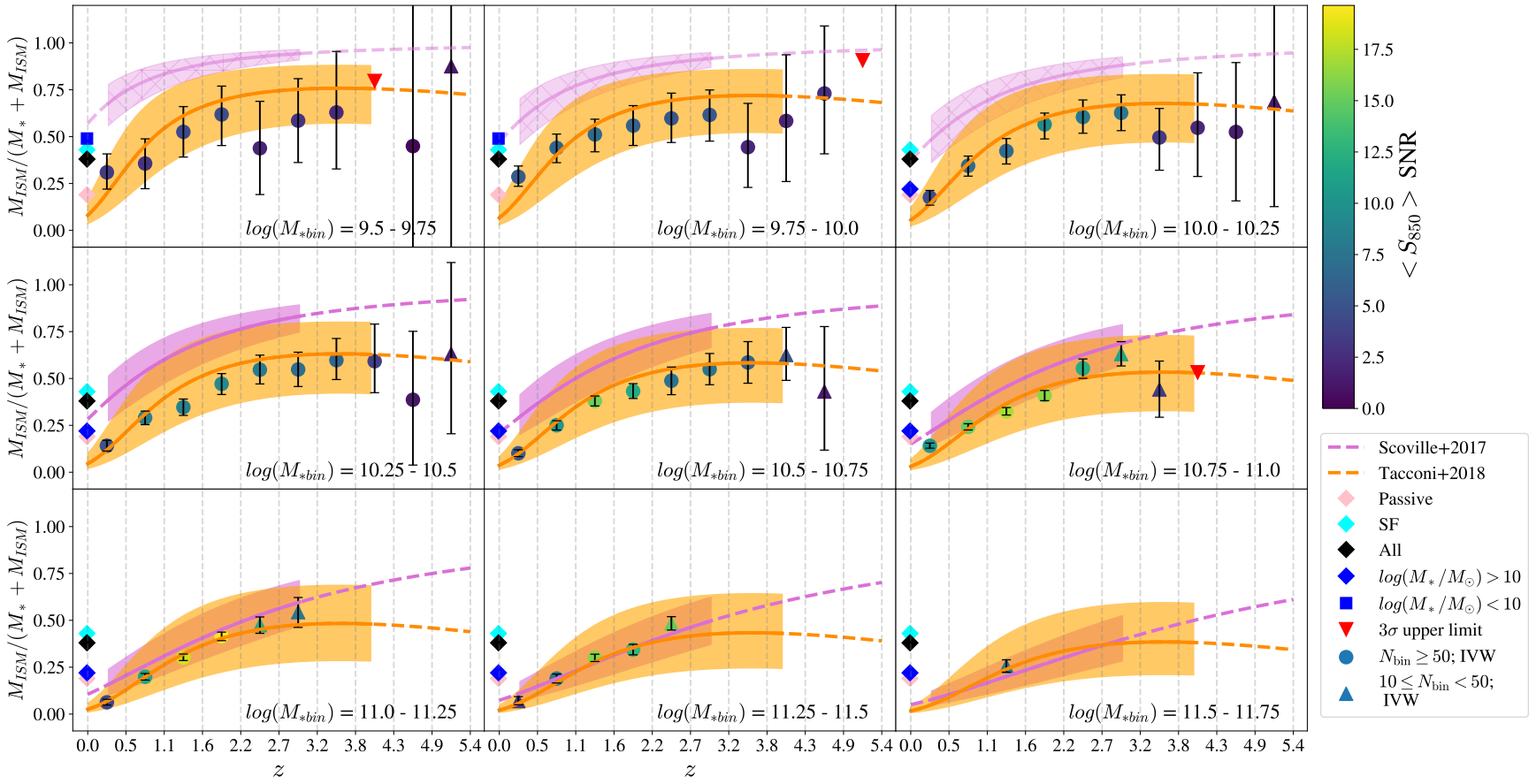

Figure 3.10: The stacked ISM mass fractions with redshift based on 850μm fluxes in the COSMOS field for star-forming galaxies. Filled circles are the IVW data for stacks with N $\geq$ 50. Filled triangles are the IVW data for stacks with 10 $\leq$ N $<$ 50. The purple and orange lines are the scaling relations from Scoville et al. 2017 and Tacconi et al. 2018 (shown as the dashed lines where the relationship extends beyond the redshift limit of their samples), for galaxies on the Main Sequence (MS). The shaded regions show the extent of the scaling relations (over the redshift ranges used in Scoville et al. 2017 and Tacconi et al. 2018) for galaxies 5 times above and below the MS. See Figure 3.6 for further details on the lines, curves and symbols.

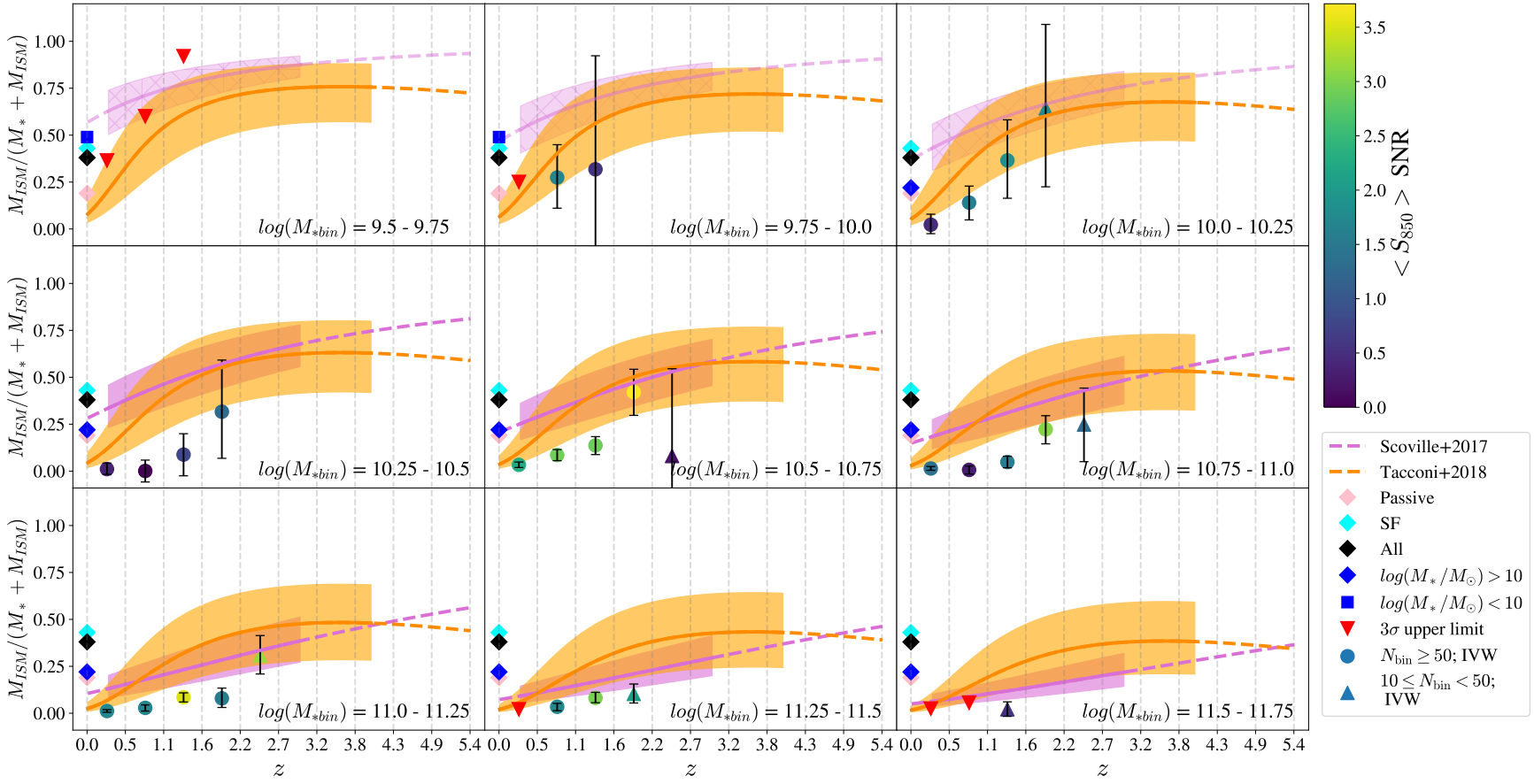

Figure 3.11: The stacked ISM mass fractions with redshift, based on 850μm fluxes in the COSMOS field for *passive galaxies*. See Figure 3.10 for details on the curves and data.

3.5 DISCUSSION AND CAVEATS

Figure 3.6 clearly illustrates that out to around $z \sim 3$, the gas mass fraction of galaxies increases. Beyond this point, gas mass fractions seem to approximately plateau. However, there are number of technical concerns we need to consider before we take these results too seriously.

We have four $(M_* - z)$ bins with non-detections. The non-detection at $z \sim 5.1$ may simply be due to the low number of galaxies in that bin. As shown in Table 3.1, all the stellar mass bins at this redshift have low numbers of galaxies (if they even have enough sources to warrant a stacking analysis at all), and all the measured fluxes, and calculated gas mass fractions, have large errors. Therefore, it is unsurprising that we have a non-detection at this redshift in one of our stellar mass bins. The non-detection at $z \sim 4$ in the lowest stellar mass bin cannot be simply attributed to a low number of galaxies in that bin - indeed, there are a significant number of galaxies in this $(M_* - z)$ bin (see Table 3.1). Measurements at this redshift in the other low mass bins have large errors, even with similarly high source counts. Also, in this stellar mass bin, the flux measurements at $z \sim 3.5$ and $z \sim 4.6$ have large errors, even if they do have a positive flux detection. Therefore, it is not surprising that we have a non-detection here too. Table 3.1 shows that the non-detection at $z \sim 4$ in stellar mass bin $\log(M_{*,bin})$ = 10.75 - 11.0 can be attributed to a low number of galaxies in this bin, particularly as the non-detection is for the highest redshift bin in this stellar mass bin. We simply lack enough high mass sources at high redshift to enable a detection of sub-mm emission from dust above the noise levels of the map. At first, the non-detection at $z \sim 0.3$ may seem unusual. But, when one considers the results of splitting the sources into star-forming and passive galaxies (Figures 3.10 & 3.11), we see that the galaxies in this bin are mostly passive galaxies, which are gas poor. It is therefore unsurprising that we do not detected significant 850μm dust emission from galaxies in this $(M_* - z)$ bin.

Inevitably, despite the faintness of the MAGPHYS catalogue magnitude limit ($i < 25$ mags), the sample we consider in this study is not complete at high redshifts, roughly $z > 1$ for the low-mass bins and $z > 2$ for the high-mass bins. Without having much deeper magnitude-limited samples, which only exist for small area fields such as GOODS-North and GOODS-South, we cannot quantify

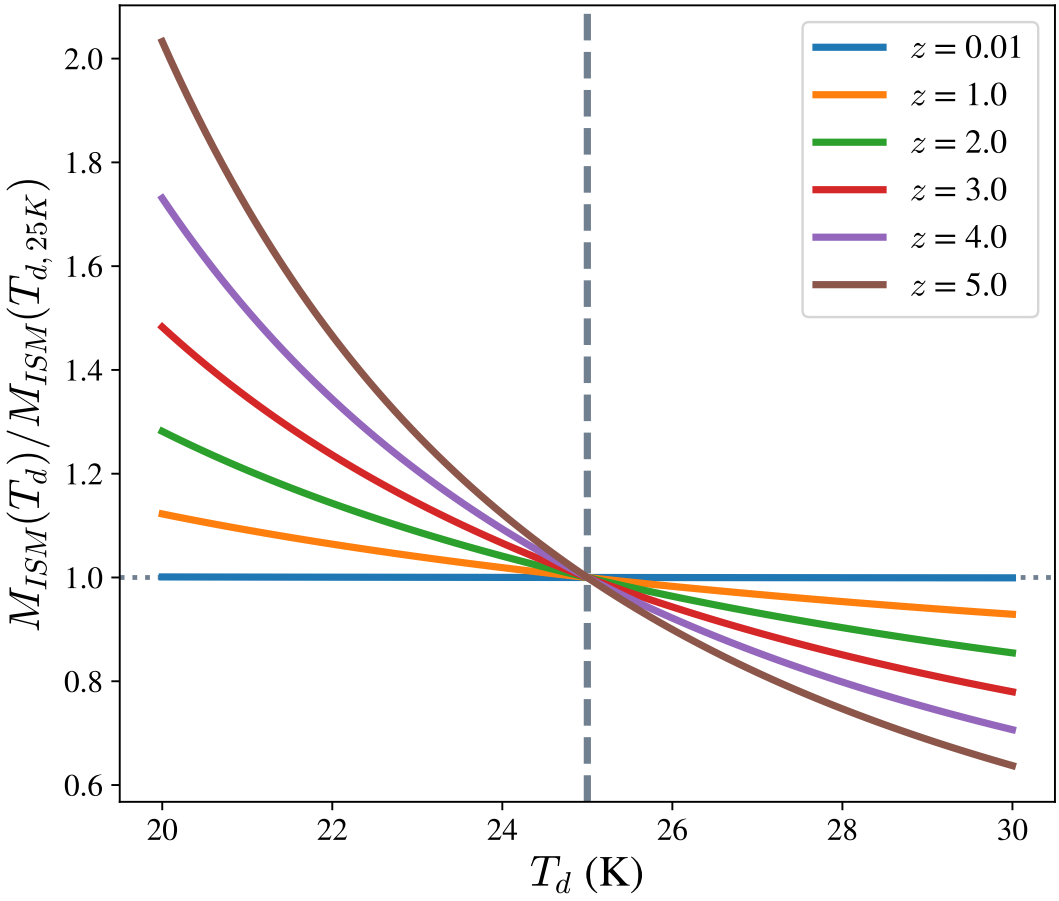

Figure 3.12: The relation between assumed mass-weighted dust temperature, T_d, and calculated ISM mass, M_{ISM}, using emission observed at 850μm, for different discrete redshifts.

the biases involved. However, the two obvious biases are that we will be missing highly-dust-obscured galaxies such as SMGs (Lang et al. 2019; Stach et al. 2019), which will be fainter because of the obscuration, and passive galaxies, which will be fainter in the rest-frame UV because of the lack of young stars. We expect a bias in the high-redshift bins toward star-forming galaxies since at a given stellar mass and redshift, these are brighter than passive galaxies and will be preferentially included in magnitude-limited samples.

Another technical issue we need to consider is the effect of the errors on the photometric redshifts. Since there are far more low-redshift galaxies in our sample than high-redshift galaxies, the errors on the photometric redshifts will produce a larger fraction of low-redshift interlopers in the high-redshift bins than

high-redshift interlopers in the low-redshift bins. Low-redshift interlopers into high redshift stacks will bias the fluxes lower; see Figure 3.4, where the average fluxes measured for the low redshift stacks are less than those measured for the high redshift stacks. Photometric redshift error will therefore tend to reduce the high redshift signal. However, as established in Section 2.4.2, although photometric redshift uncertainties increase at higher redshifts, particularly above z > 3, the photometric redshifts used in this study are reasonably accurate, so we do not anticipate low redshift interlopers into high redshift bins to be a significant issue affecting these results.

A fundamental assumption we have made is that the dust is at a constant temperature of T_d = 25 K. A higher dust temperature would lead to a lower gas fraction calculated using Equations 3.2 and 3.3; Figure 3.12 illustrates how the calculated ISM mass for an artificial source changes with assumed dust temperature for different discrete redshifts, compared with the values calculated at 25 K, when using dust emission detected at 850μm. The curved shape of the lines originates from the observation wavelength approaching the peak of the blackbody emission. Even at $z = 3$, a change in mass-weighted dust temperature to 30 K would only change the ISM mass by a factor of $\sim$20%. Beyond this redshift, the reduction in ISM mass increases - however, the fluxes measured for sources at these higher redshifts are extremely uncertain. The flux uncertainties are, at the least, comparable to the uncertainty introduced in this method by the dust temperature assumption. We conclude that even if the dust temperature assumption of 25 K is an underestimate of the mass-weighted dust temperature of galaxies, particularly at higher redshifts, the results of this study are robust against the error this assumption introduces - we will still see similar trends in the evolution of the gas masses fraction over cosmic time.

It is worth noting that in this work we are considering *mass-weighted* dust temperature, which represents the temperature of the bulk of the ISM. Large variations in this temperature between galaxies, even at different epochs, are unlikely, since this mass-weighted dust temperature depends on the mean radiation energy density to the power of $\sim$1/6 (Scoville et al., 2016). Significant variations in the ISM environment over cosmic time would be required to instigate large mass-weighted dust temperature changes, and thus far, there is little evidence to support

such variations.

Recent simulations of $z = 2 - 6$ galaxies (Liang et al., 2019) found that the mass-weighted dust temperature evolves little over these redshifts, and their results support adopting a value of 25 K to estimate the gas mass of high redshift galaxies using long-wavelength emission on the RJ, as in this study.

A caveat affecting the determination of gas mass fraction from 850μm dust emission is the assumed CO-to-H_2 conversion factor (used when deriving Equation 3.2). Scoville et al. (2016) use a single value of α_{CO} based on a standard Galactic conversion factor $X_{CO} = 3 \times 10^{20}$ cm^{-2}(K km s^{-1})$^{-1}$, and include a factor of 1.36 to account for the mass of heavy elements e.g. Helium. The exact value of X_{CO} is debated, with values between 1 and 4×10^{20} cm^{-2}(K km s^{-1})$^{-1}$ often used in general galactic or extragalactic studies (Bolatto et al. 2013; and references therein). Within this range, higher X_{CO} values are appropriate for lower metallicity regions, and lower X_{CO} values for starburst galaxies. Had Scoville et al. (2016) chosen to use a lower value of X_{CO}, the gas mass fractions determined here would be lower; similarly, a higher value of X_{CO} would see our gas mass fractions increase. The trends from Scoville et al. (2017) (Figure 3.6) would also scale in a similar manner, since they use the same equations to derive their scaling relations. Since all our gas mass fraction calculations would be affected, our overall trends would not change, just the relative normalisation.

A final big caveat is that, like Scoville et al. (2016, 2017), we have made the assumption that the dust-to-gas ratio is independent of redshift. There is a lot of evidence that in the local Universe, and above a transition metallicity (12 + log(O/H) $\simeq$ 8.0), the dust-to-gas ratio is proportional to the metallicity (James et al., 2002; Sandstrom et al., 2013; Rémy-Ruyer et al., 2014a). If this proportionality extends to all redshifts, we could, in principle, use metallicity measurements to correct the ISM measurements. This can have a large effect. For example, Tacconi et al. (2018) did decide to make corrections for metallicity. Their Equation 4 gives a relationship between metallicity and stellar mass and redshift. If we apply this equation to a galaxy at $z = 3$ with a stellar mass of $log_{10}(M_*) = 11.0$ and make the assumption of the same proportionality between metallicity and dust-to-gas ratio that exists at low redshift, we calculate that our ISM mass estimate would increase by 41%, which would increase the gas fraction plotted in Figure 3.6 by

$\simeq$20%. However, we are suspicious of making these corrections because of the assumptions required, the uncertainties in the metallicity measurements, and the fact that we would have to apply these corrections to extreme high-redshift objects with large gas fractions. In Chapter 4, we sidestep this problem completely by using our measurements to estimate dust masses rather than ISM masses, which we then compare with predictions from simulations.

None of these potential problems therefore seem big enough to invalidate our basic result that there is strong evolution in the gas fraction of galaxies.

The evolution of HI and H_2 gas mass with redshift are predicted to be very different, with the former only mildly evolving with redshift and the latter evolving by a factor of ~ 7 between $z = 0$ and $z = 3$ (Lagos et al., 2011). Their model predictions suggest that the H_2 slightly dominates over HI at $z = 2 - 5$ with HI dominating the cold gas mass at lower redshifts. With our method it is only possible to investigate the evolution of the molecular phase of the ISM. It is reassuring, both for our method and for the simulations, that we too find strong evolution over the redshift range $0 < z < 3$.

Our study and those of Scoville et al. (2017) and Tacconi et al. (2018) all find strong evolution in the gas fraction of galaxies. The samples of galaxies were selected in very different ways, with ours being based on stellar mass while the sample of Scoville et al. was selected in the far-infrared. Given the different selection methods and the other differences in the methodology, the agreement between the results from all three papers seems to us quite good (Figure 3.6). It is clear that galaxies at high redshift do have a much higher fraction of gas than those nearby. Our analysis has been based on a stacking analysis on the SCUBA-2 images. Dudzevičiūtė et al. (2019) have recently used the individual sources detected in another deep SCUBA-2 image to estimate the ISM mass function (the space-density of galaxies as a function of ISM mass), using the same basic method as ours of using the sub-millimetre continuum emission to estimate the mass of the ISM in a galaxy. They find strong evolution out to $z \sim 3$, which is broadly in agreement with the strong evolution we see in Figure 3.6.

Our results suggest the gas fraction increases rapidly with redshift until $z \sim 2 - 3$ and is then roughly constant (Figure 3.6). The precise form of this relationship seems to depend on stellar mass, with the galaxies with lower stellar

masses reaching this plateau at a lower redshift than the galaxies in the higher stellar mass bins. This apparent maximum in the gas fraction, which has a value of ~ 0.5 may be genuine or it may reflect a fundamental problem of our method - that we are relying on dust to trace the gas. The existence of dust relies on the existence of metals, and it is possible that the true gas fraction was higher at higher redshifts but not enough dust had been formed to trace the gas. Some evidence to support lack of dust in high redshift galaxies comes from the extremely blue rest-frame UV continuum slopes observed in Lyman break galaxies at $z > 5$ (Stanway et al., 2005; Wilkins et al., 2011). Therefore, the plateau in gas mass fraction that we see at the highest redshifts may actually be the result of less dust at the highest redshifts and evolution in the dust-to-gas ratio rather than evolution in the gas fraction.

This fundamental ambiguity in this method, as well as the difficulty in modelling the selection biases in our sample and in the samples of Scoville et al. (2017) and Tacconi et al. (2018), means that it is difficult to compare these results with the predictions of hydrodynamic (Davé et al., 2020) and semi-analytic models (Lilly et al., 2013; Peng & Maiolino, 2014) . We therefore suspect this method has gone as far as it can. We will next attempt to use the sub-mm emssion to estimate the mass of dust out to high redshifts rather than the mass of the ISM, a method which produces results which can relatively easily be compared with the predictions of cosmological hydrodynamic simulations.

3.6 CONCLUSIONS

In this Chapter, we have derived estimates of average gas mass fractions for a large sample of stellar mass selected galaxies using long-wavelength dust continuum emission at a single wavelength.

- We find relationships between gas fraction, stellar mass, and redshift similar to ones found in previous investigations, which have been based on samples that are biased with large star formation rates or ISM masses.

- At low redshifts, we find gas mass fractions much lower than found in studies of low-redshift galaxy samples, probably because our method is calibrated against ISM measurements that only include the molecular phase.

- We find that at low stellar masses ($\log(M_*/M_\odot) \leq 10.5$), the gas fraction increases with redshift, reaching a plateau at $z \sim 2.5 - 3$, just before the peak in star formation rate density in the Universe. At higher stellar masses ($\log(M_*/M_\odot) \geq 10.5$), the gas mass fraction increases with redshift, without clearly reaching a maximum, even out to $z = 3$. At each redshift, the galaxies with higher stellar masses have lower gas fractions.

- We show that star-forming galaxies are much more gas rich than their passive counterparts.

- Finally, we show that the results are robust against mass-weighted dust temperature variations.

CHAPTER 4
THE EVOLUTION OF DUST MASS: A VIEW FROM SIMULATIONS AND OBSERVATIONS

'A computer terminal is not some clunky old television with a typewriter in front of it. It is an interface where the mind and body can connect with the Universe and move bits of it about.'

DOUGLAS ADAMS

4.1 INTRODUCTION AND MOTIVATION

One of the fundamental measurements that can be made to describe the dust content of galaxies, particularly at different cosmic epochs, is the DMF which is defined as the space density of galaxies as a function of dust mass (Beeston et al., 2018). The first measurements of the local DMF were made using sub-mm observations at 450μm and 850μm, using an indirect technique and were hampered by small number statistics (Dunne et al. 2000; Dunne & Eales 2001b; Vlahakis et al. 2005). Early efforts to probe beyond the local Universe ($z = 1$, Eales et al. 2009;

$z = 2.5$, Dunne et al. 2003a) also suffered from poor statistics and a variety of other experimental limitations.

The advent of *Herschel*, with its better sensitivity and faster mapping speed, led to the first estimates of the DMF with good statistics. Using sub-mm data at 250μm on 1867 sources out to $z = 0.5$, Dunne et al. (2011) found evidence for dramatic evolution in the dust content of galaxies, with five times more dust observed at $z = 0.5$ than $z = 0$ i.e. over the past 5 billion years of cosmic history. More recently, Beeston et al. (2018) presented an estimate of the local DMF with the best statistics to-date, using 15,750 galaxies in the equatorial GAMA fields (Driver et al., 2011) out to a redshift of 0.1. Driver et al. (2018) later constructed an optically-selected sample to probe the dust density out to redshifts of 5, finding little evolution from $0 < z < 0.5$, in contrast to Dunne et al. (2011). Driver et al. (2018) found an increasing dust mass content at higher redshifts, with dust mass density peaking at $z = 1$.

Although more detailed observations of the Universe over the past two decades have led to a deeper understanding of the content of galaxies, we still lack knowledge of the underlying physics governing galaxy evolution. This information is difficult to garner from observations alone. One solution to this problem is the development of suites of complex cosmological hydrodynamical simulations. Modern efforts include IllustrisTNG, which evolves a mock universe from shortly after the Big Bang through to the present day, including many of the physical processes that drive galaxy evolution, such as gas radiative mechanisms, star formation in the dense ISM, stellar population evolution, chemical enrichment, and feedback and outflows (Marinacci et al. 2018; Naiman et al. 2018; Nelson et al. 2018a; Pillepich et al. 2018a; Springel et al. 2018).

However, cosmological hydrodynamical simulations such as IllustrisTNG are tuned to reproduce a selected set of observational constraints, such as the stellar mass content of galaxies and cosmic star formation rate density at $z = 0$ (Pillepich et al., 2018a). Therefore, it is vital to test these simulations by comparing their predictions to properties that they have not been tuned to reproduce.

Whilst current simulations, such as IllustrisTNG, do not model dust (although such models are in preparation e.g. McKinnon et al. 2019), dust properties

can be examined using post-processing analysis (e.g. Schulz et al. 2020; Vogelsberger et al. 2020b). A recent example of this is presented in Baes et al. (2020), who examined the infrared luminosity functions and dust mass functions for galaxies from the EAGLE cosmological simulation (Crain et al. 2015; Schaye et al. 2015) for $z < 1$. Synthetic multi-wavelength observations for EAGLE galaxies were generated using the radiative transfer code SKIRT (Baes et al. 2011; Camps & Baes 2015; Camps et al. 2016, 2018). Dust masses were then estimated by fitting a simple modified blackbody model to the synthetic luminosities generated using SKIRT at wavelengths of 160, 250, 350, and 500 μm. They found that EAGLE predicted only mild evolution in the DMF out to $z = 1$, in contrast with the observations of the DMF of Dunne et al. (2011) but consistent with the milder evolution in the dust density found by Driver et al. (2018).

In Chapters 2 and 3, we used the sub-mm emission from dust as a tracer of extra-galactic gas content over much of the history of the Universe. We estimated the average molecular gas mass fractions of galaxies in the COSMOS field using stacked 850μm fluxes and the gas scaling relations derived in Scoville et al. (2016, 2017). Stacking combines the fluxes from similar galaxies whose individual data signals are otherwise buried beneath noise to allow estimations of average galactic properties. Information on individual galaxies is lost, but is gained on the population as a whole. We calculated inverse-variance weighted average sub-mm fluxes for ~63,000 binned sources with stellar masses $9.5 \leq \log_{10}(M_*/M_\odot) \leq 12$, out to $z < 5$, extending to higher redshifts than previous studies, and including more 'normal' star-forming galaxies on the MS (e.g. Daddi et al. 2007; Karim et al. 2011; Whitaker et al. 2012; Madau & Dickinson 2014; Lee et al. 2015).

In this Chapter, we instead use the average stacked sub-mm fluxes in COSMOS field to examine the evolution of dust mass in galaxies in the local Universe and compare with predictions from simulations using post-processing of IllustrisTNG results to examine how well modern simulations trace dust. We compare our results to literature studies of Dunne et al. (2011) and Beeston et al. (2018). The work in this Chapter has been published in Millard et al. (2021).

4.2 DATASETS

4.2.1 OBSERVED DATA

Here, we will briefly summarize the observational data used to derive average dust properties of physical galaxies over cosmic time, and also describe the simulations from IllustrisTNG used in this study. The observational datasets and catalogues used to compare with the simulations are described in more detail in Chapters 1-3.

We derive the dust masses of galaxies in the S2COSMOS field by stacking on the 850μm map using the data and catalogues described in Chapter 2. In brief, we use the MAGPHYS catalogue (`MagPhysG10v05`) of Driver et al. 2018, which is based on the 22-band panchromatic photometry catalogue of Andrews et al. 2017 and contains 173,399 sources. The photometric catalogue used with MAGPHYS (`G10CosmosLAMBDARCatv06`) is i-band < 25 mag limited (Driver et al., 2018). As stated in Andrews et al. (2017), the source catalogue is complete for objects with i-band < 24.5 mag and partially complete to i < 25 mag. MAGPHYS (da Cunha et al. 2008) produces probabilistic estimates of the physical properties of galaxies by using a χ^2 minimization techique to fit pre-determined libraries of physically motivated model SEDs to panchromatic photometry data. Examples of the physical parameters returned include stellar mass estimates and star formation histories.

Redshifts for the MAGPHYS catalogue are sourced from Davies et al. (2015a), who performed an independent extraction of spectroscopic redshifts from the zCOSMOS-Bright sample (Lilly et al., 2007) and combined these redshifts with archival spectroscopic redshifts from the PRIMUS, VVDS and SDSS (Cool et al. 2013; Le Fèvre et al. 2013; Ahn et al. 2014) surveys. If spectroscopic redshifts were not available, sources were assigned photometric redshifts from COSMOS2015 (Laigle et al., 2016).

Andrews et al. (2017) advise that sources in their catalogue without matches in COSMOS2015 (Laigle et al., 2016) should be treated with caution. We cross-match the `MagPhysG10v05` catalogue (Driver et al., 2018) to the publicly available COSMOS2015 catalogue (Laigle et al., 2016) on RA and Dec, to ensure catalogue

completeness, and to extend the wavelengths for which photometric measurements are available. The cross-matched MAGPHYS-COSMOS2015 catalogue covers the central 1 deg^2 of the S2COSMOS map, where instrumental noise is lowest.

We limit ourselves to considering galaxies in the MAGPHYS-COSMOS2015 catalogue with $\log_{10}(M_*/M_\odot) \geq 9.5$. In total, our final MAGPHYS-COSMOS2015 astrophysical source catalogue, without AGN, consists of 63,658 galaxies, of which 13,955 have reliable spectroscopic redshifts[26]. We note that the MAGPHYS-COSMOS catalogue provides the RA, Dec, M_* and z for our observed galaxies. *We do not use the* MAGPHYS *dust masses in this work.*

4.2.2 SIMULATED DATA: ILLUSTRISTNG

IllustrisTNG is a suite of state-of-the-art hydrodynamical cosmological simulations designed to illuminate the underlying physical processes that drive galaxy formation (Marinacci et al. 2018; Naiman et al. 2018; Nelson et al. 2018a; Pillepich et al. 2018a; Springel et al. 2018). The simulations model both baryons and dark matter, and encode many physical processes, such as stellar evolution, galactic winds, and chemical enrichment schemes (Weinberger et al. 2017; Pillepich et al. 2018a; Pillepich et al. 2018b), to try and create realistic representations of the Universe from the Big Bang until the present day. IllustrisTNG utilises the moving mesh code AREPO (Springel, 2010) to model the evolution of galaxies over cosmic time. Galaxies and halos are identified using the SUBFIND algorithm (Davis et al. 1985; Springel et al. 2001; Dolag et al. 2009). The updated galaxy formation model used in IllustrisTNG is based on the one originally presented in the Illustris simulation (Vogelsberger et al. 2013, 2014a,b; Genel et al. 2014; Torrey et al. 2014; Sijacki et al. 2015). The Illustris TNG simulations follow the cosmology of the Planck Collaboration et al. (2016).

The simulations are run under three different resolutions - in this work, we focus on TNG100, with a box side length of 106.5Mpc. We consider snapshots from the present day, out to z=5, such that we explore a similar redshift range compared to our observational data. Of particular interest to this study are the predictions for the evolution of the neutral gas and metallicity (e.g. Nelson et al. 2018b; Pillepich

[26] For consistency the redshifts used in this study are from Driver et al. (2018), since these are the redshifts used in producing the MAGPHYS estimates of the stellar masses.

et al. 2018a; Diemer et al. 2018; Diemer et al. 2019).

In TNG100, there are a few objects that may be artifacts (Nelson et al. 2019). From our sample, we therefore remove galaxies with zero neutral gas and no metals (these are mostly satellite galaxies that have presumably undergone excessive stripping through galaxy-galaxy interactions; see Diemer et al. 2019).

When comparing to data from the literature, we impose a lower stellar mass limit of 200 times the baryonic mass resolution of the simulation ($200m_b$; $m_b = 1.4 \times 10^6 M_\odot$) to avoid galaxies that may be poorly resolved in the simulations and therefore not reliably modelled (Shen et al. 2020). In other words, we perform a stellar mass selection on IllustrisTNG galaxies, without considering other galactic baryonic mass components e.g. gas mass. When comparing to only our stacking data, we consider only TNG100 galaxies with stellar masses within the bounds imposed by the astrophysical data i.e. $9.5 \leq \log(M_*/M_\odot) \leq 12$.

In this study, we use parameter values for a galaxy that are calculated for particles and cells within two stellar half-mass radii ($2r_{0.5}$). However, to ensure the robustness of our conclusions and to check that our choice of TNG100 dataset does not influence our conclusions, we also perform the same calculations (re-running all results) but for parameter values calculated using all particles and cells gravitationally bound to the galaxy (see Chapter 5). Table 4.1 illustrates the number of TNG100 galaxies considered at each redshift, for the $2r_{0.5}$ dataset.

4.2.2.1 STELLAR MASS DISTRIBUTIONS

Before we compare dust masses for the observational and simulated data, we perform a quick check and examine the normalised stellar mass distributions of galaxies in the two datasets. We bin the galaxies in the observational MAGPHYS-COSMOS catalogue into the same redshift bins as the IllustrisTNG snapshots (Figure 4.1 and Table 4.1). We see that broadly, the stellar mass distributions are similar. We can be confident that the observed and simulated galaxies represent similar galactic populations.

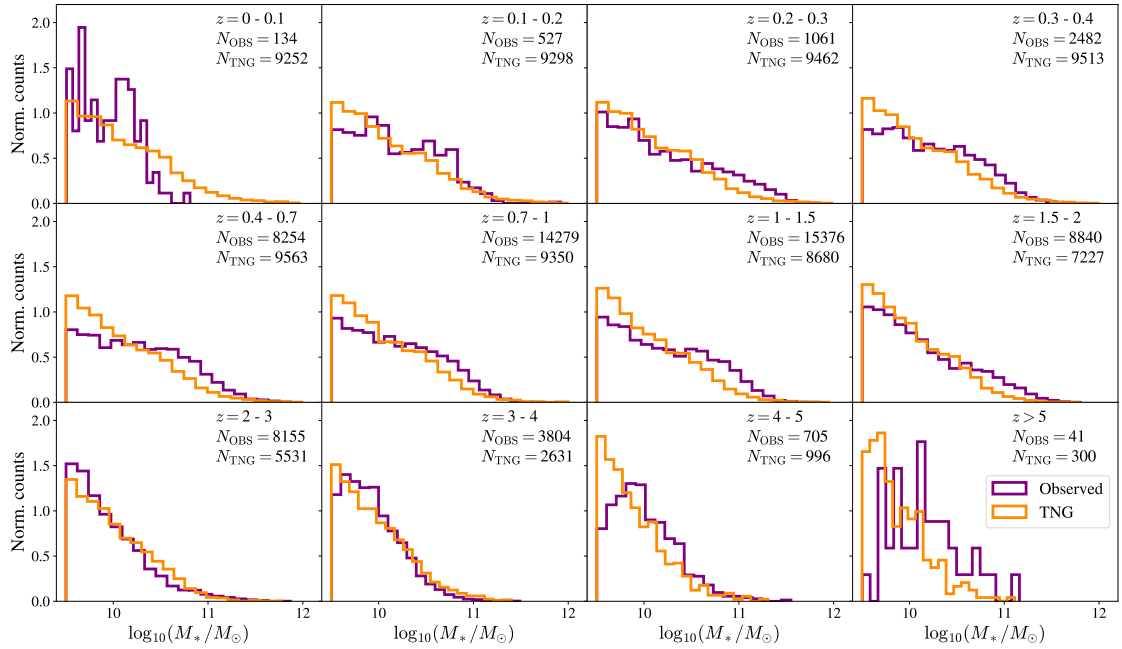

Figure 4.1: Distributions of the stellar masses of galaxies in different redshift bins for TNG100 and MAGPHYS-COSMOS sources. TNG100 stellar masses are calculated using particles and cells within $2r_{0.5}$. *Purple:* MAGPHYS-COSMOS sources used in stacking analysis to determine average dust properties. *Orange:* TNG100 galaxies.

Snapshot	z	$2r_{0.5}$	
		$N_{\rm filt}$	$N_{\rm filt,obs}$
17	5	3185	300
21	4	7394	996
25	3	14338	2631
33	2	22902	5531
40	1.5	26270	7227
50	1	27456	8680
59	0.7	27442	9350
72	0.4	26734	9563
78	0.3	26393	9513
84	0.2	26168	9462
91	0.1	25660	9298
99	0	25254	9252

Table 4.1: Number of TNG100 galaxies considered at each redshift, after removal of un-physical galaxies and resolution mass cuts to $200m_b$ ($N_{\rm filt}$), and after additional mass-cuts to allow for comparison with our observations obtained from stacking galaxies in the S2COSMOS field ($N_{\rm filt,obs}$).

4.3 DUST MASSES

4.3.1 EMPIRICAL DUST MASSES FROM STACKING ON S2COSMOS MAP

Typically, the 850μm emission from individual galaxies is below the noise level of the S2COSMOS map (Simpson et al., 2019). Therefore, in Chapter 3, we studied the 850μm emission of galaxies in the COSMOS field in a statistical manner - we binned galaxies by redshift and stellar mass to create sub-populations of these sources, and used well-established IVW stacking methodologies to estimate mean sub-mm fluxes for sources in each bin. Although this does mean that we lose information on individual galaxies, we gain information on each sub-population as a whole. We estimated 850μm stacked flux errors using Monte Carlo (MC) simulations on the location of galaxies within the S2COSMOS map. See Millard et al. (2020) for full details.

For sub-mm emission measured on the Rayleigh-Jeans tail of dust emission, dust masses, M_d, can be estimated using:

$$M_d = \frac{\langle S_{\nu_o} \rangle D_L^2}{\kappa_{\lambda_e} B_{\nu_e}(T_d)(1+z)} \tag{4.1}$$

where $\langle S_{\nu_o} \rangle$ is the average stacked flux for galaxies in a given $(M_* - z)$ bin, measured at the wavelength of observation (in this case, 850μm), D_L is the luminosity distance of the source[27], κ_{λ_e} is the assumed dust mass absorption coefficient scaled to the rest-frame emission wavelength, $B_{\nu_e}(T_d)$ is the Planck function calculated at the rest-frame emission frequency for an assumed dust temperature, T_d, and z is the middle of the redshift bin under consideration (e.g. Dunne et al. 2003a).

The value κ_{λ_e} is notoriously uncertain. Indeed, a recent study by Clark et al. (2016) showed that estimates of κ_{500} in the literature span over 3.5 orders of magnitude. We have used the freedom produced by this uncertainty to choose a value of κ_{500} that gives as good agreement as possible between the observed low-redshift DMFs (from Dunne et al. 2011 and Beeston et al. 2018) and the one predicted by

[27] In this work, we make use of the `Python` package `astropy.cosmology`, assuming `Planck15` cosmology, to calculate the luminosity distance using the centre of the redshift bin for the sub-population in question.

IllustrisTNG (Section 4.4). Rather than a formal fit, given the uncertainties and small differences in the shape of the predicted and observed $z = 0$ DMFs, we determined κ_{500} by performing a rough fit by eye to the high-mass end of the $z = 0$ DMFs. In particular, we ensured a good fit with the $z < 0.1$ DMF from Dunne et al. (2011). By performing this 'self-calibration' of κ_{500} at low redshift, we are still able to test whether IllustrisTNG predicts the correct shape of the low-redshift DMF and whether it predicts the cosmic evolution seen in the observations. We assume $\kappa_{500} = 0.14\,\mathrm{m^2 kg^{-1}}$, which is close to that found by James et al. (2002) and roughly around the middle of the range of values given by Clark et al. (2016). Note that we scale any dust masses taken from the literature to our chosen κ_{500} values. We scale the dust mass emissivity coefficient to the rest frame emission wavelength using:

$$\kappa_{\lambda_e} = \kappa_{500} \left(\frac{\lambda_{500}}{\lambda_e} \right)^{\beta} \tag{4.2}$$

where β is the dust emissivity spectral index. We assume β = 1.8 (Planck Collaboration et al., 2016), consistent with our previous stacking work and other studies upon which this work was based (see Millard et al. 2020 for details; see also Scoville et al. 2016; Scoville et al. 2017). Once again, for our stacked data from the S2COSMOS field, the rest frame emission wavelength is estimated by using the middle of the redshift bin currently being investigated. By scaling the dust mass emissivity coefficient to the wavelength of emission in the rest frame, we implicitly assume that the properties of dust grains themselves are constant throughout the Universe. We assume a mass-weighted dust temperature of 25 K, as in Millard et al. (2020) (see also Scoville et al. 2016; Scoville et al. 2017). We note that our method for calculating dust masses is simple, only depends on a few parameters, and does not have the black-box complexity of spectral energy distribution-fitting methods such as MAGPHYS. We discuss the impact of our assumptions on the values for β, κ_{500} and mass-weighted dust temperature in the following Chapter.

4.3.2 DUST MASSES FROM ILLUSTRISTNG

Dust masses are not one of the physical parameters explicitly calculated for galaxies in IllustrisTNG. Therefore, we have to calculate them in post-processing. We calculate dust masses, $M_{d,\mathrm{TNG}}$, on a cell-by-cell basis, summing over all cells

within two stellar half-mass radii of a given galaxy:

$$M_{d,\mathrm{TNG}} = \epsilon_d \left(\sum_{i=1}^{N_{2r}} \frac{f_{H,\mathrm{neutral},i}}{f_{H,i}} M_{\mathrm{gas},i} \, Z_i \right) \tag{4.3}$$

where $M_{\mathrm{gas},i}$ is the mass of gas in a given cell, Z_i is the metallicity of the gas in the cell, $f_{H,\mathrm{neutral,i}}$ is the fraction of gas in the cell that is neutral hydrogen (atomic or molecular hydrogen; HI or H_2), $f_{H,i}$ is the fraction of all the gas in a cell that is hydrogen and N_{2r} is the number of cells within two stellar half-mass radii for a given source. ϵ_d is the fraction of metals in a galaxy's ISM that are locked up in dust, a free parameter. We justify our choice of ϵ_d at the end of this Section.

In IllustrisTNG, the neutral gas fraction is calculated using two different prescriptions, depending on whether cells are classified as star-forming or not. For cells below the star formation threshold density, the neutral gas fraction is calculated self-consistently within the simulations (Vogelsberger et al. 2013). The combination of the cooling rate (from primordial hydrogen and helium cooling, metal-line cooling and inverse Compton cooling off CMB photons), the photoionisation rate (from the ultraviolet background; UVB) and gas self-shielding provide an overall UVB photoionization rate, which is used with CLOUDY look-up tables (Ferland et al. 1998) to calculate the neutral gas fraction. However, for star-forming cells where the gas density is higher, these approximations break down; the neutral gas fraction is not calculated self-consistently within the simulations (Springel & Hernquist 2003). For these cells, the model splits gas into a hot and cold phase, where the cold phase is assumed to be entirely neutral gas. The fraction of neutral hydrogen in star-forming cells is then estimated based on the density fraction of cold gas clouds, with a typical fraction between 0.9 and 1 (Springel & Hernquist 2003).

4.3.3 A CONSTANT DUST TO METALS RATIO?

The most direct estimates for the dust-to-metal ratio, ϵ_d, come from using UV spectroscopic observations of stars to measure the metal abundances within stars and in the ISM, the difference between the two being attributed to the metals depleted from the interstellar gas and locked up in dust grains (James et al. 2002). Clark et al. (2016) list 12 different estimates of ϵ_d, which have a mean value

of 0.5 and a standard deviation of 0.1. Most of these measurements, however, are ultimately based on depletion measurements in the Milky Way or rely on theoretical models of dust grains. The only other galaxies for which depletion measurements have been made using UV spectroscopy of stars are the Magellanic Clouds (Roman-Duval et al. 2019), which have much lower stellar masses than the galaxies in our COSMOS sample. The depletion measurements imply that ϵ_d in these galaxies is lower than in the Milky Way, by a factor of 1.5 for the LMC and a factor of 4 for the SMC. In an alternative approach to this question, Rémy-Ruyer et al. (2014b) and De Vis et al. (2017b, 2019), in studies of large samples of nearby galaxies, find a linear relationship between dust-to-gas ratio and metallicity for galaxies with $12 + \log(\mathrm{O/H}) > 8.0$. The former work implies a constant value of ϵ_d of $\sim$0.3 and the latter implies $\sim$0.2 for evolved galaxies[28], suggesting that only the lowest mass, lowest metallicity galaxies would likely deviate from this constant value locally. Both studies observed a broken power law where the dust-to-metals ratio starts to vary with metallicity below a 'transition' value of $12 + \log(\mathrm{O/H}) \sim 8$.

An illustrative comparison of the dust-to-metals ratio observed in the local Universe is shown in Figure 4.2, including predictions from the chemical evolution models of De Vis et al. (2017b). Following De Vis et al. (2019), we define the metal mass M_Z $M_Z = (Z \times M_{\mathrm{gas}}) + M_{\mathrm{dust}}$ where the fraction of metals in the ISM by mass Z is defined as $Z = 27.67 \times 10^{12+\log(\mathrm{O/H})-12}$ and the Solar value is $12 + \log(\mathrm{O/H})$ is 8.69. Following IllustrisTNG, we use a Solar value of $Z_\odot = 0.0127$ (Wiersma et al., 2009). The observed samples in this Figure come from DustPedia (De Vis et al., 2019), the gas-selected HSS sample (De Vis et al. 2017a;De Vis et al. 2017b), the revised parameters for the Dwarf Galaxy Sample (DGS, Madden et al. 2013) from De Vis et al. (2017a) and the *Herschel* Reference Survey (HRS, Boselli et al. 2010). A broken power-law relationship with Z observed by Rémy-Ruyer et al. (2014b) (their Table 1, using the Milky-Way $\mathrm{CO} - \mathrm{H_2}$ conversion factor) is also shown in Figure 4.2. The range of dust-to-metals predicted as a function of z from Inoue (2003) and the range proposed to match observed UV luminosity functions from $2 < z < 9$ (Vogelsberger et al., 2020b) are also included to show

[28] We note that these quoted values for ϵ_d were calculated assuming a different dust mass emissivity coefficient compared to this study. Scaling to the same κ_λ as used in this work results in a dust-to-metal ratio $\sim$20 and $\sim$30 percent higher than quoted in the original studies, thus reducing any perceived difference between the absolute values of quoted ϵ_d here and in previous works.

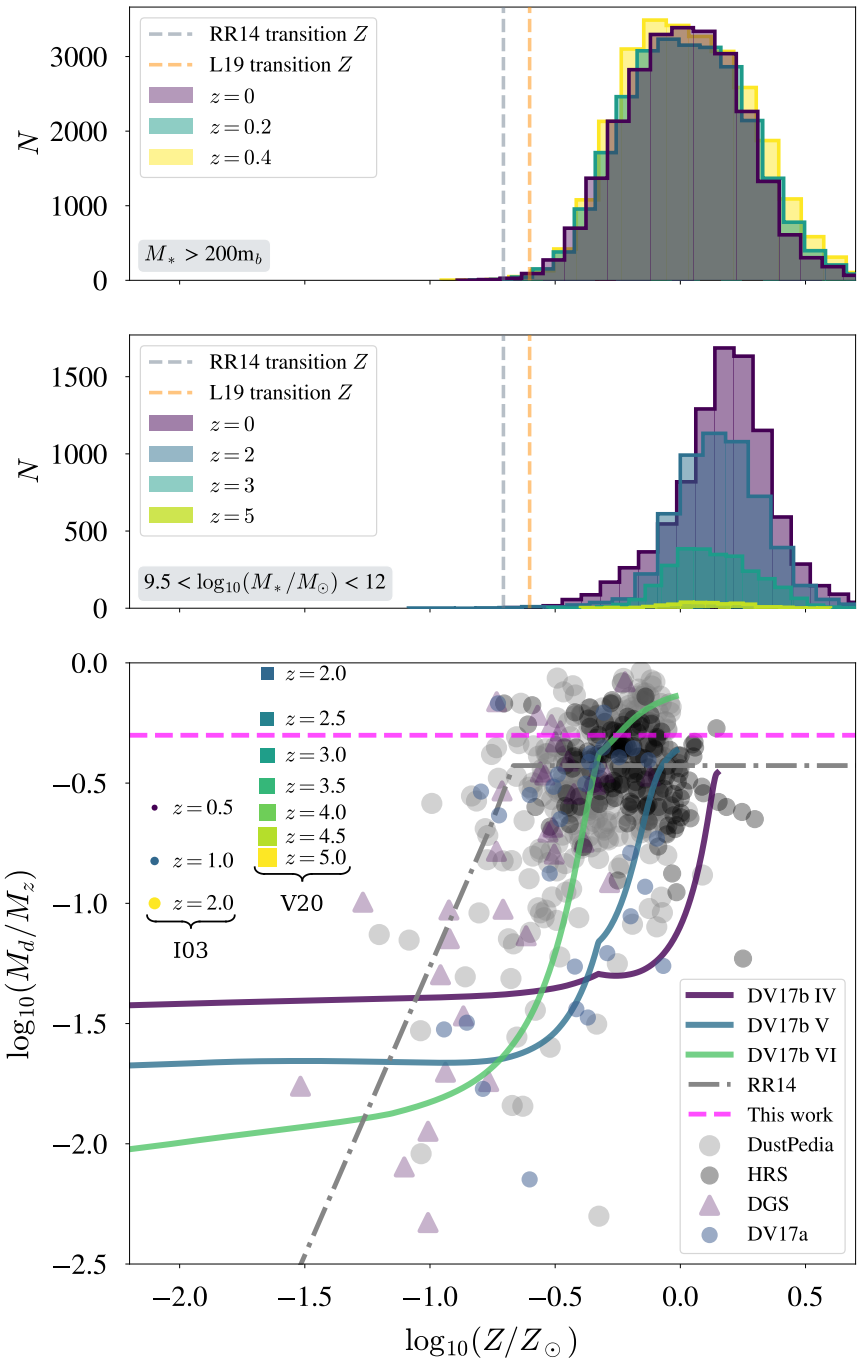

Figure 4.2: The dust-to-metal ratio for the local Universe and our samples. In the top two panels, we show the metallicities of IllustrisTNG galaxies for the two sub-samples we use in this work. The vertical lines indicate the transition metallicity from Rémy-Ruyer et al. (2014b) *(grey)* and from Lagos et al. (2019) *(orange)*. Bottom: we show local galaxy samples (see main text) with the Rémy-Ruyer et al. (2014b) broken power-law is (*dot-dashed line*) and predictions from De Vis et al. (2017b) (*solid lines*). *Coloured circles* show the dust-to-metals predicted as a function of z from Inoue (2003) (I03). *Coloured squares* show values derived from UV luminosity functions at $2 < z < 9$ (Vogelsberger et al., 2020b) (V20).

potential variations in ϵ_d with redshift.

It is not immediately clear what values of ϵ_d are appropriate at high redshifts, where high stellar mass galaxies are at an earlier stage of their evolution and therefore may have lower metallicities. However, De Vis et al. (2019) found galaxies in the local DustPedia survey with high dust-to-metal ratios ($0.2 - 0.5$) even at early evolutionary stages (defined as galaxies with high gas fractions). For the highest gas fractions in their sample ($f_{\rm gas} > 0.8$), they began to see dust-to-metal ratios as low as 0.04. Observations at high redshifts include gamma-ray bursts and damped Lyman alpha systems (De Cia et al. 2013; Zafar & Watson 2013) where the observed values of ϵ_d for high-metallicity galaxies is similar to that for the Milky Way (see also Yajima et al. 2014). De Cia et al. (2013) suggest that ϵ_d could be lower for very low-metallicity galaxies. Similarly, no obvious trend with redshift was seen by Wiseman et al. (2017), but extreme changes in ϵ_d are postulated for galaxies at $z > 6$ (see Vogelsberger et al. 2020b for more discussion). Li et al. (2019) however see little evolution in the dust-to-metal ratio from $z = 0$ to $z = 6$, instead showing it is most sensitive to the gas phase metallicity Z (though decreasing values are seen at lower stellar masses and high gas fractions; De Vis et al. 2017b).

For the redshift range used in this work, both the hydro-simulations from McKinnon et al. (2016) and semi-analytical models of Popping et al. (2017) imply that ϵ_d is different at $z = 0$ and $z = 2$. More recently, using the IllustrisTNG simulations we use in this work, Vogelsberger et al. (2020b) required a dust-to-metal ratio (their f_Z parameter) to vary with redshift over the range $2 < z < 8$ in order to match observed UV luminosity functions. Their relationship ($\epsilon_d = 0.9 \times (z/2)^{-1.92}$) predicts ϵ_d values of 0.9 - 0.1 for the redshift range which overlaps with this work ($2 < z < 5$), see Figure 4.2. We note that this $z = 2$ value is higher than that predicted by Inoue (2003) (Figure 4.2) and McKinnon et al. (2016).

Figure 4.2 compares the distribution of metallicities in the two sub-samples of the IllustrisTNG simulations used in this work: the $200m_b$ cut used for comparing with local galaxies (redshifts $0 < z < 0.4$), and the COSMOS stellar-mass cut ($9.5 \leq \log(M_*/M_\odot) \leq 12$) we use for comparison with our stacking data out to redshift $z = 5$. To investigate the the impact of metallicity on the dust estimates used in this work, we compare with the broken power-law of Rémy-Ruyer et al. (2014b) which suggest departures from a constant ϵ_d only occurs at $Z/Z_\odot < 0.2$

($Z/Z_\odot < 0.25$ for Lagos et al. 2019). For the $200m_b$ low z sample, some galaxies have metallicities equal to, or below, the Rémy-Ruyer et al. (2014b) and Lagos et al. (2019) transition metallicity, but these are small numbers - $N \sim 12$ ($N \sim 60$) for Rémy-Ruyer et al. (2014b) (Lagos et al. 2019). The majority have metallicities where a constant dust-to-metal ratio is appropriate. For the COSMOS sample, very few of our sources are at low enough metallicities, even at high redshifts. In summary, we show there is observational evidence that both our local samples of IllustrisTNG galaxies and high-metallicity systems have a fairly constant value of ϵ_d over the redshift range appropriate in this work, with a value similar to that of the the Milky Way. Figure 4.2 illustrates that a constant value of ϵ_d=0.5, the average value from the meta-analysis of Clark et al. (2016), is appropriate for the TNG100 sources used in this study. We will return to this issue in the next Chapter.

Finally, we note that a similar method was used to derive dust masses for IllustrisTNG galaxies by Hayward et al. (2020). They define ISM gas using a temperature-density cut from Torrey et al. (2012) (summing over all cells within 25kpc of the subhalo centre) and use this to compute an ISM metal mass, which they convert to a dust mass using a constant dust-to-metal ratio of 0.4.

4.4 A LOCAL DUST MASS FUNCTION

Before examining the evolution of dust mass in IllustrisTNG galaxies over much of cosmic time, we first investigate the dust content of IllustrisTNG galaxies in the local universe by calculating the IllustrisTNG DMF for $z < 0.5$. We compare these low redshift DMFs to ones from the literature - specifically, from Dunne et al. (2011) and Beeston et al. (2018). Dunne et al. (2011) used a sample of 1867 sources selected at 250μm from the Science Demonstration Phase of H-ATLAS (Eales et al., 2010) with reliable Sloan Digital Sky Survey (SDSS (DR7); Abazajian et al. 2009) counterparts. Dust masses are estimated by using both a single and multiple temperature modified blackbody models for the SEDs, assuming a κ_d value consistent with that used in MAGPHYS. Their sample covers a redshift range of $0 < z < 0.5$. Beeston et al. (2018) uses MAGPHYS to estimate dust and stellar masses for optically selected galaxies from the three equatorial fields of the Galaxy and Mass Assembly Catalogue (GAMA; Driver et al. 2011), which are the fields that also have

FIR/sub-mm data from *Herschel*-ATLAS (Eales et al., 2010). In total, they consider 15750 sources covering around 145 deg^2 of the sky, at redshifts $z < 0.1$.

We calculate the IllustrisTNG DMFs over a similar dust mass range to those in the literature[29], and bin our galaxies in stellar mass bins of 0.1 dex. We scale the DMFs from Dunne et al. (2011) and Beeston et al. (2018) to the same cosmology as assumed in the IllustrisTNG simulations, and to κ_{500} (Figure 4.3). Scaling to the κ_{500} used in this study increases the dust masses quoted in the literature studies by a factor of 1.43.

In Figure 4.3, we see that at high dust masses, beyond the knee of the DMFs, the $z = 0$ TNG DMF agrees well with the DMF from Beeston et al. (2018), and with the $z < 0.1$ DMF from Dunne et al. (2011). We note that some of this agreement is by construction since we calibrated κ_{500} by insisting on good agreement between the observed and theoretical DMF at high dust masses, but the agreement between the shapes of the DMFs (beyond the knee) is still significant. At lower dust masses, we find a higher number density of galaxies for TNG, compared to Beeston et al. (2018). We attribute the excess number of sources at low dust masses to galaxies classified as 'satellites' in the simulation, which have likely undergone excessive stripping (Diemer et al. 2019; Stevens et al. 2019), therefore reducing their dust masses as calculated using our post-processing technique and causing an excess of sources with low dust masses as compared to observations. We return to this issue and explore the differences between 'satellite' and 'central' TNG100 galaxies in the following Chapter. However, the slope of the DMF at low dust masses seems similar to that found by Beeston et al. (2018), even if there is an offset in the absolute number density.

The most striking difference between the observational and theoretical DMFs (Figure 4.3) is that we do not see the evolution in the DMF over the redshift range $0 < z < 0.5$ that is seen in the observational data. The TNG DMFs show little evolution up to $z = 0.5$, which is in stark contrast to the dust mass evolution shown in the observational data from Dunne et al. (2011). However, it is worth noting that Dunne et al. (2011) caution that their DMFs at $z > 0.3$ are estimated from galaxies that mostly only have photometric redshifts. Even so, the

[29] Specifically, our lower dust mass limit in Figure 4.3 is dictated by the average dust mass of galaxies in the lowest stellar mass bin of Figure 4.4, to avoid using dust mass bins which are affected by the sharp stellar mass cut off of $200m_b$ introduced in Section 4.2.2

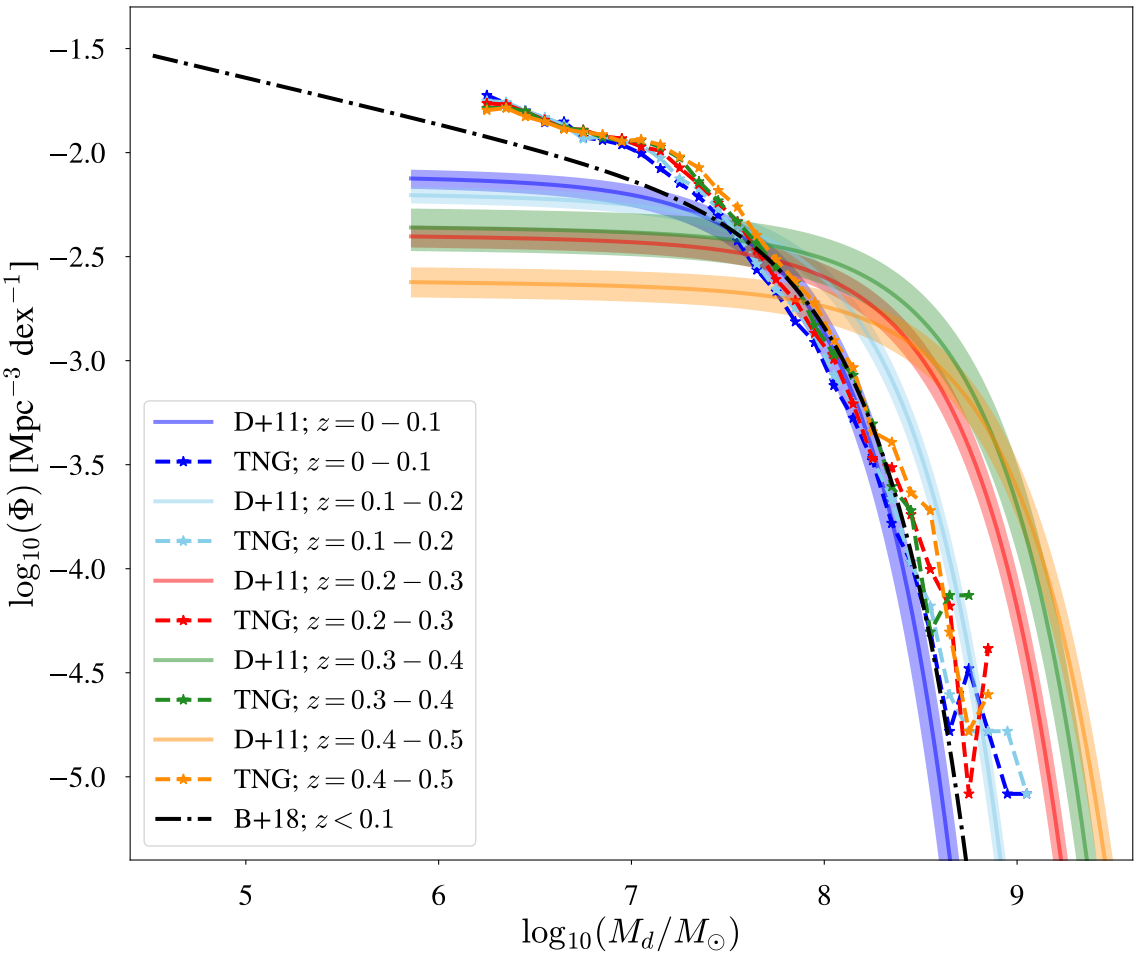

Figure 4.3: Low redshift DMFs for IllustrisTNG galaxies *(stars and dashed lines)* and local DMFs from Beeston et al. (2018) *(black dash-dot line)* and Dunne et al. (2011) *(solid colour lines)*. The DMF from Beeston et al. (2018) is based on an optically selected sample of 15750 galaxies within the redshift range $0.002 \leq z \leq 0.1$. The DMFs from Dunne et al. (2011) are based on a 250μm selected sample of 1867 galaxies with redshifts $z < 0.5$. The width of the dot-dashed line represents the error for the Beeston et al. (2018) DMF; the coloured shaded regions show the errors for the Dunne et al. (2011) DMFs. The colours of the IllustrisTNG DMFs and DMFs from Dunne et al. (2011) are chosen to indicate the same redshift bins. Local observed DMFs are scaled to IllustrisTNG cosmology with the dust masses scaled to κ_{500}.

strongest evolution in the DMFs from Dunne et al. (2011) is at redshifts below this threshold, and this evolution is clearly not apparent in the TNG100 DMFs.

We next examine the $z = 0$ ($M_* - M_d$) distribution of TNG100 galaxies and compare this distribution to local observational studies, as a sanity check that the dust mass estimates for TNG100 galaxies are consistent with those observed in the local galaxy population. First, we compare the dust masses calculated using the z=0 TNG100 data to dust masses calculated using our stacked S2COSMOS fluxes, and to dust masses from other studies of the local Universe from De Vis et al. (2017a) and Beeston et al. (2018) (Figure 4.4). De Vis et al. (2017a) use MAGPHYS to estimate dust and stellar masses for 323 galaxies that comprise the HRS (Boselli et al. 2010). The HRS is a stellar-mass selected volume-limited sample of galaxies in the nearby Universe. Sources have distances between 15 and 25Mpc, and are K-band selected, to minimise dust selection effects caused by extinction. The sample contains both late- and early-type galaxies. A brief description of the data used in Beeston et al. (2018) can be found in Section 4.4. The dust masses from De Vis et al. (2017a) and Beeston et al. (2018) are scaled to κ_{500}. In Figure 4.4, we bin the TNG100 sources by stellar mass and calculate the mean and standard error on the mean for galaxies in a given bin, as long as there are at least 50 sources in the bin.

We see that, broadly, the dust mass estimates from local studies agree with the $z = 0$ galaxies from TNG100 (Figure 4.4). However, it is worth noting that dust masses for the K-band-selected HRS, and the average dust mass in each stellar mass bin for the TNG100 simulations (which agree well with each other) are a little higher compared to the larger, but optically-selected, H-ATLAS sample from Beeston et al. (2018). The offset between our mean TNG100 values and the mean values for Beeston et al. (2018) is $\sim$0.2 dex. The 850 μm stacked sample from S2COSMOS lies somewhere between the HRS and Beeston et al. (2018). It may be possible that the small absolute offsets in average dust masses seen here are enhanced by the different selection effects and sampling issues of the observational studies. In particular, the optically-selected sample of Beeston et al. (2018) have average dust masses sitting slightly below the FIR-selected samples of H-ATLAS sources (see their Figure 10). Conversely, the TNG100 galaxy sample is not subject to such observational selection effects. The deviation could also be attributed to

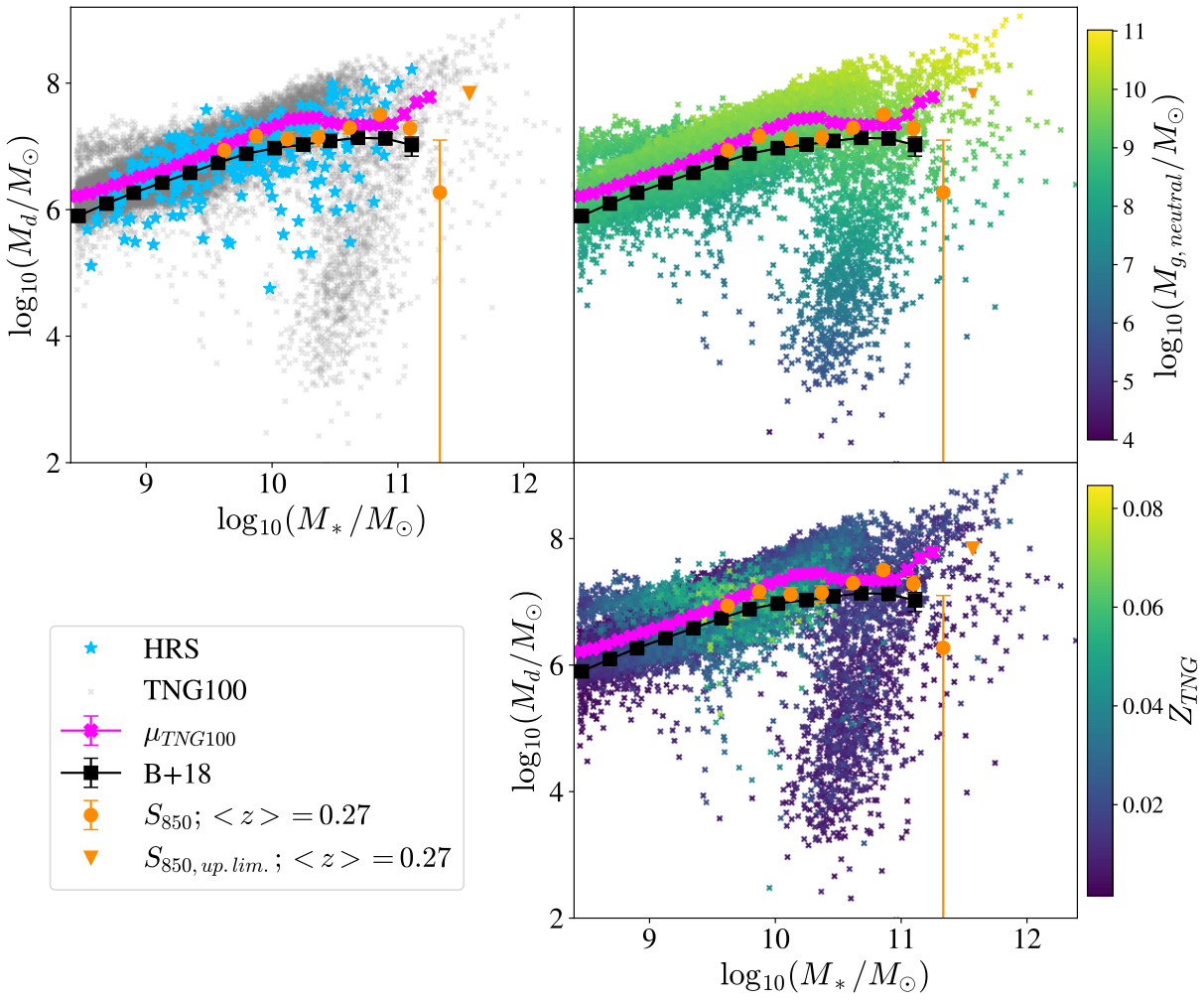

Figure 4.4: Dust mass versus stellar mass for the TNG100 galaxies at $z = 0$ and for various low-redshift galaxy samples. The left-hand panel shows the TNG100 galaxies as *grey points*; the right-hand top panel shows them as crosses with a *colour* given by each galaxy's neutral gas mass (see colour bar); and the right-hand bottom panel shows them as crosses with a colour given by each galaxy's metallicity (see colour bar). The mean and standard error on the mean for the TNG100 galaxies in a given stellar mass bin are shown by *fuchsia crosses*. The galaxies in the Herschel Reference Survey are shown as *blue stars* (De Vis et al. 2017a), the mean dust masses from the sample of Beeston et al. (2018) as *black squares*, and the mean dust masses for the galaxies in the low-redshift bins from our S2COSMOS study as *orange circles*, with the *orange triangle* showing an upper limit.

the methods used to calculate stellar and dust masses in the observational studies and the simulation data, which are not identical. However, qualitatively, the results for the datasets considered in Figure 4.4 are reasonably consistent, despite the different techniques and samples used to estimate physical parameters. We again remind the reader that the agreement shown in Figure 4.4 is, in part, by construction due to the choice of κ_{500} (see Section 4.4).

At $\log_{10}(M_*/M_\odot) \sim 10.5$ in Figure 4.4, there is a distinct population of TNG100 galaxies with a lack of dust (grey crosses). Since these are massive galaxies, low resolution is not likely to be the cause of such low dust masses. As can be seen in the top-right panel of Figure 4.4, these galaxies are devoid of neutral gas. These TNG100 galaxies are 'quenched' galaxies that have had their gas supply disrupted due to AGN feedback mechanisms. In IllustrisTNG, this stellar mass regime is the threshold at which kinetic mode feedback from AGN (in the form of black hole driven winds) becomes a dominant feedback effect (Weinberger et al. 2017, 2018; Terrazas et al. 2020; Zinger et al. 2020).

In Figure 4.4, at lower stellar masses, there is a spur of galaxies with high dust masses, which is not seen in the observed samples. These galaxies also have high metallicities (Figure 4.4, bottom-right panel). Despite some small differences, the galaxies from TNG100 broadly follow the same $(M_* - M_d)$ distribution that we see in observations at $z = 0$, showing that with the exception of the low-mass end of the IllustrisTNG DMF, our post-processing method for estimating the dust mass does a good job of predicting the dust properties of the local galaxy population. Having performed this low-redshift check, we now investigate whether the discrepancy between the observed and predicted evolution over the redshift range $0 < z < 0.5$ continues to higher redshifts.

4.5 EVOLUTION OF THE DUST MASS FRACTION AT HIGH REDSHIFTS

After calculating the dust masses for each galaxy in each TNG100 snapshot (see Section 4.3.2), we bin the galaxies into the same stellar mass bins used in our stacking analysis. For a given $(M_* - z)$ bin that has at least ten sources, we calculate the mean of the dust-to-stellar-mass ratio (M_d/M_*). The errors on the calculated

dust-to-stellar-mass ratios are taken to be the standard error on the mean. Since the TNG100 snapshots are at different redshifts to the redshift bins used in our stacking analysis, we perform quadratic interpolations to the resulting TNG100 dust-to-stellar-mass ratios in each stellar mass bin, to allow a comparison with our stacking data. Here, we focus on comparisons between the observations and simulations when considering a constant $\epsilon_d = 0.5$.

Figure 4.6 shows a comparison of the model predictions and observations. The model predicts dramatically less evolution than the observations (Figure 4.5 shows just the TNG100 predictions with a scale chosen to highlight details of the predicted evolution more clearly). At low stellar masses both the simulation and observations agree that the peak value of (M_d/M_*) is at $z \sim 3$, but TNG100 predicts much less evolution than is seen (Figure 4.6). It is interesting to note that the peak in the dust-to-stellar-mass ratio of galaxies is a little before the peak of the star formation history in the Universe. At low redshifts, the dust-to-stellar-mass ratios estimated for the TNG100 galaxies agrees well with the dust-to-stellar-mass ratios calculated in the stacking analysis for the observed galaxies, in all stellar mass bins, but we remind the reader that the agreement at low redshifts is by construction (see Section 4.4).

The simulation and the observations agree that at low redshift the galaxies with high stellar masses generally contain less dust than those with lower stellar masses. However, the difference between the predicted and observed evolution for the high-mass galaxies ($> \log(M_{*,\mathrm{bin}}) \sim 10.5$) is dramatic (Figure 4.6). The observed evolution is very large and continues out to the highest redshifts probed by our sample. In comparison, the simulated galaxies still have very small amounts of dust at high redshifts. Figure 4.6 shows that the difference in dust-to-stellar-mass ratio evolution between the simulated and observed data is highest at the highest stellar masses - except for the highest stellar mass bin, where a lack of galaxies in both datasets prohibits meaningful conclusions on the evolution of dust-to-stellar-mass ratio to be drawn.

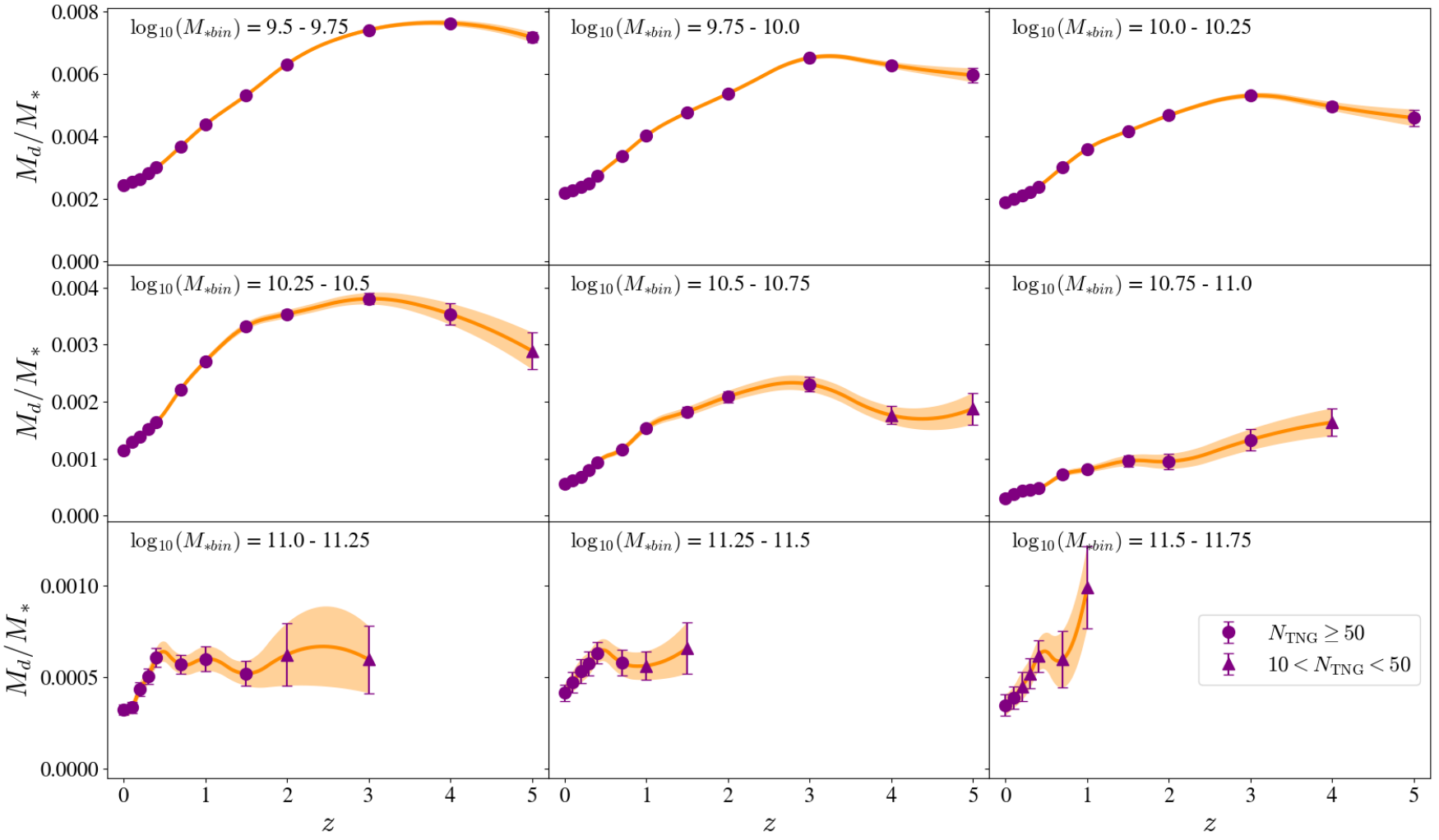

Figure 4.5: Dust-to-stellar mass ratios obtained from TNG100 simulations in redshift and stellar mass bins. *Circles:* at least 50 sources in the $(M_* - z)$ bin. *Triangles:* between 10 and 50 sources in the $(M_* - z)$ bin. The line is a quadratic interpolation to the data.

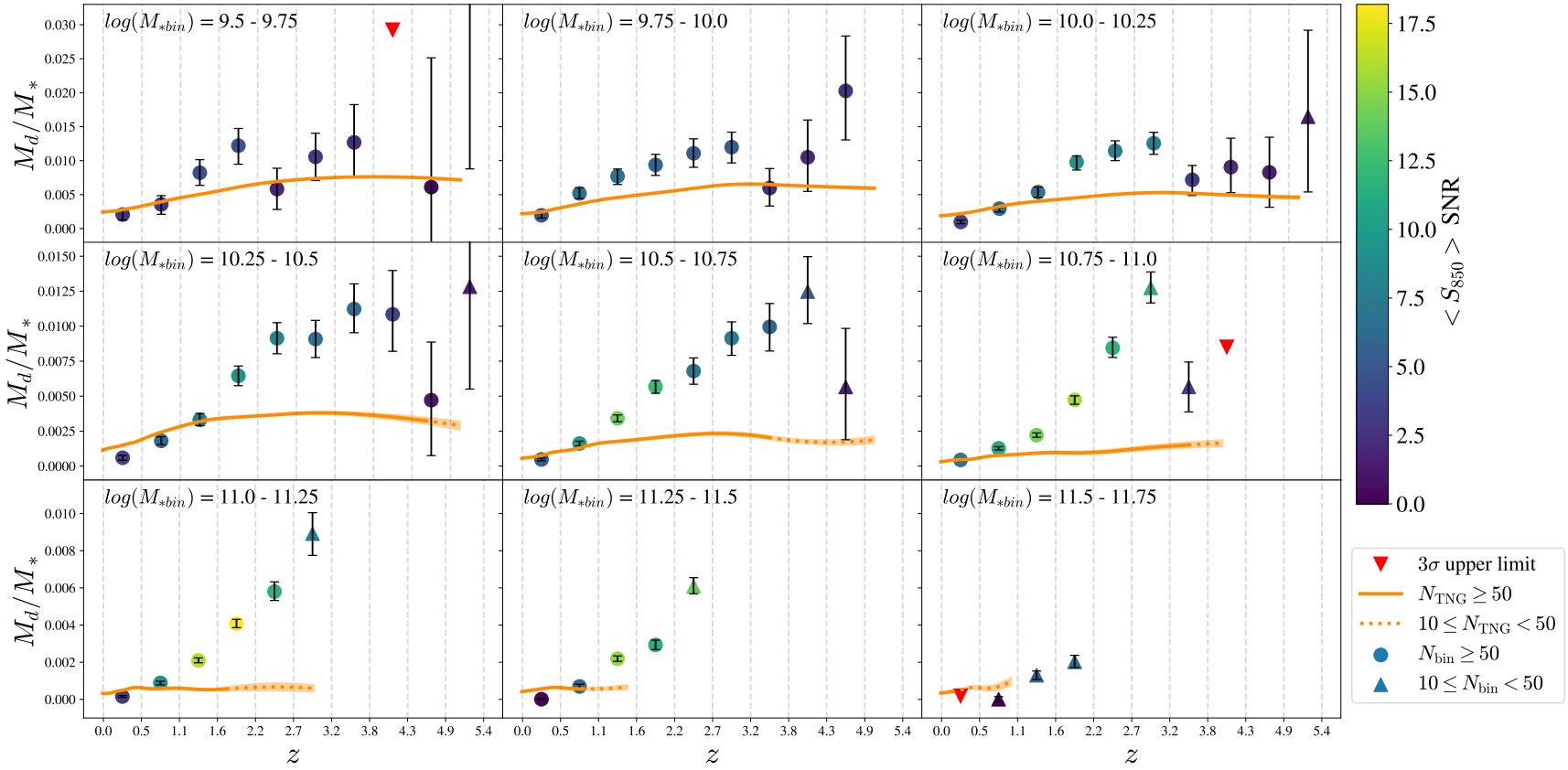

Figure 4.6: Dust-to-stellar mass ratios obtained from the stacked S2COSMOS fluxes (*symbols*, Millard et al. 2020) and TNG100 galaxies (*orange lines*). *Red triangles:* observed dust-to-stellar-mass ratios estimated using flux 3σ upper limits. *Circles:* observed dust-to-stellar mass ratios, where colour of point represents SNR of flux used to estimate dust masses, and there are at least 50 MAGPHYS-COSMOS sources in $(M_* - z)$ bin. *Triangles:* number of MAGPHYS-COSMOS sources in $(M_* - z)$ bin, $N_{\rm bin}$, between 10 and 50. *Orange line*: dust-to-stellar-mass ratio for TNG100 galaxies assuming a constant ϵ_d=0.5 (see Figure 4.5).

4.6 CONCLUSIONS

In this Chapter we used previous estimates of the dust-mass function (DMF) over the redshift range $0 < z < 0.5$ and our own estimates of the mean ratio of dust mass to stellar mass over the redshift range $0 < z < 5$. We made our predictions using the cosmological hydrodynamical simulation IllustrisTNG (TNG100), using a simple post-processing recipe in which half the metals in the cool ISM are locked up in dust grains.

- We created 'local' DMFs based on galactic dust mass estimates for TNG100 galaxies out to $z = 0.5$, and compared these to previously observed DMFs over the same redshift range. We find the DMFs from TNG100 show little evolution, which is in stark contrast with the strong evolution seen in the empirical DMFs.

- We find that the observed galactic population show a strong evolution in the dust-to-stellar-mass ratio (M_d/M_*) up to $z = 5$. For lower stellar mass bins ($\log(M_{*,\mathrm{bin}}) < 10.75$), we find that the dust-to-stellar-mass ratio peaks at $z = 3 - 4$, but we cannot locate the peak for the high-mass galaxies because of the lack of high-mass galaxies at high redshifts. We find that galaxies with a high stellar mass generally contain less dust than galaxies with a low stellar mass at the same redshift.

- The model predicts much weaker evolution than the observations over the redshift range $0 < z < 5$. At lower stellar masses ($\log(M_{*,\mathrm{bin}}) < 10.75$) the predicted evolution has a similar redshift dependence to the observed evolution but that for all stellar masses the strength of the evolution is much weaker than for the observations.

In the next Chapter we will explore reasons to explain the conflicting dust mass evolution shown between observations and simulations.

Chapter 5
Investigating the Discrepancy between Simulations and Observations

'Clever girl.'

Robert Muldoon, Jurassic Park

5.1 Introduction and Motivation

In Chapter 4, we saw dramatic differences between the predicted (IllustrisTNG) and observed (S2COSMOS) dust mass evolution in galaxies for high-mass galaxies ($> \log(M_{*,\mathrm{bin}}) \sim 10.5$, Figure 4.6). The observed evolution is very large and continues out to the highest redshifts probed by our sample. In comparison, the simulated galaxies still have very small amounts of dust at high redshifts. In this Chapter, we explore reasons to explain the conflicting dust mass evolution shown between observations and simulations. The work in this Chapter has been published in Millard et al. (2021).

5.2 CAVEATS AND ASSUMPTIONS

5.2.1 OBSERVED DUST PROPERTIES

Firstly, we consider the effect of the fundamental assumptions we have made in this work. Two big assumptions we have made are that the following parameters are time invariant; i) κ_{500}, and ii) T_d.

There is no obvious reason why we would expect κ_{500} to evolve with redshift, and we would need κ_{500} to have increased by a factor of $\sim$5 by $z = 3.5$ for galaxies with stellar masses $\log(M_{*,\mathrm{bin}}) = 10.5 - 10.75$ to bring the observations and the simulations into agreement. We are not aware of any predictions or observations showing such a large evolutionary effect in the properties of the dust itself, but we cannot rule this out. The dust emissivity spectral index depends on the physical properties of the dust grains, such as composition, size, and density (see Chapter 1). At high redshifts, the galactic environment is not identical to the local Universe - it is more violent and dynamic, with mergers common. A different ISM environment could impact grain-growth, thereby altering the composition of dust. Additionally, with more massive stars present in the low-metallicity early Universe (a top-heavy IMF), different dust formation pathways may dominate, altering the size of dust grains or even composition. For example, a top-heavy IMF in the early Universe suggests that supernovae are the dominant pathway for dust to form (Sarangi et al., 2018). Since κ_{500} is inversely proportional to grain-size (see Chapter 1, equation 1.13), smaller dust grains produced by supernovae could increase κ_{500}. However, the size of dust grains produced by supernovae is largely unknown, with some studies indicating a range of grain sizes (e.g. Todini & Ferrara 2001) and some finding evidence in the local Universe for only large dust grains surviving supernovae shocks (e.g. Gall et al. 2014). Although there is currently little evidence for evolution in the physical properties of dust grains with cosmic time, this does not mean this could not be true. However, we caution that other avenues to explain the discrepancy between observations and simulations should be exhausted first before investigating this rather controversial option.

In Equation 4.1, a higher dust temperature would lead to a lower calculated dust mass. In this work, it is important to remember that the dust temperature

assumed in Equation 4.1 is the *mass-weighted* dust temperature, and therefore represents the temperature of the bulk of the ISM (Millard et al., 2020). As described in Millard et al. (2020), mass-weighted dust temperature depends on the mean radiation energy density to the power of $\sim 1/6$ (Scoville et al., 2016), and so vast differences in the ISM environment over the history of the Universe would be required to significantly change the value of T_d. Thus far, there is little evidence to support such differences. Further, simulations of $z = 2 - 6$ galaxies by Liang et al. (2019) showed that the mass-weighted dust temperature of galaxies evolves little over this redshift range, and that a mass-weighted dust temperature of 25 K is a not an unreasonable assumption. One factor to consider is the increasing temperature of the CMB with redshift (da Cunha et al., 2013) which can become non-negligible at $z > 4$. Using Equation 10 from da Cunha et al. (2013), the expected rise in temperature due to the CMB for dust grains with $T_d = 25$ K at $z = 0$ would amount to only 0.4 K at $z = 5$.

Figure 5.1 shows how the observed dust masses change for discrete redshifts depending on the assumed dust temperature. We can see that even for an extreme increase in the mass-weighted dust temperature to 35 K, the corresponding decrease in the estimated dust masses is not enough to to reconcile the differences in the dust-to-stellar-mass ratio at high redshifts as shown in Figure 4.6.

In Equation 4.2, we assumed a value of the dust emissivity spectral index, β, of 1.8, robustly determined by Galactic ISM studies using sub-mm/mm emission from Planck (Planck Collaboration et al., 2011). This is also in agreement with a long-wavelength study of 29 Sub-millimetre Galaxies (SMGs; rapidly star-forming, highly dust-obscured massive galaxies typically found at $z \sim 2 - 4$) at $z \sim 2.7$ by Chapin et al. (2009), who find an average β=1.75. Since the observational dust masses are inversely proportional to κ_{λ_e}, the choice of β directly impacts the resulting dust masses (Equation 4.1).

Observational studies on extragalactic scales find values of β = 1-2 (e.g. Hildebrand 1983; Dunne & Eales 2001b; Chapin et al. 2009; Clements et al. 2010). Although these studies typically converge towards the idea that a value of β towards the upper end of this range is appropriate for dust in galaxies, it is worth examining the impact the choice of a lower β would have on the calculated observational dust masses. Therefore, as an example, we consider the impact on our

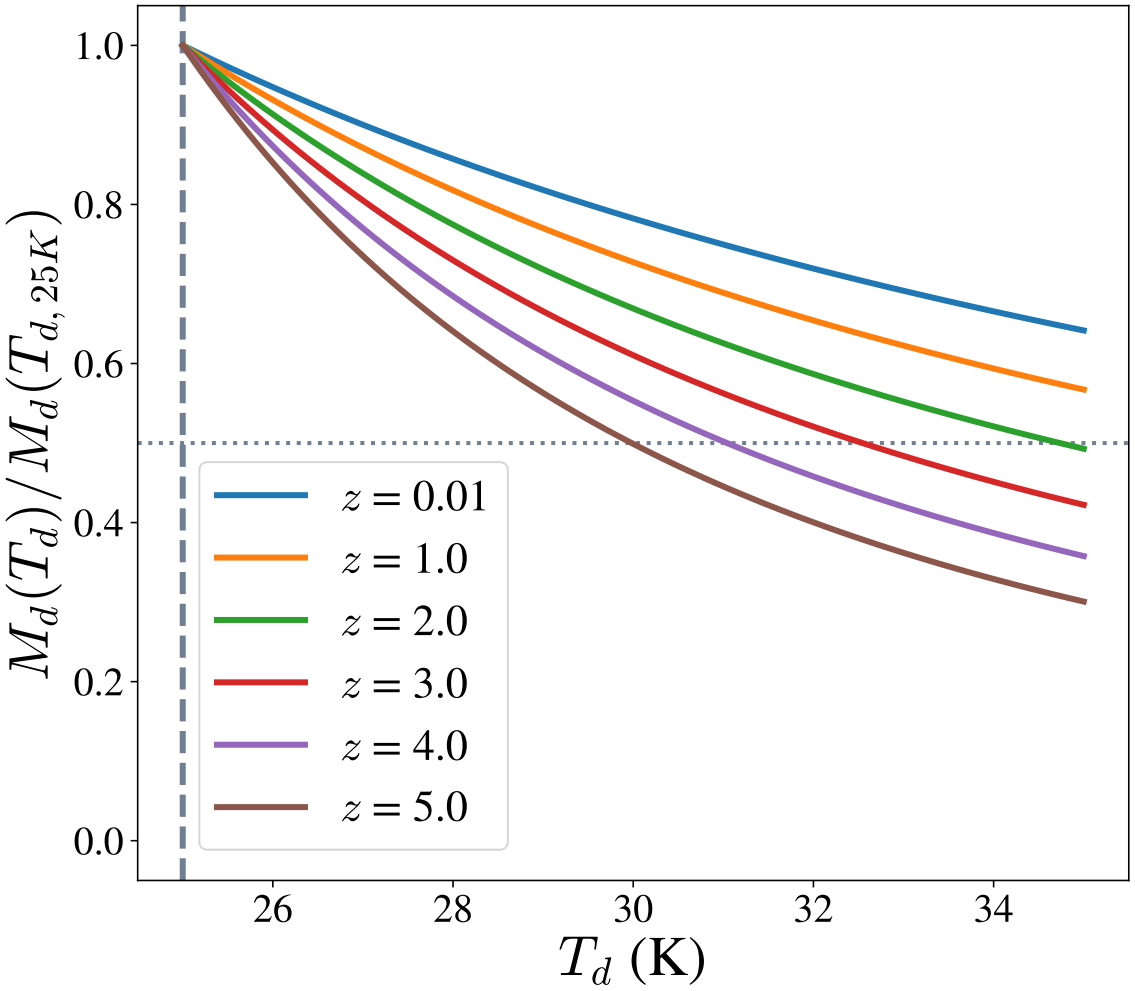

Figure 5.1: The variation of dust mass with assumed mass-weighted dust temperature for discrete redshifts. *Vertical dashed line:* the mass-weighted dust temperature assumed in this study (25 K). *Horizontal dotted line:* 50 per cent reduction in dust mass.

resulting dust masses had we chosen a significantly lower value of $\beta = 1.3$.

Figure 5.2 shows the variation in observational dust mass with redshift for our assumed value of $\beta = 1.8$ and our test value of $\beta = 1.3$. For $z \lesssim 0.7$, we see that a lower value of β would lead to lower dust masses compared to dust masses estimated using $\beta = 1.8$. However, beyond this redshift, we see that a lower value of β would lead to higher dust mass estimates, only exacerbating the difference between observations and the model seen in Figure 4.6.

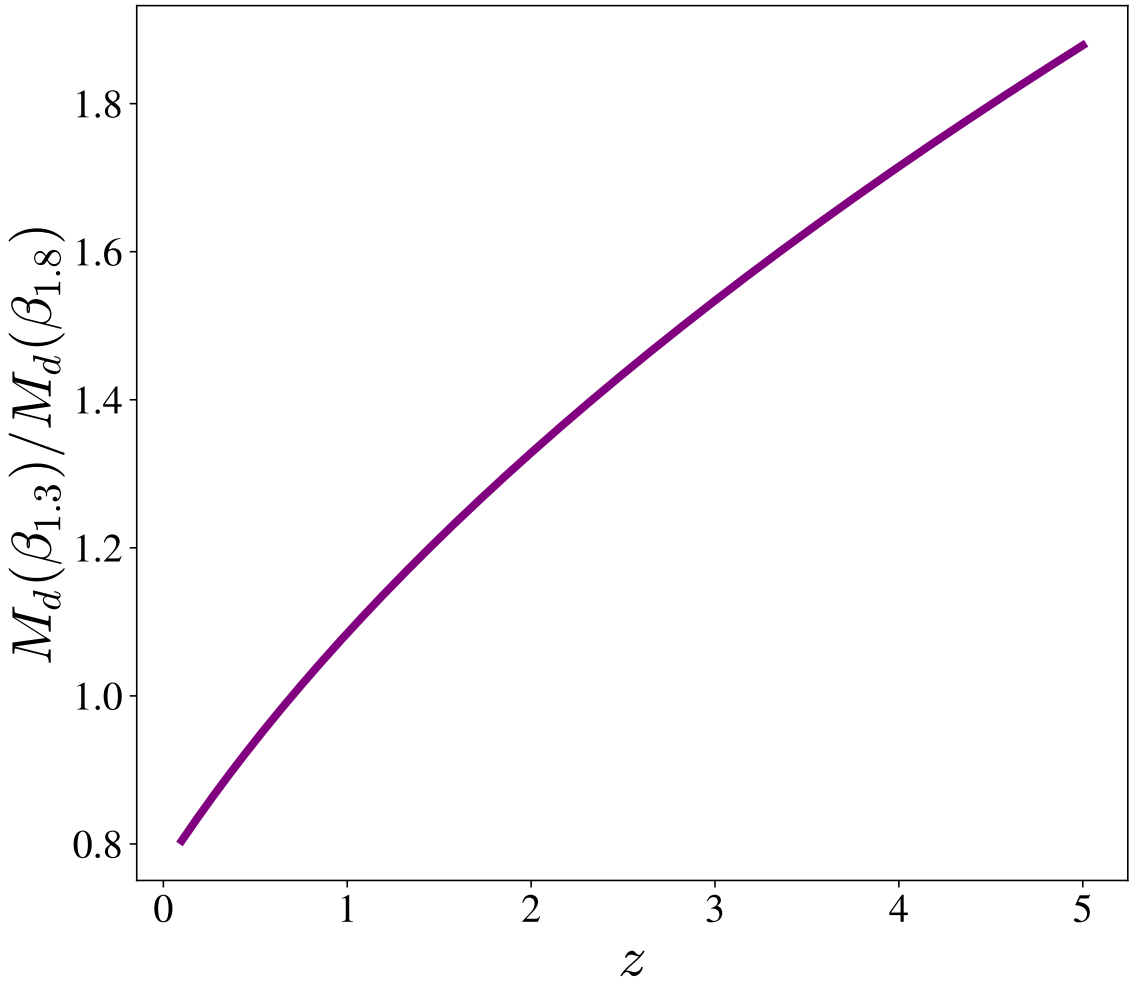

Figure 5.2: The variation of dust mass with redshift for two assumed values of the dust emissivity spectral index, β.

5.2.2 THE DUST-TO-METALS RATIO

An important assumption that we have made in estimating the dust masses for TNG100 galaxies is that the fraction of metals locked up in dust grains, ϵ_d, has a constant value (Section 4.3.3).

By setting its value to 0.5 we have left very little room to explain the discrepancy in Figure 4.6 by evolution in ϵ_d. Even incorporating all the metals in a high-redshift galaxy in dust grains would only increase the value of ϵ_d to one, which would only double the high-redshift dust masses, much less than the discrepancy in Figure 4.6. Such a scenario is not physical since the difference between the cosmic abundances of elements and the likely chemical composition of dust

grains mean that large proportions of plentiful elements such as oxygen must remain in the gas phase (Meyer et al. 1998). However, as a final check, we use the relationship of ϵ_d with z from Vogelsberger et al. (2020b) (valid for $2 \leq z < 9$) and values from Inoue (2003) for $0 < z < 2$ (their Figure 6) and re-run the analysis in Figure 4.6. As before, we perform a quadratic interpolation to the discreet TNG100 results. We note that for the variation of ϵ_d with redshift, this results in a sharp transition at around $z \sim 1.7$ as we move from the $\epsilon_d(z)$ values of Inoue (2003) used for the $z = 1.5$ TNG100 file, to the $\epsilon_d(z)$ values of Vogelsberger et al. (2020b) used for the $z \geq 2$ TNG100 files.

As shown in Figure 5.3, this variation in ϵ_d with redshift provides a moderately better agreement with the observations at intermediate redshifts ($z \sim 2$) for the three lowest stellar mass bins, where the discrepancy between the observations and simulations (assuming a constant ϵ_d) is the least. For stellar mass bins $\log(M_{*,bin}) = 10.25 - 10.75$, there is a good agreement between the observations and simulations at intermediate redshifts when using $\epsilon_d(z)$. However, this agreement requires a value of $\epsilon_d(z = 2)$ close to 1, which, as previously explained, is physically unlikely, and is still not enough to explain the discrepancy at the highest redshifts ($z > 2.5$). Out to higher redshifts, and for the higher stellar mass bins, this evolving $\epsilon_d(z)$ does not fix the dichotomy in the evolution.

It is also worth noting that the evolving $\epsilon_d(z)$ leads to worse agreement between the observations and simulations at low redshifts ($z < 2$). The relation from Inoue (2003) gives a $\epsilon_d(z)$ that decreases with redshift. Therefore, the lack of agreement with a $\epsilon_d(z)$ that decreases with redshift, combined with the agreement with the high $\epsilon_d(z)$ from Vogelsberger et al. (2020b) at intermediate redshifts and at low stellar masses, possibly indicates a requirement for an increasing $\epsilon_d(z)$ from $z = 0$ out to $z \sim 2 - 2.5$, where the star formation rate density of the Universe peaks (Daddi et al., 2007; Madau & Dickinson, 2014). Figure 4.6 also indicates that any variation in ϵ_d would need to have some dependence on galactic stellar mass. However, this is assuming that the COSMOS stacked observations are correct, and assuming that the only parameter that needs to be changed is ϵ_d.

Another parameter for which ϵ_d could vary is metallicity. To remove the discrepancy in Figure 4.6 would require a value greater than the currently assumed value of 0.5 at higher redshifts. Figure 4.2 shows that any variation in ϵ_d with

metallicity (eg Rémy-Ruyer et al. 2014b) tends to reduce the value below 0.5, locking even less metals into dust. Therefore an ϵ_d that varies with metallicity cannot explain the discrepancy.

One place where a change in ϵ_d may be important is in explaining the discrepancy between the observed and predicted low-redshift DMFs in Figure 4.3 for the *lowest dust mass* galaxies. At low dust masses the TNG100 DMF is higher than the observed DMF. The galaxies with these low dust masses have lower stellar masses than the galaxies in our COSMOS sample and are therefore more likely to resemble the low-metallicity systems for which there is some evidence that ϵ_d is lower than in the Milky Way (Section 4.3.3). Lowering ϵ_d by a factor of ~ 2 would be enough to resolve the discrepancy in the DMF at low dust mass, in agreement with the scatter in ϵ_d we see in galaxies in the local Universe (Figure 4.2). However, this cannot be responsible for the discrepancy in *the evolution* observed in the low redshift DMFs (Figure 4.3), since models that predict a variation in ϵ_d over $0 < z < 0.5$ produces a difference that is too small to account for the evolution observed in Dunne et al. (2011). For example, Inoue (2003) find a variation of only a factor of 2 in ϵ_d over this range (Figure 4.2).

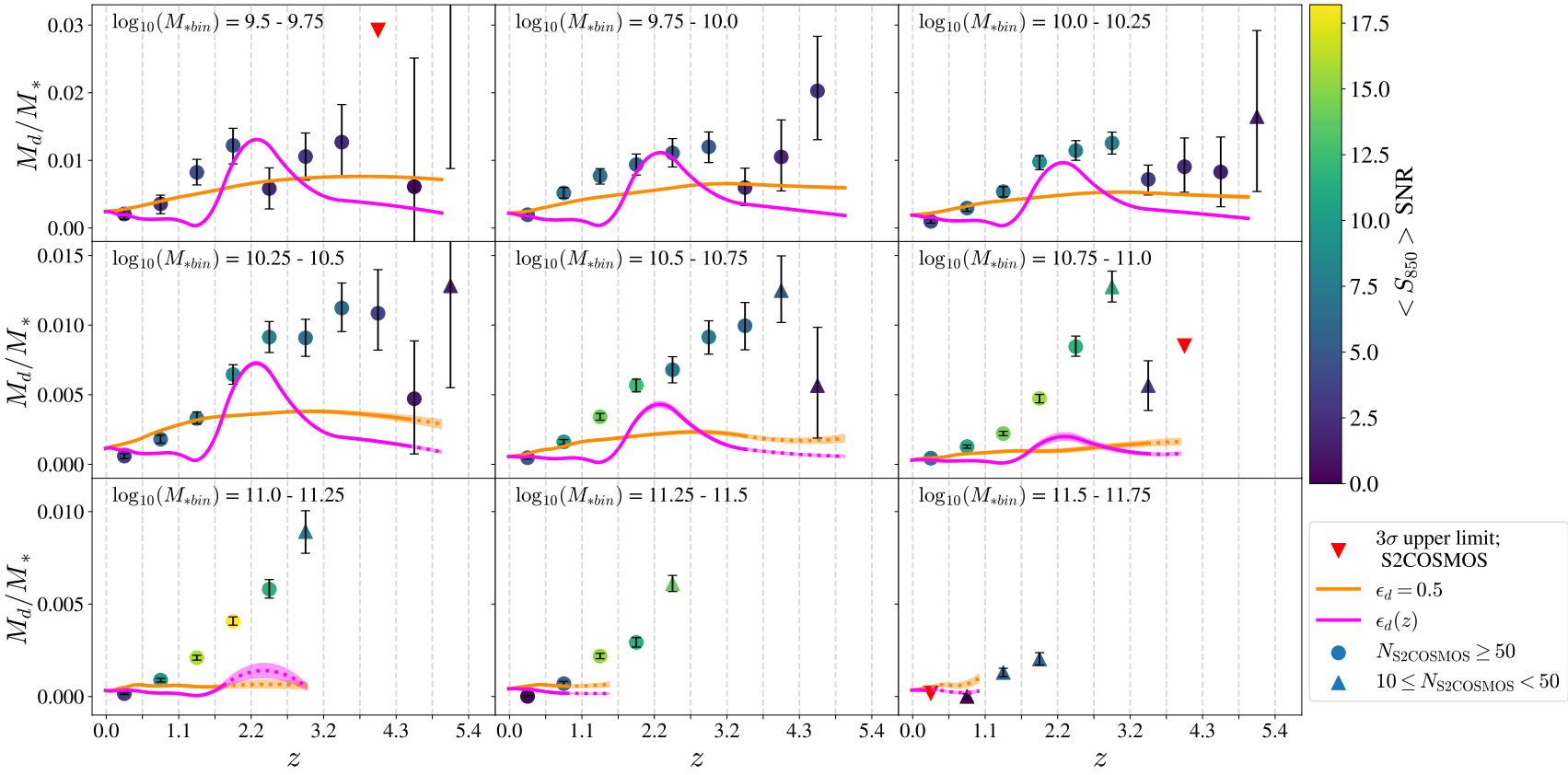

Figure 5.3: Dust-to-stellar mass ratios obtained from the stacked S2COSMOS fluxes (*symbols*, Millard et al. 2020) and TNG100 galaxies (*orange and magenta lines*). *Red triangles:* observed dust-to-stellar-mass ratios estimated using flux 3σ upper limits. *Circles:* observed dust-to-stellar mass ratios, where colour of point represents SNR of flux used to estimate dust masses, and there are at least 50 MAGPHYS-COSMOS sources in $(M_* - z)$ bin. *Triangles:* number of MAGPHYS-COSMOS sources in $(M_* - z)$ bin, $N_{\rm S2COSMOS}$, between 10 and 50. *Orange line*: dust-to-stellar-mass ratio for TNG100 galaxies assuming a constant ϵ_d=0.5 (quadratic interpolation, see Figure 4.5). The *magenta line* shows instead the results when a redshift-dependent relation for $\epsilon_d(z)$ is assumed (Inoue 2003 for $z < 2$ and Vogelsberger et al. 2020b for $z \geq 2$). Note the sharp transition at $z \sim 1.7$. *Solid line:* at least 50 TNG100 sources in$(M_* - z)$ bin. *Dashed line:* number of TNG100 sources in $(M_* - z)$ bin, $N_{\rm TNG}$, between 10 and 50.

5.3 ILLUSTRISTNG CAVEATS

We now explore global properties of the IllustrisTNG simulation in an attempt to explain the lack of evolution in the dust mass of galaxies over cosmic time as compared to observations. Specifically, in the next sections, we examine satellites versus centrals (Section 5.3.2), metal enrichment prescriptions (Section 5.3.3), the neutral gas content of galaxies (Section 5.3.5), and feedback mechanisms (Section 5.3.6).

5.3.1 BOUND VERSUS 2RAD

Next we redo all of the analysis in Chapter 4, but now we include all of the particles and cells gravitationally bound to a galaxy in the IllustrisTNG simulations. We do not focus on drawing conclusions from the bound galaxies, only highlighting similarities and differences between this and the $2r_{0.5}$ dataset used earlier in order to determine if this would affect our conclusions. We will show that using parameter values calculated for all particles and cells gravitationally bound to a source (hereafter called $_{\rm bound}$) does not change any of our conclusions.

When comparing observational results to dust masses estimated using all particles and cells bound to a given source, we assume $\kappa_{500,\rm bound} = 0.07$ m^{2}kg^{-1}.

5.3.1.1 STELLAR MASS DISTRIBUTION

In Appendix B, Figure B.1 is the same plot as Figure 4.1, but for all particles and cells bound to a given source. In this case, we see that the stellar mass distributions of the observed and IllustrisTNG galaxies in each redshift bin are reasonably similar. There are more galaxies in each redshift bin when we consider the bound stellar masses as opposed to the $2r_{0.5}$ stellar masses (Figures 4.1 and B.1). This is not unexpected, since the bound stellar mass for a given source is higher than the $2r_{0.5}$ stellar mass, and so more galaxies will cross the $200m_b$ mass resolution threshold when considering the bound stellar masses.

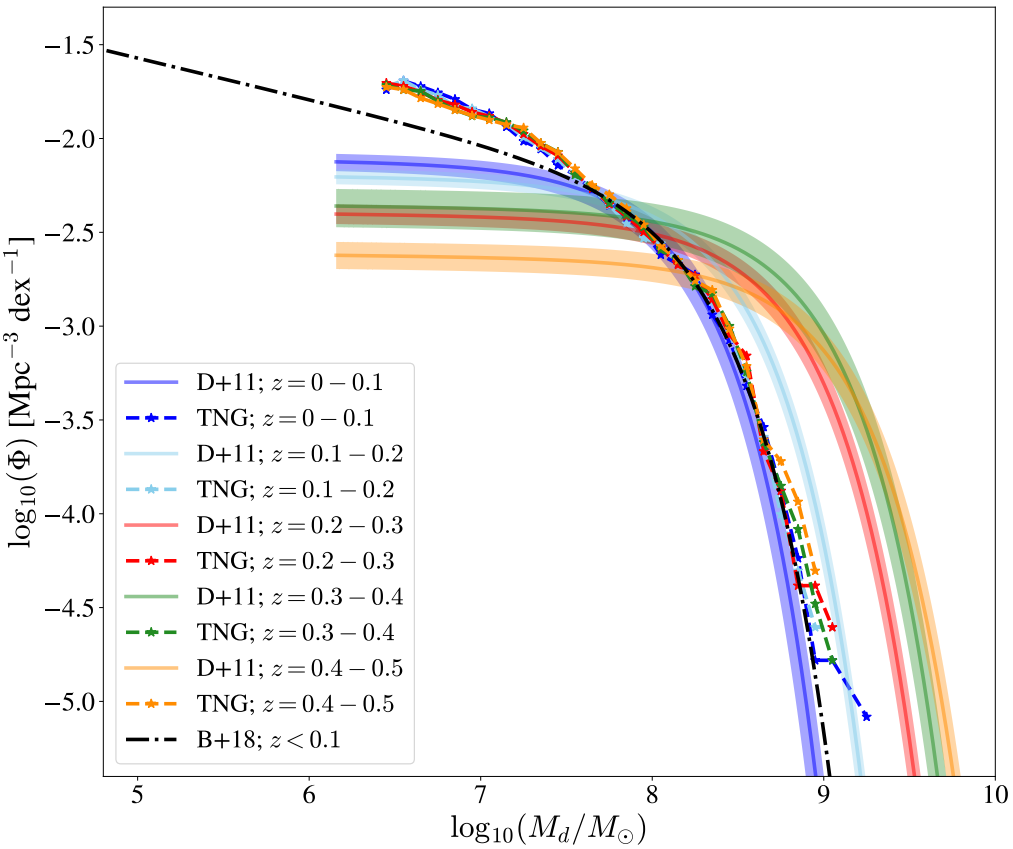

Figure 5.4: Low redshift DMFs for bound IllustrisTNG galaxies *(stars and dashed lines)* and local DMFs from Beeston et al. (2018) *(black dash-dot line)* and Dunne et al. (2011) *(solid colour lines)*. The width of the line represents the error for the Beeston et al. (2018) DMF; the shaded regions are the errors for the Dunne et al. (2011) DMFs. Local DMFs scaled to IllustrisTNG cosmology and dust masses scaled to $\kappa_{500,\mathrm{bound}}$.

5.3.1.2 LOCAL DMF

Figure 5.4 shows the low redshift DMFs for TNG100, calculated using all particles and cells bound to a given source. In Figure 5.4, the IllustrisTNG DMFs are also compared to local estimates, scaled to the same cosmology as assumed in the IllustrisTNG simulations, and with dust masses scaled to $\kappa_{500,bound}$ such that the $z = 0$ observed and simulated DMFs agree.

As can be seen in Figure 5.4, even if we use the data for all particles and cells bound to a given source, there is still a clear lack of evolution in the dust mass of TNG100 galaxies, compared to the observational data.

5.3.1.3 LOCAL DUST MASS ESTIMATES

We scale the local observed dust masses using $\kappa_{500,\mathrm{bound}}$, increasing their quoted dust masses by a factor of 2.85. As can be seen in Figure B.2 (Appendix B), we see a similar agreement between the simulated galaxies and the observed data, no matter if we consider dust masses calculated using the data within two half-mass radii, or the data using all particles and cells bound to a given source.

One difference between these Figures are the galaxies at $\log(M_*/M_\odot) \sim 10.5$ with a lack of dust. There are more of these galaxies when we consider the simulated data within two half-mass radii (Figure 4.4), compared to when we consider the data for all particles and cells bound to a given source (Figure B.2), as evidenced by the smoother average simulated dust masses line in Figure B.2. We attribute this difference to feedback from stars driving gas and dust out into the halo of simulated galaxies, or at least beyond two stellar half-mass radii. Since dust masses in the simulated galaxies are calculated using gas masses, such gas would still be encapsulated in the gravitationally bound data, thereby raising calculated dust masses for a given source, and leading to less sources with significantly less dust at $\log(M_*/M_\odot) \sim 10.5$.

5.3.1.4 HIGH REDSHIFT DUST MASS EVOLUTION

In Appendix B, Figure B.3 shows a similar evolution in the dust mass fraction with cosmic time as Figure 4.5; for stellar masses $\log(M_*/M_\odot) \leq 10.75$, the dust mass fraction of galaxies increases with increasing redshift, and as we progress to higher stellar mass bins, the overall dust mass fraction of galaxies decreases. Except for the lowest stellar mass bin, for galaxies with stellar masses $\log(M_*/M_\odot) \leq 10.75$, we see a peak in the dust mass fraction at around $z = 3 - 4$. For the lowest stellar mass bin, there are indications of a plateau in the dust mass fraction around $z = 5$, but without data beyond this redshift, it is difficult to determine if this is the true trend. A comparison of Figures 4.5 and B.3 shows that for these lower-to-mid stellar mass bins ($\log(M_*/M_\odot) \leq 11.0$), the evolution in the dust mass fraction for the simulated galaxies is similar, regardless of the dataset considered.

The same cannot be said for the three highest stellar mass bins, at first glance. However, caution must be taken when comparing these stellar mass bins

in Figures 4.5 and B.3. The bound dataset extends to higher redshifts in these high stellar mass bins, due to higher number counts introduced by the strict self-consistent $200m_b$ resolution mass threshold. We therefore caution against directly comparing the results of these two datasets at redshifts where either dataset has $N_{\rm TNG} < 50$, due to low number counts. With this in mind, comparison of Figures 4.5 and B.3 shows that both display a similar dust mass fraction evolution in the three highest stellar mass bins. Therefore, we can be confident that our conclusions in the main text would not change significantly if we had considered the bound dataset over the $2r_{0.5}$ dataset.

As can be seen in Figure 5.5, even if we use the data for all particles and cells bound to a given source, there is still a significant lack of dust evolution in TNG100 galaxies, as compared to the observational data.

5.3.2 SATELLITES VERSUS CENTRAL SOURCES

Previous studies examining the neutral gas content of IllustrisTNG galaxies at $z = 0$ have found that environment is an important influencing factor. For example, Stevens et al. (2019) showed that $z = 0$ TNG100 satellite galaxies are typically a factor of >3 poorer in HI than a central galaxy of the same stellar mass. In addition, they showed that the inherent neutral gas fractions of TNG100 satellite galaxies show a dip at around $\log(M_*/M_\odot) \sim 10.75$. They attribute the lack of gas in satellite galaxies to i) gas lost via AGN feedback (satellites are less able to reattain any gas lost due to their lack of gravitational influence); and ii) stripping and quenching. Further, Diemer et al. (2019) found a population of TNG100 galaxies, the vast majority of which are classified as satellites, that were devoid of gas. These galaxies were found to largely live in crowded environments, and so have likely been stripped of their gas by a larger halo host.

It is therefore not unreasonable to consider that such unusual gas-poor satellite galaxies may be masking more rapid dust mass evolution in TNG100 galaxies than is shown by the collective population. To test this, we split our simulated galaxy sample into satellites and centrals[30] and separately examine the dust mass evolution for these two galactic populations (Figures 5.6 and 5.7).

Figure 5.6 shows the DMFs for the satellite and central TNG100 galaxies.

[30] According to the `Subfind` classification

Considering first the central galaxies (Figure 5.6; *right*), we can see that the $z = 0$ TNG100 DMF agrees remarkably well with the $z = 0$ DMF from Beeston et al. (2018) at low and high dust masses, although the knee of the TNG100 DMF sits slightly lower than the observed dust mass function. This shows that at $z = 0$, the dust masses of TNG100 central galaxies are well-modelled by the simulations plus our post-processing recipe.

Now examining the DMFs of the satellite galaxies (Figure 5.6; *left*), we see that in comparison to observations, TNG100 satellite galaxies are particularly devoid of dust. This is not unexpected, considering the lack of neutral gas in satellite galaxies found by previous studies (e.g. Diemer et al. 2019; Stevens et al. 2019).

A comparison of Figures 4.3 and 5.6 shows that the excess number of low dust mass sources in the total DMF can be attributed to satellite galaxies with low gas content, probably due to a combination AGN feedback driving gas out of the gravitational influence of satellite galaxies, ram-pressure stripping, and quenching (Stevens et al. 2019).

However, the most striking and important feature of Figure 5.6 is that splitting the TNG100 galaxies sample into satellite and centrals *does not solve the lack of dust mass evolution* over the redshift range $0 < z < 0.5$ in TNG100 galaxies as compared to observations. Both satellites and central galaxies show a lack of evolution. This indicates that the lack of dust mass evolution in TNG100 galaxies can be attributed to global simulation properties, rather than secondary effects that manifest due to environmental effects, for example.

Next, we explore the dust mass evolution of satellite and central IllustrisTNG galaxies out to high redshifts. Figure 5.7 shows the evolution in the dust-to-stellar-mass ratio of TNG100 galaxies for galaxies with stellar masses $\log(M_*/M_\odot) \geq 9.5$. As shown in Figure 5.7, the dust-to-stellar-mass ratio evolution of satellite and central galaxies are largely similar, particularly for stellar masses $\log(M_*/M_\odot) \leq 11.0$. Above this stellar mass limit (i.e. for galaxies in the three highest stellar mass bins), the dust-to-stellar-mass ratio evolution of satellite galaxies is a little different to that of centrals and the combined sample. However, we caution against inferring too much here, since there are few satellite galaxies in these bins, and the results suffer from low number statistics.

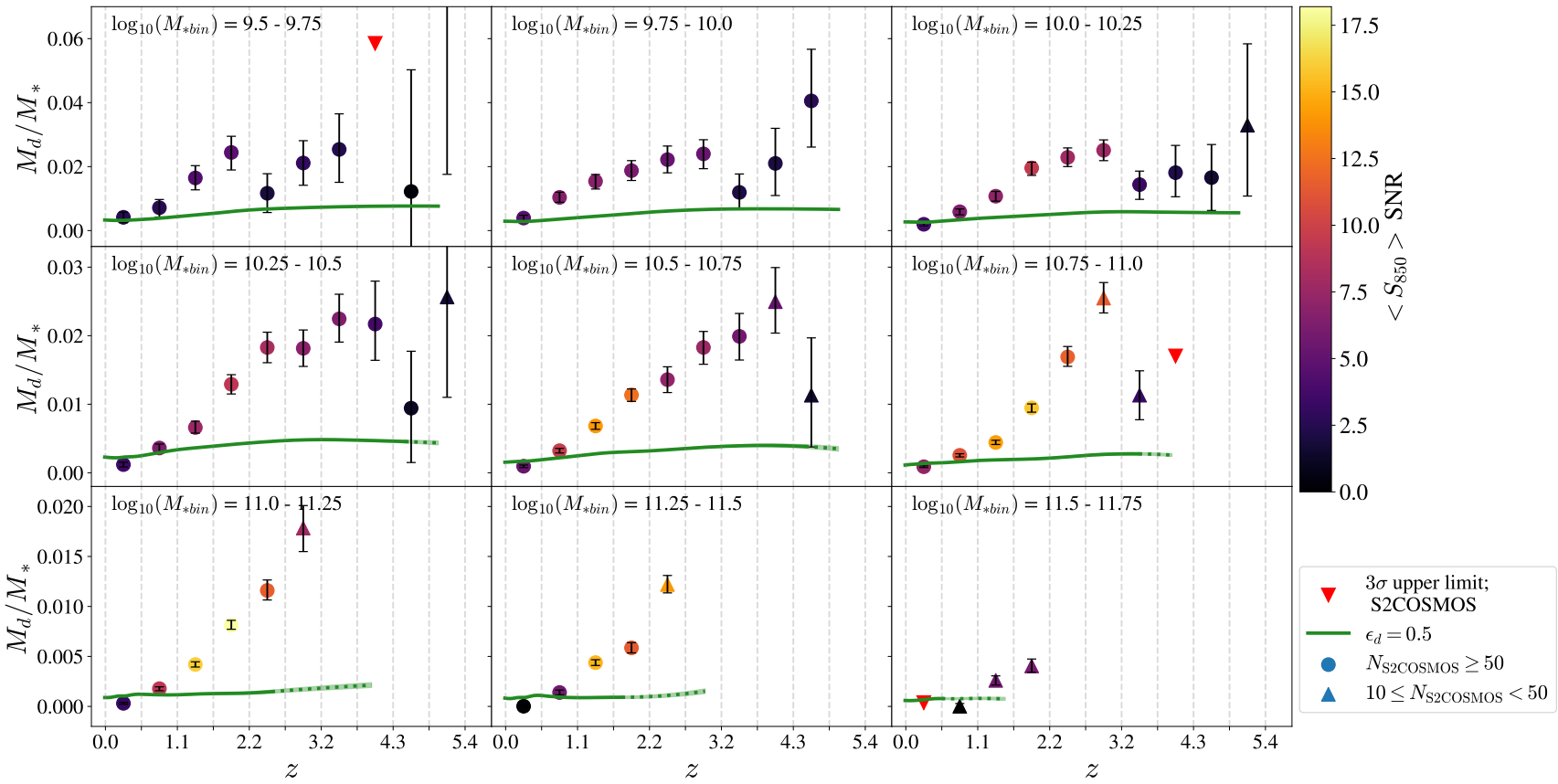

Figure 5.5: Dust-to-stellar-mass ratios of MAGPHYS-COSMOS *(symbols)* and TNG100 galaxies for bound sources *(orange line, quadratic interpolation)*. *Red triangles:* empirical dust -to-stellar-mass ratios estimated using flux 3σ upper limits. *Circles:* empirical dust -to-stellar-mass ratios, where colour of point represents SNR of flux used to estimate dust masses. *Triangles:* number of MAGPHYS-COSMOS sources in $(M_* - z)$ bin, N_{bin}, between 10 and 50. *Circles:* at least 50 MAGPHYS-COSMOS source in $(M_* - z)$ bin.

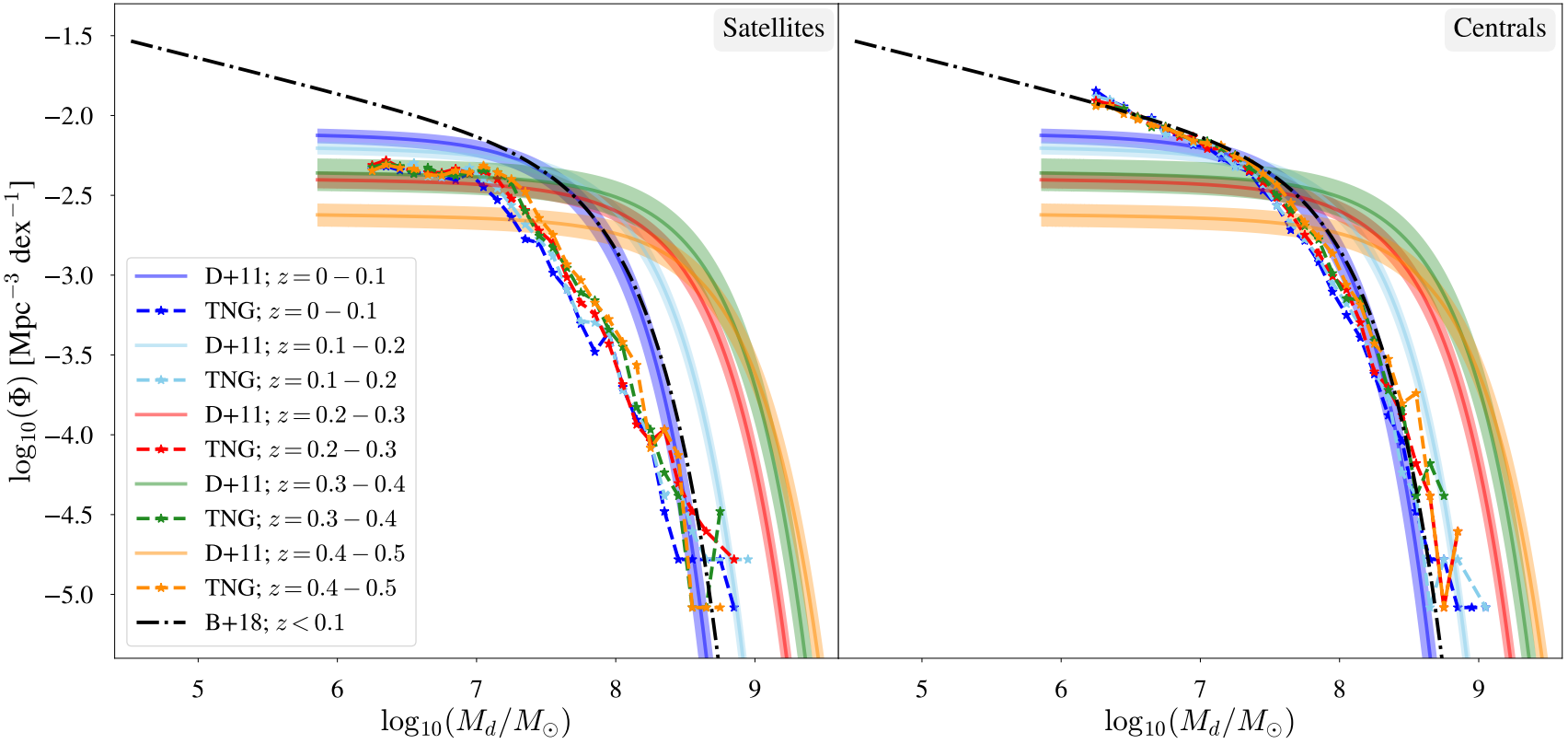

Figure 5.6: Low redshift DMFs for IllustrisTNG galaxies *(stars and dashed lines)* and local DMFs from Beeston et al. (2018) *(black dash-dot line)* and Dunne et al. (2011) *(solid colour lines)*. The IllustrisTNG sources have been split into two populations: satellite *(left)* and central galaxies *(right)*.Literature DMFs are the same as in Figure 4.3, and as before, have been scaled to IllustrisTNG cosmology and the values of the dust-mass opacity coefficient, κ_{500}, used in this paper.

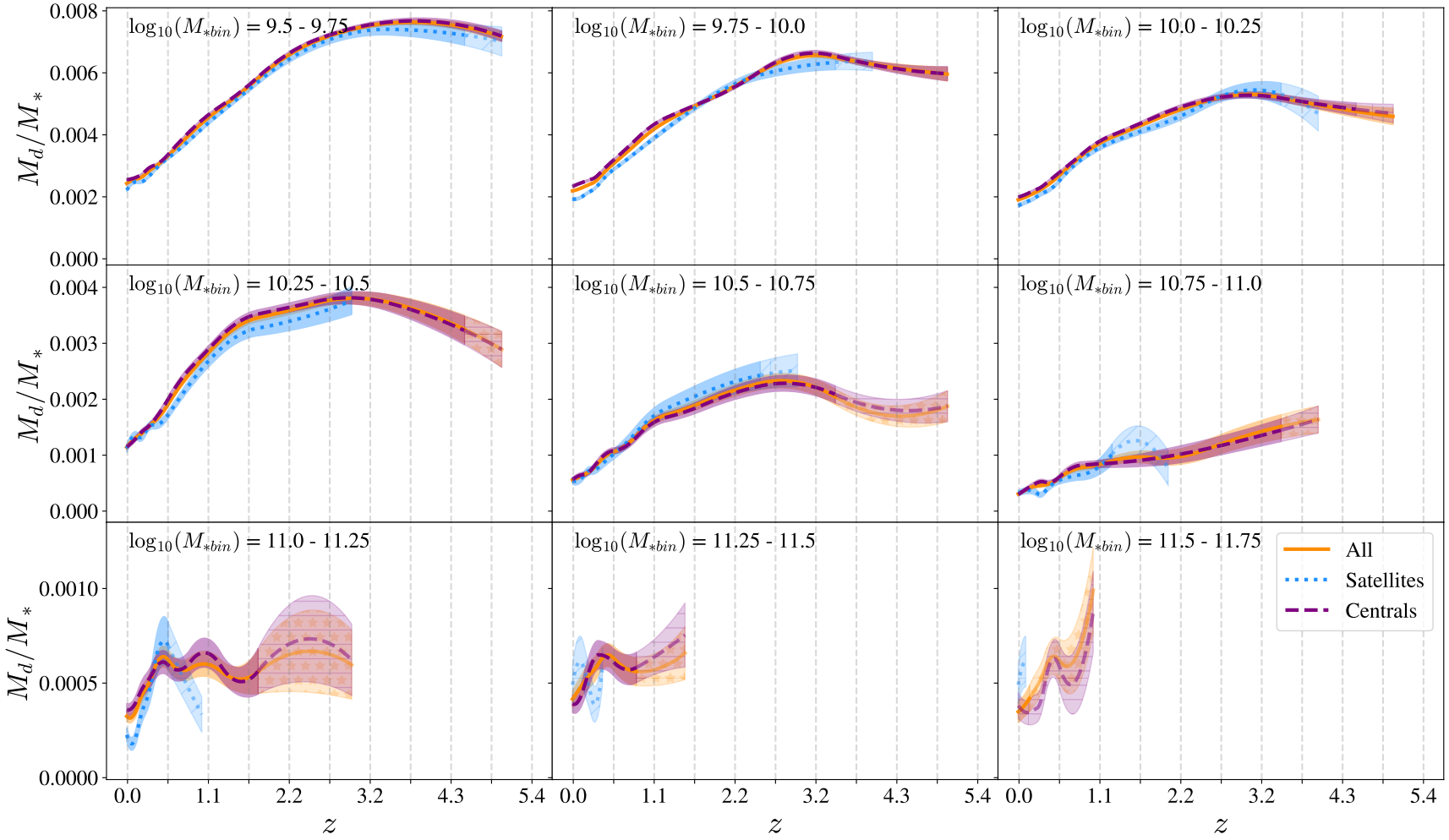

Figure 5.7: Dust-to-stellar-mass ratios for TNG100 galaxies plotted against redshift. *Orange solid line:* all galaxies. *Purple dashed line:* central galaxies. *Blue dotted line:* satellite galaxies. The paler, hatched areas represent data where the number of TNG100 sources in a given $(M_* - z)$ bin is between 10 and 50. Solid, non-hatched areas represent data where the number of sources in a given $(M_* - z)$ bin is at least 50. The lines are quadratic interpolations to discrete data points calculated at the redshifts of the TNG100 datafiles (Table 4.1). The orange line shown here is the same as in Figures 4.5 and 4.6.

It is interesting to note that in some stellar mass bins, satellite galaxies have slightly higher dust-to-stellar-mass ratios compared to the central galaxies (e.g. $\log(M_{*,\mathrm{bin}}) = 10.5 - 10.75$). In a given stellar mass bin, the average stellar mass of satellite galaxies is slightly lower than the average stellar mass of central galaxies. For galaxies with a similar dust mass, this therefore acts to marginally increase the dust-to-stellar-mass ratio for satellite galaxies.

Further, the similarity in the dust-to-stellar-mass ratio evolution of the two populations with redshift might seem strange when we consider the difference between the DMFs for satellite and central galaxies (Figure 5.6). However, in Figure 5.7, we are probing the highest stellar mass systems, and there is little difference between the high mass ends of the DMFs for the satellite and central galaxies.

Similar to Figure 5.6, the most striking and important feature of Figure 5.7 is that splitting the sample into satellite and central galaxies *does not solve the lack of dust mass evolution* over the redshift range $0 < z < 5$ in TNG100 galaxies as compared to observations.

Figure B.4 in Appendix B show the satellite and central DMFs for the bound galaxies. It is interesting to note that we still see a clear dearth in the dust content of satellite galaxies with the bound dataset. The comparative lack of dust in both the $2r_{0.5}$ and bound samples is consistent with material being driven out of a galaxy completely, through environmental effects that particularly impact satellite galaxies, such as stripping.

5.3.3 METAL ENRICHMENT PRESCRIPTIONS

As described in Torrey et al. (2019), in the IllustrisTNG simulations, metals are returned to the ISM by both supernovae explosions and asymptotic giant-branch (AGB) stars. In the TNG100 simulations (the data used in this study), individual stars are not resolved; star particles have masses of $m_* \sim 10^6 M_\odot$, and these star particles are assumed to encapsulate a Chabrier (2003) initial mass function IMF (Torrey et al., 2019). At each timestep in the simulation, stellar lifetime tables (Portinari et al., 1998) determine which stars leave the main sequence. Upon the death of stars, mass return and metal yield tables are used to determine the mass of metals returned to the ISM (Nomoto et al. 1997; Portinari et al. 1998; Kobayashi et al. 2006; Karakas 2010; Doherty et al. 2014; Fishlock et al. 2014). The returned

metal mass is spread over the nearest 64 gas cells.

In IllustrisTNG, galactic winds are probabilistically estimated, based on local SFRs (Torrey et al. 2019; see Pillepich et al. 2018b for details). They are assigned a lower metallicity than the ISM of a galaxy ($Z_{\rm wind} = 0.4Z_{\rm ISM}$), to encapsulate the dilution of metal-rich gas by metal-poor gas as the winds drive the metal-rich gas away from their origin point.

In their investigations into the IllustrisTNG mass-metallicity relation, Torrey et al. (2019) found that a significant proportion of the metals of simulated galaxies lie outside of the cool ISM, where we would expect dust to form. They also found that higher-mass IllustrisTNG galaxies are less efficient at retaining metals compared to lower-mass counterparts. We see this reflected in Figure 4.6, where the discrepancy between the evolution of dust shown in the observed and simulated galaxies is greater in the bins with higher stellar masses. Therefore, one possible explanation of the low dust masses in the model is that TNG100 ejects too many metals from the cool ISM.

5.3.4 INVESTIGATING DUST ESTIMATES USING TOTAL GAS MASS

In our post-processing method to estimate dust masses for IllustrisTNG galaxies, we considered only the neutral gas in the galaxy. The motivation behind this decision was two-fold; firstly, our long-wavelength observational data traces the coldest dust, residing in the cool neutral ISM. By estimating dust masses in IllustrisTNG using a nominally similar ISM phase, it ensures our comparison is reasonable. Secondly, very hot gas is likely to destroy dust grains, rather than preserve them. However, by considering only the dust associated with the neutral phases of the ISM, we may have omitted dust associated with HII regions (e.g. Anderson et al. 2012), although we note that these are not individually resolved in the IllustrisTNG simulations.

To explore the implications of only including the neutral gas in our IllustrisTNG dust mass estimates, in Figure 5.8, we show the mean ratio of neutral-gas-mass to total-gas-mass for IllustrisTNG galaxies as a function of redshift. We see that there is more neutral gas in the early universe compared to late times. This is not unexpected - in the past, there should be more of the fuel for star formation, and as time goes on, feedback processes can interact with the ISM, changing its

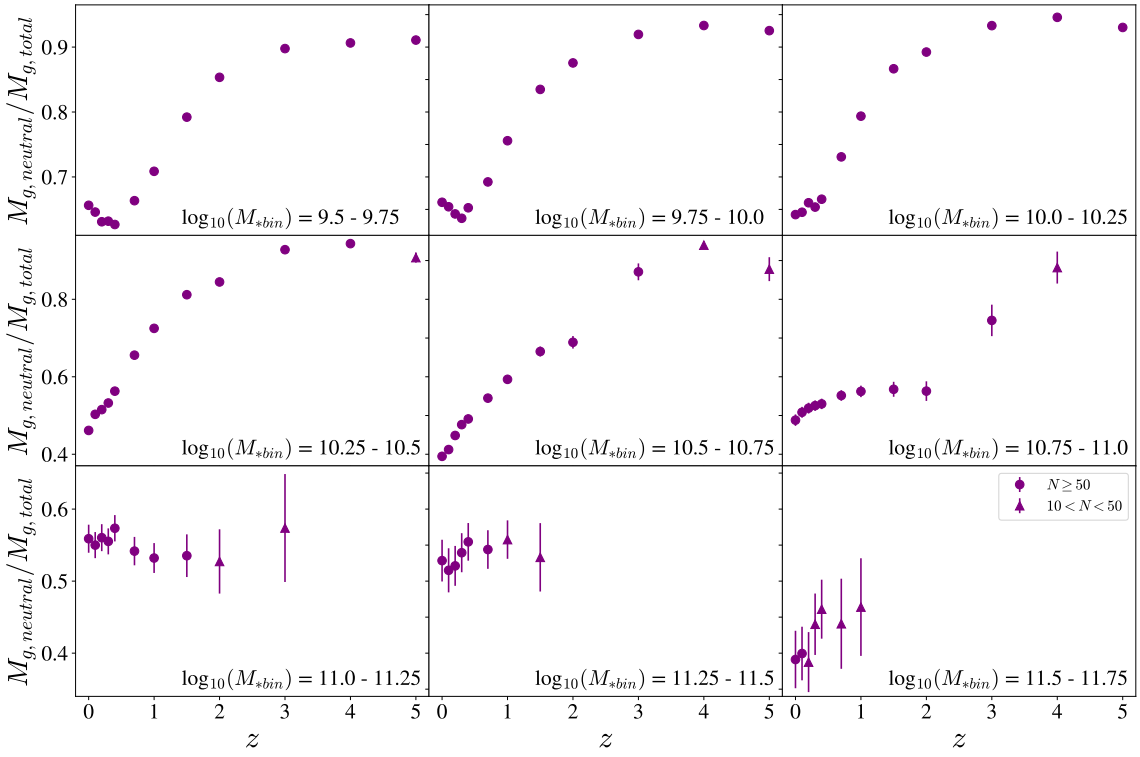

Figure 5.8: Neutral-to-total gas mass ratios for TNG100 galaxies. *Triangles:* number of TNG100 galaxies in $(M_* - z)$ bin, $N_{\rm TNG}$, between 10 and 50. *Circles:* at least 50 TNG100 sources in $(M_* - z)$ bin.

phase. We can see that from $z \sim 2$ to present day, there is a strong evolution in the fraction of total gas that is neutral, with neutral gas fraction decreasing at late times, comprising *at most* 65% of the gas in galaxies in the local universe.

Considering this local universe upper limit, had we used the total amount of gas in IllustrisTNG galaxies to trace dust, then the calculated dust masses would be some ∼50% higher compared to calculations involving solely the neutral gas. However, this in turn would have led us to calibrating our $z = 0$ observations to the simulated data with a correspondingly lower value of κ_{500}.

The evolution observed in the neutral-to-total gas mass fraction (Figure 5.8) is interesting to consider with regards to the lack of dust evolution observed in IllustrisTNG galaxies. In this discussion, we ignore any considerations of the metallicity of ionized gas. In Figure 4.3, the characteristic dust mass of the DMFs from Dunne et al. (2011) increases by around a factor of 5 over the redshift range $0 < z < 0.5$. For the two lowest stellar mass bins in Figure 5.8, the evolution in the

ratio of neutral-to-total gas mass is negative in the range $0 < z < 0.5$, with the fraction of neutral gas decreasing by up to ∼4%. This negative evolution translates to lower dust masses estimated with increasing redshift when using only the neutral gas. This also implies that had we used the total gas mass, for sources in the lowest stellar mass bins, we would have seen an additional ∼4% in dust mass (ignoring any metallicity factors) over the redshift range $0 < z < 0.5$ when compared to the dust masses estimated at $z = 0$ including the ionized gas. For higher stellar mass bins ($\log_{10}(M_*) > 10$), there is a positive evolution of no more than ∼10% in the ratio of neutral-to-total gas mass over the same redshift range, consequently increasing the calculated dust masses when using the neutral gas mass. This also means that the additional dust mass calculated using the ionized gas would decrease with redshift, when compared to dust masses estimated at $z = 0$ using the ionized gas. The positive evolution in additional dust mass from ionized gas gained for the two lowest stellar mass sources does not outweigh the negative evolution in additional dust from ionized gas for higher stellar mass bins. This, combined with the small scale of the evolutionary trends compared to the strong evolution seen in Dunne et al. (2011) means that the lack of evolution in the $z = 0 - 0.5$ TNG100 DMFs cannot be explained by the inclusion of dust from ionized gas.

In Figure 5.8, at high redshifts ($z > 2$), most (>80%) of the gas mass is in the form of neutral gas. Examination of Figure 5.3 shows that in this redshift regime, for stellar mass bins with $\log_{10}(M_*) > 10.25$, increasing the dust mass of TNG100 sources by an additional maximum 20% would not bring the simulated dust-to-stellar mass ratios in agreement with observations when considering a constant ϵ_d. The observed dust-to-stellar mass ratios are at least a factor of 2-3 larger at these higher redshifts. Around $z = 2 - 2.5$, an up to 20% increase in the dust-to-stellar mass ratio of TNG100 galaxies when considering an evolving $\epsilon_d(z)$ could bring the results from the simulations more in-line with observations. However, in this redshift regime, $\epsilon_d(z)$ from Vogelsberger et al. (2020b) requires up to 90% of the metals to be converted to dust, which is exceptionally efficient. For galaxies in stellar mass bins $\log_{10}(M_*) < 10.25$, increasing the dust-to-stellar mass ratio for TNG100 galaxies by up to 20% would help bring the observations and simulations into better agreement when considering a constant ϵ_d for $z > 2$. However, the agreement between the observations and simulations at these stellar masses is

reasonable without a small addition of extra dust from ionized gas.

At intermediate redshifts ($0.5 < z < 2$), considering $(M_* - z)$ bins with at least 50 sources, typically 20-40% of gas has been excluded by only including neutral gas, with more gas excluded at lower redshifts (Figure 5.8). Considering the lowest stellar mass bins in Figure 5.3, this additional gas mass could help reconcile the differences between the observations and simulations at intermediate redshifts when using a constant ϵ_d. However, for $\log_{10}(M_*) \geq 10.25$, whilst the additional gas mass might help reconcile small differences in the evolution, it cannot explain the lack of evolution completely. Although, small additions in the amount of dust at intermediate redshifts would make the dust-to-stellar mass ratio calculated assuming the composite $\epsilon_d(z)$ from Inoue (2003) and Vogelsberger et al. (2020b) agree better with the observations.

Overall, using the total gas mass to estimate dust masses for IllustrisTNG sources cannot explain the stark lack of dust evolution seen in IllustrisTNG galaxies as compared to observations.

5.3.5 GAS MASS EVOLUTION

Since we derive dust masses for IllustrisTNG galaxies using the neutral gas mass, the lack of evolution in the dust masses might stem from a lack of evolution in the mass of the cool ISM.

Several studies have compared the cold gas mass content of IllustrisTNG galaxies with observations of the local Universe. Stevens et al. (2019) found that the neutral gas fractions of TNG100 galaxies at $z = 0$ agree well with observations, although the most massive central galaxies ($M_* > 10^{10.7} M_\odot$) are somewhat too gas rich, and the gas content of satellite galaxies sharply dips at masses $M_* \sim 10^{10.5} M_\odot$. Similarly, Diemer et al. (2019) showed that the HI and H_2 mass fractions (M_{HI+H_2}/M_*) of TNG100 galaxies at $z = 0$ largely agree with observations, with some discrepancies in the H_2 mass fraction for the most massive galaxies ($M_* > 2 \times 10^{10} M_\odot$), which they found to be at least a factor of 4 lower compared to observations. However, Diemer et al. (2019) also found that the $z = 0$ TNG100 HI and H_2 mass functions largely agree with observations. This result is echoed in Davé et al. (2020), although they do note that the HI and H_2 mass functions of TNG100 are slightly too high at the high gas mass end.

It is worth noting that in the aforementioned studies (Davé et al. 2020; Diemer et al. 2019; Stevens et al. 2019), comparisons to observational data are not straight-forward - measuring the neutral gas content of galaxies accurately is notoriously difficult. For example, the CO-to-H_2 conversion factor, used to estimate the mass of molecular gas from observations of the CO line, is uncertain and varies from galaxy type to galaxy type (e.g. Bolatto et al. 2013; Béthermin et al. 2015; Genzel et al. 2015; Scoville et al. 2016; Popping et al. 2019), and galaxies can contain CO-dark molecular gas (Bolatto et al. 2013). When considering these observational limitations, these studies have shown that in the local Universe, the neutral gas content of IllustrisTNG galaxies agrees well with observations.

Accurately measuring the gas content of galaxies at high redshifts is even more difficult. For example, although 21cm radio emission is efficient at detecting HI gas in galaxies at $z = 0$, it is currently hard to detect 21cm radiation at $z \gtrsim 0.2$ (Catinella et al. 2010). Typically beyond the local Universe, gas mass estimates are limited to molecular gas estimates, usually derived using CO as a tracer (e.g. Solomon & Vanden Bout 2005; Coppin et al. 2009; Tacconi et al. 2010; Casey et al. 2011; Bothwell et al. 2013; Carilli & Walter 2013; Tacconi et al. 2013; Combes 2018).

Despite these difficulties, there have been several attempts to compare observations of the evolution in the cool gas in galaxies with predictions by models. Interestingly, Davé et al. 2020 found that the IllustrisTNG HI mass function shows a negative evolution with redshift, and that the H_2 mass function is mostly unevolving with redshift (out to $z < 2$), implying that the gas content of IllustrisTNG galaxies varies little with redshift. They found that the evolution in HI and H_2 was much weaker than predicted by two other simulations: EAGLE (Schaye et al., 2015) and SIMBA (Davé et al., 2019). Similar results were found by Diemer et al. (2019), who found a very weak evolution in the abundance of HI in TNG100 galaxies between $z = 1 - 4$, and a moderate evolution in the abundance of H_2 over the redshift range $z = 0 - 4$, with a peak increase of a factor of 2-3 at around $z = 2$. Recently, Popping et al. (2019) showed that the H_2 masses predicted by TNG100 for galaxies at $z > 1$ were a factor of 2-3 lower than observations (when comparing to observations using a standard CO-to-H_2 conversion factor).

All these studies suggest that TNG100 galaxies beyond $z \sim 1$ are lacking in neutral gas, and that there is little evolution in the gas content of the simulated

galaxies with redshift. Here, by using post-processing methods to compare the results of IllustrisTNG with the evolution of dust in galaxies over cosmic time, we get a similar result. The lack of evolution in the dust mass in TNG100 compared to observations could therefore be a reflection of the lack of evolution of the neutral gas content in the simulations that has been seen previously. In the next Section, we speculate as to what may be driving the different gas evolution, and therefore dust evolution, of the IllustrisTNG galaxies.

5.3.6 FEEDBACK MECHANISMS

Whether the lack of evolution in the dust predicted by TNG100 is entirely linked to the lack of evolution in the gas content (Section 5.3.5) or whether it is also linked to the ejection of metals, it is clearly linked to the model ejecting too much material outside a galaxy. It therefore seems likely to be caused by excessive galaxy outflows or feedback.

Kinetic feedback from AGN in the form of black hole driven winds becomes the dominant feedback process over other feedback methods (e.g. stellar feedback) above galactic stellar masses of $\log_{10}(M_*/M_\odot) \sim 10.5$, particularly at late times. Kinetic AGN feedback in IllustrisTNG manifests in a two-fold manner - firstly, it acts to expel star-forming gas from galaxies. Secondly, at these stellar masses, the AGN feedback increases the gas cooling time, preventing radiative cooling and future gas accretion (Terrazas et al. 2020; Zinger et al. 2020). As noted in Davé et al. 2020, at earlier epochs, it is the second of these processes, thermal feedback, which is most important, reducing the amount of cold gas in high-redshift galaxies. The fact that the disagreement between the model predictions and the observations is greatest at the high stellar masses is at least circumstantial evidence that the explanation of the discrepancy might be too vigorous AGN feedback.

5.3.6.1 INSIGHTS FROM ILLUSTRIS

Hayward et al. (2020) have recently investigated whether Illustris and IllustrisTNG can replicate the numbers of the rare luminous Sub-millimetre Galaxies (SMGs), using the star formation rates predicted by the simulations and post-processing estimates of the dust mass. They found that the predicted number counts of SMGs in Illustris was largely comparable with observations, but that

IllustrisTNG notably lacked SMGs. Further investigation led to the revelation that the identified IllustrisTNG SMGs are particularly dust-poor, with some SMGs ($\log(M_*/M_\odot) \approx 11$) at $z \sim 2$ in Illustris having a factor of three higher dust content than the IllustrisTNG counterparts. Hayward et al. 2020 ultimately traced this dichotomy to a lack of gas, as opposed to a lack of metals, in these IllustrisTNG galaxies as compared to Illustris, driven by changes to the feedback model between Illustris and IllustrisTNG - either stellar feedback outflows, and/or AGN feedback. The changes to the feedback model were made to make quenching more efficient and so bring IllustrisTNG galaxies more inline with the observed $z = 0$ colour bimodality (Weinberger et al. 2017, 2018; Nelson et al. 2018a). However, Hayward et al. (2020) point out that these changes seem to have quenched $z \sim 2 - 3$ galaxies too early, leading to a direct lack of massive dusty galaxies in IllustrisTNG as compared to observations.

Whilst the results of Hayward et al. (2020) are not directly comparable to this study due to their specific galactic population selection, the general idea that changes to feedback in IllustrisTNG have consequently quenched galaxies too soon or too frequently is inline with the results of this study. If the inability of IllustrisTNG plus our post-processing recipe to match the strong evolution in the dust masses is not caused by cosmic evolution in the properties of the dust grains themselves, it seems most likely that is caused by a lack of cool gas in the high-redshift TNG galaxies, possibly caused by over-enthusiastic AGN feedback.

5.3.7 COMPARISON WITH EAGLE SIMULATIONS

Recently, Baes et al. (2020) derived DMFs out to $z = 1$ for galaxies from the EAGLE simulation. Dust masses were estimated using modified blackbody fits to synthetic infrared luminosities at FIR wavelengths (160, 250, 350 and 500μm) generated using a post-processing 3D radiative transfer procedure (Baes et al. 2011; Camps & Baes 2015; Camps et al. 2016, 2018). Similarly to the results of this study, in the local universe ($z < 0.1$), Baes et al. (2020) found that they could reproduce the shape and normalization of the DMF fairly well, getting very good agreement with the DMFs found by Dunne et al. (2011) and Beeston et al. (2018) for dust masses $M_d < 2 \times 10^7 M_\odot$ but predicting too few galaxies at higher masses.

When examining the evolution of the EAGLE DMF up to $z = 1$, Baes

et al. (2020) found only a mild evolution in the characteristic mass of the modified schechter functions fitted to the DMFs, and very little evidence for density evolution. They did, however, find a fairly good agreement with the weak evolution in the cosmic dust mass density found by Driver et al. (2018) for this redshift range.

It is interesting that both the EAGLE and IllustrisTNG simulations show a similar lack of evolution in the DMF as compared to observations, despite two different methods to estimate dust masses in post-processing, which shows that cosmological hydrodynamical simulations are still limited in their ability to reproduce the strong evolution seen in the global properties of dust in galaxies.

5.4 CONCLUSIONS

In this work, we have compared the observed evolution of the dust in galaxies with the predictions from a model.

- We re-ran the DMF analysis for the simulated galaxies assuming the bound mass, to test if the lack of dust mass evolution observed in the full sample was biased due to the dust content in the selection of bound or 2rad from IllustrisTNG. We found no difference in the results.

- We split our simulated galaxies into two samples, satellites and centrals, and tested to see if the lack of dust mass evolution observed in the full sample was biased due to the dust content of one of these galaxy populations. We found that although satellite galaxies are typically more dust-poor than their central counterparts, both satellites and centrals show a similar lack of dust mass evolution as seen for the collective sample. Splitting the sample into satellite and central galaxies does not solve the lack of dust mass evolution over the redshift range $0 < z < 5$ in TNG100 galaxies as compared to observations.

- We find that it is very difficult to bring the observed and model dust mass evolution into agreement by changes in the assumptions underpinning our observations. The obvious ways of doing this are: i) a drastic evolution in the dust-mass opacity coefficient with redshift; ii) a non-constant dust-to-metals ratio; iii) an extreme increase in the mass-weighted dust temperature with

redshift; or iv) an extremely high value of $\beta \gg 2$. The third and fourth of these are inconsistent with observations. Therefore the only possible ways, from the observational side, of making the observations and theory consistent would be to assume that the properties of the dust itself change drastically with redshift. This would require the dust-mass opacity coefficient to be much higher at high redshifts than at low redshifts. There is currently no evidence to indicate that this should happen but we cannot rule this out. We also show that the results of our study are robust against changes to our assumption about the fraction of metals bound up in dust grains: varying ϵ_d with metallicity cannot account for the discrepancy we observe. An ϵ_d that varies with redshift, however, can reduce, though not eliminate, the discrepancy if i) it increases with redshift ii) is a strong function of stellar mass and iii) is extremely high (≥ 0.8 would be needed in the higher redshift bins).

- Although determining the root cause of the discrepancies between simulations and observations is difficult, we attribute the differences to one or more of the following in the models: i) excessive galactic winds driving metals out of the cool ISM where we expect dust to form; ii) a lack of evolution in the neutral gas content of galaxies with redshift; iii) kinetic feedback from AGN expelling gas from galaxies.

- We note that a lack of evolution in the dust content of galaxies as compared to observations is not limited to IllustrisTNG, but has also been in the $z < 1$ DMFs calculated for the EAGLE simulation, despite using a different post-processing technique for estimating dust masses.

Previous studies of neutral gas (HI+H_2) have concluded that the neutral gas content in IllustrisTNG does not show sufficient evolution with redshift. However, at high redshifts, H_2 and (more so) HI are hard to measure. It is much easier to measure the dust masses of high-redshift galaxies than their gas masses. By using IllustrisTNG with a simple post-processing technique we have been able to predict the dust masses of high-redshift galaxies. We find that the observed evolution is much stronger than the predicted evolution. If the discrepancy is not produced by cosmic evolution in the properties of interstellar dust itself, the most likely explanation seems to be that TNG does not predict strong enough evolution in the

neutral gas content of galaxies.

CHAPTER 6
DUST DENSITY: A FIRST LOOK

'Studying the behaviour of large whales has been likened to astronomy. The observer glimpses [her] subjects, often at long range; [she] cannot do experiments, and [she] must continually try to infer from data that are usually inadequate.'

HAL WHITEHEAD

6.1 INTRODUCTION AND MOTIVATION

Dust strongly influences our observational view of the Universe. In particular, it obscures star formation, the defining purpose of galaxies. Therefore, understanding how the dust content of galaxies evolves over time allows us to gain a deeper understanding of the full evolutionary picture of the Universe, especially its chemical evolution. One of the most fundamental dust parameters that can be measured is the comoving dust mass density, and its evolution with time.

Several studies in the past have estimated the comoving dust mass density, ρ_d, in both the local and distant Universe. Beeston et al. (2018) provided an estimate of the dust mass density in the local Universe using a sample of 15,750 optically selected galaxies from the overlapping areas of the GAMA and H-ATLAS surveys at $z < 0.1$. They estimated $\rho_d = (1.51 \pm 0.03) \times 10^5 M_\odot$ Mpc^{-3} where they

integrated their DMF down to a mass limit of $10^4 M_\odot$. Dunne et al. (2011) also constructed DMFs using mass estimates for 1867 galaxies observed with *Herschel* in the Science Demonstration Phase (SDP) of the *Herschel*-ATLAS survey, selected at 250μm. They were able to produce DMFs over a redshift range of 0-0.5, and discovered a strong evolution in the dust mass density out to $z = 0.5$. They estimated ρ_d = (0.95–2.7) $\times 10^5 M_\odot$ Mpc^{-3} (integrated to a lower limit of $5 \times 10^5 M_\odot$). Later, Driver et al. (2018) estimated the evolution of the dust mass density out to higher redshifts, using an optically selected sample of hundreds of thousands of galaxies. At $z = 0$, Driver et al. (2018) found dust mass densities consistent with Dunne et al. (2011). However, in contrast to Dunne et al. (2011), Driver et al. (2018) found little evolution in the dust mass density out to $z = 0.5$. Instead they found evidence for a peak in the dust mass density at $z \sim 1$, which may possibly coincide with the peak of star formation history in the Universe (Madau & Dickinson, 2014) (or at least a lag of no more than a few Gyr behind the peak of star formation). The dust mass density estimates from Driver et al. (2018) indicate that the overall dust content of the Universe is decreasing at later times, implying that dust is currently being destroyed faster than it forms, and that the Universe is becoming more transparent. A similar conclusion was reached by Dunne et al. (2011) but in much more recent history (5 billion years compared to $\sim$ 8 billion years). Most recently, Pozzi et al. (2020) used a far-IR (160μm) *Herschel* selected catalogue of $\sim$5300 galaxies in the COSMOS field to estimate the DMF for galaxies up to high redshifts ($z \sim 2.5$). The dust mass density was found by integrating the best-fitting DMFs for each redshift bin down to $M_d = 10^4 M_\odot$. Similarly to Driver et al. (2018), Pozzi et al. (2020) found a peak in the dust mass density at around $z \sim 1$, with an increase up to $z \sim 1$ from higher redshifts. However, Pozzi et al. (2020) also found a rapid increase in the dust mass density of galaxies at low redshifts in agreement with Dunne et al. (2011).

The studies of Dunne et al. (2011), Beeston et al. (2018) and Driver et al. (2018) used dust masses inferred using energy-balancing SED fitting routines - but for Beeston et al. (2018) and Driver et al. (2018), not all of the galaxies in their samples had sub-mm detections. In Pozzi et al. (2020), dust masses were estimated by fitting a single temperature modified black-body to sources with at least 3 far-IR ($\lambda_{\rm rest} > 50 \mu m$) photometric points. Here, we take a more direct approach, by using

dust masses estimated directly using the sub-mm emission from dust in galaxies at 850μm. Compared to the *Herschel* observations used in the four aforementioned studies, our longer wavelength data means that we are on the Rayleigh-Jeans tail for dust emission for longer i.e. up to higher redshifts. Although we do not have individual dust mass measurements for all the galaxies in our catalogue, we do have empirical stacked sub-mm fluxes, which can be used to determine average dust masses for binned galaxies, as shown in Chapter 4.

In this Chapter, we present a first-look estimate of the evolution of the dust mass density for galaxies in the COSMOS field using dust masses derived using our stacking methodology (Chapters 3 and 4).

6.2 DATASETS

In order to estimate dust mass densities, we need to integrate dust mass functions. Since we cannot measure individual dust masses for galaxies in the MAGPHYS-COSMOS2015 catalogue, we cannot measure dust mass functions directly. We therefore make use of the previously published stellar mass functions for the COSMOS field from Davidzon et al. (2017) (hereafter, D17), which we multiply by dust-to-stellar-mass ratios calculated using our previously described stacking technique to estimate dust mass functions. We emphasize here that the work presented in this Chapter requires finessing, but is a good test to examine the viability of such a study. In Chapter 7, we discuss ways to improve this work in the future.

6.2.1 DUST-TO-STELLAR-MASS RATIOS FROM MAGPHYS-COSMOS2015

In this preliminary investigation into estimating the evolution of the dust mass density with cosmic time, we calculate dust masses and dust-to-stellar-mass ratios following the same stacking methodology previously described in Chapter 3, and use the same dust mass equations as presented in Chapter 4 (Equations 4.1 and 4.2). We stack on our 850μm S2COSMOS map using the same MAGPHYS-COSMOS2015 sample as consistently used throughout this Thesis, initially presented in Chapter 2. We perform a Monte Carlo simulation to derive flux errors

(and therefore dust mass errors) as before, but we refrain from performing the sophisticated bootstrap analysis presented in Chapter 3 to determine the appropriate value to assume for the centre of the stellar mass bin as used in previous chapters, opting instead to assume simply the centre of the stellar mass bin as our representative stellar mass value. We showed in Chapter 3 that the bootstrapped stellar mass value and bin centre are only negligibly different in nearly all bins.

6.2.2 STELLAR MASS FUNCTIONS FROM DAVIDZON ET AL. 2017

The stellar mass functions of D17 are based on sources and physical parameters from the COSMOS2015 catalogue of Laigle et al. (2016) (hereafter, L16), but with some key differences at high redshifts. For $z \leq 2.5$, D17 use galaxy physical parameters of the original `LePhare` (Arnouts et al. 2002; Ilbert et al. 2006) SED fitting results from the COSMOS2015 catalogue of L16. Hereafter we explicitly denote redshifts from COSMOS2015 as $z_{\rm L16}$. However, for higher redshift sources, D17 recalculate the photometric redshift and stellar mass estimates. We denote these redshifts as $z_{\rm D17}$. D17 follow the same procedure as in L16, but with settings optimized for high-redshift galaxies (see D17 for full details)[31]. As in our MAGPHYS catalogue, D17 exclude from their catalogue galaxies with an X-ray counterpart from either XMM (Brusa et al., 2007) or *Chandra* (Marchesi et al., 2016), to ensure they do not consider galaxies that are likely to have their photo-z or M_* estimates contaminated by emission from AGN. By using the normalised median absolute deviation (Hoaglin et al., 1983), they estimate that their photo-z precision is $\sigma_z = 0.03(1+z)$. Overall, there is a good agreement between the photometric redshifts of sources as calculated between L16 and D17. For sources from the UltraDeep region of the COSMOS2015 catalogue that have IRAC 3.6μm < 25 mag, for 68 per cent of sources, $|z_{L16} - z_{D17}| < 0.05$ (Davidzon et al., 2017). Although, it is worth noting there is a subset of sources that are reassigned as high-redshift dusty galaxies in D17, moving from $z_{\rm L16} < 1$ to $z_{\rm D17} \sim 3$ (Leslie et al., 2020). At $z > 3$, the number of galaxies in D17 increases by 5-10 per cent as compared to galaxies

[31] Davidzon et al. (2017) enlarge the redshift range of the probability density functions used to estimate redshifts up to $z = 8$ as opposed to the original upper limit of $z = 6$ used in Laigle et al. (2016), and include additional high-z SED templates of extremely active galaxies with rising star formation histories and those which are highly attenuated. They also improve the method for removing stellar interlopers.

from L16 (Davidzon et al., 2017).

Galaxy stellar masses are again estimated using `LePhare` with redshift fixed. The SEDs use the stellar population synthesis model of Bruzual & Charlot (2003) and similarly to MAGPHYS, the stellar masses are determined as the median of the PDF marginalised over the other parameters. The simple stellar populations (SSP) of Bruzual & Charlot (2003) have a Chabrier (2003) initial mass function (IMF). Dust extinction follows that of Calzetti et al. (2000), with an additional 2175Å feature (Scoville et al., 2015). Galaxy stellar mass errors incorporate the additional uncertainty from the re-calculated photo-z.

In L16, a K_s-band selection was used to estimate a stellar mass completeness limit, which is valid up to $z \sim 4$. However, beyond this redshift, this observer-frame wavelength selection probes a part of the galaxy spectrum sensitive to recent star formation. Therefore, D17 argue an IRAC 3.6μm (hereafter [3.6]) selection is suitable for $z > 4$. For their $z > 2.5$ analysis, D17 consistently select galaxies at [3.6], even though for some of this redshift range, a K_s-band selection is equally valid. Even so, D17 still expect to miss very red galaxies i.e. galaxies with strong dust extinction at high redshifts. D17 determine a limit of [3.6]=25 magnitude as a completeness guide up to $z \sim 6$, calculated using sources in the UltraVISTA UltraDeep Stripes (McCracken et al., 2012). For their catalogue, the completeness mass limit is $M_{\rm lim}(z) = 6.3 \times 10^7 (1+z)^{2.7} M_\odot$. For L16, using a K_s-band selection, the catalogue reaches a 90 per cent completeness limit of $10^{10} M_\odot$ to $z = 4$.

6.3 CATALOGUE COMPARISON

Although the photometric redshifts of sources in our MAGPHYS-COSMOS2015 are taken from L16, the spectroscopic redshifts are extracted from an independent analysis of the available spectroscopic redshift data (see Chapter 2). Therefore, we cannot simply assume that the redshifts of sources in our MAGPHYS-COSMOS2015 catalogue are the same as those used in L16, and therefore D17, for sources with $z < 2.5$. Due to the re-calculation of galaxy physical parameters at $z > 2.5$ in D17, it would be unwise to assume the redshifts of sources in our MAGPHYS-COSMOS2015 galaxy catalogue are the same as those in D17 at high-redshift. We perform a comparison of the MAGPHYS-COSMOS2015 and D17

catalogues to examine whether the sources in our MAGPHYS-COSMOS2015 catalogue are reasonably representative of the sources used in calculating the stellar mass functions of D17. This allows us to determine if the average dust properties calculated using stacking methods can be combined with the D17 stellar mass functions to produce a first-look evolving dust mass density of galaxies in the COSMOS field.

6.3.1 CROSS-MATCHING BY POSITION

The D17 catalogue is made up of two catalogues - at $z_{D17} \leq 2.5$, D17 use redshifts and galaxy parameters from L16, but at higher redshifts, D17 use their modified values. As we wish to use our dust-to-stellar-mass ratios with D17 stellar mass functions, we first combine the L16 and D17 catalogues to create the final D17 catalogue. In the following catalogue comparison, we impose the same redshift upper limit as used in D17 of $z_{D17} < 6$. We remove 1313 sources with an X-ray counterpart as detected by XMM (Brusa et al., 2007) or *Chandra* (Marchesi et al., 2016). Following L16 and D17, we apply flux-cuts to sources. Explicitly, for sources with $z_{D17} \leq 2.5$ where we use data from the COSMOS2015 catalogue of L16, for sources in the UltraVISTA UltraDeep Stripes, we select sources with K_s-band < 24.7 magnitude. For those not in the UltraVISTA UltraDeep Stripes, we select sources with K_s-band < 24.0 magnitude. We use magnitudes calculated within 3″. For sources with $z_{D17} > 2.5$, we apply an IRAC 3.6μm cut of [3.6] < 25 mag. D17 note that this may not be appropriate for sources not in the UltraVISTA UltraDeep Stripes, but since they do not explicitly calculate a magnitude limit for sources not in the UltraDeep Stripes, we apply caution and use the UltraVISTA UltraDeep Stripe flux cut as an upper limit to all the data - though we note this means we may be incomplete for some high stellar mass bins when considering the D17 catalogue.

We then cross-match to the MAGPHYS-COSMOS2015 catalogue using position, finding 47,956 matches for sources at $z_{D17} \leq 2.5$, and 7,792 matches for sources at $z_{D17} > 2.5$, a total of 55,748 matches of a possible 63,658 matches. The separation of matched sources is on the order of 10^{-5}″, which we attribute to computational rounding errors in RA and Dec values. In Figure 6.1, we see that most of the non-matched sources in our MAGPHYS-COSMOS2015 catalogue are around bright stars. This is explained by more aggressive bright star masking in the D17

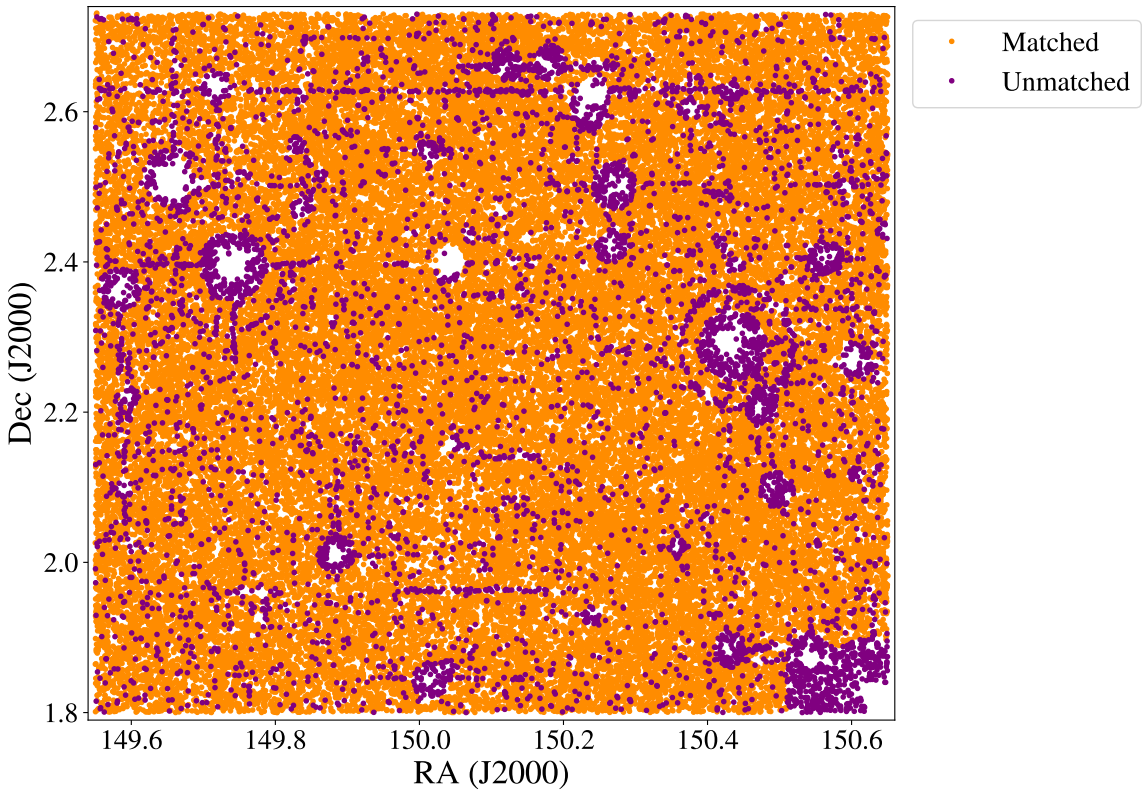

Figure 6.1: The distribution of matched and un-matched sources between the galaxy catalogue of D17 (Davidzon et al., 2017) and the MAGPHYS-COSMOS2015 catalogue used in this thesis. Most of the un-matched sources are around bright stars, where the catalogue from D17 employs more aggressive bright star masking.

catalogue compared to the MAGPHYS-COSMOS2015 catalogue.

As we will combine stacked dust-to-stellar mass ratios based on MAGPHYS-COSMOS2015 and the D17 stellar mass functions to create dust mass functions, we next compare the redshifts and stellar masses of matched sources in the D17 and MAGPHYS-COSMOS2015 catalogues.

6.3.2 COMPARING REDSHIFTS

In Figure 6.2, we compare the redshifts of sources in the two catalogues. Unsurprisingly, for $z_{D17} \leq 2.5$, there is a good agreement between the redshifts assigned to a given source. The agreement in assumed redshift value beyond $z \sim 1.3$ (Figure 6.2) is not surprising, since both catalogues use photometric redshifts from L16 at $z < 2.5$ and there are few spectroscopic redshifts above $z \sim 1.3$ (Chapter 2, Figure 2.3). For $z_{D17} \leq 2.5$ there is a large scatter in the redshifts in Figure 6.2

though the dispersion of the redshift differences is low (0.038).

At high redshifts, the agreement is not as good. Although the dispersion of the entire sample is still low: 0.064 for all sources and 0.034 for sources where the redshift difference is less than 0.2 (Figure 6.2), there is a clear offset in the distribution of redshifts at $z_{D17} > 2.5$ of ~ 0.05. This indicates that the MAGPHYS-COSMOS2015 galaxy parameters used in this Thesis may not be the same as those used in calculating the D17 stellar mass functions at $z_{D17} > 2.5$. If so, this would limit the accuracy of combining the D17 stellar mass functions (SMFs) and dust-to-stellar mass ratios from this work to derive DMFs.

6.3.3 COMPARING STELLAR MASSES

Next, we examine the stellar mass distribution of matched sources in L16 and D17 (Figure 6.3), where the stellar masses are the 50th-percentiles of the PDF distributions resulting from the two different SED fitting routines (MAGPHYS and `LePhare`). There is quite a large scatter, as indicated by a total dispersion of 0.215 dex for all sources, and a dispersion of 0.166 if we exclude sources with a stellar mass difference above 0.5 dex. If we consider sources with $z_{D17} < 2.5$, the stellar mass dispersion is slightly smaller, at 0.197 for all sources and 0.16 for sources with a stellar mass difference of less than 0.5 dex. Fitting the data with a fixed gradient of zero, we see a tendency for sources from D17 to have lower stellar masses (`LePhare` compared to MAGPHYS). The offset of the fixed-gradient line is $\sim$ 0.03 dex for all sources. The 90th-percentile of the stellar mass differences is $\sim$0.3 dex, whether we consider the total sample, or the $z_{D17} < 2.5$ subset (Figure 6.3).

Although at first glance the scatter in the stellar mass estimates from the two SED fitting routines may seem alarming, Hunt et al. (2019) performed a comprehensive comparison of three SED fitting routines on 61 nearby galaxies, and found a maximum rms deviation of 0.19 dex, compared to the 'true' stellar masses estimated using a luminosity-dependent mass-to-light ratio method. Therefore, the scatter in stellar mass on a source-by-source basis in Figure 6.3 is not unreasonable, particularly since different assumed redshifts will compound this.

In this Thesis, we have calculated average dust and dust-to-stellar mass

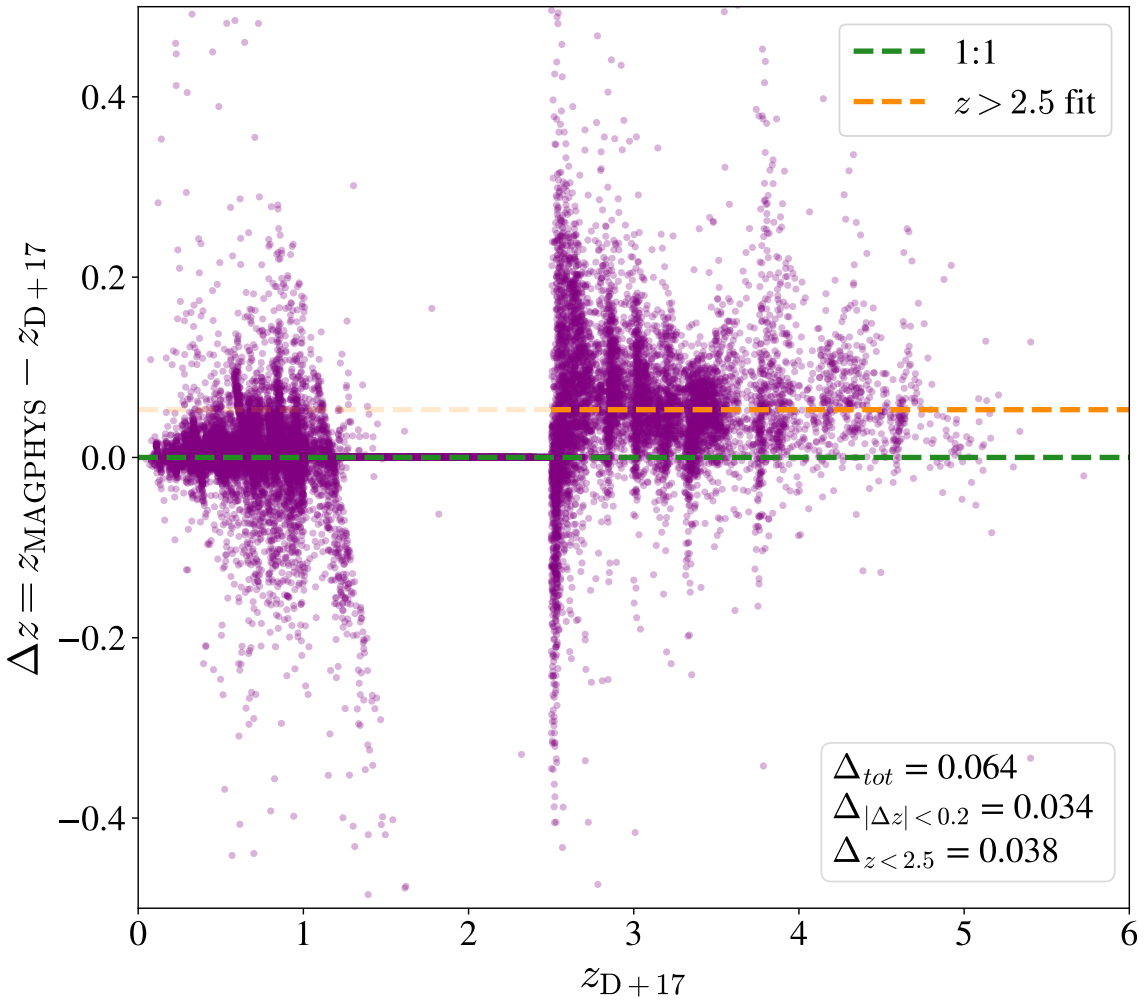

Figure 6.2: A comparison of the redshifts for sources matched between the COSMOS catalogue of D17 (Davidzon et al., 2017) and the MAGPHYS-COSMOS2015 catalogue (based on L16). *Green dashed line*: 1:1 line. *Orange dashed line*: best fit to the distribution for sources with $z_{D17} > 2.5$, with a fixed gradient of zero. Dispersion values, Δ for various data subsets are labelled. Δ_{tot} is the dispersion of the whole sample, $\Delta_{|\Delta z|<0.2}$ is the dispersion for sources with $|\Delta z| < 0.2$ and $\Delta_{z<2.5}$ is the dispersion of sources with $z_{D17} < 2.5$.

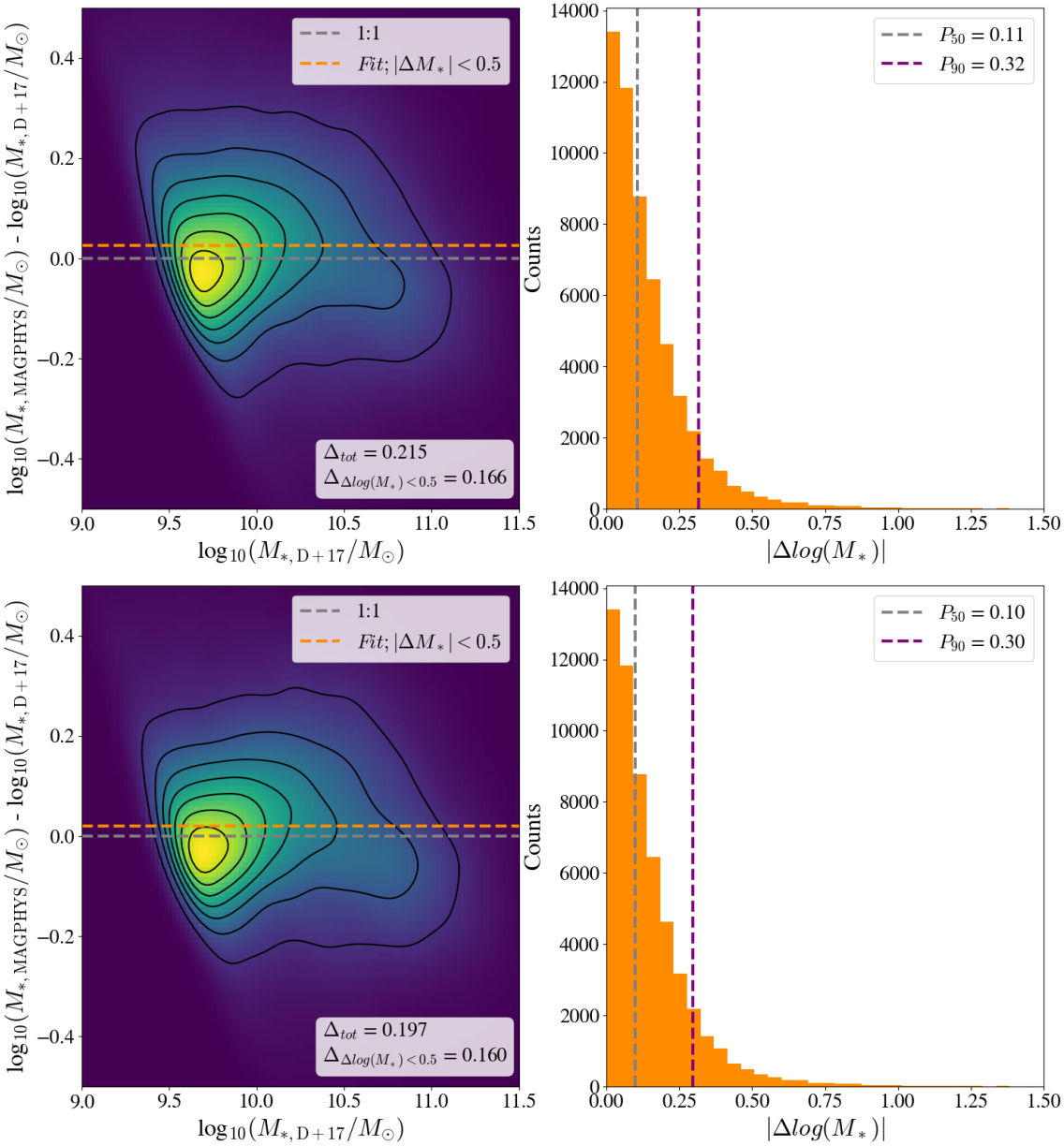

Figure 6.3: Comparing the 50th-percentile stellar masses for sources matched between the MAGPHYS-COSMOS2015 and Davidzon et al. (2017) catalogues. *Left:* density plots showing the distribution of sources. The *grey dashed horizontal line* is the 1:1 line. The *orange dashed horizontal line* is a fit to the distribution with a fixed gradient of zero for sources where the difference between the stellar masses is 0.5 dex. *Right:* histograms of the absolute value of the differences in the galactic stellar masses reported for the two catalogues for a given source, with vertical lines illustrating the 50th-percentile (*grey dashed*) and 90th-percentile (*purple dashed*) values of the distributions. *Top:* all sources. *Bottom:* sources with $z_{D17} < 2.5$.

properties such that small absolute differences in redshift and stellar mass estimates on a source-by-source basis are not concerning *if the overall distribution of galaxies in ($M_* - z$) space are reasonably similar* between the D17 source catalogue used to estimate COSMOS SMFs and our MAGPHYS-COSMOS2015 catalogue used to determine average dust masses. If this is a valid assumption, we could combine the D17 catalogue and our stacking data from the MAGPHYS-COSMOS2015 catalogue, though caution that is likely to be an increasingly unreliable assumption for $z > 2.5$ as per the reasons discussed above.

6.3.4 DISTRIBUTION IN STELLAR MASS - REDSHIFT SPACE

In our stacking routine, we bin sources into stellar mass bins with a width of 0.25 dex. Therefore, since the total dispersion of matched sources is $\sim$0.2 dex, it is likely we may not be considering exactly the same galaxies in a given stellar mass bin when calculating average dust properties as were considered by Davidzon et al. (2017) when calculating the COSMOS SMFs. However, since our stacking method gives only average dust properties for sources in a given ($M_* - z$) bin, we now examine if the distribution of sources in ($M_* - z$) space is reasonably similar for matched sources.

In Figure 6.4, we bin matched sources in the two catalogues into the same redshift bins as used in D17 when computing the COSMOS stellar mass functions at different redshifts, and the same stellar mass bins as used in our original MAGPHYS-COSMOS2015 stacking analysis. We show the percentage difference in the number counts between matched sources in the two catalogues, where we explicitly define percentage difference as:

$$\text{Percentage difference} = \frac{N_{\text{D17}} - N_{\text{MAG}}}{N_{\text{MAG}}} \times 100 \tag{6.1}$$

where N_{D17} is the number counts for matched sources in a given bin using redshift and stellar mass estimates from the D17 catalogue, and N_{MAG} is the number counts for matched sources in a given bin using redshift and stellar mass estimates from the MAGPHYS-COSMOS2015 catalogue.

At high stellar masses ($\log_{10}(M_*/M_\odot)$>11.25), the percentage difference in counts in a given bin is often large. This is unsurprising, since this is the regime

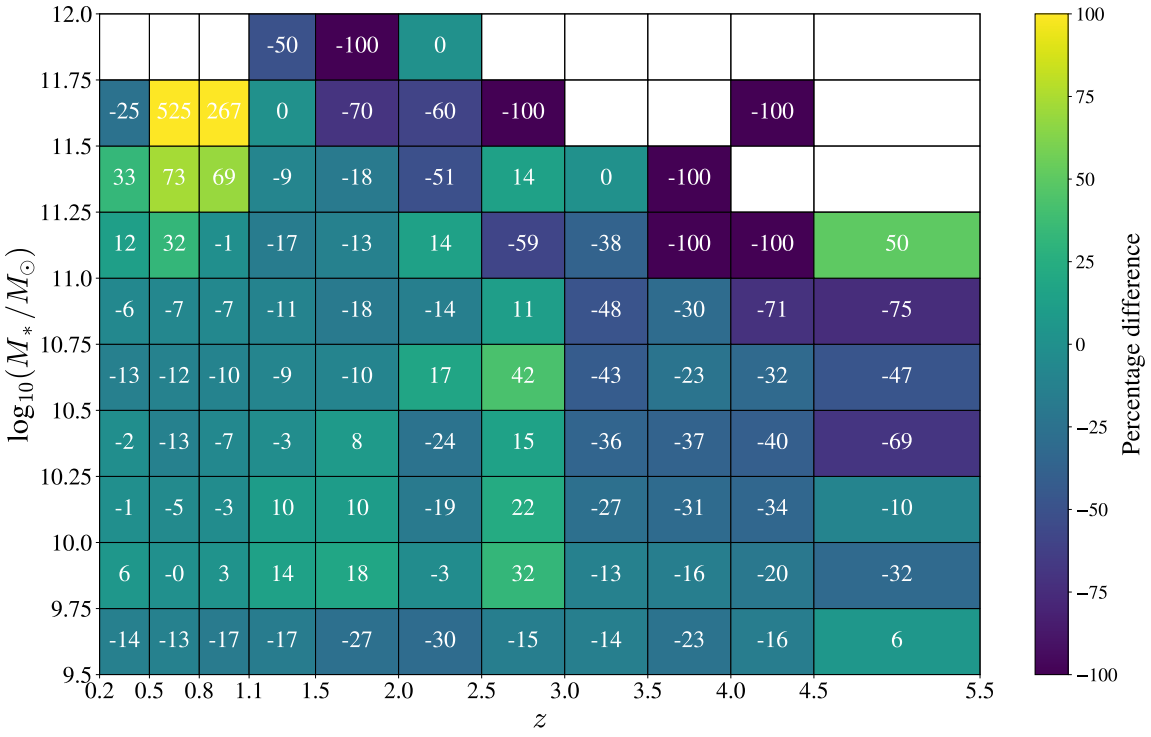

Figure 6.4: The percentage difference in $(M_* - z)$ bin number counts for the D17 catalogue and MAGPHYS-COSMOS2015 catalogue for matched sources. Note that the colour scale is fixed to highlight more subtle differences at low percentage difference values. The numbers in the boxes label the percentage difference for that given bin.

of low number counts (see Chapter 3, Table 3.1), particularly at high redshifts, and so small differences in absolute number counts manifest as large percentage differences. However, it is worth noting that the yellow bins in Figure 6.4 have a large percentage difference because the number counts in this bin differ significantly - from 4 in the MAGPHYS-COSMOS2015 catalogue to 25 in D17. Below this stellar mass limit, for $z < 2.5$, the number counts of sources in a given $(M_* - z)$ bin are reasonably similar between the two catalogues. The percentage difference is larger for the lowest stellar mass bin, but excluding these bins, the magnitude of the percentage difference is typically $\sim$10 per cent. Despite redshift and (more so) stellar mass estimates varying on a source by source basis, for low-to-intermediate redshifts, and for most of the stellar mass range explored in this work, we show here then that the galaxies of the MAGPHYS-COSMOS2015 catalogue are a reasonable representation of the D17 catalogue used to calculate the COSMOS SMFs. For

sources with $z > 2.5$, there are significant differences in the number counts for a given $(M_* - z)$ bin, reflecting the additional optimizations D17 made to their SED fitting routine. In this redshift range, the physical parameters we use in this Thesis for galaxies in our MAGPHYS-COSMOS2015 catalogue are therefore not statistically representative of those used to determine the stellar mass functions for COSMOS galaxies at $z > 2.5$. Therefore, in this Chapter, in order to carry out our preliminary investigation into the evolution of dust mass density with time, we limit ourselves to considering only sources with $z < 2.5$. Additionally we exercise caution when considering parameters calculated using high ($\log_{10}(M_*/M_\odot) > 11.25$) and low ($\log_{10}(M_*/M_\odot) < 9.75$) mass galaxies.

6.4 RECALCULATED DUST-TO-STELLAR-MASS RATIOS

6.4.1 DERIVING SUB-MILLIMETRE FLUXES - RESTACKING

We bin sources in our MAGPHYS-COSMOS2015 catalogue into the same redshift bins as used in D17 to calculate COSMOS SMFs. We use the same S2COSMOS 850μm data and error maps (Simpson et al., 2019), and the same IVW stacking method from Chapter 2, calculating flux errors using a Monte Carlo simulation on the location of sources within the map. Figure 6.5 shows the resulting average fluxes against redshift for sources in a given stellar mass bin. Similarly to Figure 3.4, we see that the average 850μm flux emission from dust increases with redshift out to $z = 2.5$. This trend may not hold for the lowest stellar mass bin ($\log_{10}(M_{*,bin}) = 9.5 - 9.75$), and is not so obvious in the second lowest stellar mass bin ($\log_{10}(M_{*,bin}) = 9.75 - 10.0$). However, these low mass bins suffer with lower number counts, giving noisy flux measurements, so it is not surprising that it is difficult to discern if the trend of increasing 850μm emission from dust with redshift is also applicable to these galaxies.

In the highest stellar mass bin ($\log_{10}(M_{*,bin}) = 11.5 - 11.75$), there is no data point at $z \sim 0.95$. This is because the number of sources in this $(M_* - z)$ bin falls below our self-imposed lower limit of 10. In general, for most stacks, the SNR of measured fluxes is good (73 per cent of measured fluxes have SNR$\geq$3), but for the two lowest redshift stacks in the highest stellar mass bin, a negative flux is measured, indicating non-detections. As before, upper limits on dust masses are

calculated based on the 3σ flux errors, determined from Monte Carlo simulations. Finally, we note that the magnitude of the measured 850μm flux in this reanalysis is similar to that of our previous stacking analysis, a good sanity check.

6.4.2 DUST-TO-STELLAR MASS RATIOS

Using these re-stacked fluxes, we now calculate average dust-to-stellar-mass ratios for MAGPHYS-COSMOS2015 galaxies up to $z = 2.5$. We follow the same method described in Chapter 4, using Equation 4.1 to calculate dust masses. We assume the same value of the dust mass absorption coefficient, $\kappa_{500} = 0.14$ m^2 kg^{-1}. However, for a given stellar mass bin, we simply assume the middle of the stellar mass bin as our representative stellar mass value, rather than performing a full bootstrap analysis as previously done in Chapter 3.

Figure 6.6 shows the recalculated dust-to-stellar-mass ratios for MAGPHYS-COSMOS2015 galaxies re-binned to the same redshift bins as used to calculate COSMOS SMFs in Davidzon et al. (2017). For all bins except for the highest stellar mass bin, there is a strong increase in the dust-to-stellar-mass ratio with redshift, similar to the results shown in Chapter 4. It is difficult to say whether this trend holds for the highest stellar mass bin, since at low redshifts, dust-to-stellar-mass ratios could only be estimated using 3σ flux upper limits. Although, from these upper limits, the indication is that the trend holds for the highest stellar mass bin. Additionally, in the lowest stellar mass bin, there is a decrease in the dust-to-stellar-mass ratio at $z \sim 2.2$. However, the SNR of this point is low.

In the next Section, we use these re-calculated dust-to-stellar-mass ratios and the SMFs of Davidzon et al. (2017) to derive estimates of the COSMOS DMF out to $z \sim 2.5$, which we then use to estimate the evolution of the dust mass density of the Universe.

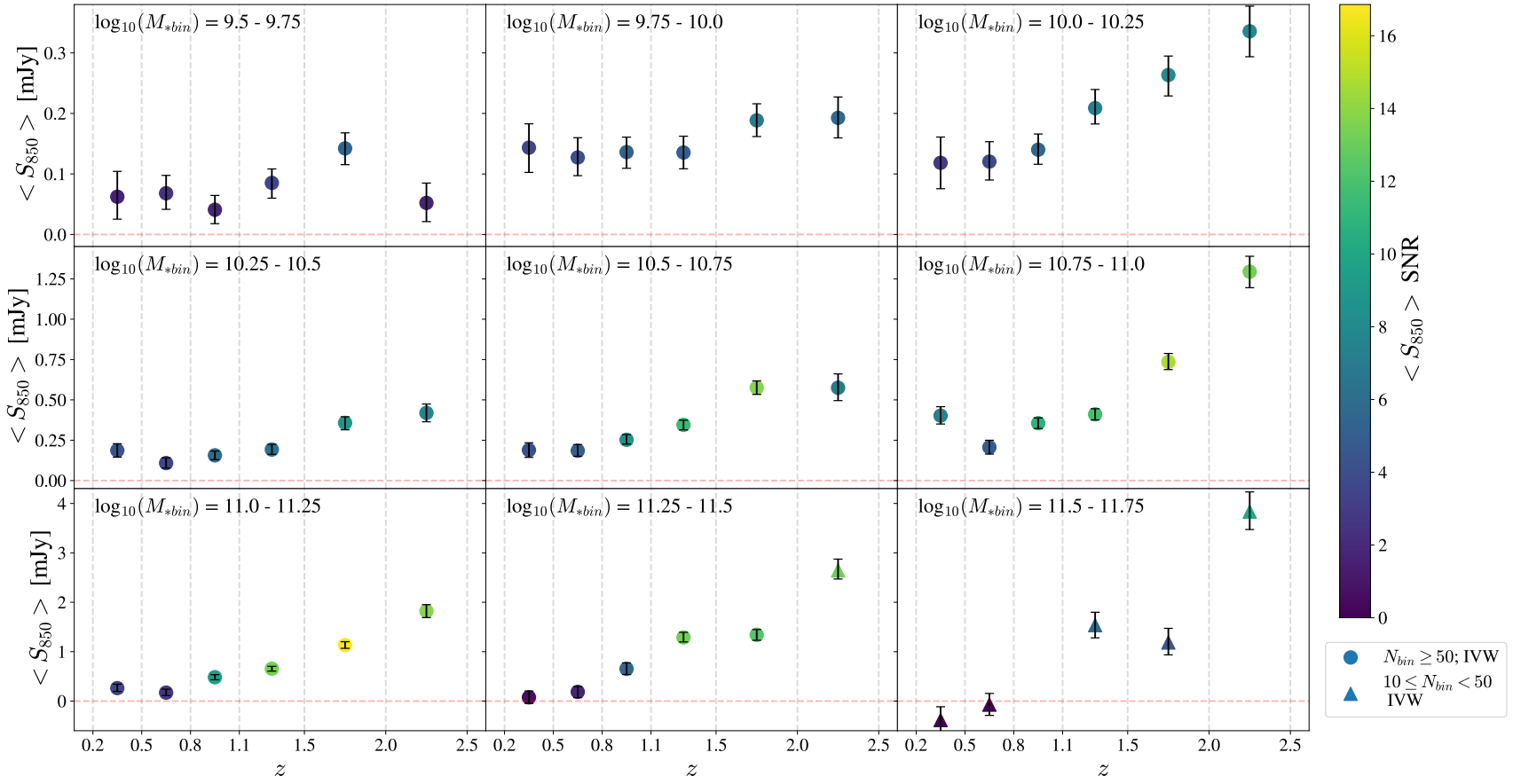

Figure 6.5: The resulting stacked 850μm fluxes using the IVW method and redshift bins corresponding to those used to calculate the COSMOS SMFs in Davidzon et al. (2017). Filled circles are the IVW fluxes for stacks containing at least 50 sources. Filled triangles are the IVW fluxes for stacks containing at least 10 sources, but less than 50 sources. The colour of the points represents the SNR of the stacked flux for that given bin. The stellar mass bin that each subplot represents is labelled in the top left of the respective subplot. A horizontal red dashed line denotes $\langle S_{850} \rangle$=0. Vertical grey dashed lines mark borders of redshift bins.

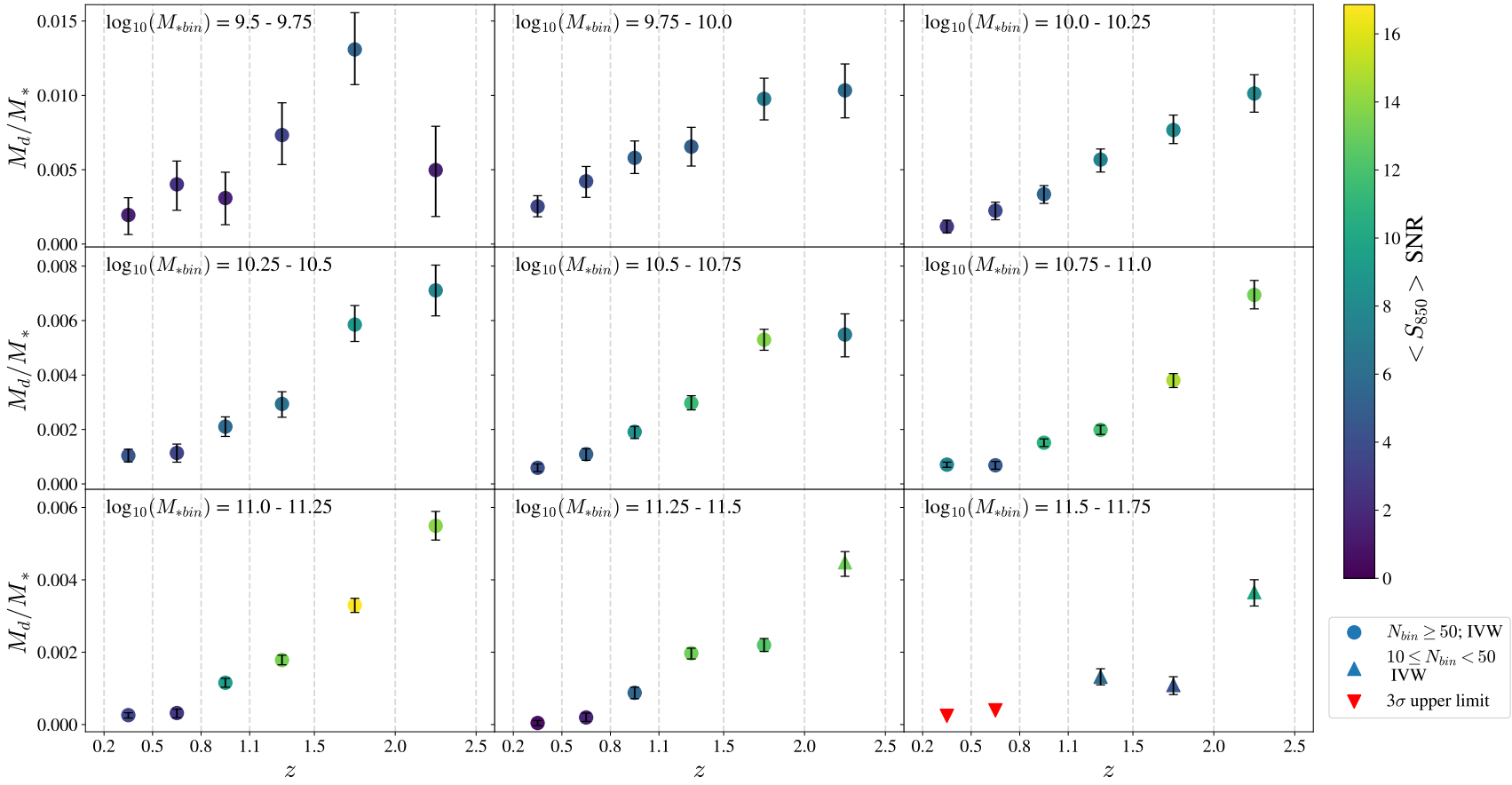

Figure 6.6: Dust-to-stellar-mass ratios obtained from the restacked S2COSMOS fluxes. *Red triangles:* dust-to-stellar-mass ratios estimated using 3σ upper limits. *Circles:* dust-to-stellar-mass ratios where there are at least 50 MAGPHYS-COSMOS2015 sources in the $(M_* - z)$ bin, and the colour of the point represents the SNR of the flux used to estimate dust masses. *Triangles:* similar, but the number of MAGPHYS-COSMOS2015 sources in the $(M_* - z)$ bin is between 10 and 50. The stellar mass bin that each subplot represents is labelled in the top left of the respective subplot. Vertical grey dashed lines mark borders of redshift bins.

6.5 DUST MASS DENSITY

6.5.1 DUST MASS FUNCTIONS

To estimate DMFs for galaxies in the COSMOS field using our stacked dust masses for a given redshift bin, we use the SMFs from D17. For our redshift range, D17 find the COSMOS SMFs are best described by a double Schechter function:

$$\phi \ \mathrm{d}\log M = \ln(10) e^{-10^{\log M - \log M^*}} \left[\phi_1^* (10^{\log M - \log M^*})^{\alpha_1 + 1} + \phi_2^* (10^{\log M - \log M^*})^{\alpha_2 + 1} \right] \mathrm{d}\log M \quad (6.2)$$

where ϕ is the number volume density at a given mass M, M^* is the characteristic mass, ϕ^* is the number volume density at the characteristic mass, α is the power law index of the low mass slope, and the subscripts [1] and [2] denote the combined Schechter functions (see Chapter 1 for additional details). Equation 6.2 is expressed in $\log M$ space for convenience (e.g. Weigel et al. 2016). We use Schechter parameters for the 'total sample' from D17 (their Table 1). Figure 6.7 shows the D17 SMFs for $z = 0.2 - 2.5$ scaled to the cosmology used in this Thesis.

To estimate COSMOS DMFs using our stacked dust masses, for each redshift, we extract the galaxy number volume density, ϕ, from the cosmology-scaled SMFs from D17 at the centre of each of the stellar mass bins used in our stacking analysis. Corresponding dust masses are evaluated by simply multiplying the observed dust-to-stellar-mass ratios from stacking by the stellar mass bin centres. This crude methodology allows us to estimate DMFs for galaxies in the COSMOS field (Figure 6.7). As before, errors on dust masses are derived from flux errors. Errors on the number density of galaxies are simply estimates of the Cosmic Variance for a given $(M_* - z)$ bin, calculated using the 'Cosmic Variance Cookbook' of Moster et al. (2011). Explicitly, we use values taken from their Tables 1, 3 and 4, their Equations 10 and 13, and the recipe presented in their Section 3.4. This allows us to evaluate the Cosmic Variance (CV) as a varying function of redshift and stellar mass. The calculated CV is a stronger function of stellar mass than redshift, although it does vary a little with redshift. Depending on the exact $(M_* - z)$ bin, the CV varies from around 6-15 per cent. We note that in estimating the COSMOS

DMFs, we do not use dust masses calculated using 3σ upper flux limits.

As shown in Figure 6.7, we see a strong evolution in the estimated DMFs for galaxies in the COSMOS field at the higher dust mass regime ($\log_{10}(M_d) > 8.0$). This agrees with the statement from Driver et al. (2018) that galaxies were dustier in the past (for the redshift regime explored in this study). An interesting trend we see is that with increasing redshift, the number density of galaxies decreases strongly. Particularly at the highest redshifts, we see the number density of very dusty galaxies decreases significantly. However, we have not corrected for incompleteness. Particularly since our original source catalogue is *i*-band selected, at higher redshifts, we might expect fainter and/or dustier (and therefore more obscured or redder sources) to be missing from our sample catalogue. Therefore we do not focus on this apparent trend. Unfortunately, the dust masses probed in this study do not extend low enough for us to comment on the evolution of the faint end slope.

Arguably, most of the estimated DMFs approximate to a Schechter function, but this is not true for the lowest redshift DMF (Figure 6.7), which has a curious 'banana' shape with the high-mass end of the DMF curving to seemingly disproportionately low dust masses. Examination of Figure 6.6 shows that for the lowest redshift bin of stellar mass bins $\log_{10}(M_{*,bin}) = 11.0 - 11.25$ and $\log_{10}(M_{*,bin}) = 11.25 - 11.5$, the dust-to-stellar-mass ratio is very small, particularly for the latter. Additionally, the SNR of fluxes measured for these two bins are low. Further, in the highest stellar mass bin, no 850μm dust emission is detected in the lowest redshift bin. Combined, these indicate that the 'banana' shape is either caused by: i) a severe lack of dust in massive galaxies at low redshifts, or ii) a lack of massive galaxies at low redshifts in this study. Since our study contains both star-forming and passive galaxies, it could be that in the nearby Universe, the average dust masses of massive galaxies are biased low by including passive galaxies in our sample. Additionally, the second option is not unreasonable, since we do not correct for incompleteness. Using the 'Cosmic Variance Cookbook' of Moster et al. (2011), in this ($M_* - z$) regime, the CV is at least 13 per cent. Due to the small size of the COSMOS field on the sky, there could easily be a deficit of such massive nearby galaxies in our statistical study, lowering our estimated dust-to-stellar-mass ratios for these ($M_* - z$) bins and causing the unusual banana

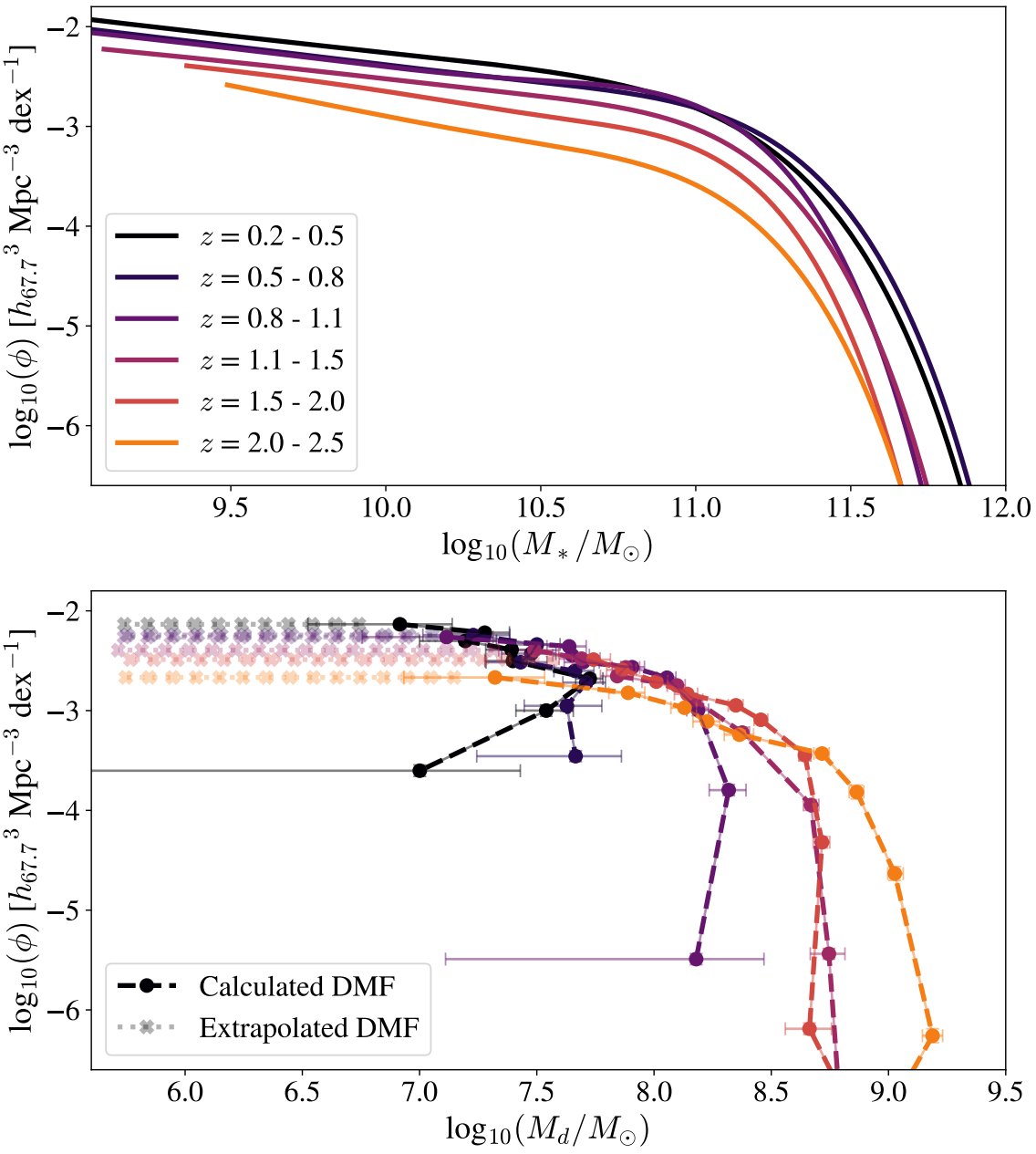

Figure 6.7: *Upper:* Stellar mass functions (SMFs) from D17 (scaled to our assumed cosmology). The lower stellar mass limit is restricted to the stellar mass of their lowest data bin for a given redshift. We extend the SMFs to higher stellar masses than in their data bins for clarity. *Lower:* Dust mass functions (DMFs) calculated using the SMFs from D17 and our stacked dust-to-stellar-mass ratios (Figure 6.6). Note that number density errors for the DMFs are cosmic variance, estimated using the Cosmic Variance Cookbook of Moster et al. (2011). Following the shape of the low-mass end of the DMFs from Dunne et al. (2011) (see Figure 4.3), we artificially extend our DMFs to lower dust masses as a test for our calculated dust mass density *(crosses)*. The lower dust mass limit is the same as Dunne et al. (2011) but scaled to our assumed κ_{500}. The colours of the SMFs and DMFs are designated to indicate the same redshift ranges.

shape in the DMF.

We now use these estimated DMFs to examine the evolution of the dust mass density with cosmic time.

6.5.2 DUST MASS DENSITY

As a first-look estimate of the dust mass density, ρ_d, instead of fitting Schechter functions to the crude DMFs, we integrate under the DMFs using the following approximation:

$$\rho_{d,z} = \sum_{M_{*,bin}} \rho_{d,M_*bin,z} = \sum_{M_{*bin}} \phi_{M*bin,z}\, M_{d,bin,z}\, \sigma_{M*bin,z} \tag{6.3}$$

where $\rho_{d,z}$ is the dust mass density at a given redshift. In Equation 6.3, to get the dust mass density at a given redshift, we sum over the dust mass density calculated for each stellar mass bin at that redshift, $\rho_{d,M_*bin,z}$. In each stellar mass bin, the dust mass density ($\rho_{d,M_*bin,z}$) is calculated by multiplying together the number density of galaxies, $\phi_{M*bin,z}$ [per Mpc^3 per dex], the dust mass evaluated at the centre of the given stellar mass bin, $M_{d,bin,z}$ [$M_\odot$], and the width of the stellar mass bin, $\sigma_{M*bin,z}$ [dex]. Errors on the dust mass density are calculated following error propagation of the errors on the number density of galaxies and dust masses.

Figure 6.8 shows our estimated dust mass density, along with several values from the literature scaled to our assumed cosmology and κ_{500}. In our study, we see a smooth but substantial decline in the dust mass density of the Universe from $z \sim 1$ to $z \sim 0.35$, with ρ_d decreasing by a factor of 2. The peak of the dust mass density is broad, with a relatively constant value between $z = 1 - 1.8$. There is also an increase in the dust mass density at higher redshifts to the start of the peak at $z \sim 1.8$. This peak in the dust mass density is consistent with the peak of the cosmic SFR density, around $z \sim 2$ (Madau & Dickinson, 2014).

6.5.3 DISCUSSION AND CAVEATS

In Figure 6.8, we compare our first-look dust mass density estimates to examples from the literature (see Section 6.1 for details about the studies we compare to). One of the most notable differences between our dust mass densities and those

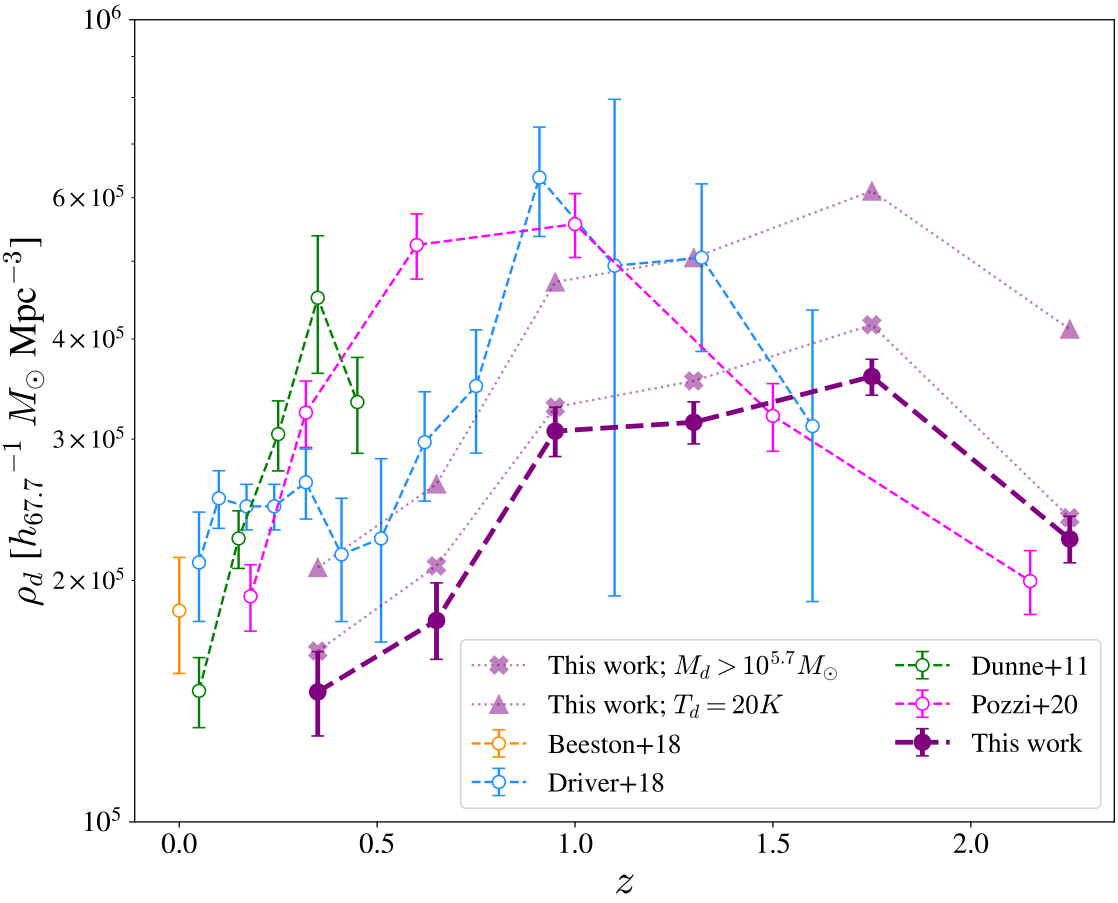

Figure 6.8: The evolution of the dust mass density with redshift, estimated by approximately integrating under the DMFs shown in Figure 6.7. *Purple filled circles:* dust mass density estimated used our calculated DMFs with an assumed mass-weighted dust temperature of T_d=25 K. Errors are a combination of stacked flux errors and cosmic variance estimates. *Purple crosses:* A test dust mass density estimated using our DMFs extrapolated to a lower dust limit of $M_d = 10^{5.7} M_\odot$ with an assumed mass-weighted dust temperature of T_d=25 K. *Purple triangles:* A test dust mass density estimated using dust masses calculated for an assumed mass-weighted dust temperature of T_d=20 K and only the calculated DMFs (not the extrapolated data). For clarity on the test dust mass densities, we do not show errors. We compare to several literature estimates of the dust mass density which have all been scaled to our assumed cosmology and κ_{500}; *(green circles)* Dunne et al. (2011), with error shown as calculation error (these errors are less than cosmic variance); *(orange circle)* Beeston et al. (2018), with error showing the estimated cosmic variance since statistical error is ∼2 per cent; *(blue circles)* Driver et al. (2018), with error showing maximal error from including objects without far-IR measurements (these errors are greater than errors from cosmic variance); *(magenta circles)* Pozzi et al. (2020), with statistical errors shown. Note that all literature values are taken from the review paper of Péroux & Howk (2020) (their Figure 12, supplementary Table 6).

of the literature is that our dust mass densities are somewhat lower, by a factor of $\sim 1.5-3$, depending on redshift and the study in question. There are some key differences between the literature studies and our first-look that might explain why our values seem comparably lower. Firstly, all of the studies we compare to calculate their dust mass densities by integrating down to much smaller dust masses ($M_d = 10^4 - 10^5 M_\odot$)[32], compared to our lower limit of $M_d \sim 10^7 M_\odot$. As a test to probe the impact of including the contribution from galaxies with low dust masses, we extrapolate our DMFs to low dust masses following a flat low mass slope, as in Dunne et al. (2011), down to their lower dust mass limit (scaled to our assumed κ_{500}; see Figure 6.7). In Figure 6.8, we can see that including the contribution from galaxies with lower dust masses helps to marginally increase our estimated dust mass densities, but this is not enough to reconcile them with other studies. However, had we used a steeper faint end slope, like that of Beeston et al. (2018), the agreement might have been improved. Pozzi et al. (2020) found a very steep low mass slope ($\alpha = -1.48$) for their 160μm selected DMFs for galaxies in the COSMOS field. They tested the effect of having a flatter faint end slope ($\alpha = -1.2$), refit their Schechter functions, and found the corresponding dust mass densities to be a factor of 1.5-2 lower. Therefore, extrapolating to smaller dust masses using a steeper faint mass slope than assumed in the test here might help reconcile the differences between our first-look dust mass densities and those from the literature.

We also tested our assumption of mass-weighted dust temperature ($T_d = 25\,\mathrm{K}$), by instead assuming a lower temperature of $T_d = 20\,\mathrm{K}$, and recalculating ρ_d. In Figure 6.8, by assuming a lower mass-weighted dust temperature, we find that our estimated values of ρ_d increase by a factor of $\sim 1.4-1.8$, depending on redshift. At low-to-intermediate redshifts, this brings us more inline with the dust mass density from Driver et al. (2018). A slightly lower dust temperature is supported by other *Herschel* based studies, which advocate for a dust temperatures between $T_d = 15-35\,\mathrm{K}$ (Dunne et al. 2011; Dale et al. 2012; Auld et al. 2012; Magnelli et al. 2014). However, since many (more recent) studies argue that a mass-weighted dust temperature of 25 K is suitable (e.g. Scoville et al. 2016; Scoville et al. 2017; Liang et al. 2019), we suggest that any offsets caused by methodology approximations and/or methodology differences should be considered in a more

[32] Assuming their cosmology and κ_{500}

robust analysis before changing the assumed mass-weighted dust temperature.

Despite using very different methodologies but the same initial source catalogue as Driver et al. (2018), there are some interesting differences and similarities in the evolution of ρ_d with redshift as shown in our study and that of Driver et al. (2018). Ignoring the offset between the results of the two studies, which we can at least partially attribute to not accounting for incompleteness in our study and integrating to a higher lower dust mass limit, we see that the two studies show a similar evolution in the dust mass density for $z \sim 0.3 - 1$. The dust mass densities from Driver et al. (2018) seem to peak at $z \sim 1$, whereas we see a much broader peak, spanning $z \sim 1 - 1.8$. However, Driver et al. (2018) do advise caution with regards to their last data point, and do not place any significance on the turn-down, given the large errors on this data point. In that case, out to $z \sim 1.4$, the dust mass density from Driver et al. (2018) may also hint at a broader, flatter peak in the dust mass density - it is impossible to say for sure, since they do not probe to higher redshifts.

The 160μm selected study of Pozzi et al. (2020) shows a quite rapid increase in the dust mass density of galaxies at low redshifts ($z < 0.7$), in agreement with the 250μm selected study of Dunne et al. (2011). Similarly to Driver et al. (2018), we do not see such a rapid increase in the dust mass density at low redshifts, although we note we do not explore to low enough redshifts to compare to the rapid evolution of the dust mass density in the local Universe as shown by Dunne et al. (2011). However, in Figure 6.8, at $z \sim 0.35$, we see that our dust mass density estimates are a factor of $\sim$2.5-3 lower than that of the FIR selected studies. These differences may be due to selection effects, since both the studies of Dunne et al. (2011) and Pozzi et al. (2020) use far-IR selected catalogues and so their studies sample galaxies with high dust content. Additionally, the studies of Dunne et al. (2011) and Pozzi et al. (2020) select galaxies near to the peak of dust emission of galaxies, whereas our study involves examining dust emission low down on the Rayleigh-Jeans tail of dust emission. However, it is difficult to quantify how such selection effects and different analyses may affect the calculation of dust mass density.

We do not probe the local Universe, so we cannot directly compare to Beeston et al. (2018), other than to say our estimated dust mass density is lower at $z \sim 0.35$ than their local Universe estimate. However, assuming that a more robust

analysis of the dust mass density following the methodology presented in this Thesis increases the normalization of ρ_d to values similar to Driver et al. (2018), then we might be more in agreement with the local Universe estimate.

The peak of the dust mass density distribution coinciding with the peak of the cosmic SFR density at around $z \sim 2$ (Madau & Dickinson, 2014) is interesting. It implies that star formation and dust production are linked, that dust production from stellar deaths is an important pathway for dust to form in the Universe. The decline in the dust density of the Universe in our study from $z \sim 1$ to the nearby Universe implies that at later times, dust is being destroyed faster than it is being formed, and the Universe is becoming more transparent (Driver et al., 2018). However, it is worth noting that the dust might not necessarily be being destroyed - it might just be disappearing from typical galaxy boundaries, and so be beyond our measurements. For example, dust might be being efficiently ejected from galaxies, into the halo or even the intergalactic medium (Driver et al., 2018).

Despite the many approximations made to the methodology presented here to estimate the evolution of the dust mass density with cosmic time, there is remarkably good general agreement in the shape of the evolution with other more robust literature studies, which gives hope for a proper treatment of this method in the future. This includes using the same galaxy catalogue to estimate SMFs and stacked dust masses, fitting Schechter functions to resulting DMFs, and a more thorough error analysis. The advantage of this method is that by using the long-wavelength emission from dust on the Rayleigh-Jeans tail, we can estimate dust masses in an empirical way, relying on fewer assumptions compared to SED modelling.

6.6 CONCLUSIONS

In this Chapter, we showed that for $z < 2.5$, we could combine dust-to-stellar-mass ratios calculated using our MAGPHYS-COSMOS2015 catalogue with the stellar mass functions of Davidzon et al. (2017) to test a method for deriving estimates of the dust mass density using long-wavelength dust emission on the Rayleigh-Jeans tail.

- We re-binned sources in our MAGPHYS-COSMOS2015 catalogue into the

same redshift bins as used in Davidzon et al. (2017) for calculating COSMOS SMFs and re-did our stacking analysis. We found a similar evolution in the dust-to-stellar-mass ratio of galaxies as found in Chapter 4, with the dust-to-stellar-mass ratio of galaxies increasing with redshift out to $z \sim 2.5$.

- We calculated COSMOS DMFs by combining the results of our stacking analysis with the SMFs of Davidzon et al. (2017). We found a strong evolution in the estimated DMFs for the high dust mass regime ($\log_{10}(M_d) > 8.0$), showing that galaxies were dustier in the past (up to $z \sim 2.5$). We found that most of the estimated DMFs approximate to a Schechter function, except for the lowest redshift DMF, which has a curious 'banana' shape. We attribute the 'banana' shape to either a severe lack of dust in massive galaxies at low redshifts, due to contamination of average dust masses by passive galaxies that typically lack dust, or a lack of massive galaxies at low redshift, which may be due to not correcting for incompleteness.

- We estimated the evolution of the dust mass density of COSMOS galaxies with redshift by approximately integrating under our calculated DMFs. We found a peak in the dust mass density from $z \sim 1 - 1.8$, and a smooth but substantial decline in the dust mass density of the Universe from $z \sim 1$ to $z \sim 0.35$, with ρ_d decreasing by a factor of 2. We also found a decrease in the dust mass density to earlier times.

- Despite agreeing with literature values on the location of the peak of the evolution of dust mass density with redshift, we found our first-look dust mass density values to be a factor $\sim 1.5 - 3$ lower. Aside from the calculation approximations used in this first-look estimate, we attribute this to integrating to a higher low dust mass limit. However, our dust mass estimates can be brought more inline with literature values if we assume a lower mass-weighted dust temperature. We also do not see the rapid evolution in the dust mass density at low redshifts ($z < 0.7$) seen in FIR-selected studies, though this could be a selection effect.

- We found the peak of the first-look dust mass density to be consistent with the peak of cosmic SFR density, at around $z \sim 2$, implying that dust production from stellar deaths is an important pathway for dust to form in the

Universe.

- Despite using only crude approximations to calculate the dust mass density using the methodology described in this Chapter, we found a remarkably good general agreement in the shape of the evolution of ρ_d with redshift as compared to more robust literature studies. This gives hope for a proper treatment of this method in the future, with dust masses estimated in a more empirical way.

Chapter 7
Conclusions

'I may not have gone where I intended to go, but I think I have ended up where I needed to be.'

Douglas Adams

In this Thesis, we have explored the evolution of the dust and gas content of galaxies over much of the history of the Universe, using both observational data for galaxies in the COSMOS field and results from the state-of-the-art cosmological hydrodynamical simulation IllustrisTNG. We used stacked long-wavelength emission from dust on the Rayleigh-Jeans tail as a tracer of the average gas properties of COSMOS galaxies. Compared to previous works, we extended to higher redshifts, considered more galaxies on the Main Sequence, and split our sample into star-forming and passive galaxy populations. We developed a post-processing method to estimate the dust content of IllustrisTNG galaxies, and compared this data to robust dust mass observations. Whilst the observational data showed a strong evolution in the dust content of galaxies with cosmic time, the evolution in the dust content of IllustrisTNG galaxies was comparatively weak. This study provided independent evidence that feedback mechanisms imposed in IllustrisTNG to allow the simulations to better reproduce physical trends in the local Universe may be too aggressive at intermediate-to-early times, forcing a weak evolution in the neutral gas content of IllustrisTNG galaxies. Alternatively, the dichotomy in the evolutionary results from our COSMOS stacking and post-processed IllustrisTNG analysis may be evidence for a strong evolution in the physical properties of dust

with cosmic time. Finally, we presented a first-look study examining the evolution of the comoving dust mass density with cosmic time, estimated by combining stacked dust masses with previously published stellar mass functions for the COSMOS field. We found a peak in the dust mass density at $z \sim 1 - 1.8$, with dust mass density decreasing to later times, in remarkable agreement with more robust literature studies, despite the approximations presented in this first-look study. The peak in dust mass density is roughly coincident with the peak of the cosmic SFR density at around $z \sim 2$, indicating that dust production from stellar deaths is an important pathway for dust to form in the Universe.

In this Chapter, we review the research conducted in this Thesis and summarize our main findings. We also explore ideas for future work that builds on the results of this research.

7.1 KEY RESULTS I - THE EVOLUTION OF GAS MASS USING DUST EMISSION

In a nutshell: We used the deepest 850μm maps of the COSMOS field to-date from the S2COSMOS survey to examine the evolution of the gas mass fraction of galaxies over cosmic time, probing redshifts beyond the peak of star-formation activity. We used a galaxy catalogue containing more 'normal' galaxies on the Main Sequence than previous studies, and derived average gas masses from empirical measurements of the sub-mm emission from dust on the Rayleigh-Jeans tail using a stacking analysis. We found that our stacking results broadly agree with previous literature studies that used significantly smaller and more biased galaxy samples. We found tentative evidence for a peak in the gas mass fraction of galaxies at around $z \sim 2.5 - 3$, just before the peak of the star-formation history of the Universe. We split our sample into passive and star-forming sub-samples, and examined the evolution of the gas mass fraction of these two populations, showing that passive galaxies are particularly devoid of gas. We found that even at high redshifts, high stellar mass galaxies contain significant amounts of gas.

In Chapter 2, we constructed a source catalogue by first comparing galaxy

stellar masses calculated using two different SED fitting routines, MAGPHYS and CIGALE. We cross-matched the two catalogues, and after filtering for sources with similar assumed redshifts in the two catalogues, examined the stellar mass distributions of matched sources. We concluded that our choice of source catalogue was not likely to be the largest source of error, and that choosing to use galaxy stellar masses from the CIGALE catalogue would not change our conclusions. We ultimately chose to use the MAGPHYS catalogue, since it was confined to the lowest noise areas of the 850μm map. We constructed a final source catalogue by cross-matching the MAGPHYS catalogue to the COSMOS2015 catalogue, to ensure completeness and exploit the additional photometry available in COSMOS2015. After removing AGN, and establishing a stellar mass limit of $9.5 < \log_{10}(M_*/M_\odot) < 12$, we ended with a final galaxy catalogue containing 63,658 sources out to $z \sim 5$.

In Chapter 3, we introduced our inverse variance weighted stacking methodology, binned our sources into redshift and stellar mass bins, and calculated average 850μm fluxes for galaxies in a given $(M_* - z)$ bin, estimating flux errors using a Monte Carlo simulation. We introduced the empirically derived scaling relation used in this Thesis to convert long-wavelength dust emission on the Rayleigh-Jeans tail into ISM gas mass estimates (Scoville et al., 2017), and used our stacked 850μm fluxes to examine the evolution of the average gas mass fraction of galaxies with redshift.

In the lower stellar mass bins ($\log_{10}(M_*/M_\odot) < 10.5$), we found the ISM mass fraction in galaxies to increase with redshift, up to a maximum at around $z = 2.5 - 3$, and then plateau out to higher redshifts. It is interesting to note that this peak in the gas mass fraction of galaxies is a little before the peak of star-formation in the Universe, which is at $z \sim 2$. For higher stellar mass bins ($\log_{10}(M_*/M_\odot) \geq 10.5$), we found the ISM mass fraction in galaxies to increase with redshift, without clearly reaching a maximum, even out to $z \sim 3$. We also found that more massive galaxies are more gas-poor, in agreement with previous studies. We compared the gas mass fractions calculated using our stacked fluxes to scaling relations in the literature developed using smaller and more biased galaxy samples (that is, fewer galaxies on the Main Sequence). We found that the general

trends produced by our stacking analysis are in agreement with these scaling relations. We found that local estimates of the gas mass fraction in galaxies are somewhat higher at $z = 0$ compared to our stacking analysis and scaling relations from the literature, probably because the local estimates incorporate atomic gas mass measurements. We suggested that small differences between our stacking results and scaling relations from the literature may be attributed to differences in sample selections. To test this, we split our sample into passive and star-forming populations, and showed that compared to the scaling relation from Scoville et al. (2017), our sample contains more normal star-forming galaxies, and some passive galaxies. We also showed that the inclusion of more passive galaxies into our sample at low redshift biases our gas fractions low compared to local Universe literature values.

We explored several of the caveats associated with this study, including a bias for excluding highly-dust-obscured SMGs and a lack of passive galaxies, introduced by using an i-band selected source catalogue. We showed that the results of this study are robust against the mass-weighted dust temperature assumption used in this work ($T_d = 25\,\mathrm{K}$), and that assuming a different X_{CO} factor would change only the normalisation of the scaling relations and results.

Despite our study and the ones of Scoville et al. (2017) and Tacconi et al. (2018) using galaxy samples selected in very different ways and quite different methodologies, all three studies conclude that galaxies in the past were considerably more gas-rich than their local counterparts. Our results suggest that the gas fraction increases rapidly with redshift out to $z \sim 2-3$, with the redshift limit depending on stellar mass, and then is roughly constant. The maximum gas fraction of $\sim$0.5 may be a genuine physical limit, or a manifestation of the limitations of using the dust to trace the gas. At early times, not enough dust may have formed to properly trace the gas content of these galaxies, and so the plateau at high redshifts may be due to an evolution in the dust-to-gas ratio rather than evolution in gas fraction.

7.2 KEY RESULTS II - CONFLICTING DUST MASS EVOLUTION IN OBSERVATIONS AND SIMULATIONS

In a nutshell: We investigated the evolution in galactic dust mass over cosmic time through i) empirically derived dust masses using our previously calculated stacked submillimetre fluxes at 850μm in the COSMOS field, and ii) dust masses derived using a robust post-processing method, developed as part of this Thesis, on the results from the cosmological hydrodynamical simulation IllustrisTNG. We performed a 'self-calibration' of the dust mass absorption coefficient by choosing a value of κ_{500} such that the model and observations agree at low redshifts. This then allowed us to examine and compare the evolution shown by the observations and predicted by the model. We calculated DMFs using the results of the IllustrisTNG simulations from $0 < z < 0.5$ and compared to previously observed DMFs from the literature. In contrast to the rapid evolution seen in empirically derived estimates of the low redshift DMF, we found a distinct lack of evolution in the DMFs derived from IllustrisTNG. Additionally, our observational stacking results show a strong evolution in the dust-to-stellar-mass ratio of galaxies over the redshift range $0 < z < 5$, whereas the corresponding dust-to-stellar-mass ratios of IllustrisTNG galaxies showed relatively little evolution. This lack of evolution was not rectified after splitting the sample into satellites and centrals, and could not be explained by using a different dataset from IllustrisTNG. The large discrepancy seen between the simulations and observations requires either i) a strong evolution in the properties of dust grains with cosmic time or ii) limitations in the model, which may be connected to previous claims that the neutral gas content of galaxies in IllustrisTNG does not evolve fast enough with time.

In Chapter 4, we introduced the IllustrisTNG dataset used in this Thesis and two methods for deriving dust masses; i) using our measured stacked fluxes at a single wavelength on the Rayleigh-Jeans tail of dust emission from Chapter 3, and ii) a new post-processing method developed as part of this Thesis for estimating dust masses for galaxies from IllustrisTNG. We defined our choice of dust mass absorption coefficient as one that allowed the high-mass end of the $z = 0$ DMF from

IllustrisTNG to agree with robust local DMFs from the literature. By forcing the observations and simulations to agree at $z = 0$, we could justifiably comment on and compare the evolution of the dust content of galaxies from the two datasets. We also justified our choice of assuming a constant dust-to-metals ratio in estimating dust masses for IllustrisTNG galaxies, since the majority of these galaxies have high metallicities where the assumption of a constant dust-to-metals ratio is appropriate.

We calculated DMFs for IllustrisTNG galaxies over the range $0 < z < 0.5$. In contrast to the strong evolution seen in observational DMFs calculated over this redshift range from Dunne et al. (2011), the IllustrisTNG DMFs showed a distinct lack of evolution. Additionally, compared to the $z = 0$ DMF from Beeston et al. (2018), the IllustrisTNG DMFs showed an excess number of sources at low dust masses. We attributed the excess number of sources to satellite galaxies in the simulation which have likely undergone excessive stripping, thereby reducing their calculated dust mass as determined using our post-processing method.

We then examined the evolution of the dust-to-stellar-mass ratio of galaxies in our MAGPHYS-COSMOS2015 and TNG100 catalogues out to $z \sim 5$. We found that the model predicts significantly less dust mass evolution than the observations, although at low stellar masses ($\log_{10}(\mathrm{M}_*, \mathrm{bin}) < 10.5$) both the observations and simulations show that the peak in (M_d / M_*) occurs at $z \sim 3$. It is interesting to note that the peak in the dust-to-stellar-mass ratio of galaxies occurs a little before the peak in the star-formation history of the Universe. At low redshifts, the dust-to-stellar mass ratios from both observations and simulations agree, but this is in part by construction due to the method used to derive an appropriate value of κ_{500}. Additionally, both the observations and simulations show that the dust content of galaxies decreases with increased galaxy stellar mass. For high stellar mass galaxies ($\log_{10}(\mathrm{M}_*, \mathrm{bin}) > 10.5$), the galaxies in IllustrisTNG are particularly devoid of dust, in contrast to the observations which continue to show a strong evolution in the dust-to-stellar-mass ratio of galaxies out to high redshifts.

In Chapter 5, we explored reasons to explain the conflicting dust mass evolution shown between observations and simulations. Firstly, we considered the effect of the fundamental assumptions made in this work, two of them being that

κ_{500} and T_d are time invariant. We are not aware of any predictions or observations that would allow the required large increase in κ_{500} with redshift to bring the observations and simulations into agreement. We also show that changing our assumption of a constant mass-weighted dust temperature of $T_d = 25\,\mathrm{K}$ to a higher dust temperature at high redshifts cannot reconcile the differences in the dust-to-stellar-mass ratio. We also show that choosing a lower value of the dust emissivity spectral index, β, would only exacerbate the difference in the evolution of the dust-to-stellar-mass ratio shown between our observational stacking analysis and TNG100 plus post-processing. We test an evolving dust-to-metal ratio and show that whilst an extreme evolution ($\epsilon_d(z = 2) \sim 0.9$) may help reconcile the results from observations and simulations at intermediate redshifts, it cannot explain the discrepancy at the highest redshifts. We also show that a dust-to-metal ratio that varies with metallicity cannot explain the discrepancy, and that using the total gas mass to calculate post-processed dust masses in IllustrisTNG galaxies instead of just the neutral gas mass cannot explain the stark lack of dust evolution seen as compared to observations.

We re-ran our analysis using an alternative dataset from TNG100, using all particles and cells gravitationally bound to a source as opposed to only considering those within two stellar half mass radii, and showed that the same evolutionary trends in dust-to-stellar-mass ratio emerge from this dataset too. We split our TNG100 sample into satellite and central sources to see if unusual gas-poor satellite galaxies may be masking more rapid dust mass evolution in TNG100 galaxies than is shown by the collective population. We found that splitting the TNG100 galaxies sample into satellites and centrals does not solve the lack of dust mass evolution as compared to observations.

We considered the metal enrichment prescriptions used in the IllustrisTNG simulations and postulated that one possible explanation of the comparatively low dust masses in the model is that TNG100 ejects too many metals from the cool ISM. We note that the lack of evolution in the dust mass of TNG100 galaxies compared to observations could be a reflection of the lack of evolution of the neutral gas content in the simulations, as previously seen. We speculate that the lack of evolution in the neutral gas content of IllustrisTNG galaxies may be caused by over-enthusiastic AGN feedback.

7.3 KEY RESULTS III: A FIRST-LOOK AT THE EVOLUTION OF DUST MASS DENSITY

In a nutshell: We presented a first-look estimate of the evolution of the comoving dust mass density of galaxies with cosmic time, estimated by combining stacked dust masses evaluated using long-wavelength 850μm dust emission and previously published stellar mass functions for galaxies in the COSMOS field. We estimated DMFs for COSMOS galaxies up to $z \sim 2.5$, and found they show a strong evolution in the high dust mass regime ($\log_{10}(M_d) > 8.0$), indicating that galaxies were dustier in the past. We approximately integrated under our calculated DMFs to estimate the evolution of the dust mass density of COSMOS galaxies with redshift. We found a peak in the dust mass density from $z \sim 1 - 1.8$, with a decrease in dust mass density to later times (a factor of 2 by $z \sim 0.35$). We also found a decrease in the dust mass density to earlier times. Despite agreeing with previous literature studies on the location of the peak of dust mass density with redshift, we found our first-look estimates to be a factor of $\sim 1.5 - 3$ lower than other studies. We attributed this normalization difference to either calculation approximations and integrating to a higher low dust mass limit, or the assumed mass-weighted dust temperature used in this study. A lower mass-weighted dust temperature brings our first-look estimates more inline with previous results. The peak of the first-look dust mass density is consistent with the peak of cosmic SFR density, at $z \sim 2$, implying that dust production form stellar deaths is an important pathway for dust to form.

In Chapter 6, we compared the galaxy catalogues used to construct literature COSMOS stellar mass functions and our stacked dust masses, to examine whether the sources in our MAGPHYS-COSMOS2015 catalogue are reasonably representative of the sources used in calculating the COSMOS2015 stellar mass functions. Specifically, we compared redshift and stellar mass estimates for galaxies matched between our MAGPHYS-COSMOS2015 catalogue and the galaxy catalogue of Davidzon et al. (2017). We found that although galaxy parameters vary on a source-by-source basis due to the different fitting routines used to derive galaxy

parameters in each of the catalogues, we found that up to $z < 2.5$, the overall distribution of galaxies in $(M_* - z)$ space was reasonably similar. We concluded that we could reasonably carry out a preliminary investigation into the evolution of dust mass density out to $z < 2.5$.

We re-binned sources in our MAGPHYS-COSMOS2015 catalogue into the same redshift bins as for the literature stellar mass functions, and using the same S2COSMOS 850μm data and error maps and IVW stacking method presented in Chapter 2, we repeated our stacking analysis. Using the methodology presented in Chapter 4, we calculated dust masses using our new stacked fluxes. As before, we found that the dust-to-stellar-mass ratio of galaxies strongly increases with redshift (out to $z \sim 2.5$).

We combined literature stellar mass functions with our restacked dust-to-stellar-mass ratios to estimate DMFs for galaxies in the COSMOS field up to $z < 2.5$. In the higher dust mass regime ($\log_{10}(M_d) > 8.0$), we found a strong evolution in the DMFs, showing that galaxies were dustier in the past (for the redshift regime explored). We also saw a strong decrease in the number density of galaxies with redshift, with the number density of very dusty galaxies low at high redshifts. However, in this first-look study, we did not attempt to correct for incompleteness, so we did not place too much emphasis on this trend.

We found the shape of most of the estimated DMFs approximated to Schechter functions, apart from the lowest redshift DMF ($z = 0.2 - 0.5$), which has a curious 'banana' shape. The high-mass end of the DMF seems to curve to disproportionately low dust masses. We attributed this unusual shape to either: i) a severe lack of dust in massive galaxies at low redshifts, with average stacked dust masses possibly biased low due to the inclusion of passive galaxies in our sample, or ii) a lack of massive galaxies at low redshifts in this study, which is not unreasonable since we do not correct for incompleteness in this first-look study.

Finally, we approximately integrated underneath our COSMOS DMFs to examine the evolution of the comoving dust mass density with cosmic time. We found a smooth but substantial decline in the dust mass density from $z \sim 1$ to $z \sim 0.35$, with ρ_d decreasing by a factor of 2. We found a broad peak in the dust mass density of the Universe, with a relatively constant value between $z = 1 - 1.8$. We also found a decrease in the dust mass density to earlier times.

We compared our first-look estimate of the dust mass density calculated using stacked dust masses with previous studies from the literature. We found that the peaks of the dust mass densities from the literature roughly agree with our values. However, we found our dust mass density estimates to be a factor of $\sim 1.5 - 3$ lower than other studies. We attributed this difference to integrating our DMFs to a higher low dust mass limit and the calculation approximations made in this first-look study, including not correcting for completeness. Although, we also found that assuming a lower mass-weighted dust temperature brings our dust mass density estimate more inline with the literature.

We found that the peak of the dust mass density distribution coincides with the peak of the cosmic SFR density, at around $z \sim 2$. This implies that star-formation and dust production are linked, that dust production from stellar deaths is an important pathway for dust to form in the Universe. Additionally, the decline in dust mass density at late times (from $z \sim 1$ to $z \sim 0.35$) implies that dust is being destroyed faster than it forms - or, it is at least disappearing from typical galaxy boundaries, and so is beyond our measurements. For example, dust may be being ejected from galaxies into the halo or intergalactic medium.

Despite the many approximations made to the methodology presented in Chapter 6 to estimate the evolution of the dust mass density with cosmic time, there is remarkably good general agreement in the shape of the evolution with other more robust literature studies, which gives hope for a proper treatment of this method in the future.

7.4 FUTURE WORK

There are several research projects that could springboard off the work done in this Thesis. Below we outline some of the more interesting options.

1. **Stacking at longer wavelengths.** In order to probe the gas and dust content of galaxies at earlier epochs than examined in this Thesis, it is imperative to use longer wavelength data, where dust emission will still be on the Rayleigh-Jeans tail and the relations used in this Thesis are still applicable. Fortunately, two new instruments are due to imminently[33] come online

[33] Ideally in 2021...

at the 50m Large Millimetre Telescope (LMT) in Mexico that will be able to offer large-scale maps of the sky at the required longer wavelengths. MUSCAT (Mexico UK Submillimetre Camera for Astronomy; Tapia et al. 2020) will offer a superior resolution of $\sim 6''$ FWHM and an unprecedented sensitivity of 1mJy r.m.s at 1.1mm. Additionally, TolTEC will offer observations at 1.1, 1.4 and 2.1mm, again with unprecented resolution at sensitivity at these wavelengths (Schloerb et al., 2019). Pope et al. (2019) predict that surveys with TolTEC will yield tens of thousands of millimetre detections, with around 1/3 of these sources expected to be at $z > 3$. More sensitive and resolved observations of the gas and dust content of these high redshift galaxies are key to understanding the driving factor behind the evolution of the star-formation history of the Universe. Beyond individual detections, a high-resolution millimetre map of a well-studied field like COSMOS could enable revolutionary statistical studies of the general galactic population out to high redshifts.

2. **Incorporating dust processes into cosmological simulations.** To better compare the results from cosmological simulations to the robust observational dust mass estimates now available for much of the history of the Universe, dust-processes must be incorporated. Arguably, even current state-of-the-art computational processes cannot allow large-scale hydrodynamical simulations like IllustrisTNG to be run at resolutions comparable to dust formation and destruction scales. However, there is clearly a requirement for dust processes to be incorporated, and this could be done using sub-resolution approximations, much in the way current enrichment processes are modelled in simulations. Some progress has been made in this field - for example, the SIMBA cosmological simulations (Davé et al., 2019) include an on-the-fly dust production, growth, and destruction model. It would be useful for different simulations to try incorporating different assumed dust models and laws, to examine which best fit the observational data. In turn, this will greatly improve our understanding of the underlying dust physics governing our observations.

3. **Dust density calculated using the updated COSMOS2020 catalogue.** The next COSMOS galaxy catalogue, COSMOS2020, is due to be released within

the next few months. Since this catalogue will contain superior estimates of galaxy properties, such as redshift and stellar mass, it would be worth deriving stellar mass functions for galaxies in the COSMOS field using this improved dataset, and then use these stellar mass functions to repeat the dust density analysis in this Thesis but in a more robust way. For example, the stacking analysis should use the exact same COSMOS2020 catalogue as used in constructing updated stellar mass functions, and a full, comprehensive error analysis should be conducted, including Poisson noise and a proper treatment of Cosmic Variance. Incompleteness should also be accounted for, and the (minor) impact of the CMB. Additionally, dust mass density estimates could be extended to higher redshifts. As an aside, it would be interesting to compare the evolution of the dust mass density calculated using the results from IllustrisTNG (and/or other simulations) to the updated observational one.

7.5 SEEING THE WOOD FOR THE TREES

Much of the work in a PhD thesis involves diving into rabbit-holes and focusing on the minutiae - something that astronomers[34] are delightfully adept at. This thesis is certainly no exception. To end, we review the thesis holistically, in a rare attempt to focus on the bigger picture, for fear of forever being lost in the beautiful details.

In this thesis, we have studied 'the stuff between the stars' in a statistical way, focusing on the galactic population as a whole throughout cosmic time, rather than considering a small, biased, limited sample as in previous studies. In doing this, we have shown that methods to trace the molecular gas in galaxies using dust emission derived using small, biased galaxy samples can be successfully applied to a more general and representative population. We have shown that the gas content of the general galactic population evolves significantly over cosmic time, with galaxies being much more gas-rich in the past. Additionally, this work represents the limit of usefulness for this dust-tracing-the-gas method. It cannot be taken further until longer-wavelength data is available and we have a better understanding

[34] Particularly this astronomer, to the despair of her supervisors...

of gas and dust in the high-z Universe for calibration purposes.

Having reached the gas-tracing limit, we took a step back and instead focused on the uniquely brilliant idea of using dust emission to study... dust. We used robust, empirical dust mass observations to test a recent cosmological hydrodynamical simulation, challenging it against results it was not tuned to reproduce. In doing so, we provided additional independent (and arguably more robust) evidence that feedback mechanisms imposed in the simulation to allow it to replicate local Universe relations are too aggressive at intermediate-late times. This resulted in a lack of dust (and gas) evolution over cosmic time, in stark contrast to our observations. Alternatively, and rather controversially, if the relative lack of evolution in the interstellar medium of simulated galaxies is correct, we have shown that our assumption that the properties of dust grains are the same throughout the Universe is wrong. If true, this has enormous implications for dust astronomy[35].

Finally, we tested a new way to calculate the evolution of the dust mass density of galaxies throughout cosmic time, a direct probe of the chemical evolution of the Universe (and an indirect measure of just how good galaxies are at their jobs of converting gas into stars). This new method is more empirical, since it simply uses the emission directly from dust, rather than complex multi-wavelength modelling. Despite many (many) assumptions and approximations, there was reasonable agreement with previous results, giving hope for this method in the future.

7.5.1 FINAL REMARKS

Studying 'the stuff between the stars' is hard. Poor resolution limits our ability to study individual objects, and directly detecting gas beyond the local Universe in anything but a few extreme objects is nigh-on impossible. However statistics, stacking, and emission from 'pesky' dust offer a surprising solution. With these tools, we can build up a picture of the general galaxy population and the evolution of the cosmos as a whole. We can probe both the fuel for star formation and the ashes. Simulations push the limits of our understanding - and allow us to break the Universe, one way or another, real or fake. With large-scale longer-wavelength

[35] Although, being primarily a dust-astronomer, I would argue that all other options be ruled out before resorting to suggesting something as terrifying as dust not being the same throughout the Universe...

(>1mm) surveys of the sky imminent, and tests to include dust physics in simulations beginning, the quest for finally understanding 'the stuff between the stars' is well underway.

To end, dear reader, I leave you with this thought. The majority of the work in this thesis has been conducted using light invisible to the human eye. Over 3 years of work poured into something I cannot see, in a patch of sky I can hide beneath the tip of an outstretched finger.

So when you look up at the night sky tonight, ask yourself - what *don't* you see?

Clear skies, my friend.

'I think we've outgrown full-time education ... Time to test our talents in the real world, d'you reckon?'

FRED WEASLEY

Appendices

CHAPTER A
ESTIMATING INTERSTELLAR GAS MASS USING DUST EMISSION

Here, we show the derivations of Equations 3.2 and 3.3, introduced in Chapters 3. This derivation is largely taken from Scoville et al. (2016) but with extra explicit steps shown here for additional clarity.

A.1 DEFINING THE CONSTANT OF PROPORTIONALITY

At long wavelengths, on the Rayleigh-Jeans tail of blackbody dust emission, the emission from dust is nearly always optically thin. Therefore, this emission is a direct probe of total dust mass, and since dust is pervasive throughout most phases of the ISM, it can be used to probe the mass of the ISM. However, this requires knowledge on the dust emissivity per unit mass, and also the dust-to-gas ratio, quantities which are largely unconstrained. An alternative approach to take in using dust emission to trace the mass of the ISM is to empirically calibrate the combination of the two, coupling the unknown parameters into a single conversion factor which can be constrained using observations of dust emissivity and independent measurements of the ISM mass of galaxies.

Assuming our observations are of dust emission on the Rayleigh-Jeans tail, the flux density in the observers frame is:

$$S_{\nu_o} = \frac{\left(1 - e^{(-\tau_{\nu_e})}\right) B_{\nu_e}(T_d)(1+z)}{D_L^2} \tag{A.1}$$

where we take the form accounting for the cosmological model describing the Universe, including emission frequency compression at high redshifts, factor $(1+z)$, and distance is the luminosity distance, D_L. $B_{\nu_e}(T_d)$ is the Planck function for the rest frame emission frequency, ν_e, and T_d is the assumed mass-weighted dust temperature. τ_{ν_e} is the optical depth at the emitted frequency. The optical depth is described by:

$$\tau_\nu = \kappa_\nu \times 1.36 N_H m_H = \kappa_\nu \times M_{ISM} \tag{A.2}$$

where we define κ_ν as the absorption coefficient of the dust per unit total mass of gas. N_H is the column density of H nuclei and the factor 1.36 if to account for ISM mass from heavier atoms (mostly He). Defining κ_ν in terms of gas mass as opposed to dust mass is a matter of convenience because we are calibrating dust opacity against ISM molecular gas mass. It is essentially an amalgamation of the dust opacity coefficient per unit dust mass and the dust-to-gas ratio.

For optically thin emission at long wavelengths, where $\tau_{\nu_e} \ll 1$, and substituting the definition of τ_ν:

$$S_{\nu_o} = \frac{M_{\rm ISM} \kappa_{\nu_e} B_{\nu_e}(1+z)}{D_L^2}. \tag{A.3}$$

We then substitute the Rayleigh-Jeans approximation of the Planck function, which is appropriate at long wavelengths:

$$S_{\nu_o} = \frac{M_{\rm ISM} \kappa_{\nu_e} 2 k_B T_d (\nu_e/c)^2 \Gamma_{\rm RJ}(1+z)}{D_L^2} \tag{A.4}$$

where $\Gamma_{\rm RJ}$ is the correction for departure in the rest frame of the Planck function from the Rayleigh-Jeans approximation:

$$\Gamma_{\rm RJ} = \frac{B_{\nu_e}}{R J_{\nu_e}} = \frac{h\nu_o(1+z)/k_B T_d}{e^{h\nu_o(1+z)/k_B T_d} - 1}. \tag{A.5}$$

In these equations, k_B is the Boltzmann constant, c is the speed of light, and h is the Planck constant.

We can also write flux density in terms of specific luminosity in the rest frame of the galaxy:

$$L_{\nu_e} = \frac{S_{\nu_o} 4\pi D_L^2}{(1+z)} \tag{A.6}$$

and substituting in Equation A.4 for the flux density:

$$L_{\nu_e} = \kappa_{\nu_e} 8\pi k_B T_d (\nu_e/c)^2 \Gamma_{\rm RJ} M_{\rm ISM}. \tag{A.7}$$

We can write the dust opacity coefficient in terms of a power-law:

$$\kappa_\nu = \kappa_{850\mu m} \left(\frac{\lambda}{850\mu m}\right)^{-\beta} = \kappa_{850\mu m} \left(\frac{\nu}{\nu_{850\mu m}}\right)^{\beta} \tag{A.8}$$

where, as in Scoville et al. (2016), we adopted a fiducial wavelength of 850μm, corresponding to the SCUBA-2 observations used in this work. Additionally, we assume $\beta = 1.8$, again in line with the assumptions made in this work. Therefore, from Equation A.6, the rest frame luminosity-to-mass ratio at this fiducial wavelength is:

$$\frac{L_{850\mu m}}{M_{\rm ISM}} = \kappa_{850\mu m} \frac{8\pi k_B \nu^2}{c^2} T_d \Gamma_{\rm RJ} \tag{A.9}$$

and we define the constant of proportionality between $L_{850\mu m}$ and $M_{\rm ISM}$ as:

$$\alpha_{850\mu m} = \frac{L_{850\mu m}}{M_{\rm ISM}} = \kappa_{850\mu m} \frac{8\pi k_B \nu^2}{c^2} T_d \Gamma_{\rm RJ}. \tag{A.10}$$

A.2 DERIVING THE ISM MASS EQUATION

In Scoville et al. (2016), the value of $\alpha_{850\mu m}$ was empirically derived using $M_{\rm ISM}$ estimates from CO measurements, and $L_{850\mu m}$ from dust emission. We therefore need an expression for $L_{850\mu m}$ in terms of observable quantities.

We begin with Equation A.9 at the fiducial wavelength written explicitly as:

$$L_{850\mu m} = \kappa_{850\mu m}\, 8\pi k_B T_d \frac{\nu^2_{850\mu m}}{c^2} \Gamma_{\rm RJ,0}\, M_{\rm ISM} \tag{A.11}$$

where we denote $\Gamma_{\rm RJ,0}$ to refer to the Rayleigh-Jean correction for the fiducial observations at $\nu_{850\mu m}$ and $z = 0$. We substitute in for $M_{\rm ISM}$ from Equation A.4:

$$L_{850\mu m} = \kappa_{850\mu m}\, 8\pi k_B T_d \frac{\nu^2_{850\mu m}}{c^2} \Gamma_{\rm RJ,0} \frac{S_{\nu_o} D_L^2 c^2}{\kappa_{\nu_e} 2 k_B T_d \nu_e^2 \Gamma_{{\rm RJ},z} (1+z)} \tag{A.12}$$

where we denote $\Gamma_{RJ,z}$ to refer to the Rayleigh-Jean correction needed at the observation frequency (which may not be $\nu_{850\mu m}$) and at a given redshift. Substituting in for κ_{ν_e} from Equation A.8:

$$L_{850\mu m} = \kappa_{850\mu m}\, 8\pi k_B T_d \frac{\nu_{850\mu m}^2}{c^2}\, \Gamma_{RJ,0} \frac{S_{\nu_o} D_L^2 c^2 \nu_{850\mu m}^{\beta}}{\kappa_{850\mu m} \nu_e^{\beta} 2 k_B T_d \nu_e^2 \Gamma_{RJ,z}(1+z)} \tag{A.13}$$

which, after collating terms and substituting in for $\beta = 1.8$ and $\nu_e = \nu_o(1+z)$:

$$L_{850\mu m} = 4\pi S_{\nu_o} \left(\frac{\nu_{850\mu m}}{\nu_o(1+z)}\right)^{3.8} \frac{D_L^2}{(1+z)} \frac{\Gamma_{RJ,0}}{\Gamma_{RJ,z}} \tag{A.14}$$

and for observed fluxes in terms of Jy:

$$\begin{aligned} L_{850\mu m} = 1.19 \times 10^{27} S_{\nu_o}[\mathrm{Jy}] \left(\frac{\nu_{850\mu m}}{\nu_o(1+z)}\right)^{3.8} \\ \times \frac{(D_L[\mathrm{Mpc}])^2}{(1+z)} \frac{\Gamma_{RJ,0}}{\Gamma_{RJ,z}}\ [\mathrm{ergs\,sec^{-1}\,Hz^{-1}}]. \end{aligned} \tag{A.15}$$

Using this equation, and standard relations from the literature for determining ISM masses from CO(1-0) observations, Scoville et al. (2016) determine a value of $\alpha_{850} = 6.7 \times 10^{19}$ erg sec^{-1} Hz^{-1} M$_\odot^{-1}$.

With an established value of α_{850}, what we are interested in now is an expression to determine the ISM mass from dust emission using only observable quantities and the now-quantified conversion factor. Substituting in the left side of Equation A.10:

$$\begin{aligned} \alpha_{850} M_{\mathrm{ISM}} = 1.19 \times 10^{27} S_{\nu_o}[\mathrm{Jy}] \left(\frac{\nu_{850\mu m}}{\nu_o(1+z)}\right)^{3.8} \\ \times \frac{(D_L[\mathrm{Mpc}])^2}{(1+z)} \frac{\Gamma_{RJ,0}}{\Gamma_{RJ,z}}\ [\mathrm{ergs\,sec^{-1}\,Hz^{-1}}] \end{aligned} \tag{A.16}$$

and rearranging, including unit conversion factors to go from [ergs] $\rightarrow$ [J][36], from

[36] 1 erg = 1 $\times 10^{-7}$J

[Mpc] $\rightarrow$ [Gpc], and from [Jy] $\rightarrow$ [mJy]:

$$M_{\rm ISM} = 1.78\, S_{\nu_o}[\rm mJy](1+z)^{-4.8}\left(\frac{\upsilon_{850\mu m}}{\nu_o}\right)^{3.8}(D_L[\rm Gpc])^2 \times \left\{\frac{6.7\times10^{19}}{\alpha_{850}}\right\}\frac{\Gamma_0}{\Gamma_{\rm RJ}}10^{10}M_\odot. \tag{A.17}$$

Chapter B
Evolution of Simulated and Observed Dust Mass Functions including all Bound Particles in IllustrisTNG

Here we show the same plots as Chapter 4 but for all particles and cells bound to a source in IllustrisTNG.

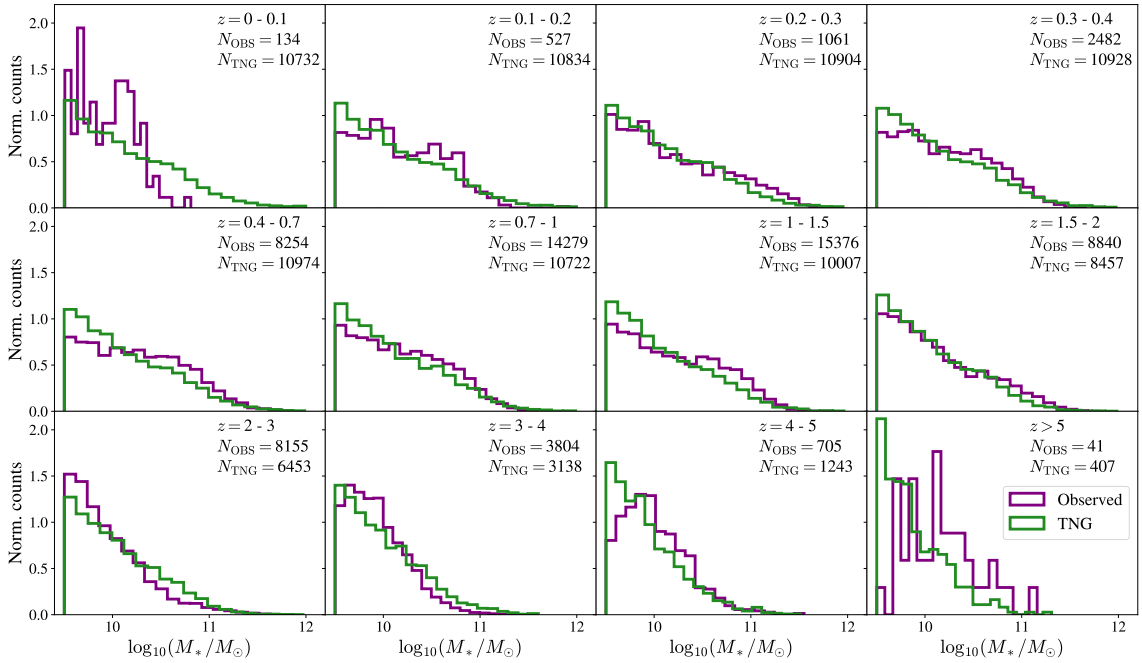

Figure B.1: Distributions of the stellar masses of galaxies in different redshift bins for TNG100 and MAGPHYS-COSMOS sources. TNG100 stellar masses are calculated using all particles and cells gravitationally bound to a galaxy. *Purple:* MAGPHYS-COSMOS sources used in stacking analysis to determine average dust properties. *Green:* TNG100 galaxies.

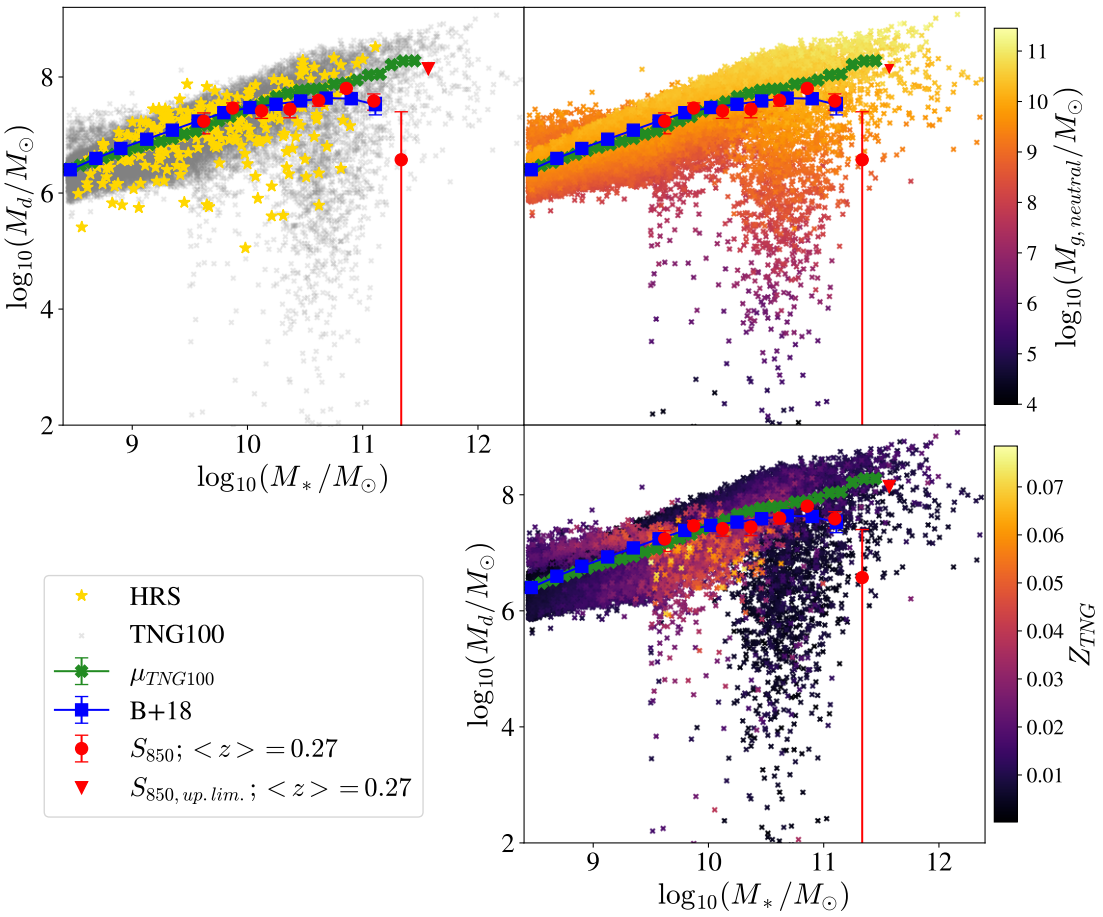

Figure B.2: Dust mass versus stellar mass for the bound TNG100 galaxies at $z = 0$ and for various low-redshift galaxy samples. The left-hand panel shows the TNG100 galaxies as *grey points*; the right-hand top panel shows them as crosses with a *colour* given by each galaxy's neutral gas mass (see colour bar); and the right-hand bottom panel shows them as crosses with a colour given by each galaxy's metallicity (see colour bar). The mean and standard error on the mean for the TNG100 galaxies in a given stellar mass bin are shown by *green crosses*. The galaxies in the Herschel Reference Survey are shown as *yellow stars* (De Vis et al. 2017a), the mean dust masses from the sample of Beeston et al. (2018) as *blue squares*, and the mean dust masses for the galaxies in the low-redshift bins from our S2COSMOS study as *red circles*, with the *red triangle* showing an upper limit.

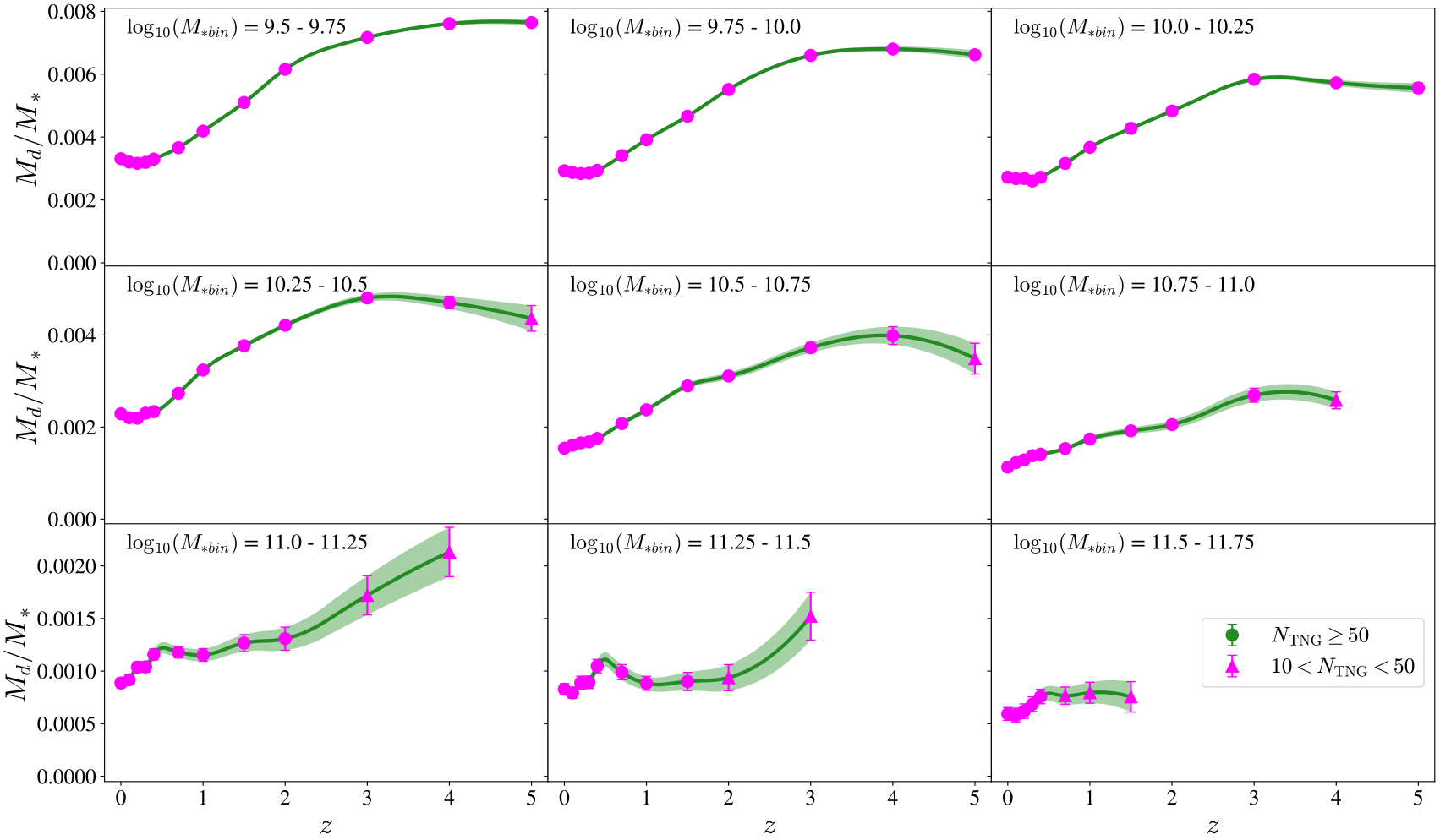

Figure B.3: Dust -to-stellar-mass ratios of TNG100 galaxies. *Circles:* at least 50 sources in the $(M_* - z)$ bin. *Triangles:* between 10 and 50 sources in the $(M_* - z)$ bin. The line is a quadratic interpolation to the data.

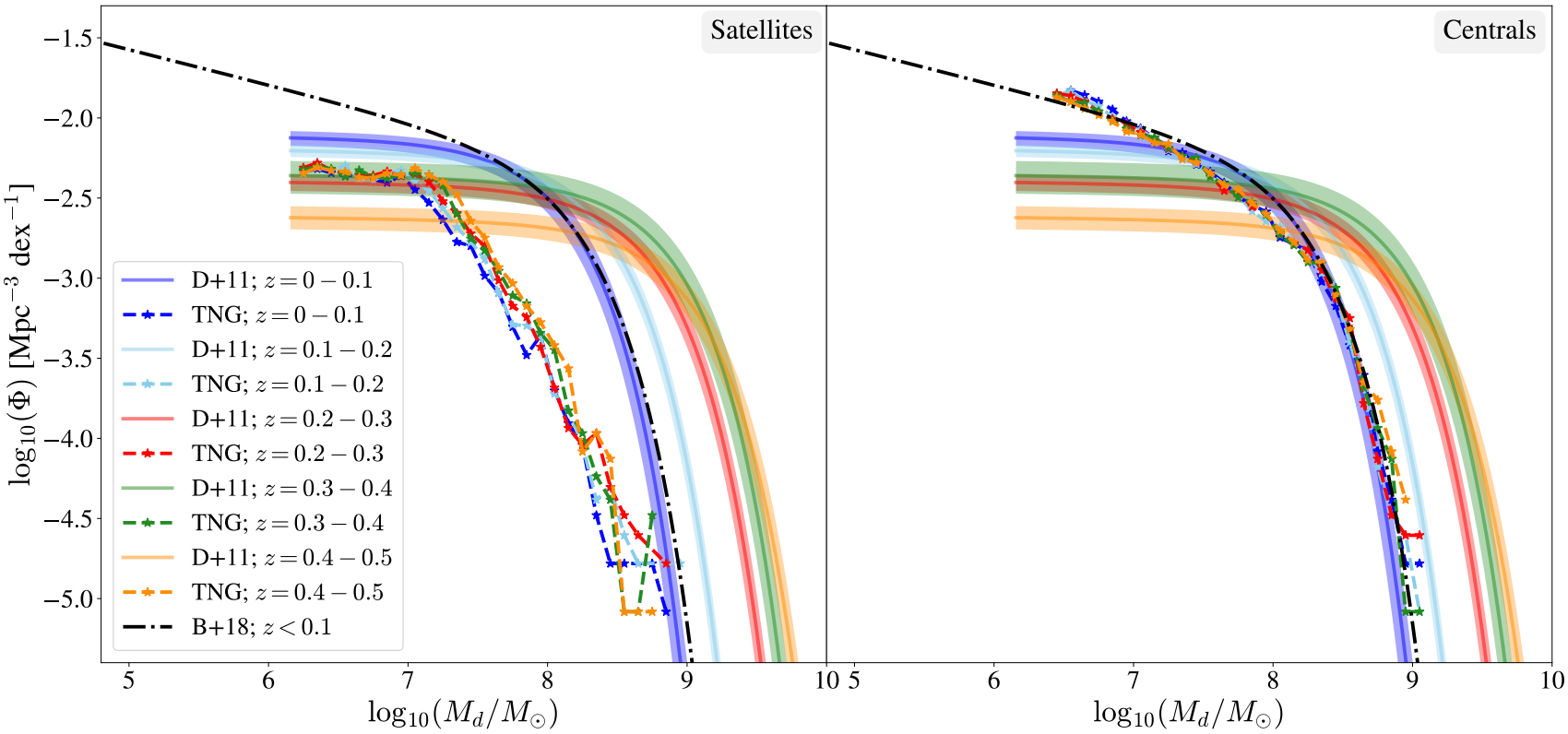

Figure B.4: Low redshift DMFs for IllustrisTNG galaxies *(stars and dashed lines)* and local DMFs from Beeston et al. (2018) *(black dash-dot line)* and Dunne et al. (2011) *(solid colour lines)*. The IllustrisTNG sources have been split into two populations: satellite *(left figure)* and central galaxies *(right figure)*. The DMF from Beeston et al. (2018) is based on an optically selected sample of 15750 galaxies within the redshift range $0.002 \leq z \leq 0.1$. The DMFs from Dunne et al. (2011) are based on a 250μm selected sample of 1867 galaxies with redshifts $z < 0.5$. The width of the line represents the error for the Beeston et al. (2018) DMF; the shaded regions are the errors for the Dunne et al. (2011) DMFs. The colours of the IllustrisTNG DMFs and DMFs from Dunne et al. (2011) are chosen to indicate the same redshift bins. Local observed DMFs are scaled to IllustrisTNG cosmology and dust masses scaled to $\kappa_{500,\mathrm{bound}}$.

BIBLIOGRAPHY

Abazajian K. N., et al., 2009, ApJS, 182, 543

Abdurro'uf Masayuki A., 2018, MNRAS, 479, 5083

Ahn C. P., et al., 2014, The Astrophysical Journal Supplement Series, 211, 17

Albareti F. D., et al., 2017, ApJS, 233, 25

Anderson L. D., et al., 2012, A&A, 542, A10

Andrews S. K., Driver S. P., Davies L. J. M., Kafle P. R., Robotham A. S. G., Wright A. H., 2017, MNRAS, 464, 1569

Arnouts S., et al., 2002, MNRAS, 329, 355

Astropy Collaboration et al., 2013, A&A, 558, A33

Auld R., et al., 2012, MNRAS, 420, 1882

Baes M., Verstappen J., De Looze I., Fritz J., Saftly W., Vidal Pérez E., Stalevski M., Valcke S., 2011, ApJS, 196, 22

Baes M., et al., 2020, MNRAS, 494, 2912

Barai P., Viel M., Murante G., Gaspari M., Borgani S., 2014, MNRAS, 437, 1456

Barnard E. E., 1907, ApJ, 25, 218

Barnard E. E., 1910, ApJ, 31, 8

Baum W. A., 1959, PASP, 71, 106

Beeston R. A., et al., 2018, MNRAS, 479, 1077

Bell E. F., McIntosh D. H., Katz N., Weinberg M. D., 2003, ApJS, 149, 289

Bertin E., Arnouts S., 1996, A&AS, 117, 393

Béthermin M., et al., 2015, A&A, 573, A113

Bieri R., 2018, PhD thesis, Université Pierre et Marie Curie

Bisigello L., Caputi K. I., Grogin N., Koekemoer A., 2018, A&A, 609, A82

Bolatto A. D., Wolfire M., Leroy A. K., 2013, ARA&A, 51, 207

Boquien M., Burgarella D., Roehlly Y., Buat V., Ciesla L., Corre D., Inoue A. K., Salas H., 2019, A&A, 622, A103

Boselli A., Gavazzi G., 2006, PASP, 118, 517

Boselli A., et al., 2010, PASP, 122, 261

Boselli A., Cortese L., Boquien M., Boissier S., Catinella B., Gavazzi G., Lagos C., Saintonge A., 2014, A&A, 564, A67

Bothwell M. S., et al., 2013, MNRAS, 429, 3047

Brusa M., et al., 2007, ApJS, 172, 353

Bruzual G., Charlot S., 2003, MNRAS, 344, 1000

Cañameras R., et al., 2018, A&A, 620, A61

Calistro Rivera G., et al., 2018, ApJ, 863, 56

Calzetti D., Armus L., Bohlin R. C., Kinney A. L., Koornneef J., Storchi-Bergmann T., 2000, ApJ, 533, 682

Camps P., Baes M., 2015, Astronomy and Computing, 9, 20

Camps P., Trayford J. W., Baes M., Theuns T., Schaller M., Schaye J., 2016, MNRAS, 462, 1057

Camps P., et al., 2018, ApJS, 234, 20

Carilli C. L., Walter F., 2013, ARA&A, 51, 105

Casasola V., et al., 2020, A&A, 633, A100

Casey C. M., et al., 2011, MNRAS, 415, 2723

Casey C. M., Narayanan D., Cooray A., 2014, Phys. Rep., 541, 45

Catinella B., et al., 2010, MNRAS, 403, 683

Cattaneo A., Dekel A., Faber S. M., Guiderdoni B., 2008, MNRAS, 389, 567

Cazaux S., Tielens A. G. G. M., 2002, ApJ, 575, L29

Cernicharo J., 2011, Infrared Astronomical Satellite. Springer Berlin Heidelberg, Berlin, Heidelberg, pp 809–810, doi:10.1007/978-3-642-11274-4_785, https://doi.org/10.1007/978-3-642-11274-4_785

Chabrier G., 2003, PASP, 115, 763

Chapin E. L., et al., 2009, MNRAS, 398, 1793

Charlot S., Fall S. M., 2000, ApJ, 539, 718

Chawner H., et al., 2019, MNRAS, 483, 70

Chowdhury A., Kanekar N., Chengalur J., Sethi S., Dwarakanath K. S., 2020, arXiv e-prints, p. arXiv:2010.06617

Cibinel A., et al., 2019, MNRAS, 485, 5631

Ciesla L., et al., 2015, A&A, 576, A10

Ciesla L., et al., 2016, A&A, 585, A43

Civano F., et al., 2016, ApJ, 819, 62

Clark C. J. R., et al., 2015, MNRAS, 452, 397

Clark C. J. R., Schofield S. P., Gomez H. L., Davies J. I., 2016, MNRAS, 459, 1646

Clark C. J. R., et al., 2019, MNRAS, 489, 5256

Clemens M. S., et al., 2013, MNRAS, 433, 695

Clements D. L., Dunne L., Eales S., 2010, MNRAS, 403, 274

Combes F., 2015, in Ziegler B. L., Combes F., Dannerbauer H., Verdugo M., eds, IAU Symposium Vol. 309, Galaxies in 3D across the Universe. pp 182–189 (arXiv:1408.1591), doi:10.1017/S1743921314009636

Combes F., 2018, A&A Rev., 26, 5

Cool R. J., et al., 2013, ApJ, 767, 118

Coppin K. E. K., et al., 2009, MNRAS, 395, 1905

Corcho-Caballero P., Ascasibar Y., López-Sánchez Á. R., 2020, MNRAS,

Cortese L., 2012, A&A, 543, A132

Cortese L., et al., 2010, A&A, 518, L49

Cox D. P., 2005, ARA&A, 43, 337

Crain R. A., et al., 2015, MNRAS, 450, 1937

Daddi E., et al., 2007, ApJ, 670, 156

Dale D. A., et al., 2012, ApJ, 745, 95

Davé R., Anglés-Alcázar D., Narayanan D., Li Q., Rafieferantsoa M. H., Appleby S., 2019, MNRAS, 486, 2827

Davé R., Crain R. A., Stevens A. R. H., Narayanan D., Saintonge A., Catinella B., Cortese L., 2020, arXiv e-prints, p. arXiv:2002.07226

Davidzon I., et al., 2017, A&A, 605, A70

Davies L. J. M., et al., 2015a, MNRAS, 447, 1014

Davies L. J. M., et al., 2015b, MNRAS, 452, 616

Davies J. I., et al., 2017, PASP, 129, 044102

Davis M., Efstathiou G., Frenk C. S., White S. D. M., 1985, ApJ, 292, 371

De Cia A., Ledoux C., Savaglio S., Schady P., Vreeswijk P. M., 2013, A&A, 560, A88

De Vis P., et al., 2017a, MNRAS, 464, 4680

De Vis P., et al., 2017b, MNRAS, 471, 1743

De Vis P., et al., 2019, A&A, 623, A5

Decarli R., et al., 2016, ApJ, 833, 70

Dempsey J. T., et al., 2013, MNRAS, 430, 2534

Diemer B., 2018, The Astrophysical Journal Supplement Series, 239, 35

Diemer B., et al., 2018, ApJS, 238, 33

Diemer B., et al., 2019, MNRAS, 487, 1529

Doherty C. L., Gil-Pons P., Lau H. H. B., Lattanzio J. C., Siess L., 2014, MNRAS, 437, 195

Dolag K., Borgani S., Murante G., Springel V., 2009, MNRAS, 399, 497

Dole H., et al., 2006, A&A, 451, 417

Donley J. L., et al., 2012, ApJ, 748, 142

Draine B. T., Li A., 2007, ApJ, 657, 810

Driver S. P., et al., 2009, Astronomy and Geophysics, 50, 5.12

Driver S. P., et al., 2011, MNRAS, 413, 971

Driver S. P., et al., 2018, MNRAS, 475, 2891

Dudzevičiūtė U., et al., 2019, arXiv e-prints, p. arXiv:1910.07524

Duncan K. J., et al., 2018a, MNRAS, 473, 2655

Duncan K. J., Jarvis M. J., Brown M. J. I., Röttgering H. J. A., 2018b, MNRAS, 477, 5177

Dunne L., Eales S. A., 2001a, MNRAS, 327, 697

Dunne L., Eales S. A., 2001b, MNRAS, 327, 697

Dunne L., Eales S., Edmunds M., Ivison R., Alexander P., Clements D. L., 2000, MNRAS, 315, 115

Dunne L., Eales S. A., Edmunds M. G., 2003a, MNRAS, 341, 589

Dunne L., Eales S., Ivison R., Morgan H., Edmunds M., 2003b, Nature, 424, 285

Dunne L., et al., 2011, MNRAS, 417, 1510

Dwek E., Cherchneff I., 2011, ApJ, 727, 63

Dwek E., Galliano F., Jones A. P., 2007, ApJ, 662, 927

Eales S. A., Wynn-Williams C. G., Duncan W. D., 1989, ApJ, 339, 859

Eales S., et al., 2009, ApJ, 707, 1779

Eales S., et al., 2010, PASP, 122, 499

Eales S., et al., 2012, ApJ, 761, 168

Eales S., et al., 2018a, MNRAS, 473, 3507

Eales S. A., et al., 2018b, MNRAS, 481, 1183

Elbaz D., et al., 2007, A&A, 468, 33

Ewen H. I., Purcell E. M., 1951, Nature, 168, 356

Ferland G. J., Korista K. T., Verner D. A., Ferguson J. W., Kingdon J. B., Verner E. M., 1998, PASP, 110, 761

Fernández X., et al., 2016, ApJ, 824, L1

Ferrarotti A. S., Gail H. P., 2006, A&A, 447, 553

Ferrière K. M., 2001, Reviews of Modern Physics, 73, 1031

Field G. B., Goldsmith D. W., Habing H. J., 1969, ApJ, 155, L149

Fishlock C. K., Karakas A. I., Lugaro M., Yong D., 2014, ApJ, 797, 44

Fixsen D. J., Dwek E., Mather J. C., Bennett C. L., Shafer R. A., 1998, ApJ, 508, 123

Fritz J., Franceschini A., Hatziminaoglou E., 2006, MNRAS, 366, 767

Galilei G., 1610, Starry Messenger

Gall C., et al., 2014, Nature, 511, 326

Geach J. E., et al., 2017, MNRAS, 465, 1789

Genel S., et al., 2014, MNRAS, 445, 175

Genel S., et al., 2018, MNRAS, 474, 3976

Genzel R., et al., 2015, ApJ, 800, 20

Gomez H. L., et al., 2010, A&A, 518, L45

Gomez H. L., et al., 2012, ApJ, 760, 96

Gould R. J., Salpeter E. E., 1963, ApJ, 138, 393

Greve T. R., et al., 2005, MNRAS, 359, 1165

Guth A. H., 1981, Phys. Rev. D, 23, 347

Harrington K. C., et al., 2018, MNRAS, 474, 3866

Harrison C. M., 2017, Nature Astronomy, 1, 0165

Harrison C. M., Costa T., Tadhunter C. N., Flütsch A., Kakkad D., Perna M., Vietri G., 2018, Nature Astronomy, 2, 198

Hayward C. C., Hopkins P. F., 2017, MNRAS, 465, 1682

Hayward C. C., et al., 2020, Submillimetre galaxies in cosmological hydrodynamical simulations – an opportunity for constraining feedback models (arXiv:2007.01885)

Herschel W., 1785, Philosophical Transactions of the Royal Society of London Series I, 75, 213

Herschel W., 1800, Philosophical Transactions of the Royal Society of London Series I, 90, 255

Herschel W., 1811, Philosophical Transactions of the Royal Society of London Series I, 101, 269

Hildebrand R. H., 1983, QJRAS, 24, 267

Hoaglin D., Mosteller F., Tukey J., 1983, Understanding robust and exploratory data analysis. Wiley series in probability and mathematical statistics: Applied probability and statistics, Wiley

Holland W. S., et al., 1999, MNRAS, 303, 659

Holland W. S., et al., 2013, MNRAS, 430, 2513

Hollenbach D., Salpeter E. E., 1970, J. Chem. Phys., 53, 79

Hollenbach D., Salpeter E. E., 1971, ApJ, 163, 155

Hollenbach D. J., Werner M. W., Salpeter E. E., 1971, ApJ, 163, 165

Hubble E. P., 1925, Popular Astronomy, 33, 252

Hubble E. P., 1926, ApJ, 64, 321

Hubble E. P., 1929, ApJ, 69, 103

Hubble E. P., 1936, Realm of the Nebulae

Hung C.-L., et al., 2013, ApJ, 778, 129

Hunt L. K., et al., 2019, A&A, 621, A51

Hunter J. D., 2007, Computing in Science Engineering, 9, 90

Hurley P. D., et al., 2017, MNRAS, 464, 885

Ilbert O., et al., 2006, A&A, 457, 841

Inoguchi M., Hosokawa T., Mineshige S., Kim J.-G., 2020, MNRAS, 497, 5061

Inoue A. K., 2003, PASJ, 55, 901

James A., Dunne L., Eales S., Edmunds M. G., 2002, MNRAS, 335, 753

Jenkins E. B., 2009, ApJ, 700, 1299

Jones A. P., 2004, in Witt A. N., Clayton G. C., Draine B. T., eds, Astronomical Society of the Pacific Conference Series Vol. 309, Astrophysics of Dust. p. 347

Jones A. P., Nuth J. A., 2011, A&A, 530, A44

Jones A. P., Tielens A. G. G. M., Hollenbach D. J., 1996, ApJ, 469, 740

Jones M., Lambourne R., Adams D., Cayless A., Jones A., 2004, An Introduction to Galaxies and Cosmology. S 282, Open University, https://books.google.co.uk/books?id=36K1PfetZegC

Kant I., 1755, Universal Natural History and Theory of the Heavens

Kapteyn J. C., 1909, ApJ, 29, 46

Karakas A. I., 2010, MNRAS, 403, 1413

Karim A., et al., 2011, ApJ, 730, 61

Kelvin L. S., et al., 2014, MNRAS, 444, 1647

Kim S.-H., Martin P. G., Hendry P. D., 1994, ApJ, 422, 164

Kirchhoff G., 1860, Annalen der Physik, 185, 275

Klessen R. S., Glover S. C. O., 2016, Saas-Fee Advanced Course, 43, 85

Klimentowski J., Łokas E. L., Knebe A. e., Gottlöber S., Martinez-Vaquero L. A., Yepes G., Hoffman Y., 2010, MNRAS, 402, 1899

Kobayashi C., Umeda H., Nomoto K., Tominaga N., Ohkubo T., 2006, ApJ, 653, 1145

Lagos C. D. P., Baugh C. M., Lacey C. G., Benson A. J., Kim H.-S., Power C., 2011, MNRAS, 418, 1649

Lagos C. d. P., et al., 2019, MNRAS, 489, 4196

Lah P., et al., 2007, MNRAS, 376, 1357

Laigle C., et al., 2016, ApJS, 224, 24

Lang P., et al., 2019, ApJ, 879, 54

Le Fèvre O., et al., 2013, A&A, 559, A14

Leavitt H. S., Pickering E. C., 1912, Harvard College Observatory Circular, 173, 1

Lee N., et al., 2015, ApJ, 801, 80

Lee B., et al., 2018, ApJ, 853, 131

Leroy A. K., et al., 2011, ApJ, 737, 12

Leslie S. K., et al., 2020, ApJ, 899, 58

Li Q., Narayanan D., Davé R., 2019, MNRAS, 490, 1425

Liang L., et al., 2019, MNRAS, p. 2072

Lilly S. J., et al., 2007, The Astrophysical Journal Supplement Series, 172, 70

Lilly S. J., Carollo C. M., Pipino A., Renzini A., Peng Y., 2013, ApJ, 772, 119

Liske J., et al., 2015, MNRAS, 452, 2087

Luo W., Yang X., Zhang Y., 2014, ApJ, 789, L16

Madau P., Dickinson M., 2014, Annual Review of Astronomy and Astrophysics, 52, 415

Madden S. C., et al., 2013, PASP, 125, 600

Magnelli B., et al., 2014, A&A, 561, A86

Małek K., et al., 2018, A&A, 620, A50

Malek K., Buat V., Burgarella D., Roehlly Y., Shirley R., the HELP team 2019, arXiv e-prints, p. arXiv:1904.12498

Marchesi S., et al., 2016, ApJ, 817, 34

Marinacci F., et al., 2018, MNRAS, 480, 5113

Matsuura M., et al., 2011, Science, 333, 1258

Matsuura M., et al., 2015, ApJ, 800, 50

McCracken H. J., et al., 2010, ApJ, 708, 202

McCracken H. J., et al., 2012, A&A, 544, A156

McKee C. F., Ostriker J. P., 1977, ApJ, 218, 148

McKinney W., 2010, in van der Walt S., Millman J., eds, Proceedings of the 9th Python in Science Conference. pp 51 – 56

McKinnon R., Torrey P., Vogelsberger M., 2016, MNRAS, 457, 3775

McKinnon R., Kannan R., Vogelsberger M., O'Neil S., Torrey P., Li H., 2019, arXiv e-prints, p. arXiv:1912.02825

Messier C., 1774, Memoirs of the French Academy of Sciences for 1771, pp 435–461

Meyer D. M., Jura M., Cardelli J. A., 1998, ApJ, 493, 222

Michałowski M. J., Murphy E. J., Hjorth J., Watson D., Gall C., Dunlop J. S., 2010a, A&A, 522, A15

Michałowski M. J., Watson D., Hjorth J., 2010b, ApJ, 712, 942

Michałowski M. J., et al., 2017, MNRAS, 469, 492

Millard J. S., et al., 2020, MNRAS, 494, 293

Millard J. S., Diemer B., Eales S. A., Gomez H. L., Beeston R., Smith M. W. L., 2021, MNRAS, 500, 871

Miyazaki S., et al., 2002, PASJ, 54, 833

Morgan H. L., Edmunds M. G., 2003, MNRAS, 343, 427

Morganti R., 2017, Frontiers in Astronomy and Space Sciences, 4, 42

Moster B. P., Somerville R. S., Newman J. A., Rix H.-W., 2011, ApJ, 731, 113

Naiman J. P., et al., 2018, MNRAS, 477, 1206

Narayanan D., Krumholz M. R., Ostriker E. C., Hernquist L., 2012, MNRAS, 421, 3127

Neistein E., van den Bosch F. C., Dekel A., 2006, MNRAS, 372, 933

Nelson D., et al., 2018a, MNRAS, 475, 624

Nelson D., et al., 2018b, Monthly Notices of the Royal Astronomical Society, 477, 450

Nelson D., et al., 2019, Computational Astrophysics and Cosmology, 6, 2

Nguyen H. T., et al., 2010, A&A, 518, L5

Noeske K. G., et al., 2007, ApJ, 660, L43

Noll S., Burgarella D., Giovannoli E., Buat V., Marcillac D., Muñoz-Mateos J. C., 2009, A&A, 507, 1793

Nomoto K., Iwamoto K., Nakasato N., Thielemann F. K., Brachwitz F., Tsujimoto T., Kubo Y., Kishimoto N., 1997, Nucl. Phys. A, 621, 467

Oemler Augustus J., Abramson L. E., Gladders M. D., Dressler A., Poggianti B. M., Vulcani B., 2017, ApJ, 844, 45

Parsons W., 1850, Philosophical Transactions of the Royal Society, 140, 499

Pearson E. A., et al., 2013, MNRAS, 435, 2753

Peebles P. J. E., 1980, The large-scale structure of the universe

Peng Y.-j., Maiolino R., 2014, MNRAS, 443, 3643

Peng Y.-j., et al., 2010, ApJ, 721, 193

Perets H. B., Biham O., Manicó G., Pirronello V., Roser J., Swords S., Vidali G., 2005, ApJ, 627, 850

Pilbratt G. L., et al., 2010, A&A, 518, L1

Pillepich A., et al., 2018a, MNRAS, 473, 4077

Pillepich A., et al., 2018b, MNRAS, 475, 648

Pineda J. L., Langer W. D., Velusamy T., Goldsmith P. F., 2013, A&A, 554, A103

Pirronello V., Biham O., Liu C., Shen L., Vidali G., 1998, in Chela-Flores J., Raulin F., eds, Exobiology: Matter, Energy, and Information in the Origin and Evolution of Life in the Universe. Springer Netherlands, Dordrecht, pp 287–290

Planck Collaboration et al., 2011, A&A, 536, A21

Planck Collaboration et al., 2016, A&A, 594, A13

Pope A., Aretxaga I., Hughes D., Wilson G., Yun M., 2019, in American Astronomical Society Meeting Abstracts #233. p. 363.20

Popping G., Somerville R. S., Galametz M., 2017, MNRAS, 471, 3152

Popping G., et al., 2019, ApJ, 882, 137

Portinari L., Chiosi C., Bressan A., 1998, A&A, 334, 505

Pozzi F., Calura F., Zamorani G., Delvecchio I., Gruppioni C., Santini P., 2020, MNRAS, 491, 5073

Price-Whelan A. M., et al., 2018, AJ, 156, 123

Puget J. L., Abergel A., Bernard J. P., Boulanger F., Burton W. B., Desert F. X., Hartmann D., 1996, A&A, 308, L5

Péroux C., Howk J. C., 2020, Annual Review of Astronomy and Astrophysics, 58, 363

Rémy-Ruyer A., et al., 2014a, A&A, 563, A31

Rémy-Ruyer A., et al., 2014b, A&A, 563, A31

Renzini A., Peng Y.-j., 2015, ApJ, 801, L29

Riechers D. A., et al., 2013, Nature, 496, 329

Rieke G. H., et al., 2004, ApJS, 154, 25

Riess A. G., Casertano S., Yuan W., Macri L. M., Scolnic D., 2019, ApJ, 876, 85

Roberts J. F., Rawlings J. M. C., Viti S., Williams D. A., 2007, MNRAS, 382, 733

Robitaille T., 2019, APLpy v2.0: The Astronomical Plotting Library in Python, doi:10.5281/zenodo.2567476, https://doi.org/10.5281/zenodo.2567476

Robitaille T., Bressert E., 2012, APLpy: Astronomical Plotting Library in Python, Astrophysics Source Code Library (ascl:1208.017)

Rodighiero G., et al., 2011, ApJ, 739, L40

Roman-Duval J., et al., 2019, ApJ, 871, 151

Saintonge A., et al., 2011, MNRAS, 415, 61

Saintonge A., et al., 2012, ApJ, 758, 73

Saintonge A., et al., 2016, MNRAS, 462, 1749

Saintonge A., et al., 2017, ApJS, 233, 22

Sandstrom K. M., et al., 2013, ApJ, 777, 5

Santini P., et al., 2010, A&A, 518, L154

Santini P., et al., 2014, A&A, 562, A30

Sarangi A., Matsuura M., Micelotta E. R., 2018, Space Sci. Rev., 214, 63

Sargent B. A., et al., 2010, ApJ, 716, 878

Sargent M. T., et al., 2014, ApJ, 793, 19

Schaye J., et al., 2015, MNRAS, 446, 521

Schechter P., 1976, ApJ, 203, 297

Schloerb P., et al., 2019, in Bulletin of the American Astronomical Society. p. 148

Schreiber C., et al., 2015, A&A, 575, A74

Schulz S., Popping G., Pillepich A., Nelson D., Vogelsberger M., Marinacci F., Hernquist L., 2020, arXiv e-prints, p. arXiv:2001.04992

Scoville N., et al., 2007, The Astrophysical Journal Supplement Series, 172, 1

Scoville N., et al., 2014, ApJ, 783, 84

Scoville N., Faisst A., Capak P., Kakazu Y., Li G., Steinhardt C., 2015, ApJ, 800, 108

Scoville N., et al., 2016, ApJ, 820, 83

Scoville N., et al., 2017, ApJ, 837, 150

Seymour N., et al., 2008, MNRAS, 386, 1695

Shapley H., 1919, ApJ, 49, 311

Shapley H., Curtis H. D., 1921, Bulletin of the National Research Council, 2, 171

Shen X., et al., 2020, arXiv e-prints, p. arXiv:2002.10474

Sheth K., et al., 2008, ApJ, 675, 1141

Shirley R., et al., 2019, arXiv e-prints, p. arXiv:1909.04003

Sijacki D., Vogelsberger M., Genel S., Springel V., Torrey P., Snyder G. F., Nelson D., Hernquist L., 2015, MNRAS, 452, 575

Simpson J. M., et al., 2019, ApJ, 880, 43

Smith M. W. L., et al., 2012, ApJ, 756, 40

Solomon P. M., Vanden Bout P. A., 2005, ARA&A, 43, 677

Sorba R., Sawicki M., 2015, MNRAS, 452, 235

Sorba R., Sawicki M., 2018, MNRAS, 476, 1532

Springel V., 2010, MNRAS, 401, 791

Springel V., Hernquist L., 2003, MNRAS, 339, 289

Springel V., White S. D. M., Tormen G., Kauffmann G., 2001, MNRAS, 328, 726

Springel V., et al., 2018, MNRAS, 475, 676

Stach S. M., et al., 2019, MNRAS, 487, 4648

Stanway E. R., McMahon R. G., Bunker A. J., 2005, MNRAS, 359, 1184

Steinicke W., 2012, Journal of Astronomical History and Heritage, 15, 19

Stevens A. R. H., et al., 2019, MNRAS, 483, 5334

Strateva I., et al., 2001, AJ, 122, 1861

Struve F. G. W., 1847, Etudes d'Astronomie Stellaire: Sur la voie lactee et sur la distance des etoiles fixes

Sugerman B. E. K., et al., 2006, Science, 313, 196

Suh H., et al., 2019, ApJ, 872, 168

Symeonidis M., Giblin B. M., Page M. J., Pearson C., Bendo G., Seymour N., Oliver S. J., 2016, MNRAS, 459, 257

Tacconi L. J., et al., 2010, Nature, 463, 781

Tacconi L. J., et al., 2013, ApJ, 768, 74

Tacconi L. J., et al., 2018, ApJ, 853, 179

Takeuchi T. T., Morokuma-Matsui K., Iono D., Hirashita H., Tee W. L., Wang W.-H., Momose R., 2016, arXiv e-prints, p. arXiv:1603.01938

Taniguchi Y., et al., 2007, ApJS, 172, 9

Taniguchi Y., et al., 2015, PASJ, 67, 104

Tapia M., et al., 2020, in American Astronomical Society Meeting Abstracts #236. p. 243.01

Taylor M. B., 2005a, in Shopbell P., Britton M., Ebert R., eds, Astronomical Society of the Pacific Conference Series Vol. 347, Astronomical Data Analysis Software and Systems XIV. p. 29

Taylor M. B., 2005b, in Shopbell P., Britton M., Ebert R., eds, Astronomical Society of the Pacific Conference Series Vol. 347, Astronomical Data Analysis Software and Systems XIV. p. 29

Terrazas B. A., et al., 2020, MNRAS, 493, 1888

Thomas D., Davies R. L., 2006, MNRAS, 366, 510

Tielens A. G. G. M., Allamandola L. J., 1987, Composition, Structure, and Chemistry of Interstellar Dust. p. 397, doi:10.1007/978-94-009-3861-8_16

Tielens A. G. G. M., McKee C. F., Seab C. G., Hollenbach D. J., 1994, ApJ, 431, 321

Timberlake T., 2011, arXiv e-prints, p. arXiv:1112.3635

Todini P., Ferrara A., 2001, MNRAS, 325, 726

Tomczak A. R., et al., 2016, ApJ, 817, 118

Torrey P., Vogelsberger M., Sijacki D., Springel V., Hernquist L., 2012, Monthly Notices of the Royal Astronomical Society, 427, 2224–2238

Torrey P., Vogelsberger M., Genel S., Sijacki D., Springel V., Hernquist L., 2014, MNRAS, 438, 1985

Torrey P., et al., 2019, MNRAS, 484, 5587

Trumpler R. J., 1930, Lick Observatory Bulletin, 420, 154

Vaccari M., 2016, in The Universe of Digital Sky Surveys. p. 71 (arXiv:1508.06444), doi:10.1007/978-3-319-19330-4_10

Valiante R., Schneider R., Bianchi S., Andersen A. C., 2009, MNRAS, 397, 1661

Valiante R., Schneider R., Salvadori S., Bianchi S., 2011, MNRAS, 416, 1916

Vidali G., Roser J., Manicó G., Pirronello V., Perets H. B., Biham O., 2005, in Journal of Physics Conference Series. pp 36–58 (arXiv:astro-ph/0504543), doi:10.1088/1742-6596/6/1/003

Viero M. P., et al., 2013, ApJ, 779, 32

Virtanen P., et al., 2020, Nature Methods, 17, 261

Visvanathan N., 1981, A&A, 100, L20

Vlahakis C., Dunne L., Eales S., 2005, MNRAS, 364, 1253

Vogelsberger M., Genel S., Sijacki D., Torrey P., Springel V., Hernquist L., 2013, MNRAS, 436, 3031

Vogelsberger M., et al., 2014a, MNRAS, 444, 1518

Vogelsberger M., et al., 2014b, Nature, 509, 177

Vogelsberger M., Marinacci F., Torrey P., Puchwein E., 2020a, Nature Reviews Physics, 2, 42

Vogelsberger M., et al., 2020b, MNRAS, 492, 5167

Wakelam V., et al., 2017, Molecular Astrophysics, 9, 1

Weigel A. K., Schawinski K., Bruderer C., 2016, MNRAS, 459, 2150

Weigel A. K., et al., 2017, ApJ, 845, 145

Weinberger R., et al., 2017, MNRAS, 465, 3291

Weinberger R., et al., 2018, MNRAS, 479, 4056

Whitaker K. E., van Dokkum P. G., Brammer G., Franx M., 2012, ApJ, 754, L29

Whitaker K. E., et al., 2014, ApJ, 795, 104

Whittet D., 2002, Dust in the Galactic Environment, 2nd Edition. Series in Astronomy and Astrophysics, Taylor & Francis, https://books.google.co.uk/books?id=k21lk4s0RpEC

Wiersma R. P. C., Schaye J., Theuns T., Dalla Vecchia C., Tornatore L., 2009, MNRAS, 399, 574

Wilkins S. M., Bunker A. J., Stanway E., Lorenzoni S., Caruana J., 2011, MNRAS, 417, 717

Wilman D. J., Erwin P., 2012, ApJ, 746, 160

Wiseman P., Schady P., Bolmer J., Krühler T., Yates R. M., Greiner J., Fynbo J. P. U., 2017, A&A, 599, A24

Wright T., 1750, An Original Theory or New Hypothesis of the Universe. Printed for the author, sold by H. Chapelle

Wright E. L., 2006, PASP, 118, 1711

Wright A. H., et al., 2016, MNRAS, 460, 765

Yajima H., Nagamine K., Thompson R., Choi J.-H., 2014, MNRAS, 439, 3073

Yin J., Hou J. L., Prantzos N., Boissier S., Chang R. X., Shen S. Y., Zhang B., 2009, A&A, 505, 497

Zafar T., Watson D., 2013, A&A, 560, A26

Zinger E., et al., 2020, arXiv e-prints, p. arXiv:2004.06132

al-Sufi A. a. R. 964, Book of Fixed Stars

da Cunha E., Charlot S., Elbaz D., 2008, MNRAS, 388, 1595

da Cunha E., et al., 2013, ApJ, 766, 13

van Maanen A., 1916, ApJ, 44, 210

van de Hulst H., 1945, Nederlands Tijdschrift voor Natuurkunde, 11, 210

van de Hulst H. C., 1949, The solid particles in interstellar space.

van der Walt S., Colbert S. C., Varoquaux G., 2011, Computing in Science Engineering, 13, 22

van der Wel A., et al., 2014, ApJ, 788, 28

'Mischief Managed!'

HARRY POTTER